RELIABILITY ASSESSMENT OF DRAG ANCHORS AND DRILL STRINGS IN FLOATING OFFSHORE DRILLING UNITS

by

© Mohammad Javad Moharrami

A Thesis Submitted to the
School of Graduate Studies

in partial fulfillment of the requirements for the degree of

Doctor of Philosophy

Faculty of Engineering and Applied Science

Memorial University of Newfoundland

February 2021

St. John's Newfoundland Canada

ABSTRACT

As the oil and gas explorations move to deep and ultra-deep water, reliable and economical operation of floating offshore drilling units becomes significantly important. Despite significant improvements achieved in design of all of the components involved in drilling operation, there are still operation failure reports that threaten the vulnerable offshore environment. This, in turn, mandates the reliability assessment of the key elements of these floating drilling units. The station keeping of drilling platform in harsh environment and the structural integrity of the drilling system under both vibrations and environmental loads are the key areas of concern that affect the reliability of these systems. In this study, two crucial elements affecting the overall system reliability was investigated, including the reliability of drag embedment anchors, as a key element of station keeping, and the fatigue reliability of drill strings, as a key element of structural integrity. First, a comprehensive reliability analysis of drag embedment anchors was conducted through the probabilistic modelling of anchor capacity and incorporation of inherent uncertainties. A plastic yield loci was used to characterize the fluke-soil interaction and failure states. The embedded profile and the frictional capacity of the anchor chain at the seabed were also considered in the calculation of ultimate holding capacity. A 3D coupled finite element (FE) model was developed to obtain the characteristic mean and maximum dynamic line tensions for 100 years return period sea states, as well as the design line tension and corresponding line angle at mudline. Catenary mooring system was considered to maximize the vessel motions and approach the worst case scenarios. First order reliability method (FORM) was used through an iterative procedure to obtain the probabilistic failures. The study revealed the

sensitivity of the reliability to key components of anchor geometry, seabed soil properties, and the environmental loads. The study revealed that the reliability index depends on the fluke length and is largely irrelevant to the anchor weight. As well, the level of the reliability indices obtained for drag embedment anchors was found to be lower than the other anchoring solutions such as suction caissons.

Second, the fatigue reliability assessment of the drill string under stick-slip vibration and first-order vessel motions was comprehensively investigated. An efficient approach for FE modeling of stick-slip vibrations of the full drill strings was developed, and a comprehensive analysis was conducted to observe the influence of the field operating parameters on the structural dynamic response of the full-scaled drill string under stick-slip vibration. The model was developed based on a rate-dependent formulation of bit-rock interaction, for which the cutting process is integrated through the frictional contact. The nonlinear effects of large rotations, the geometrically nonlinear axial-torsional coupling, and the effect of energy dissipation due to the presence of drill mud were taken into account. The performance of the developed numerical model was verified through comparisons with a lumped-parameter model and published field test results. Time-domain analyses were conducted by incorporation of both stick-slip vibration and vessel motion under the environment loads. Then the fatigue reliability assessment of drill string was conducted by damage calculation under different excitation scenarios using the deterministic S-N curve approach and defining the safe, low risk, and high risk damage zones. The points of most severe fatigue damage and the corresponding risk under simultaneous drilling vessel motions and mechanical vibrations were identified. The results showed the significant influence of the rotary table velocity on the stick-slip characteristics

of the drill string in comparison with other field operating parameters, i.e., weight-on-bit and damping ratio. It was found that the coexistence of stick-slip vibrations and horizontal vessel motions is detrimental to reliable performance of the drill string and can result in premature fatigue failure of the top-most drill pipe, the drill pipe passing through the BOP, and the lower drill pipe connected to drill collar.

Overall, the study provided an in-depth insight into this challenging area of engineering and resulted in developing robust methodologies for reliability assessment of the key components of floating drill systems from station keeping to drill string.

STATEMENT OF AUTHORSHIP

I had the opportunity to conduct an industrially relevant R&D project on the reliability of drag anchors for TechnipFMC under the supervision of my supervisor Dr. Hodjat Shiri from March 2018 to October 2018. Also, I conducted collaborative research work as a visiting student at the Offshore Mechanics Laboratory (LMO), University of São Paulo (USP), Brazil, under supervision of Prof. Clóvis de Arruda Martins. The visit was financially supported by Mitacs Globalink Research Award. Throughout my visit at USP, I consistently prepared and delivered weekly progress reports to my home supervisor Dr. Hodjat Shiri, elaborating the selected research topic, methodology, difficulties, conducted works, and possible solutions to the problem. During the visit, I was fortunate to attend the "Advanced Analytical Mechanics" course taught by Prof. Celso Pupo Pesce, Prof. Clóvis de Arruda Martins, and Dr. Renato Maia Matarazzo Orsino. I also took the "Design of Ocean Systems" course taught by Prof. Kazuo Nishimoto, as well as the "Advanced Sciences on Nonlinear Dynamics" workshop.

Contributions of the author of this thesis include data curation, investigation, methodology, software, validation, visualization, and writing original drafts. Contributions of Dr. Hodjat Shiri include funding acquisition, conceptualization, supervision, writing - review and editing. Contributions of Prof. Clóvis de Arruda Martins include conceptualization, supervision, writing - review and editing.

To my mother, father, and brother.

ACKNOWLEDGMENT

I would like to express my sincere gratitude to my supervisor, Dr. Hodjat Shiri, for providing me with the great opportunity to join his research team and involving me in this challenging research topic. I am grateful for his unconditional supports, keen supervision, professional guidance, and excellent writing advice throughout this research study. His role in my personal and professional growth is undoubtedly constructive.

I would like to extend my heartfelt appreciation to Prof. Clóvis de Arruda Martins for his excellent directions and supervision, and vast knowledge during my visit at the University of São Paulo and afterwards. I am also grateful to Prof. Celso Pupo Pesce for his kind supports and inspiring manners; I learned a lot from his insights.

My special thanks to Fernando Geremias Toni and Eduardo Ribeiro Malta for their invaluable discussions on finite element modeling of drill string in ABAQUS. Also, thanks must go to Amir Hamed and Rahim Shoghi for their engineering/scientific discussions.

I would also like to thank my supervisory committee members at Memorial University, Dr. Amgad A. Hussein and Dr. Noori Saady for their support and encouragement.

I gratefully acknowledge the financial support of this research by the Research and Development Corporation (RDC) (now TCII) through the Ignite funding program, the Memorial University of Newfoundland through VP start-up funding support, Natural Sciences and Engineering Research Council of Canada (NSERC) through the Engage funding program, and Mitacs through Globalink program. Special thanks are extended to the School of Graduate Studies (SGS) and Faculty of Engineering and Applied Science at

Memorial University for providing financial supports and excellent resources to conduct this research project.

Indeed, I would have not been where I am now without the help of my family and friends. In particular, I would like to extend my boundless and heartfelt appreciation to my family for their unconditional love, supports, sacrifices, prayers, and encouragement throughout my life. Also, thanks to my friends for enriching my life and increasing my sense of belonging and purpose.

Contents

List of Figures

List of Tables

List of Symbols

Roman

2A	peak-to-peak amplitude of angular velocity
b_c	chain of effective width
b_f	fluke width
b_s	shank width
B	number of stress range blocks
c_b	equivalent viscous damping coefficient of drill collars/bit
c_p	equivalent viscous damping coefficient of drill pipe
$\hat{c}$	viscous damping coefficient per unit length of the drill pipe
d_a	padeye embedment depth
d_c	drill collar inner diameter
d_f	fluke thickness
d_p	drill pipe inner diameter
d_t	fluke tip depth
d_w	wave direction
d_{wc}	current direction relative to wave
d_{ww}	wind direction relative to wave
D	damage ratio
D_c	drill collar outer diameter
D_p	drill pipe outer diameter

E	Young´s modulus
f	form factor (Neubecker and Randolph 1996)
f	yield locus function
f_D	dominant frequency
f_n	natural frequency
F	friction force
F_1, F_2	normal and sliding shank resistance
G	shear modulus
H	load component parallel to the top face of the fluke
H	wave height
H_1	offset H for curve fitting (H when $\delta h = 0$)
H_{max}	maximum load capacity parallel to the top face of the fluke
H_s	significant wave height
I_c	polar moment of inertia of the drill collar section
I_p	polar moment of inertia of the drill pipe section
J	mass moment of inertia matrix
J_b	mass moment of inertia of drill bit
J_c	mass moment of inertia of drill collar
J_p	mass moment of inertia of drill pipe
k_a	surface condition modification factor
k_b	size modification factor
k_c	reliability factor
k_f	stress concentration factor for fatigue

k_p	torsional stiffness of drill pipe
K	torsional stiffness matrix
L_1	height from bit to stabilizer
L_2	height from seabed to flex joint
L_c	drill collar length
L_f	caisson length (Silvia-Gonzalez et al., 2013)
L_f	fluke length
L_p	drill pipe length
L_s	shank length
m, c	positive constants of S-N curve
m, n	curve fitting parameters for failure locus
n	mode number
n	safety factor
n_i	number of stress cycles in the i-th stress block
M	magnitude of all frictional moments acting on the bit about the longitudinal axis
M	mass matrix for Rayleigh damping
M	moment about a particular reference point on the fluke
M_1	offset M for curve fitting (M when $\delta\psi = 0$)
M_{max}	maximum moment to be applied on the fluke
M_{sl}	sliding friction moment about the longitudinal axis
N_c	fluke bearing factor
N_{dc}	number of finite elements on drill collar section

N_{dp}	number of finite elements on drill pipe section
N_i	number of cycles to failure at constant stress range
p, q	curve fitting parameters for failure locus (O'Neill et al.)
p_F	probability of failure
p_{Fa}	annual probability of failure
Q	normal soil reaction on chain segment
$\overline{Q}$	average normal resistance of chain over embedment depth
R	anchor capacity at mudline
R_a	anchor capacity at padeye
R_b	bit radius
R_d	design anchor capacity at mudline
$R_{d,a}$	design resistances at the padeye
s	length of chain
s_u	undrained shear strength profile
s_{u0}	intercept undrained shear strength at mudline
s_{ug}	undrained shear strength gradient with depth
S_a	alternating stress causing crack initiation
S_e	corrected endurance limit
S_u	ultimate tensile strength of the material
S_y	minimum yield strength
$S_e^{'}$	experimental endurance limit (at 10^6 cycles)
T	line tension

T_0	break-away torque (maximum static friction torque)
T_a	line tension at the padeye
T_b	frictional torque-on-bit
T_d	design line tension at mudline
$T_{d,a}$	design tensions at the padeye
$T_{dyn,max}$	mean maximum dynamic line tension
$T_{dyn,max-C}$	characteristic mean maximum dynamic tension
T_{mean}	mean line tension
T_{mean-C}	characteristic mean line tension
T_o	chain tension at mudline
T_p	spectral peak period
T_r	torque delivered by the rotary table to the drill strin
T_{sl}	sliding friction torque
T_{st}	reaction torque during the stick phase
T_z	wave zero up-crossing period
U_{10}	wind velocity
U_c	surface current velocity
V	load component perpendicular to the top face of the fluke
V_1	offset V for curve fitting (V when $\delta v = 0$)
V_d	threshold angular velocity of rotary table
V_{max}	maximum load capacity perpendicular to the top face of the fluke
w	chain self weight per unit length
W_a	anchor dry weight

W_a'	anchor submerged weight
W_b	weight-on-bit
x	horizontal position of the drill pipe
X	horizontal position of the drilling vessel
x*	horizontal distance normalised by d_a
x, y, z	translational degrees of freedom
x_a	padeye drag length
y_{max}	maximum axial displacement
z	depth below mudline
z*	depth normalised by d_a

Greek

τ	shear stress
φ	angular position of drill pipe
φ_r	angular position of rotary table
ϕ_1	angular displacement of drill pipe 1
ϕ_2	angular displacement of drill pipe 2
ϕ_3	angular displacement of drill pipe 3
ϕ_b	angular displacement of bit
ϕ_r	angular displacement of rotary table
ϕ_x	rotational degree of freedom around x
ϕ_y	rotational degree of freedom around y

ϕ_z	rotational degree of freedom around z
$\dot{\phi}_b$	bit angular velocity
$\dot{\phi}_r$	rotary table angular velocity
Ω_b	bit angular velocity
Ω_r	rotary table angular velocity
Ω_{max}	maximum angular velocity
μ	chain-soil friction coefficient
μ_c	kinetic (Coulomb) friction coefficient
μ_s	static friction coefficient
α	Rayleigh damping mass coefficient
α	soil profile index
α_s	side shear factor
β	Rayleigh damping stiffness coefficient
β	reliability index
γ	constant decay coefficient
γ_{dyn}	partial safety factor on dynamic line tension
γ_{mean}	partial safety factor on mean line tension
δh	displacement component parallel to the top face of the fluke
δv	displacement component perpendicular to the top face of the fluke
$\delta\psi$	fluke rotation
Δt	fixed time step in the Implicit finite element analysis
θ	line tension angle

θ_a	line tension angle at the padeye
θ_{fs}	fluke-shank angle
θ_o	line tension angle at mudline
θ_w	resultant angle
Θ	vector of environmental variables
λ	mean annual rate of extreme sea states
$\mu(\dot{\phi}_b)$	static-kinetic exponential decay friction
ρ	steel density
σ	standard deviation of angular velocity
σ_a	alternating stress amplitude obtained from Rainflow counted cycle
$\sigma_{a,max}$	maximum amplitude of von Mises stress
σ_{eq}	equivalent alternate stress amplitude causing crack initiation at zero mean
σ_m	mean axial stress
σ_{vM}	von Mises stress
$\sigma_{vM,max}$	maximum von Mises stress
σ_{yy}	axial stress (including bending)
ψ	inclination of fluke top face to the horizontal
ψ_i	initial inclination of fluke
ω_n	natural frequency (rad/s)

1. Chapter 1

Introduction

1.1. Overview

The increasing demand of oil and gas has resulted in significant development of deep and ultra-deep water offshore fields. Oil and gas exploration and exploitation in deep water are conducted from floating structures, and incorporate complex equipment and techniques. Despite significant improvements achieved in design of all of the components involved in drilling operation, there are still operation failure reports that threaten the vulnerable offshore environment (Ma et al., 2013; Hill et al., 1992). Therefore, the reliability assessment of the key elements of these floating drilling units is necessary for a safe and cost-effective operation. Two important areas of concern that affect the reliability of these systems include the station keeping of the drilling platform, particularly in harsh environment, and the reliability of the drilling system under operational vibrations and environmental loads. In this research work, two crucial elements affecting the overall system reliability were investigated, i.e., the reliability of drag embedment anchors, as a key element of station keeping, and the fatigue reliability of drill strings, as a key element of structural integrity (see Figure 1-1).

Floating offshore drilling platforms are typically kept in position by means of mooring systems or dynamic positioning (DP) system. Temporary mooring systems with catenary lines and drag embedment anchors hold better economics for long-term drilling operations in deep-water fields in comparison with the dynamic positioning system. Due to the

complex interaction between soil and anchor, uncertainties in the estimated anchor capacity and mooring line loading, as well as inaccessibility for monitoring and maintenance, reliability assessment of drag embedment anchors is vital to the safety of the whole floating facility.

Drill string is another essential component of drilling operation. A drill string is subjected to a variety of complicated dynamical phenomena. Safety and efficiency are the crucial aspects of deep water drilling operation, which can be significantly tainted by the mechanical vibrations occurring in the drill string. The mechanical vibrations decrease the efficiency of drilling operation, and result in premature fatigue and failure of drilling tools and equipment. From an economical point of view, these failures are not favourable to the industry as they may cost millions of dollars for the drilling campaign. Moreover, the mechanical vibrations provoke a less reliable drilling performance with regard to the social and environmental hazards. The first key step to reduce costs and enable safer operation is to understand the particular characteristics of the vibration modes and develop mitigation methods for the benefit of the entire project.

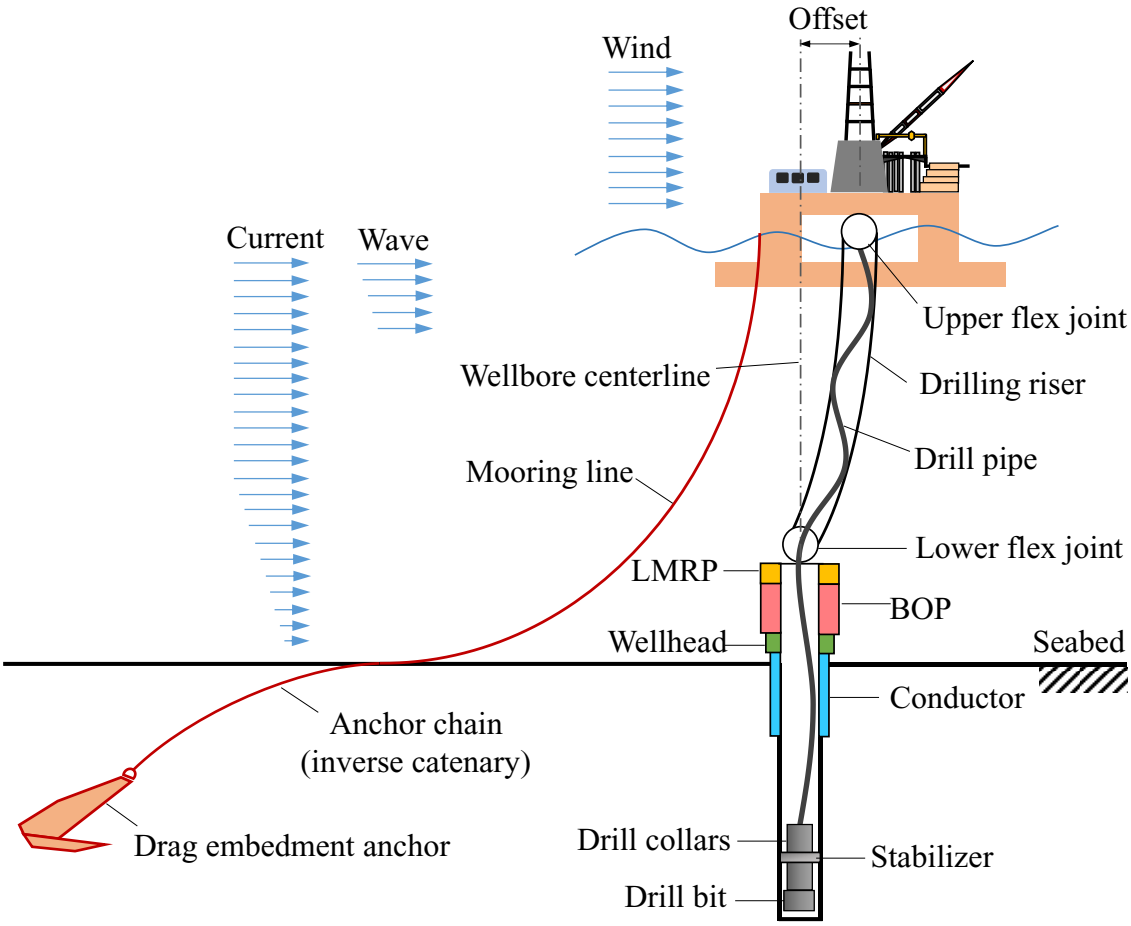

Figure 1-1. Schematic representation of a semisubmersible drilling rig with catenary mooring system and drilling equipment

1.2. Research objectives

The main objective of this research work was the reliability assessment of anchoring system and drill string of floating drilling systems that was achieved in two steps as follows:

- *Reliability of Drag Embedment Anchors*

  Drag embedment anchors are the most popular anchoring solution, easy to install, but challenging to predict the ultimate capacity because of range of inherent uncertainties.

Reliability of this type of anchoring solution is thus important in station keeping of floating systems. Despite excellent advances in design and application of drag embedment anchors, their performance under uncertain environmental loads and seabed soil conditions is under question. The uncertainties originate from probabilistic soil properties and metocean parameters combined with inspection and maintenance challenges. The primary objective of the present work was to assess the reliability of anchor performance in a certain soil type, taking into account the complex anchor-seabed interaction and the associated uncertainties which have never been explored in the past. To maximize the vessel motions and cover the worst case scenarios, catenary mooring system was considered.

- *Fatigue reliability of drill string*

  Stick-slip vibration is a catastrophic phenomenon detrimental to drill string life. This research work aimed first at developing a robust and practical finite element model of the entire drill string in order to conduct a comprehensive dynamic analysis under dangerous vibrations. The developed model was used to reveal new features of both drill pipes and drill collars response subjected to stick-slip vibration. Also, comprehensive parametric analyses were performed to predict drill string performance under different operational conditions. Second, the study used the developed models to perform a fatigue reliability assessment of drill string under the combined effects of stick-slip vibration and wave frequency vessel motions to determine the risk zones with low, normal, and high failure consequences.

1.3. Organization of the Thesis

The thesis has been prepared as a paper-based document. Each chapter presents a published or submitted manuscript.

Chapter 1 presents a short introduction to the tackled challenge and outlines the main objectives along with the thesis structure. Chapter 2 presents a comprehensive literature review of both the drag embedment anchors and drill string vibrations as the key components of the current study. Also, the later chapters containing the prepared manuscripts have their own literature review as independent manuscripts. Chapter 3 presents a journal paper published in *Marine Structures*. This paper establishes a new direction in reliability assessment of commonly used drag embedment anchors, incorporating the uncertainties in load and capacity mechanisms. A conference paper was also extracted from Chapter 3 with a specific focus on the harsh environment in Newfoundland and Labrador's offshore territory. This conference paper that was presented in the 71st Canadian Geotechnical Conference (GeoEdmonton 2018) and published in the conference proceeding is presented in Appendix A.

Chapter 4 presents journal paper published in *Applied Ocean Research*, in which a robust and practical finite element model of the entire drill string under stick-slip vibration was developed. This model involved nonlinear bit-rock contact, mud damping, nonlinear effects of large rotations and geometrically nonlinear axial-torsional coupling. To validate the performance of the developed numerical model, a 5 degree-of-freedom lumped-parameter model was developed and the results were compared. Chapter 5 presents another under-review journal manuscript in which a comprehensive numerical investigation of drill

string stick-slip vibration was conducted using the finite element model developed in Chapter 4. The investigation included dynamic analysis of drill pipes and drill collars under stick-slip in time and frequency domain, which revealed new features of system response. A parametric study was also carried out to gain insight into the effect of operational parameters such as rotational velocity, weight-on-bit, and damping on the overall dynamical behavior of drill string as an integrated system. Chapter 6 presents a conference paper addressing the fatigue reliability assessment of drill string. The study considered the combined effect of stick-slip vibration and wave-frequency vessel motion to capture the cumulative fatigue damage and determine the risk zones with normal, low, and high consequences. This chapter will be presented in the 31st International Symposium on Offshore and Polar Engineering (ISOPE2021, Greek). Chapter 7 include summarizing the key findings and conclusions of the conducted study along with recommendations for future studies. Appendix B and Appendix C present the additional contributions of the student into the research field through co-authorship of two conference papers tackling the simulation of drilling riser dynamics and seabed-interaction effects on wellhead-conductor system fatigue performance.

1.4. Thesis outcomes

The outcomes of this research work are listed below:

- Journal papers and manuscripts
  - Moharrami MJ, Shiri H. (2018) “Reliability Assessment of Drag Embedment Anchors in Clay for Catenary Mooring Systems”, Marine Structures, 58:342–360.

- Moharrami MJ, Martins CA, Shiri H. (2020a) “Nonlinear Integrated Dynamic Analysis of Drill Strings under Stick-Slip Vibration”, Applied Ocean Research, 108; 102521.
- Moharrami MJ, Shiri H, Martins CA. (2020b) “Numerical Investigation of the Nonlinear Drill String Dynamics under Stick-Slip Vibration”, under review as journal manuscript, Journal of Sound and Vibration.

- Conference papers
  - Moharrami MJ, Shiri H. (2018) “Reliability of Drag Embedment Anchors for Applications in Canadian Deep Offshore”, Proceedings of the 71st Canadian Geotechnical Conference and the 13th Joint CGS/IAH-CNC Groundwater Conference, Geo Edmonton 2018. September 23-26, 2018, Edmonton, Alberta, Canada.
  - Akpan, E., Dong, X., Moharrami, M.J., and Shiri, H. (2019) “Analytical Modeling of Well-Conductor Seabed Interaction in Complex Layered Soil in Newfoundland Offshore”, GeoSt.John's2019, September 2019, St. John's, NL, Canada.
  - Akpan, E., Dong, X., Moharrami, M.J., and Shiri, H. (2019) “Analytical Assessment of the Drilling Risers Stability in Newfoundland Deep Offshore”, GeoSt.John's2019, September 2019, St. John's, NL, Canada.
  - Moharrami MJ, Shiri H. (2021) “Fatigue Reliability Assessment of Drill String Due to Stick-Slip Vibrations and Wave-Frequency Vessel Motions”, 31st International Ocean and Polar Engineering Conference, June 2021, Rhodes, Greece.

References

Hill, T.H., Seshadri, P.V., Durham, K.S., 1992. A Unified Approach to Drillstem-Failure Prevention. Society of Petroleum Engineers. doi:10.2118/22002-PA

Ma KT, Duggal A, Smedley P, L'Hostis D, Shu H., 2013 A historical review on integrity issues of permanent mooring systems. Proceedings of Offshore Technology Conference OTC 24025; May 6-9; Houston, Texas. https://doi.org/10.4043/24025-MS

2. Chapter 2

Literature Review

2.1 Drag Embedment Anchors

2.1.1 Overview

During past decades, floating structures have been intensively used as the most preferred method in deep water oil and gas exploration and exploitation. The emerge of floating structures such as semisubmersible platforms, floating production, storage, and offloading (FPSO) facilities, tension-leg platforms (TLPs), and spars enabled the extraction of oil and gas in water depths greater than 1000 m. Figure 2-1 illustrates different types of floating structures.

Amongst floating facilities, semisubmersible platforms have a diverse application in the offshore oil and gas industry including exploration and drilling, testing, appraisal, production, heavy lifting, accommodation, or their combination. During all of these applications, the platform is subjected to environmental loads from wind, wave, and current, and requires a mooring system to smoothly minimize the induced static and dynamic motions. Drag anchors have been commonly used to provide mooring for semisubmersible platforms and FPSO systems. The resistance of drag anchors primarily depends on the anchor geometry, soil properties, and mooring line tension. All these parameters include some uncertainties which can affect the estimated capacity of anchor.

Figure 2-1. Different types of floating structures. (a) Petrobras P-51 Semi-submersible Platform in Brazil (Wikipedia), (b) Shell Appomattox TLP Hull in Gulf of Mexico (Courtesy of COSCO Shipping), (c), Armada Kraken Harsh Environment FPSO in North Sea (Courtesy of Bumi Armada) (d) Gulfstar One Spar in Gulf of Mexico (Courtesy of Williams Partners)

2.1.2 Offshore Drilling Operation

For deep water drilling operation, the drill rig is placed on a mobile offshore drilling unit (MODU) which can be either a drillship or a semisubmersible platform. The drill rig can also be a part of a floating production unit. These units employ either a mooring system, a dynamic positioning (DP) system, or a combination of both to withstand the environmentally induced motions.

Drilling semisubmersible platform is a favorable method in harsh environments compared to drillship due to good stability and seakeeping characteristics owing to its deep draft. To drill a borehole in the seabed, the drill bit is deployed from the drill rig located on the semisubmersible platform by means of drill string. The drill string passes through a pipe called drilling riser, which connects the blow-out preventer (BOP) to the rig. Due to environmental loads (wind, wave, and current), the floating vessel is subjected to translational and rotational motions. The primary purpose of mooring system is to keep the horizontal motions of the floating platform within offset limits, and thus, (i) enforce the angle of drilling riser to be within a limit, (ii) minimize the interaction between the rotating drill string and riser, especially at the upper and lower flex joints of riser.

2.1.3 Mooring systems

Mooring systems are used to connect the floating vessel to the seabed and keep it in position during operation. There are two broad class of mooring systems, namely, catenary and taut mooring lines. The applicability of these mooring lines depends primarily on the water depth. Catenary mooring lines have been traditionally used in shallow to deep waters. The lines are comprised of chain and steel/synthetic wires, and are positioned symmetrically around the floating vessel, usually grouped in three or four lines. The catenary mooring line touches the seabed horizontally, such that the angle between the line and the seabed is almost zero at the touchdown point, and thus, the anchor is subjected to only horizontal loads. For ultra-deep waters (>1000 m), the weight of catenary mooring line significantly increases and acts as a limiting factor in the design of the floating vessel (O'Neill et al., 1999). To overcome this problem, taut line moorings were developed. The taut line

mooring arrives at the seabed at an angle to the horizon, typically 30° to 45° (Randolph and Gourvenec, 2011), and thus, the anchoring point is subjected to both horizontal and vertical forces. Figure 2-2 shows the catenary and taut line mooring systems.

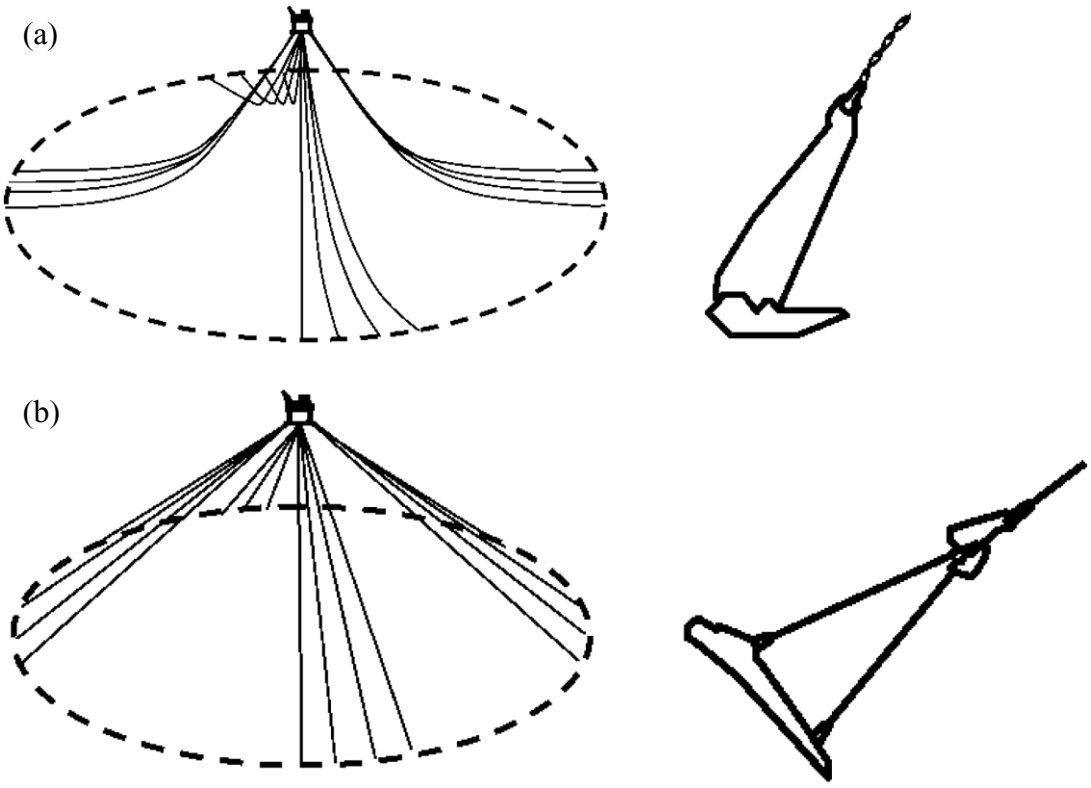

Figure 2-2. Mooring configuration. (a) Catenary mooring system with drag embedment anchor, (b) taut line mooring system with vertically loaded anchor (VLA) (adopted from Randolph and Gourvenec, 2011)

2.1.4 Anchoring Methods

There are many anchoring methods that may be used with mooring systems of floating vessels to provide efficient and reliable station-keeping, as illustrated in Figure 2-3 and Figure 2-4. This section presents a brief overview of drag embedment and suction anchors.

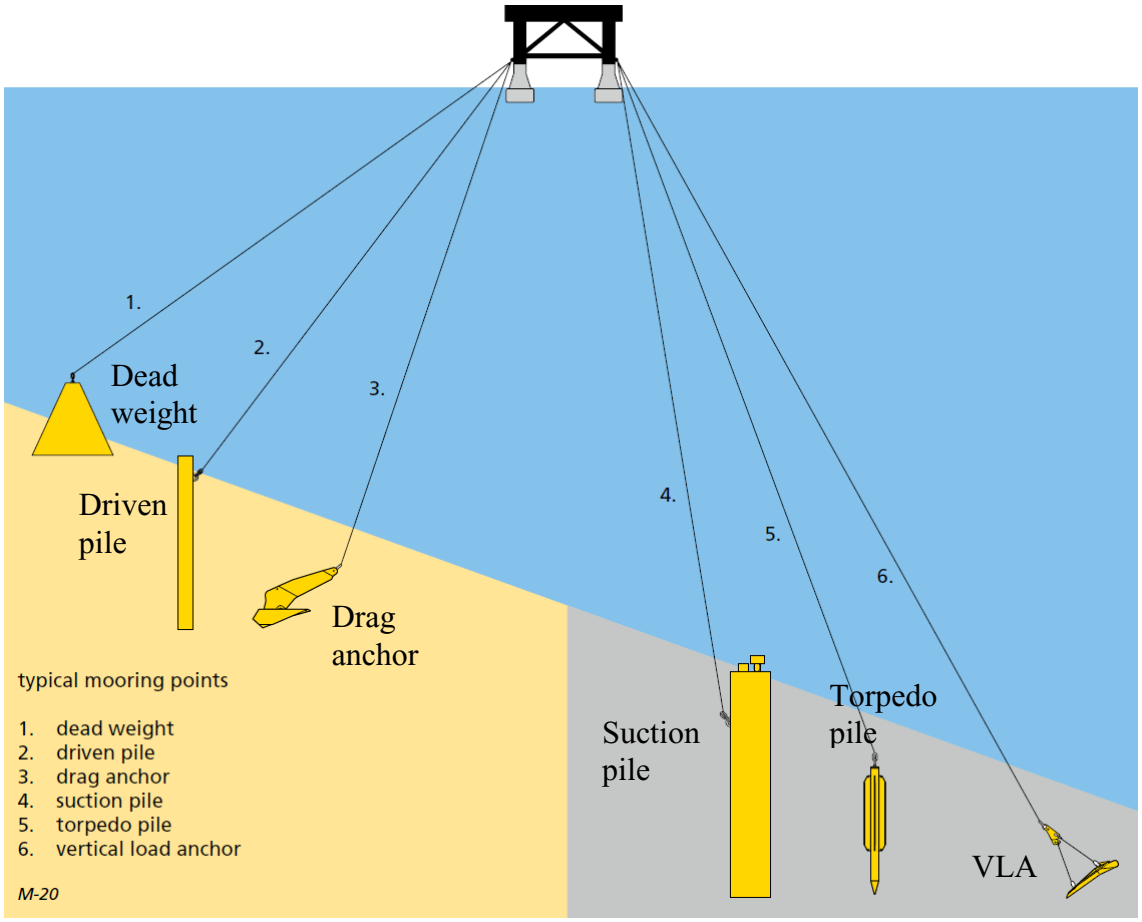

Figure 2-3. Schematic representation of marine anchors (Courtesy of Vryhof Manual, 2015)

Figure 2-4. Types of marine anchors. (a) Drag embedment anchor (Courtesy of Vryhof Anchors), (b) vertically loaded anchor (Courtesy of Vryhof Anchors), (c) pile anchor (Courtesy of InterMoor), (d) suction anchor (Courtesy of InterMoor), (e) torpedo pile (Courtesy of Deep Sea Anchors)

2.1.4.1 Drag Embedment Anchors

Drag embedment anchors are the most simple and economic anchoring solution for catenary mooring system due to their relatively low installation cost and high holding capacity, which were evolved from traditional ship anchors. These anchors can be easily handled, installed, retrieved, and re-installed, making them ideal for floating vessels used in short- or medium-term operations, such as semisubmersible drilling rigs; see Figure 2-5. Drag embedment anchors were originally developed for catenary mooring systems in which the anchor is mainly subjected to horizontal load.

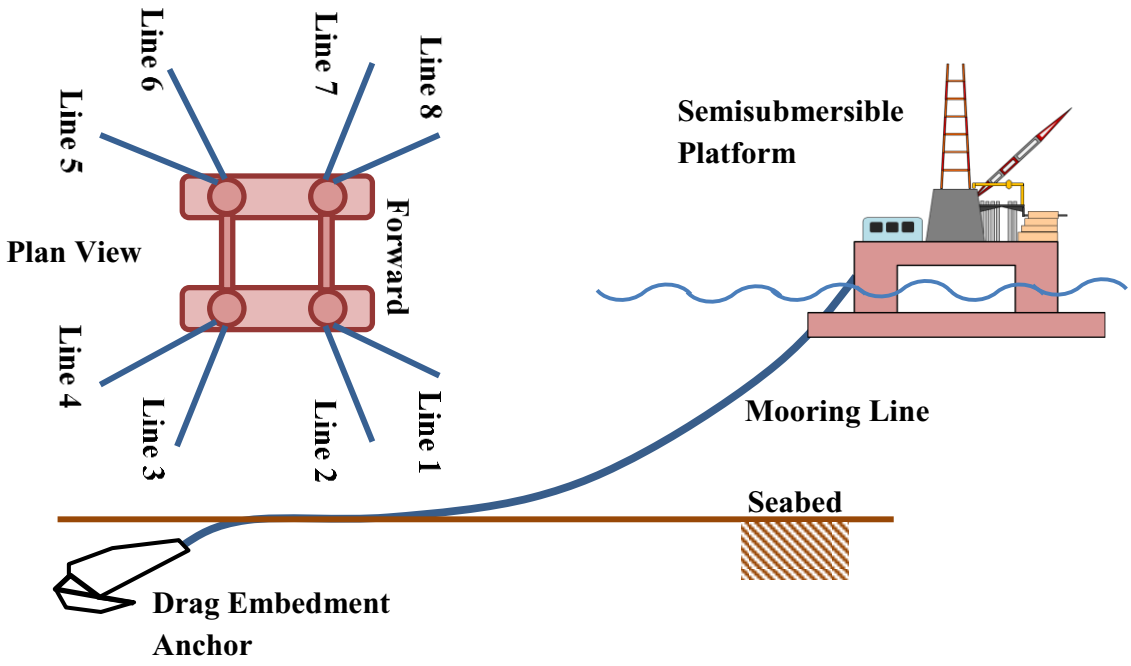

Figure 2-5. Schematics of a semisubmersible platform with catenary mooring and drag anchor

The main components of drag embedment anchor are fluke, shank, and padeye, as illustrated in Figure 2-6. The anchor holding capacity is due to the frictional interaction between fluke and soil, and the penetration into the seabed. The interaction between fluke

and soil increases with the fluke area, while the penetration of anchor is facilitated by the fluke tips, and depends on soil type, shank shape (hollow shank provides deeper penetration), and mooring line load.

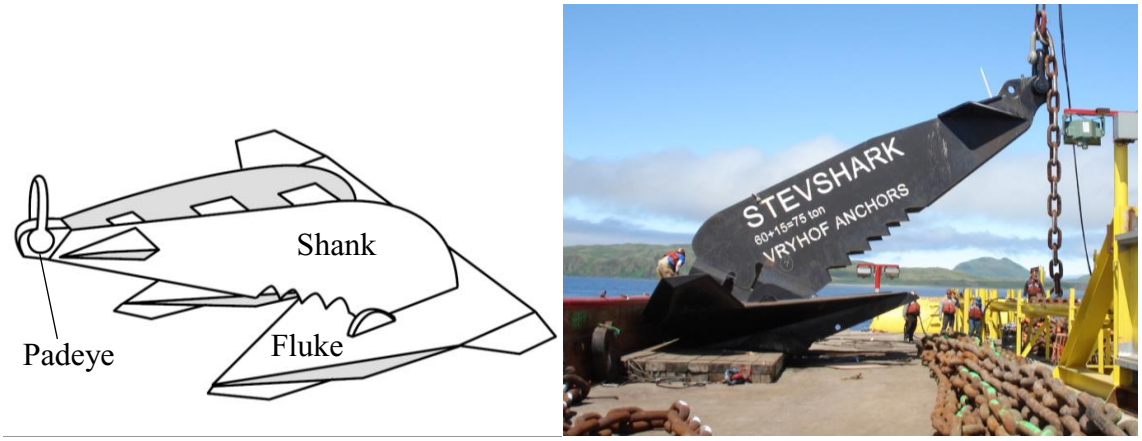

Figure 2-6. Stevshark Mk5 anchor used in hard soil conditions, i.e., Arctic locations. (Left) form Vryhof (2000), (right) from Ruinen (2012)

As illustrated in Figure 2-7, during the installation, the anchor is placed onto the seabed and the attached mooring line is pulled horizontally so that the anchor penetrates into the seabed. The dragging process continues until the anchor is penetrated to a certain depth and the required holding capacity is reached. The achieved holding capacity is produced by the resistance of the soil in front of the anchor, and can be increased to the ultimate value by increasing the penetration. The penetration of drag anchor into the seabed is largely influenced by the angle between fluke and shank. This angle is about 50° for very soft clay and about 30° for hard clay or sand, and is typically pre-defined, but can be altered prior to penetration depending on soil conditions, see Figure 2-7 and Figure 2-8. One of major advantage of drag anchors is their capability of providing continuous resistance without further drag and penetration, even if the ultimate holding capacity is reached

(O'Neill et al., 1999). Another major advantage of drag anchors is their economical weight efficiency (holding capacity/dry weight) exceeding 20 for anchors in sand (O'Neill et al., 1999).

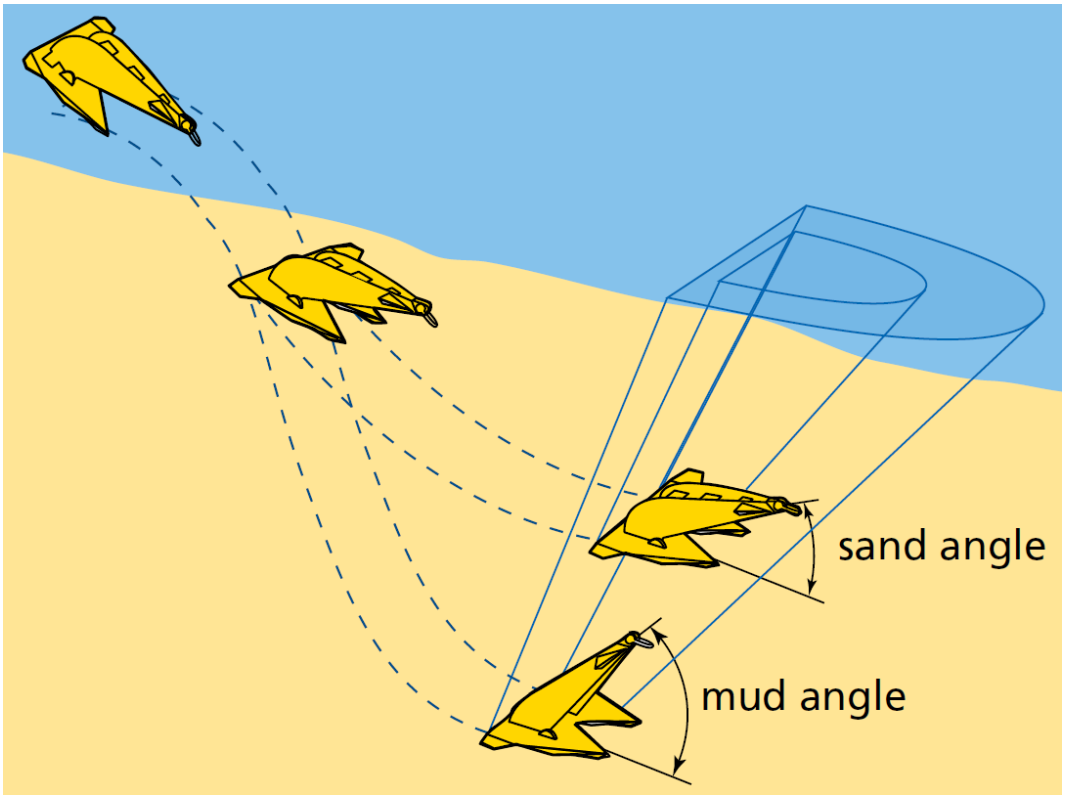

Figure 2-7. Installation of drag embedment anchor (Vryhof Manual, 2015)

There are a number of limitations to the use of drag anchors. Although drag anchors are well-suited for resisting large horizontal loads, they have relatively low resistance to vertical loads, making them applicable only to catenary mooring systems in which the anchoring point at the seabed is only subjected to horizontal forces. To overcome this limitation, vertically loaded anchors (VLAs) were developed in 1990s to be used in soft cohesive soils. Design of vertically loaded anchor is obtained with replacing the rigid shank in the traditional drag embedment anchors by a system of wires connected to a plate.

Installation of vertically loaded anchor is similar to conventional drag embedment anchor, but with deeper penetration. When the vertically loaded anchor is embedded deep enough into the seabed, and thus, rotated, the anchor mode is changed from installation (horizontal) to vertical loading. This type of anchor is always loaded in a direction normal to the fluke, and thus, provides significant vertical resistance, making it more suitable for taut-leg moorings.

Due to nature of drag anchors and installation method, they embed themselves into the seabed, and thus, they are not suitable for use in hard or rocky seabed (O'Neill et al., 1999). The uncertainties associated with the anchor's final location during installation is another major problem with the drag anchors. Furthermore, the characteristics of drag anchor, i.e., the attainable ultimate holding capacity and the optimum fluke angle, are fairly sensitive to soil conditions.

Figure 2-8. Cut section with fluke anchor in: (a) sand, (b) clay (Ozmutlu, 2009)

2.1.4.2 Suction Anchors

Suction (or caisson) anchors are short large-diameter cylinders ranging from 3-8 m, with small embedment depth to diameter (aspect) ratio typically less than 5 to ensure the stability at touchdown (Randolph and Gourvenec, 2011); see Figure 2-9.

Figure 2-9. Suction anchors used with the Johan Castberg FPSO mooring system in the Barents Sea (Courtesy of Island Offshore)

For installation, the anchor is initially placed on the seabed with mooring line attached, and the penetration is achieved by self-weight. Following initial penetration, the water pumps located on the top cap are activated and the water is pumped out from the inside of the anchor, creating a hydrostatic pressure difference between the top and the bottom of the anchor. The net hydrostatic or "suction" force drives the anchor downwards into the seabed until the full embedment depth.

The primary advantage of suction anchors is their capability of resisting both horizontal and vertical loads, making them a practical anchoring solution for catenary mooring lines where the horizontal loads dominate, or taut-leg mooring lines where a considerable portion of load is in vertical direction (D'Souza et al., 1993; Sparrevik, 1998). This capability is provided by the loading mechanism of suction anchors in which the horizontal holding capacity is derived from bearing resistance between the soil and the vertical

projected area of the anchor, while the vertical holding capacity is derived from the skin friction resistance along the external anchor surface and the upward end-bearing resistance mobilized at the bottom cross-sectional area of the anchor. It is assumed that the upward resistance is only capable of resisting relatively short-term environmental loads, but not suitable for longer-term loads due to pretension (Clukey et al., 2000). Another advantage of suction anchors is that they can be extracted from the seabed by reversing the installation process and pumping the water back into the anchor, due to which the anchor is pushed out of the seabed and can be reused in a different location.

One limitation of suction anchors is that they are only suitable for soft clayey or sandy seabed, and their capability for penetrating into hard seabed is unknown.

The main purpose of reliability assessment of anchors is to determine whether or not a limit state below a certain value is maintained over the life span of the anchor. The primary challenge in reliability analysis of anchors is probabilistic modeling of anchor capacity and mooring line tension, which introduce uncertainty into the model. The uncertainties are typically associated with spatially varying soil properties, anchor capacity obtained from analytical, numerical, or experimental measurements, and mooring line loads. Probabilistic modeling of suction anchor capacity can be achieved through the available analytical models such as plastic limit model (PLM) or finite element modeling of caisson-soil interaction under the effect of mooring line tension. The latter, however, is not computationally cost-effective. On the other hand, probabilistic modeling of mooring line tension involves the uncertain metocean parameters such as significant wave height, peak

period, and wind velocity. These parameters are random in nature, and usually expressed in terms of probability distributions.

Reliability of drag embedment anchors has never been studied before, while there are several studied on reliability assessment of suction anchors. Due to relatively close concept of the overall reliability analysis procedure for these anchors, some of the key studies on suction anchor reliability are detailed in this section.

Clukey et al. (2000) conducted a preliminary reliability analysis of suction caissons for deep water applications. As at the time of this research only the working stress design (WSD) method was available for suction caissons, this work was intended to provide the reliability-based load and resistance factor design (LRFD) approach for suction caissons. The authors determined the potential impacts of spatial variation of soil properties on foundation reliability. The ultimate caisson resistance under combined lateral and axial uplift load components was determined using the upper-bound limit analysis (Murff and Hamilton, 1993). Reliability analyses were conducted using first-order reliability method (FORM) and second-order reliability method (SORM) by means of a computer program RELACS. To obtain probability of failure, uncertainties were assigned to both loading and foundation resistance parameters in terms of probability distributions. Three sources of uncertainty were considered, namely, mooring line tension, undrained shear strength of soil, and foundation response. The mooring line tension acting on caisson was related to significant wave height (H_s) using a simple function as follows:

$$F_t = cH_s^a \varepsilon_t \quad (1)$$

where c is a constant depending on vessel, a = 1.45 is a constant calibrated to from a Spar platform, and ε_t is a random variable accounting for uncertainty in the simple loading

model. Gumbel function was used to represent the cumulative probability distribution of the significant wave height. Linear response surfaces were used to express the probabilistic axial and axial-lateral resistance of caisson in terms of shear strength for catenary and taut-leg mooring, respectively. Reliability was calculated assuming a simple limit state function in terms of mooring load and caisson resistance.

Silva-Gonzalez et al. (2013) studied reliability of suction caissons for floating systems considering mooring line tensions and caisson capacity at mudline. Samples of caisson capacity were generated at padeye using a calibrated plastic limit method and simulations of undrained shear strength, side shear factor, reverse-end bearing factor, and loading angle at padeye. The loading capacities at padeye were evaluated against a 3D finite element model of caisson-soil interaction subjected to three different loading inclination ranges, namely, pure translation, pure pullout, and combined translation and pullout. Due to interaction between soil and embedded segment of the mooring line, the net load transferred to the caisson's padeye depends on the soil shear strength. The statistical dependence between line tension and caisson capacity can impose further difficulties in reliability analysis. Therefore, the generated capacity samples at padeye were transferred to mudline taking into account the effects of soil-chain interaction by means of Neubecker and Randolph (1995) formulation. Reliability analysis were conducted using FORM considering statistically independent mooring line tension and caisson capacity at mudline. The limit state function was formulated at mudline as follows:

$$M\left(R, H_s, T_p, U_{10}\right) = R - T_{mean}\left(H_s, T_p, U_{10}\right) - \mu_{Tdyn,max}(H_s, T_p, U_{10}) \quad (2)$$

where R is the caisson capacity at mudline, T_{mean} is the mean line tension due to line pretension and mean environmental loads, $\mu_{Tdyn,max}$ is the expected maximum dynamic line tension during an extreme sea state induced by low-frequency and wave-frequency vessel motions. Both $\mu_{Tdyn,max}$ and T_{mean} were obtained at mudline as functions of significant wave height H_s, peak period T_p, and wind velocity U_{10}. Response surfaces were used to model the mean and the expected maximum dynamic tension of catenary and taut-leg mooring lines at mudline in terms of uncertain environmental variables

2.2 Drill Strings

2.2.1 Overview

The increasing demand of oil and gas has resulted in development of deep water offshore fields. The oil and gas exploration and exploitation in deep water are associated with technical and economic challenges, particularly with respect to drilling operations. Offshore drilling involves drilling holes in the ocean seabed, which is amongst the most expensive and hazardous activities in the oil and gas industry.

The main purpose of well drilling operation in oil and gas industry is to create a borehole using a cutting tool, the so-called drill bit, and reach the reservoirs several kilometres beneath the ocean floor; see Figure 2-10. Rotary drilling is a standard oil-well drilling method, in which all the operations are performed by rotary drilling rigs. This method is based on a combination of the mechanical and hydraulic systems to transfer the energy and material (Jansen and van den Steen, 1995). The mechanical system mainly includes a drill bit to break the rocks and drill through the ocean floor, a drill string to rotate the drill bit, a rotary drive at the surface to provide rotational force on the rotary table (the top end of

the drill string), and a rig to support the drill string and the rotary drive. The hydraulic system includes the drilling fluid (the so-called drilling mud), pumps, and a transport channel, i.e., drilling riser. The drilling mud is pumped from the surface down to the wellbore through the drill string. The main functions of the drilling mud are to clean the wellbore, cool and lubricate the drill bit, and equalize the wellbore pressure. The drilling mud also has a significant damping effect in certain vibration modes. In deep water, the drilling rig is placed on a floating vessel, which can be a drill ship or a semisubmersible platform. The drill string and drilling equipment are raised and lowered by a hoisting system.

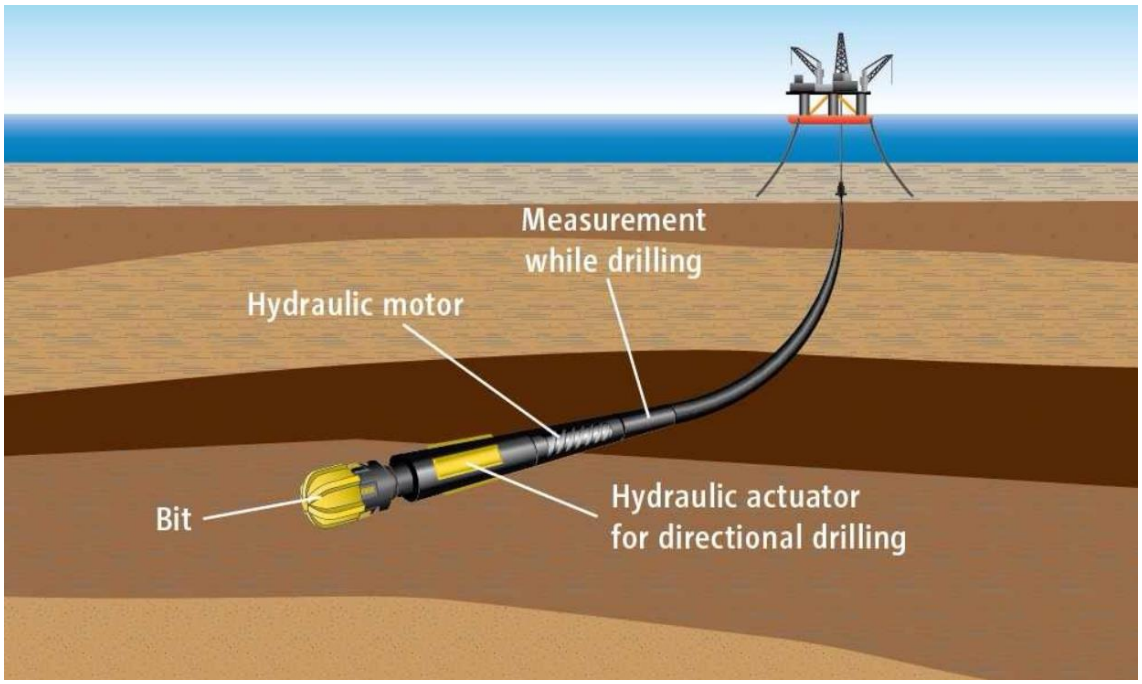

Figure 2-10. A typical drill string configuration for deep water drilling

(https://copperalliance.eu/about-copper/conductivity-materials/copper-nickel-silicon/mwd/)

The drill string consists mainly of thin-walled drill pipes connected by threaded connections which create and extremely slender structure with a length of several kilometres. The lowest part of the drill string, the bottom-hole assembly (BHA), performs under compression, and thus, is mainly made of thick-walled drill collars to prevent buckling of the BHA and provide the axial weight-on-bit (WOB). The WOB is required to penetrate the surface of the rock and facilitate the drilling operation. The BHA also includes other tools and equipment such as stabilizers, mud motor, reamers, and heavy-weight drill pipes, and has a total length of several hundred meters.

2.2.2 Static Loading

The main functions of drill string are to transmit torque and to transport the drilling mud to the drill bit, which result in torque and hydrostatic pressure acting on drill string, respectively. The torque-on-bit (TOB) varies between 0.5 and 10 kNm (Jansen and van den Steen, 1995). However, due to the frictional contact at the bit-rock interface and the drill string-borehole wall, the required torque at the surface may be up to 50 kNm. The hydrostatic pressure due to presence of drilling mud acts at the pipe-collar junction and the bottom of the drill collar where the bit is located. Another source of static load in a drill string is the self-weight, due to which an extremely large tensile force is applied to the drill pipes. The drill collars and the bit, however, are supported by the bottom of the wellbore, and thus, under compression. The large bending stiffness of the drill collars along with the aid of stabilizers minimize the dangerous buckling phenomenon in this region of the drill string. Drill string is subjected to spatially varying axial forces, namely, the hook load, the mud hydrostatic force (acting downward at the collar-pipe junction and upward at the

bottom of the drill collar), and the self-weight. Also, the upward weight-on-bit is applied at the bit location. The performance of drill string is usually evaluated by the static strength analysis of its components. The effective stress due to the combined tension, bending, torsion, and pressure is compared to yield strength of the material. (Jansen and van den Steen, 1995).

2.2.3 Dynamic Modes of Motion

Drill string is subjected to three primary vibration modes, namely, axial, lateral, and torsional, which lead to bit bouncing, whirling, and stick-slip, respectively; see Figure 2-11. These vibration modes can be coupled due to the inherent coupled nature of the bit-rock and drill string-well bore interaction, the axial stiffening stemming from the gravitational field, and the drill string curvature due to doglegs of the wellbore.

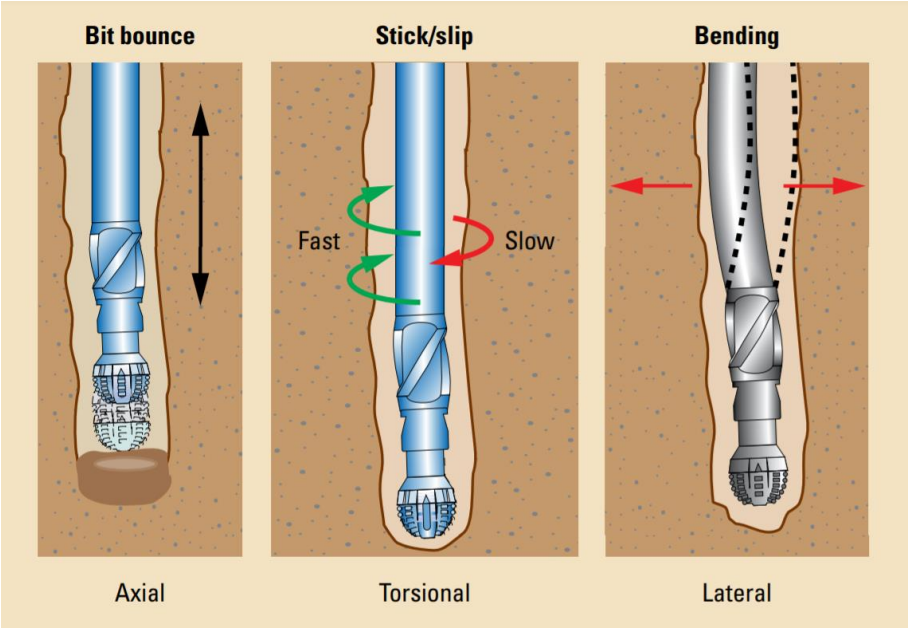

Figure 2-11. Drill string vibration modes (Courtesy of Schlumberger)

2.2.3.1 Torsional vibration

The torsional vibration is one of the mechanical vibrations in the drill strings and can occur during 50% of the total time of a classical rig step (Dufeyte and Henneuse, 1991; Challamel et al., 2000). The stick-slip is a phenomenon takes place due to the low torsional stiffness of the drill string structure (Dufeyte and Henneuse, 1991). This type of vibration results in a fluctuating rotational velocity at the drill bit despite the constant rotational velocity at the surface, as depicted in Figure 2-12. In the most severe form of torsional vibration, the so-called stick-slip, the drill bit experiences a periodic motion with two phases, namely, the stick phase and the slip phase. In the stick phase, the bit momentarily stops while the top of the drill string rotates at a constant rotational velocity. In the slip phase, the bit rotates at a velocity often more than twice the rotational velocity at the surface (Jansen and van den Steen, 1995). In practice, the stick-slip vibration can be detected through downhole and surface measurements (Lesso et al., 2011; Pavone and Desplans, 1994). The stick-slip can introduce severe problems into the drilling system such as failure of the threaded connections, low ROP, equipment wear, and damage of the drill bit (Brett, 1992). The frequency of the stick-slip vibration is typically about the first natural torsional frequency of the drill string and varies between 0.05 Hz to 0.5 Hz.

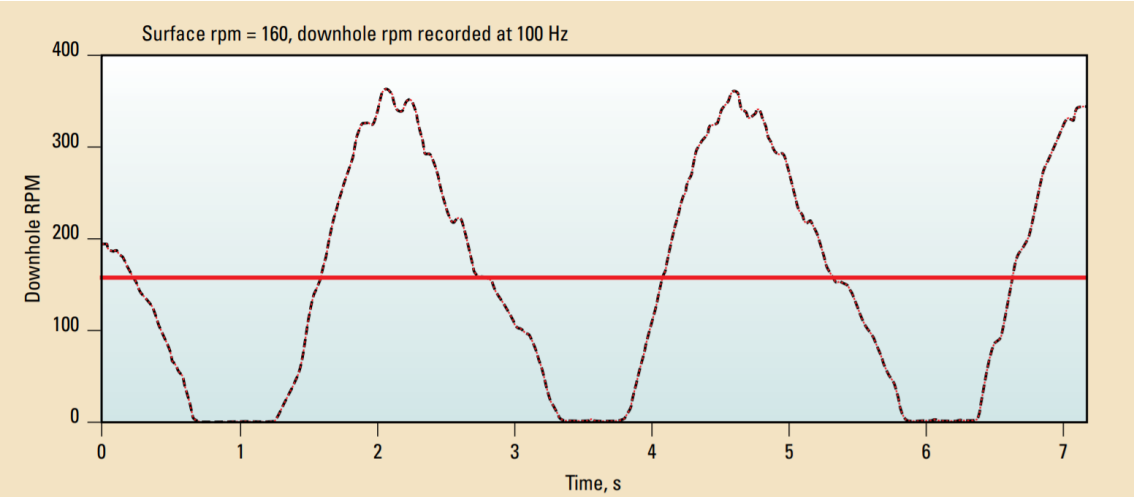

Figure 2-12. Downhole measurement of bit angular velocity during stick-slip (Courtesy of Schlumberger)

The nonlinear contact between the drill bit and the rock is identified as the primary cause of stick-slip vibration (Jansen and van den Steen, 1995). More precisely, the stick-slip vibration is due to the nonlinear exponentially decaying relationship between the frictional torque-on-bit and the bit angular velocity. At the start of drilling operation, the entire drill string will not rotate until a certain torque-up level is reached. This torque-up level should be large enough to overcome the static friction at the bit-rock interface, and is a function of the bit type, the friction coefficient between the rock and the formation surfaces, and the WOB (Ghasemloonia, 2013). As the static friction is overcome, the bit starts to rotate. The rotational motion of the drill bit itself creates a nonlinear frictional torque-on-bit which excites the drill string with periodic torsional vibrations. Thus, the stick-slip phenomenon is classified as self-excited vibration, for which no external force is required to maintain the torsional oscillations (Jansen and van den Steen, 1995).

The stick-slip vibration can impose several problems into the drill string system, leading to deficiency and failure of the drilling operation. These problems include reduced ROP, excessive bit wear, premature fatigue of the drill pipes and BHA, and breakage of the drill bit (Richard and Detournay, 2000). This type of vibration is one of the most dangerous modes of vibrations especially at low rotational velocities.

2.2.3.2 Axial vibration

The second type of drill string vibration is the axial vibration. This type of vibration can be easily observed at the surface, since the axial waves have a high velocity and travel upwards along the drill string to the surface. Drill string resonance can lead to a severe form of axial vibration with large amplitude, the so-called bit bouncing, due to which the bit loses contact with the bore bottom and bounces up and down. This type of vibration is common in vertical wells with hard formations and tricone bits due to limited drill string-wellbore interaction and small damping (Chevallier et al., 2003). The axial vibrations have severe negative effects such as tool wear, broken tooth cutters, and reduction in the rate-of-penetration (ROP) (Ashley et al., 2001). However, the axial vibrations can be beneficial if they are induced into the system in a controlled manner, such as in Resonance Enhanced Drilling (RED) technology. The main idea of this technology is to create resonance condition between the drill bit and the formation at a specific frequency, and enhance the ROP (Pavlovskaia et al., 2015).

2.2.3.3 Lateral vibration

The third type of drill string vibration is the lateral vibration, which typically occurs at the lower parts. The major excitation sources for the lateral vibration are the bit-formation

contact and the multiple lateral impacts between the drill string and the borehole wall. The detection of downhole lateral vibration at the surface, however, is very difficult. This is due to the low velocity of the bending waves compared to the axial and torsional waves propagating long the drill string. Moreover, the damping effects of drilling mud and borehole wall contact, as well as the increasing tension along the drill string, decrease the amplitude of bending waves as they travel upwards along the string. The frequency of lateral vibration is between 0.5 to tens of hertz. (Jansen and van den Steen, 1995). The lateral vibration usually occurs at the BHA, as this section of the drill string performs under compression and is vulnerable to buckling.

The unwanted mechanical vibrations along the drill string increase the failure risk of drilling tools and equipment, and deduce the efficiency of the drilling operation. Thus, it is of great importance for the oil and gas industry to design and implement vibration suppression tools, control methods, and drilling guidelines, in order to mitigate the harmful vibrations and reduce the consequent costly failures. The key step to achieve the above goals is to study the dynamical behaviour of the drill string under the vibration modes, and gain a deep understanding on the mechanics of the drill string.

The primary difference between the onshore and offshore deep water drilling operation lies within the stability of the drilling rig and the environmental loads acting on the drilling system

2.2.4 Drill String Modeling

Axial, lateral, and torsional vibration modes usually appear simultaneously in drill string. The coupling between vibration modes primarily originates from nonlinear drill bit-

formation and drill string-well bore interactions, and dogleg. Some of the models in the literature have been developed to study each of these modes in an uncoupled manner. Uncoupled models can provide an insight into dynamical aspects of drill string under a single vibration mode, and are beneficial to design of control systems. Nevertheless, studying the coupled vibration modes is of great importance to reveal the underlying dynamical aspects of drill string. Coupled models include axial-lateral, axial-torsional, and axial-lateral-torsional vibration modes with an extensive complexity due to the interplay between the modes.

Intensive theoretical and experimental research activities have focused on characterization of drill string dynamics under dynamical vibrations. The basic theoretical methods to investigate the nonlinear dynamical phenomena of a continuous drill string system include analytical models described by low-dimensional lumped mass models which consider a few dominant vibration modes, and full scale continuous models described by numerical methods, i.e., Finite element Method (FEM) analysis.

2.2.5 Lumped-Parameter Models

A wide range of research efforts have been made to investigate the stick-slip behaviour of drill string within lumped parameter models. The use of these models in dynamic vibration analysis is urged by the necessity of a simple representation of the drill string system. One of the most commonly used lumped parameter models for describing drill string dynamic response is the torsional pendulum. In this model, the drill pipes are assumed as inertialess torsional springs, the twisting of the relatively stiff BHA is neglected (i.e., rigid body), and the rotary table velocity is constant. Several torsional pendulum models with different

degrees of freedom (DOF) have been proposed in the literature to study the stick-slip vibration of the drill string (Brett, 1992; Jansen and van den Steen, 1995; Halsey et al., 1988; Lin and Wang, 1991; Abbassian and Dunayevsky, 1998; Serrarens et al., 1998; Yigit and Christoforou, 1998; Yigit and Christoforou, 2000; Mihajlovic et al., 2004; Richard et al., 2007). Although the torsional pendulum models are easy to implement and provide useful information on the dynamics of BHA/bit they cannot consider two important characteristics of the drill string system: (i) the increase in the length as the drilling operation proceeds, (ii) the vibrations along the entire drill string, i.e., drill pipes and drill collars. To overcome such shortcomings, a generic *n*-DOF torsional model was proposed by Navarro-Lopez and Cortes (2007). Particular cases of this generic lumped parameter model with three degrees-of-freedom including rotary table, drill pipes, and BHA/drill bit (Navarro-Lopez, 2009), and four degrees-of-freedom including rotary table, drill pipes, drill collars, and drill bit (Navarro-Lopez and Liceaga-Castro, 2009) were used to study the stick-slip characteristics of the drill string. Later on, Liu et al. (2013) developed an eight degree-of-freedom lumped-parameter model considering the axial, lateral, and torsional dynamics of both the drill pipes and BHA. The following provides detailed review of some of the lumped-parameter models.

Jansen and van den Steen (1995) studied the stick-slip vibration of the drill string using the torsional pendulum. The drill pipes were represented by a torsional spring, while the BHA was considered as a rigid body, as shown in Figure 2-13. The equation of motion of the drill string was described by the torsional pendulum model, as follows:

$$J_1\ddot{\phi}_1 + c_1\dot{\phi}_1 + k(\phi_1 - \phi_2) - T_b = 0 \quad (1)$$

where ϕ_1 and ϕ_2 are the rotational displacements of the bit/drill collars and rotary table, respectively, J_1 is the equivalent mass moment of inertia of the drill collars and the drill pipes, c_1 is the equivalent viscous damping coefficient, k is the equivalent torsional stiffness of the drill pipes. The nonlinear torque-on-bit T_b was represented as a combination of bit-rock interaction and the frictional forces along the drill collars. To capture the behaviour of torque-on-bit during the switch from stick to slip phase, a simple step law was implemented to represent the drop in the torque-on-bit, as follows:

$$T_b \geq -T_{sl} \text{ if } \dot{\phi}_1 = 0 \text{ and } T_b \geq -T_{sl} \text{ if } \dot{\phi}_1 > 0 \quad (2)$$

where T_{st} is the static torque-on-bit during the stick phase, and T_{sl} is the dynamic torque-on-bit during the slip phase.

The drive system was characterized by three components, namely, the rotary table, the gearbox, and an electronic motor. It was assumed that the connection between the rotary table and the electronic motor was stiff enough to consider their inertias in a unified manner. Thus, the equation of motion of the drive system with a separately excited DC motor was defined as:

$$J_2\ddot{\phi}_2 + c_2\dot{\phi}_2 + k(\phi_1 - \phi_2) - nT_m = 0 \quad (3)$$

$$L\dot{I} + RI + V_b - V = 0, V_b = K\dot{\phi}_3 = Kn\dot{\phi}_2, \text{ and } T_m = KI \quad (4)$$

where J_2 is the combined mass moment of inertia of the rotary table and the motor, c_2 is the damping coefficient of the drive system, I is the armature current, L is the armature inductance, R is the armature resistance, V_b is the back-electromotive force, V is the armature voltage, K is a constant, and T_m is a linear torque produced by the motor. The first natural torsional frequency of the drill string and the drive system were 0.12 rad/s (0.18

Hz) and 13.2 rad/s (2.10 Hz), indicating that the drill string and drive system were only lightly coupled.

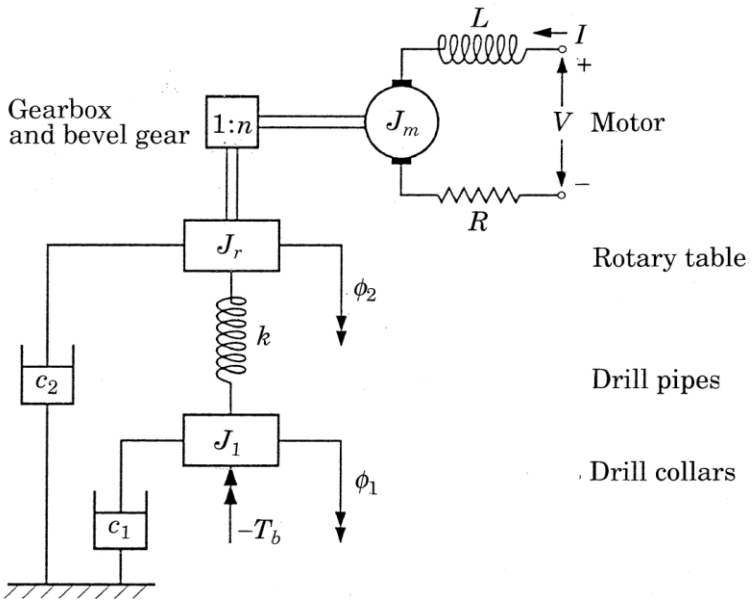

Figure 2-13. Representation of drill string/drive system as a torsional pendulum driven by an electric motor (Jansen and van den Steen, 1995)

It was shown that a damping ratio higher than a threshold value could remove the stick-slip vibration of the drill string. This was related to the fact that a high viscous damping absorbed too much energy from the drill string, and thus, the oscillations were gradually damped-out. Cancellation of the stick-slip vibration was also achieved when the rotational velocity exceeded a threshold value, or the difference between the static and dynamic torque dropped below a threshold value. Note that under a constant WOB, the static and dynamic torque-on-bit are directly related to the static and dynamic coefficients of friction, respectively. Thus, it can be inferred from the authors' work, that the stick-slip can be removed if the difference between the static and dynamic friction coefficients is smaller than a certain value.

Richard et al. (2007) developed a two degree-of-freedom lumped parameter model to study the coupled axial-torsional vibration with drag bits. The system was represented by three mechanical elements, namely, a point mass for the BHA, a corrected mass moment of inertia for the BHA and drill pipes, and a massless spring with a torsional stiffness for the drill pipes. The coupling between the axial and torsional vibration was gained through a rate-independent bit-rock interaction law, in which both the torque-on-bit and weight-on-bit were decomposed into cutting and friction components. The cutting process occurs at the cutting face of the blades on the drill bit and defines the removal of the rock, while the friction component is due to the contact between the wearflat (the underside of the blades) and the borehole bottom. These components were represented as functions of depth of cut and coefficient of friction. Despite some other studies in which the coefficient of friction was related to the angular velocity of the drill bit (velocity-weakening behavior), the authors used a velocity-independent coefficient. In this model, the damping of the system was neglected, because most of the energy dissipation in the drill string was attributed to the frictional contact at the bit-rock interface. The model accounted for the loss of contact at the bit-rock interface due to small amplitude axial vibrations of the drill bit, as well as the time-delay effects associated with the cutting process. Under a constant bit angular velocity, the time-delay is defined as the required time for the drill bit to rotate over the angel between two successive blades (Liu et al., 2014). The state-dependent time-delay, however, accounts for the variations of the time-delay due to system dynamics. The developed model is a novel state-dependent dynamical system with discontinuous boundary conditions. The authors concluded that the self-excited nature of vibrations were due to the delayed and coupled nature of the cutting process. It was observed that the

decrease of the torque-on-bit with the angular velocity, the so-called rate-independent behaviour of the torque-on-bit, was a result of the stick-slip vibration, rather than a reason for the stick-slip.

Navarro-Lopez and Cortes (2007) proposed a lumped-parameter model for the torsional vibration of the drill string, which simplifies the analysis and system simulation compared to partial derivative models; see Figure 2-14. The model was a generalized form of the other drill string torsional lumped-parameter models such as (Brett, 1992; Kyllingstad and Halsey, 1988; Lin and Wang, 1991, Abbassian and Dunayevsky, 1998;, Jansen and van den Steen, 1995; Mihajlovic et al., 2004), but accounted for the increasing length of the drill string during operation and the torsional vibrations along the connected drill pipes and drill collars. The proposed model was an n-dimensional lumped-parameter discontinuous model, in which the discontinuity at the bit-rock contact interface was captured by a dry friction with exponential-decaying law. The torque-on-bit was represented as a combination of viscous damping and dry friction components. The viscous damping component approximated the effect of drilling mud on the bit. The bit-rock interaction was modeled as a dry friction with exponentially decaying variation. The authors identified the transition between several bit dynamics, and observed that these transitions were dependent on the weight-on-bit and the motor torque at the surface. The authors showed that the stick-slip and the bit sticking phenomena obtained from an n-dimensional lumped-parameter model were characterized by the dynamics of the drill collars, rather the dynamics of the top-rotary mechanism in a two degree-of-freedom model. The authors studied the local Hopf bifurcations of the system for rotary velocities greater than zero. The behaviour of the drill string under variation of three bifurcation parameters was studied, namely, the

weight-on-bit, the top rotary velocity, and the motor torque. Using the local bifurcations for rotary velocities greater than zero, the authors determined the regions of rotary velocity and weight-on-bit in which non-desired vibrations were present.

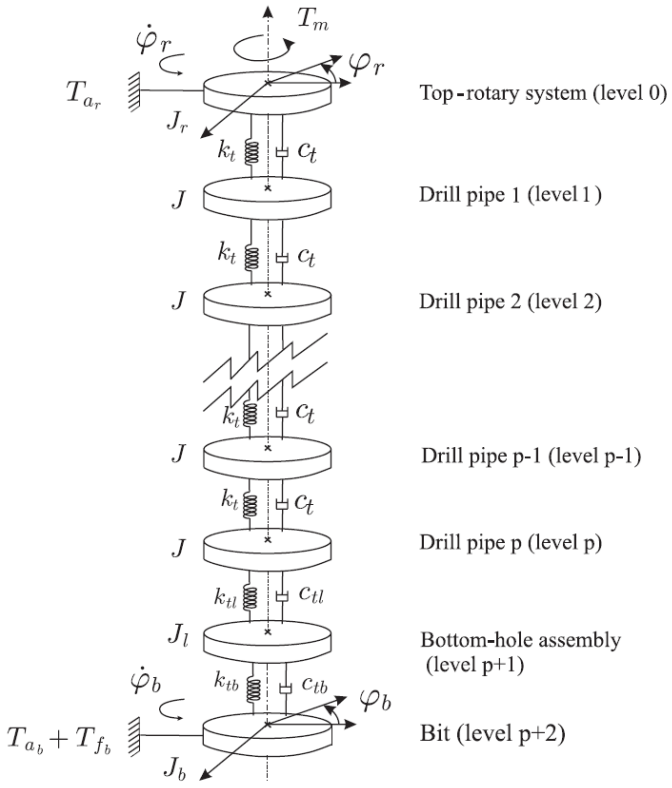

Figure 2-14. Schematic illustration of torsional model of drill string (Navarro-López and Cortes, 2007)

Liu et al. (2013) developed an eight degree-of-freedom lumped-parameter model for the coupled axial-torsional-lateral vibration of both the drill pipes and drill collars. The model accounted for the nonlinearities due to the dry friction, loss of contact, collisions, and the state-dependent time-delays associate with the axial and lateral cutting actions. The excitation forces were considered as a result of contact and friction at the bit-rock and drill pipe-wellbore interfaces. The equations of motion of the discrete model of the spatially

continuous drill string system was derived using the Lagrange's equations. The model involved two disks, each with four degrees-of-freedom including one for axial motions, one for torsional motions, and two for lateral motions. The drill pipes were modeled with two identical, massless, elastic elements with axial, torsional, and bending potential energy contributions. The contact interactions between the drill pipes and wellbore were modeled following the studies of Leine et al. (2002) and Liao et al. (2011), accounting for the normal and tangential forces. The model of contact interactions between the drill bit and the rock involved the state-dependent time-delay, which represented the time during which the bit rotated through an angular displacement equal to the angel between two successive blades. As the bit angular velocity varies due to stick-slip vibrations, the time-delay is not constant. The tangential torque and normal force at the bit-rock contact interface were decomposed into cutting component (proportional to the cutting depth) and frictional component (independent of the cutting depth). The frictional components of the tangential torque and normal force were represented as velocity-weakening friction, different than the rate-independent friction models previously used in Richard et al. (2004) and Richard et al. (2007). The authors showed that there was no direct relation between the drive frequency and the frequency content of the drill string response during vibrations. It was observed that the presence of stick-slip motions were due to the stick-slip and time-delay effects, which match the results obtained earlier in Richard et al. (2004) and Richard et al. (2007). The study of the whirling motions of the drill pipes in the presence of the frictional contact between the pipes and wellbore showed that forward whirling occurred at low friction values, while backward whirling occurred at high friction values.

2.2.6 Finite Element Models

Limitations and difficulties of analytical models in appropriate treatment of complicated boundary conditions and forces such as fluid-drill string interaction, friction, drill string-wellbore contact, and bit-rock interaction, along with the development of fast processing computers, have lead many researchers to extensively use numerical methods such as FEM to investigate the dynamical behavior of drill string system. Even though the FEM models are more computationally costly compared to the lumped parameter models, they maintain significant benefits in capturing accurate dynamic behavior of the drill string under realistic loads and boundary conditions. One of the early drill string analyses using the FEM was conducted by Millheim et al. (1978), where a custom FE package MARC-CDC was used to model the BHA dynamics.

Many FEM analyses were dedicated to investigating the dynamic characteristics of non-rotating BHA including evaluation of mechanical properties, modal characteristics, harmonic analyses (Besaisow and Payne, 1986; Burgess et al., 1987; Mitchell and Allen, 1987; De SM Costa and Rebeiro, 1997) and forced frequency response analysis considering the effect of mud damping (Apostal et al., 1990), as well as transient response of rotating BHA taking into account the bit-rock interaction (Baird et al., 1985).

Spanos et al. (1997) developed an FEM formulation to study the damped lateral BHA vibrations under monochromatic harmonic excitation using Euler-Bernoulli beam element. The finite element formulation of the BHA included the effect of axial on lateral vibrations. Because the compressive loads reduce the natural frequency of the system. During the analysis, any zero or imaginary natural frequencies were considered as an indication of the

BHA buckling under the compressive loads. This criterion is based on the fact that the compressive loads reduce the natural frequency of the system, and result in zero or negative natural frequencies if they exceed a critical value. A transfer function was implemented based on modal superposition to predict the dynamic response of the system accounting for the nonlinear wellbore contact and frequency dependant added mass. Experiments were carried out to obtain damping ratio as an emperical function of vibration frequency and mud density. The total dynamic mass matrix of the BHA was described as a combination of the consistent mass of the BHA, the mud mass inside the drill collar, and the frequency dependent added mud mass between the drill collar and the wellbore. The boundary condition at the bit was defined as an axial upward force (WOB) and a lateral force. Also the upper node of the BHA was free of constraints, while other nodes along the BHA were laterally restricted. It was shown that the fluid added mass significantly affected the natural frequencies of the BHA, while the WOB had a weak effect on the system response due to short element spacing and small value of WOB compared to the critical buckling load.

Some researchers, on the other hand, used FEM to study the dynamic behavior of the whole drill string.

Axisa and Antunes (1992) studied the uncoupled transverse-torsional behavior of the drill string through the FE computer code ROTOR. The drill string was modeled using Timoshenko beam elements to include shear deformation and flexural rotary inertia of the cross-sections. The fluid-elastic forces due to the coupled flow rotation surrounding the drill string were taken into account. The effect of nonlinear gravitational axial stiffening was not addressed in the model.

The coupling between vibration modes of a drill string has been studied through linear or nonlinear FEM models. Dunayevsky et al. (1993) applied FEM to investigate the parametric lateral insatiability of the drill string due to axially induced bit excitation. The axial excitation force WOB was divided into a static component, and a fluctuating component modeled as a monoharmonic signal. In that model, the time series of the drill string response was not introduced, and the gyroscopic effect and axial stiffening due to gravitational effect were neglected. Berlioz et al. (1996) conducted experimental and numerical investigation of lateral behavior of a rotating drill string induced by lateral-torsional and lateral-axial coupling effects. The experimental tests were carried out in vertical straight and vertical 2D curved positions to study the lateral behavior of a plain rod and FEM model validity. The numerical FEM formulations were derived for six degrees-of-freedom shaft element based on rotor dynamics theory. The axial stiffening was neglected, while both gyroscopic and fluid-elastic effects were taken into account.

Sampaio et al. (2007) developed a geometrically nonlinear FE model to analyze the coupled axial-torsional vibrations of the drill string subjected to axial WOB and rotation. The proposed model accounted for the large rotations and nonlinear strain-displacement relations in addition to the nonlinear torque-on-bit. The drill string was subjected to a distributed axial load due to the self-weight, which resulted in geometrical stiffening. The variational strain energy approach was used to derive the equations of motion of the drill string with large displacement and small deformations. The variational strain energy involved both the linear and nonlinear strain energy, where the linear model was obtained by removing the geometrical stiffening from the nonlinear model. The damping effects were modeled using mass proportional Rayleigh damping for both axial and torsional

motions. The finite element model was obtained through discretization of the virtual work components of strain, inertia, damping, and applied forces. The discretization was conducted using linear shape functions for both axial and rotational displacements. The discretized equations of motion were defined as:

$$M\ddot{q} + D\dot{q} + \left[K_e + K_g(q)\right]q = F_g + F_f + F_T \quad (5)$$

where M, D, K_e, K_g are the global matrices of mass, damping, elastic stiffness and geometric stiffness, respectively, while F_g is the global vector of gravity force, F_f is the axial reaction due to rock formation, and F_T is the torque-on-bit due to bit-rock contact. The comparison between the proposed linear and nonlinear models revealed quantitative and qualitative differences between the results, especially under stick-slip vibrations. The nonlinear model, in which the axial and torsional vibrations were geometrically coupled, resulted in higher angular velocity peaks compared to the linear model under stick-slip vibrations.

Khulief and Al-Naser (2005) used the Lagrangian approach together with FEM to develop the equation of motion of a rotating drill string including drill pipes and drill collars. Two-node finite shaft elements with six degrees-of-freedom at each node were used, where a total of 140 degrees-of-freedom was obtained for the drill string after applying the boundary conditions. The model accounted for the axial stiffening, torsional-bending inertia coupling, gyroscopic effects, and the gravitational force field effects, while the drill pipe-wellbore contact, internal damping, and flow-induced forces were neglected. The gravitational force field and the WOB divide the drill string into two fields of axial force,

namely, the tension field (drill pipes) and compression field (drill collars). The equations of motion of the drill string was given as:

$$[M]\{\ddot{e}\} + [G]\{\dot{e}\} + [K]\{e\} = \{Q\} \quad (6)$$

with

$$[M] = [M_t] + [M_r] + \left[M_\varphi\right] - 2[M_e], [K] = [K_a] + [K_b] + \left[K_\varphi\right] + \left[K_{gs}\right] \quad (7)$$

where [M] is the global assembled mass matrix, [G] is the gyroscopic matrix, [K] is the global stiffness matrix, {e} is the deformation vector, $[M_t]$ is the translational mass matrix, $[M_r]$ is the rotary inertia mass matrix, $[M_\varphi]$ is the torsional mass matrix, $[M_e]$ is the torsional-transverse inertia coupling mass matrix, $[K_a]$ is the axial stiffness matrix, $[K_b]$ is the bending stiffness matrix, $[K_\varphi]$ is the torsional stiffness matrix, and $[K_{gs}]$ is the axial stiffness matrix due to the gravitational field accounting for the stiffening effect in the tension field (i.e., drill pipes) and softening effect on the compression field (i.e., drill collars). A reduced order model with five degrees-of-freedom was obtained using the modal transformation, and its response was compared with the full order (140 degrees-of-freedom) model. The modal contents, i.e., bending natural frequencies and lateral response time series of the drill string without contact and stick-slip at the bit were calculated in both reduced and full order models. As the hydrostatic force due to the presence of mud was not considered in this model, the authors adjusted the WOB to determine the location of the neutral point along the drill string. The first ten bending modes of the system for different locations of the neutral point were obtained. It was observed that under an initial lateral velocity applied to the midpoint of drill pipes, an eight degree-of-freedom reduced-order model approached the response of the FEM model more accurately than the five degrees-

of-freedom model. This is due to the nature of impact loads which excite the higher modes of the system and require a higher degree-of-freedom discrete model. This model was adopted by Khulief et al. (2007) by integrating the stick-slip excitation within the proposed FEM formulation. The effects of damping were neglected in this model. The vertical force WOB at the bit-rock contact interface was assumed to oscillate harmonically about a mean value, as expressed in Yigit and Christoforou (1998) and Richard and Detournay (2000):

$$WOB = W_0 + k_f x_0(1 - \sin 2\pi f t) \tag{8}$$

where f is the frequency of fluctuations, and x_0 is the depth of cut in one bit revolution, assuming that the bit rotates at angular velocity $\dot{\varphi}_0$ and travels at axial velocity $\dot{x}$. The authors also assumed that the frequency of the axial motion $1/(x_0/\dot{x})$ and torsional motion $1/(2\pi/\dot{\varphi}_0)$were equal. To include the effect of axial motion on the torsional vibrations, the axial degree of freedom and angular velocity were coupled through the nonlinear torque-on-bit, as follows:

$$TOB = \mu_k WOB \xi(\dot{\varphi}) \tag{9}$$

where $\mu_k$is the coefficient of kinetic friction, and $\xi(\dot{\varphi})$ is a nonlinear continuous function relating the torque-on-bit to the bit angular velocity, which was similar to the one adopted by Tucker and Wang (1999) as follows:

$$\xi(\dot{\varphi}) = \tanh(\dot{\varphi}) + \frac{\alpha_1 \dot{\varphi}}{1 + \alpha_2 \dot{\varphi}^2} \tag{10}$$

In another study, Khulief et al. (2008) expanded the FEM model originally developed by Khulief et al. (2007) by incorporating the contact-impact behavior of the drill string under coupled lateral-torsional vibrations. The model included the gyroscopic effects, the gravitational force field effects, the torsional-bending inertia coupling, and the axial-

bending geometric nonlinear coupling. A total of 24 finite shaft elements with six degrees of freedom at each node were used to model the drill pipes and drill collars. The impact force due to drill string-borehole contact was modeled using a continuous force-displacement law, where the material stiffness and damping coefficients at the contact zone were obtained from energy balance formulations.

Ritto et al. (2009a) proposed a coupled axial-lateral-torsional model of the drill string to study the effect of mud flow on the natural frequencies and dynamical behavior of the system. The equations of motion were obtained using the extended Hamilton principle and were discretized by means of FEM. 3D Timoshenko beam elements with two nodes and six degrees-of-freedom per node were used to model the drill string including drill pipes and drill collars. The coupling of vibration modes was achieved through finite strain assumption. The geometric stiffness matrix was used to model the pre-stressed configuration of the drill string under axial loads. The impact and rubbing between the drill string and borehole were modeled as elastic force and frictional torque, respectively. These forces were applied if the radial displacement of a node exceeded the gap between the drill string and the borehole. In the BHA region, the stabilizers were represented as elastic elements to diminish the amplitude of lateral vibrations. The bit-rock interaction was expressed in terms of the WOB and the torque-on-bit similar to Tucker and Wang (2003). A simplified fluid-structure interaction model with a linear assumption of the pressure distribution along the drill string was proposed to simulate the fluid flow inside and outside of the drill string. The proposed simplified fluid-structure interaction model was a 3D extension of the model originally developed by Paidoussis et al. (2008), assuming that the inside flow is inviscid, whereas the outside flow is viscid. To include the flow effects, three

matrices, namely, the fluid mass, the fluid damping, and the fluid stiffness, were added to the standard FEM formulation of the equations of motion. The effect flow induced by rotation of the string was neglected. However, the influence of damping was not analyzed in detail. The results showed that the lateral natural frequencies of the drill string under pre-stressed state were completely different (greater) compared to the model without the pre-stressed state. However, the axial and torsional natural frequencies were little affected by the pre-stressed configuration. It was observed that the presence of the fluid did not change the axial and torsional natural frequencies, but significantly increased or decreased the lateral natural frequencies for different modes. It was revealed that due to the presence of the fluid, the amplitude of the axial and torsional vibrations were little affected, but the self-excited frequency of the system, which is related to the first torsional natural frequency, was changed. In another study, Ritto et al (2009b) used the similar model and incorporated the uncertainties in bit-rock interaction using a non-parametric probabilistic method. Also Ritto and Sampaio (2012) studied dynamic response of the drill string under the influence of uncertainties associated with the drive speed and bit-rock interaction parameters using the developed FEM model.

Germay et al. (2009) studied the self-excited axial and torsional dynamic response of a drill string system using FE formulation. The FE formulation of the model was based on a continuum representation of the drill string, which was an expanded version of the two degrees-of-freedom model originally developed by Richard et al. (2007). The obtained FE model was capable of capturing multiple torsional and axial natural vibration modes, rather than the original torsional pendulum model with single natural frequency. The axial and torsional vibration modes were geometrically uncoupled. The bit-rock interaction was

considered to describe the stick and slip phases for both axial and rotational motions. The drill string was modeled using Euler-Bernouli beam elements. Due to the discontinuity of the cross-section of the drill string at the pipes and collars junction, parts of an incident wave will be transmitted to the other section, and parts of it will be reflected. To account for these phenomena, the authors obtained the coefficients of transmission and reflection by applying the continuity of the velocity and the balance of force conditions at the pipe-collar junction in both the axial and rotational degrees-of-freedom. To model the bit-rock contact interface, both the WOB and torque-on-bit were divided into cutting and friction components. The coupling between the axial and torsional vibrations at the bit was obtained through the bit-rock interaction law, which related the torque-on-bit to the WOB and the depth of cut. The effect of damping in the numerical simulation was taken into account by means of stiffness proportional Rayleigh damping for both axial and torsional modes. The authors studied the stick-slip vibration, bit-bouncing, and the effect of varying WOB and rotational speed on these phenomena. It was observed that increasing the WOB or decreasing the rotational speed enhanced the occurrence of the stick-slip and bit-bouncing. The implementation of the FE model revealed new features of the self-excited response of the drill string, that is, stick-slip vibrations can occur at frequencies higher than the first natural frequency of the drill string.

Jafari et al. (2012) implemented FEM to study the effects of drilling mud flow rate, drill string weight, WOB, and angular velocity on the stability of a rotating drill string. The axial and lateral vibrations were coupled through the geometrical shortening effect. It was observed that the critical height of the neutral point decreased with increasing drilling mud flow rate and angular velocity. As well, increasing WOB was shown to decrease the natural

frequency and increase the amplitude of lateral vibrations, whereas increasing drilling mud flow rate reduced both the natural frequency and amplitude of lateral vibrations.

Trindade et al. (2005) constructed a nonlinear axial-bending FE model of a non-rotating drill string considering nonlinear strain-displacement formulations. Euler-Bernoulli beam elements with six degrees of freedom were used, where the full FE model had a total of 87 DOF. The drill string was subjected to axial distributed self-weight, concentrated reaction force acting on the bit, vibro-impact force due to the drill string-borehole contact, and perturbation force due to induced vibrations.

Ghasemloonia et al. (2013) developed an FEM model of the drill string to study the coupled axial-lateral dynamics of the system under the influence of vibration-assisted rotary drilling tools. The FEM model was generated using ABAQUS Explicit package. Hermite cubic beam elements with no shear flexibility were used to model the drill pipes and drill collars. The interaction between BHA and wellbore was modeled using the Kinematic contact algorithm in ABAQUS, where the sliding friction was neglected in the model. Mass proportional Rayleigh damping was employed in both axial and lateral directions to simulate mud damping effects. The mass proportional damping coefficient was not addressed. The effects of geometric nonlinearity were taken into account. The developed FEM model was validated with a nonlinear coupled axial-lateral elastodynamic analytical model. The governing equations were derived using the Bypassing PDE's method based on the Lagrangian approach. The effects of nonlinear axial stiffening, spatially varying axial force, driving torque, multispan contact, and mud damping (assumed as hydrodynamic drag force) were included in the analytical model.

Kapitaniak et al. (2015) developed an experimental drilling assembly using real drill bit and rock sample in order to study the stick-slip dynamics of helically buckled drill string, and calibrate the high dimensional FE and low dimensional mathematical models. The experimental rig was able to consider two configurations, namely, a rigid shaft to simulate the bit-rock interaction and measure the torque on bit, and a flexible shaft to simulate the drill string oscillations. The torsional stiffness and viscous damping coefficient of the flexible shaft were determined as a function of tensile force (i.e. the mass attached to the shaft) by applying an initial angular displacement at the bit and measuring the decaying free torsional vibrations. To achieve a simple frictional model, the authors considered the bit-rock interface as two surfaces sliding on each other with an equivalent exponentially decaying coefficient of friction. The equivalent friction model was proposed accounting for the constant friction, the static-kinetic exponentially decaying friction, and the Stribeck effect, as follows:

$$T_{b,sl}(\omega_b, \gamma_f) = \begin{cases} \dfrac{2}{3}\lambda_s W_s, \omega_b = 0 \\ \dfrac{2}{3}\lambda_k W_b + \dfrac{2W_b(\lambda_s - \lambda_k)}{\lambda_d^3 \omega_b^3}\left(2 - e^{-\lambda_d \omega_b}(\lambda_d^2 \omega_b^2 + 2\lambda_d \omega_b + 2)\right), \omega_b > 0 \end{cases} \quad (11)$$

with

$$\lambda_s = \mu_s R, \lambda_k = \mu_k R, \lambda_d = d_c R \quad (12)$$

where $T_{b,sl}$ is the reaction torque-on-bit during the sliding phase, ω_b is the bit angular velocity, μ_s and μ_k are the is the static and kinetic coefficients of friction, respectively, d_c is a constant, $R > 0$ is the radius of the contact surface, W_b is the weight-on-bit. The FE model of the experimental rig was developed in ABAQUS software to calibrate the low

dimensional model. The flexible shaft representing the drill string was modeled by 1000 hexahedral 3D elements using anisotropic material to take into account the low lateral and high torsional stiffness of the drill string. The drill bit was modeled as a cylinder with fixed transversal degrees of freedom. A low dimensional lumped mass model based on the torsional pendulum was used, where the massless rotary table was connected to the BHA through an elastic spring with torsional stiffness and damping, and the bit-rock interaction was described by the equivalent friction model. For both low and high dimensional models, the time series and phase planes of the bit stick-slip oscillations were shown to be in agreement with each other. However, the results of the FE model were a little closer to the experimental rig.

Real et al. (2018) proposed a hysteresis bit-rock interaction model to study the torsional vibrations of the drill string by means of FEM. The continuous drill string was discretized into 100 finite elements with fixed-free boundary conditions where the first five natural frequencies were obtained. The stick-slip vibrations were shown to be larger when using the hysteretic bit-rock interaction model. Liu et al. (2020) employed FE formulation to develop an integrated nonlinear, spatially continuous model of the drill string to study axial-torsional vibrations. Two node bar elements with two DOF at each node were used. Internal structural damping and external mud viscous damping in both axial and torsional directions, as well as the effects of gravity and buoyancy were considered in the model.

References

Abbassian F., Dunayevsky V.A. (1998), Application of stability approach to torsional and lateral bit dynamics, SPE Drilling Completion. 13(2) 99-107.

Apostal MC, Haduch GA, Williams JB (1990). A Study to determine the effect of damping on finite-element-based, forced-frequency response models for bottomhole assembly vibration analysis, SPE 20458, Proceedings of the 65th SPE Annual Technical Conference and Exhibition, New Orleans, LA, September 23–25.

Ashley, D. K., McNary, X. M., and Tomlinson, J.C., 2001, Extending BRA Life With Multi-Axis Vibration Measurements, SPE/IADC# 67696, IADC/SPE Drilling Conference, Amsterdam, Netherlands.

Axisa F, Antunes J. (1992). Flexural vibration of rotors immersed in dense fluids: part I – theory. J. Fluids Struct. 6(1)3–21.

Baird JA, Caskey BC, Wormley DN, Stone CM. (1985). GEODYN2: a bottom hole assembly geological formation dynamic interaction computer program. In: Proceedings of the SPE#14328, SPE Annual Technical Conference and Exhibition. Las Vegas, Nevada.

Berlioz A, Hogopian JD, Dufour R, Draoui E (1996). Dynamic behavior of a drillstring: experimental investigation of lateral instabilities. Trans ASME, J Vib Acoust 118:292–8.

Besaisow AA, Payne ML (1986). A study of excitation mechanisms and resonances inducing bottomhole-assembly vibrations, SPE No. 15560, Proceedings of the 61st Annual Technical Conference and Exhibition of the Society of Petroleum Engineers, New Orleans, LA, October 5–8.

Brett J.F. (1992), The genesis of bit-induced torsional drillstring vibrations, SPE Drill. Eng. 7;168–174.

Burgess TM, McDaniel GL, Das PK (1987). Improving BHA tool reliability with drillstring vibration models: field experience and limitations, SPE 16109, Proceedings of the SPE/ADC Drilling Conference, New Orleans, LA, March 15–18.

Challamel N., Sellami H., Chenevez E., Gossuin L., (2000), A Stick-slip Analysis Based on Rock/Bit Interaction: Theoretical and Experimental Contribution, Society of Petroleum Engineers.

Chevallier A.M. Politis N.P. Payne M.L. Spanos, P.D. (2003). Oil and gas well drilling: A vibrations perspective. Shock and Vibration Digest, 35(2).

Clukey, E., Banon, H., Kulhawy, F. 2000. Reliability assessment of deepwater suction caissons. Proceedings of Offshore Technology Conference OTC 12192, Houston, Texas.

De SM Costa F, Rebeiro PR (1997). Finite Element modeling of the mechanical behavior of unbalanced drill collars, SPE 39025, Proceedings of the Fifth Latin American and Caribbean Petroleum Engineering Conference and Exhibition, Rio de Janeiro, Brazil, August 30–September 3.

D'Souza, R. B., Dove, P. G. S., and Kelly, P. J. (1993). Taut Leg Spread Moorings: A Cost-Effective Stationkeeping Alternative for Deepwater Platforms. Offshore Technology Conference, Houston, Texas, USA.

Dufeyte, M.-P., & Henneuse, H. (1991, January 1). Detection and Monitoring of the Slip-Stick Motion: Field Experiments. Society of Petroleum Engineers. doi:10.2118/21945-MS.

Dunayevsky VA, Abbassian F, Judzls A. (1993). Dynamic stability of drillstrings under fluctuating weight on bit. SPE Drill. Complet. 8(2), 84–92.

Germay C, Denol V, Detournay E (2009). Multiple mode analysis of the self-excited vibrations of rotary drilling systems. J Sound Vib325(1–2):362–81

Ghasemloonia A, Rideout DG, Butt SD. (2013). Vibration analysis of a drillstring in vibration-assisted rotary drilling: finite element modeling with analytical validation. ASME J. Energy Resour. Technol. 135(3), 032902-1-032902-18

Ghasemloonia, A., (2013) Elastodynamic and finite element analysis of coupled lateral-axial vibration of a drillstring with a downhole vibration generator and shock sub. Doctoral (PhD) thesis, Memorial University of Newfoundland.

Halsey G.W., Kyllingstad A., Kylling A., (1988). Torque feedback used to cure stick-slip motion, SPE Annual Tech. Conf. and Exhibition.

Jafari AA, Kazemi R, Mahyari MF (2012). The effects of drilling mud and weight bit on stability and vibration of a drill string. J Vib Acoust Trans ASME;134(1)

Jansen J.D., van den Steen L. (1995), Active damping of self-excited torsional vibrations in oil well drillstrings, J. Sound Vib. 179 (4) 647–668.

Kapitaniak M, Vaziri Hamaneh V, Chávez JP, Nandakumar K, Wiercigroch M (2015). Unveiling complexity of drill-string vibrations: experiments and modelling. Int. J. Mech. Sci., 101–102, pp. 324-337, 10.1016/j.ijmecsci.2015.07.008

Khulief YA, Al-Naser H. (2005). Finite element dynamic analysis of drillstrings. J. Finite Elem. Anal. Des. 41,1270–1288.

Khulief YA, Al-Sulaiman FA, Bashmal S (2007). Vibration analysis of drillstrings with self-excited stick–slip oscillations. J. Sound Vibr. 299, 540–558

Khulief YA, Al-Sulaiman FA, Bashmal S. (2008). Vibration analysis of drillstrings with string-borehole interaction. Int. J. Mech. Eng. Sci., IMechE Part C 222, 2099–2110

Kyllingstad A, Halsey GW. (1988, December 1). A Study of Slip/Stick Motion of the Bit. Society of Petroleum Engineers. doi:10.2118/16659-PA.

Leine, R.I., van Campen, D.H., Keultjes, W.J.G. (2002) Stick-slip whirl interaction in drillstring dynamics. J. Vib. Acoust. 124(2), 209–220.

Lesso B., Ignova M., Zeineddine F., Burks J., and Welch B. (2011). Testing the combination of high frequency surface and downhole drilling mechanics and dynamics data under a variety of drilling conditions. In SPE/IADC Drilling Conference and Exhibition, SPE/IADC 140347, Amsterdam, Netherlands.

Liao, C.-M., Balachandran, B., Karkoub, M., Abdel-Magid, Y.L. (2011) Drill-string dynamics: reduced-order models and experimental studies. J. Vib. Acoust. 133(4), 041008

Lin Y.Q., Wang Y.H. (1991), Stick-slip vibration of drillstrings, ASME J. Eng. Ind. 113 (1) 38–43.

Liu X, Long X, Zheng X, Meng G, Balachandran B (2020). Spatial-temporal dynamics of a drill string with complex time-delay effects: Bit bounce and stick-slip oscillations. International Journal of Mechanical Sciences 170;105338.

Liu X, Vlajic N, Long X, Meng G, Balachandran B (2013). Nonlinear motions of a flexible rotor with a drill bit: stick-slip and delay effects, Nonlinear Dyn. 72 (1-2) 61-77.

Liu X., Vlajic N., Long X., Meng G., Balachandran B., (2014), Coupled axial-torsional dynamics in rotary drilling with state-dependent delay: stability and control, Nonlinear Dyn.

Ma, K.T., Luo, Y., Thomas Kwan, C.T., Wu, Y., (2019). Mooring System Engineering for Offshore Structures, Elsevier.

Mihajlovic N, van Veggel AA, van de Wouw N, Nijmeijer H, (2004) Analysis of friction-induced limit cycling in an experimental drill-string system, ASME J. Dynam. Systems Measurement Control 126;709-720.

Millheim K, Jordan S, Ritter C (1978). Bottom-hole assembly analysis using the finite element method, SPE paper no. 6057;p.265–74.

Mitchell RF, Allen MB (1987). Case studies of BHA vibration failure, SPE 16675, Proceedings of the 62nd SPE Annual Technical Conference & Exhibition, Dallas, TX, September 27–30.

Murff, J. D. and Hamilton, J. M. (1993). P-Ultimate for Undrained Analysis of Laterally Loaded Piles, J. Geot. Eng. Div., ASCE, 119(1), Jan, pp. 91-107.

Navarro-López EM (2009). An alternative characterization of bit-sticking phenomena in a multi-degree-of-freedom controlled drillstring. Nonlinear Anal Real World Appl 10(5):3162–74.

Navarro-López EM, Cortes D. (2007) Avoiding harmful oscillations in a drillstring through dynamical analysis. J. Sound Vib. 307,152–171.

Navarro-López EM, Licéaga-Castro E (2009). Non-desired transitions and sliding-mode control of a multi-DOF mechanical system with stick–slip oscillations. Chaos Solitons Fractals 41(4):2035–44.

Neubecker, S.R., Randolph, M.F. Performance of embedded anchor chains and consequences for anchor design Proceedings, offshore technology conference, OTC 7712, Houston, Texas (1995), pp. 191-200.

O'Neill, M. P., Randolph, M. F., and House, A. R. (1999, March 1). The Behaviour of Drag Anchors In Layered Soils. International Society of Offshore and Polar Engineers.

Ozmutlu, S. (2009, January 1). The Value of Model Testing in Understanding the Behavior of Offshore Anchors: Towards New Generation Anchors. Offshore Technology Conference. doi:10.4043/20035-MS

Paidoussis MP, Luu TP, Prabhakar S. (2008). Dynamics of a long tubular cantilever conveying fluid downwards, which then flows upwards around the cantilever as a confined annular flow. Journal of Fluids and Structures, vol. 24, pp. 111–128.

Pavlovskaia E., Hendry D. C., and Wiercigroch M. (2015). Modelling of high frequency vibro-impact drilling. International Journal of Mechanical Sciences, 91(0):110 – 119.

Pavone D.R., Desplans J.P., (1994), Application of high sampling rate downhole measurements for analysis and cure of stick–slip in drilling, Society of Petroleum Engineers.

Randolph, Mark, and Susan Gourvenec. Offshore Geotechnical Engineering, Taylor & Francis Group, 2011. ProQuest Ebook Central

Real FF, Batou A, Ritto TG, Desceliers C, Aguiar RR (2018). Hysteretic bit/rock interaction model to analyze the torsional dynamics of a drill string. Mechanical Systems and Signal Processing 111; 222–233

Richard T, Germay C, Detournay E (2007). A simplified model to explore the root cause of stick-slip vibrations in drilling systems with drag bits. J Sound Vib 305(3):432–56.

Richard T., Detournay E., (2000), Stick-Slip Vibrations of PDC Bits, American Rock Mechanics Association.

Richard, T., Germay, C., Detournay, E. (2004) Self-excited stickslip oscillations of drill bits. C. R., Méc. 332(8), 619–626

Ritto TG, Sampaio R (2012). Stochastic drill-string dynamics with uncertainty on the imposed speed and on the bit-rock parameters. Int J Uncertain Quantif;2(2)

Ritto TG, Sampaio R, Soize C (2009a). Drill-string nonlinear dynamics accounting for the drilling fluid. 30º CILAMCE-Iberian-Latin-American Congress on Computational Methods in Engineering, Armação dos Búzios, Rio de Janeiro, Brazil

Ritto TG, Soize C, Sampaio R, (2009b). Non-linear dynamics of a drill–string with uncertain model of the bit–rock interaction. Int J Non-Linear Mech;44:865–76

Ruinen, R. (2012, January 1). The Use of Drag Embedment Anchors in Arctic Conditions. The Society of Naval Architects and Marine Engineers.

Sampaio R, Piovan MT, Lozano GV. (2007). Coupled axial/torsional vibrations of drill-strings by means of non-linear model. J. Mech. Res. Commun. 34,497–502.

Serrarens A.F.A., van de Molengraft M.J.G., Kok J.J., van den Steen L. $H\infty$ control for suppressing stick–slip in oil well drillstrings IEEE Control Systems Magazine, 18 (1998), pp. 19-30

Silva-Gonzalez F, Heredia-Zavoni E, Valle-Molina C, Sanchez-Moreno J, Gilbert RB. Reliability study of suction caissons for catenary and taut-leg mooring systems. J. Struct. Saf. 2013;45:59–70.

Spanos PD, Payne ML, Secora CK. (1997). Bottom-hole assembly modeling and dynamic response determination. ASME J. Energy Resour. Technol. 119(3), 153–158

Sparrevik, P. (1998), Suction Anchors – A Versatile Foundation Concept Finding its Place in the Offshore Market, OMAE 98-3096, 17th International Conference on Offshore Mechanics and Arctic Engineering, Lisbon, Portugal.

Trindade MA, Wolter C, Sampaio R. (2005). Karhunen–Loeve decomposition of coupled axial/bending vibrations of beams subject to impacts. J. Sound Vib. 279, 1015–1036

Tucker RW, Wang C (1999). On the effective control of torsional vibrations in drilling systems, Journal of Sound and Vibration 224;101–122.

Tucker, R.W. Wang, C., 2003. Torsional vibration control and cosserat dynamics of a drill-rig assembly. Meccanica, vol. 38, n. 1, pp. 143–159.

Vryhof (2000), Anchor Manual, Vryhof Anchors B.V., Krimpen a/d Yssel, The Netherlands.

Vryhof Manual (2015), The Guide to Anchoring, Vryhof Anchors B.V., 2015

Yigit A.S., Christoforou A.P (1998), Coupled torsional and bending vibrations of drillstrings subject to impact with friction. J. Sound Vib. 215;167–181.

Yigit A.S., Christoforou A.P. (2000), Coupled torsional and bending vibrations of actively controlled drillstrings Journal of Sound and Vibration, 234, pp. 67-83

3. Chapter 3

Reliability Assessment of Drag Embedment Anchors in Clay for Catenary Mooring Systems

Mohammad Javad Moharrami[1], Hodjat Shiri[2]

1: Department of Civil Engineering
Memorial University of Newfoundland
e-mail: mjmoharrami@mun.ca

2: Department of Civil Engineering
Memorial University of Newfoundland
e-mail: hshiri@mun.ca

This chapter was published as a journal paper in Marine Structures.

Abstract

Drag embedment anchors are attractive anchoring solutions, which are widely used for temporary and permanent station keeping of floating structures. The number of floating facility incidents related to mooring system failure continues to raise concerns in the industry in general. This necessitates the reliability assessment of mooring components and their contribution to system integrity. The reliability of drag embedment anchors as a key component of popular mooring systems has never been explored before due to the high complexity of anchor-soil interaction and extensive inherent uncertainties. In this paper, the reliability of drag anchors for catenary mooring lines was investigated with attention to the seabed condition and environmental loads. The probabilistic modelling of anchor capacity was conducted using plastic yield loci to characterize the fluke-soil interaction and failure states. The embedded profile and the frictional capacity of the anchor chain at the seabed were also considered in the calculation of ultimate holding capacity. The uncertainties of the environmental loads, metocean variables, and consequently the stress distribution throughout the catenary lines were accounted for using the response surface method. First order reliability method (FORM) was used through an iterative procedure to obtain the probabilistic failures. The results show an acceptable level of reliability for these anchor families and reveal its sensitivity to key components of anchor geometry.

Keywords: Reliability analysis; Drag embedment anchor; Catenary mooring; Response surface; Numerical method; Undrained shear strength

3.1. Introduction

Drag embedment anchors are one of the most popular elements in station keeping of floating facilities. These anchors provide the required holding capacity to maintain the floating system in-place under environmental loads. Mooring lines transfer the load generated by vessel motions to the padeye located at the end of the anchor shank, which transfer the load to the fluke and surrounding seabed soil (Figure 3-1). Drag embedment anchors are usually the simplest to install and the most challenging to analyse. Catenary mooring lines ending with drag embedment anchors are usually used when large horizontal offsets of the floating system are expected under environmental loads.

Besides excellent achievements in design and application of mooring line components, the number of mooring system related incidents involving floating facilities (on an average of more than two incidents per year (Ma et al., 2013) continue to raise concerns in the industry in general. The large uncertainties in seabed parameters and environmental loads combined with the inaccessibility for monitoring, inspection, and maintenance mandates the reliability assessment of mooring components.

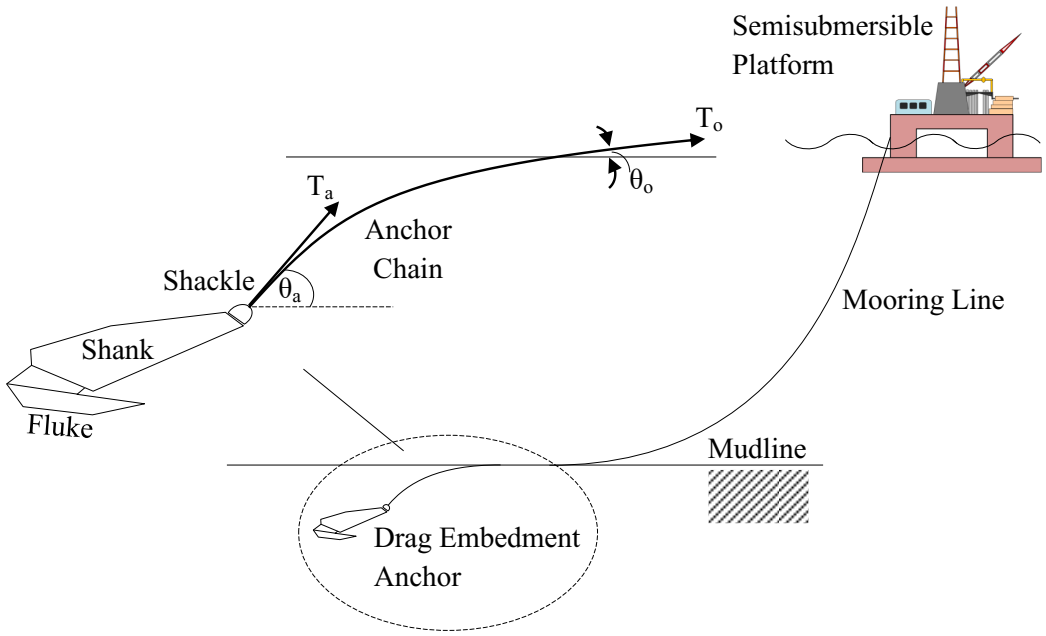

Figure 3-1. Catenary mooring system and soil interaction with drag embedment anchor.

Anchors are critical components of mooring system and their reliability assessment can have a significant contribution to the reliability of the whole system. A critical review of the literature shows that the reliability of deepwater anchors implementing the complex anchor-seabed interaction is less explored. Only a few studies have been published within recent years, most of them focusing on reliability assessment of suction caissons. There is almost no study on reliability assessment of drag embedment anchors that are the most common anchoring solution in offshore industries. These anchors are widely used in a range of water depths and geographical locations, and this was the motivation of the current study.

3.2. Review of Reliability Studies for Suction Anchors

Despite drag anchors, there are several studies conducted on reliability assessment of suction anchors. Considering a relatively close concept of the overall reliability assessment methodologies for these anchor families and the absence of any published works in reliability of drag embedment anchors, it is worth shortly reviewing some of the key studies conducted on suction anchors. This can provide a basis on how to develop a reliability assessment methodology for drag embedment anchors as well.

Clukey et al. (2000) studied the reliability of suction caissons. They used linear response surface and defined the lateral holding capacity as a function of soil shear strength and mooring line tension. The authors considered a limit state function for lateral and axial failures to model the catenary and taut-leg mooring and assessed the reliability. Choi (2007) conducted a reliability assessment of suction caissons estimating the caisson capacity at padeye using the upper bound plastic limit formulation proposed by Aubeny et al. (2003). They used the Neubecker and Randolph (1995(a)) formulations at mudline to account for soil-chain interactions. The biases and variation factor of caisson capacity were calculated using the analytical methods and validated against the test results. In terms of environmental load, authors simulated the hurricane and loop current sea states in the Gulf of Mexico. The dynamic mooring line tensions were assumed Gaussian and the reliability assessment was conducted in terms of median safety factors, and biases and coefficients of variation for loads and capacity. Valle-Molina et al. (2008) modelled the mean and expected maximum dynamic tensions as functions of the extreme environment using response surfaces obtained from catenary mooring lines of a Floating, Production, Storage

and Offloading System (FPSO). The authors fitted Weibull distributions to few selected total line tensions, which in turn were obtained from simulating the environmental variables and response surfaces. Valle-Molina et al. (2008) used Monte Carlo simulation to evaluate the reliability, estimating the caisson capacity based on plastic limit equations proposed by Aubeny et al., 2003(a), 2003(b) and 2003(c). Silva-Gonzalez et al. (2013) assessed the reliability of suction caissons through probabilistic modelling of caisson capacities based on simulations using a plastic limit model. The authors applied first order reliability method (FORM) and established linear relationships between caisson height and failure probability calibrating partial safety factors for line tensions and caisson capacity. Review of the published works shows that proper characterization of anchor capacity is a significant aspect in reliability assessment, particularly considering the significant differences in terms of loading and capacity that is highly affected by anchor-seabed interaction.

3.3. Methodology

In this study, the reliability of drag embedment anchors was assessed based on the calculation of the anchor capacity and mooring line tension at mudline. A limit equilibrium model (LEM) originally proposed by Neubecker and Randolph (1995(b)) and a yield envelope approach proposed by O'Neill et al. (2003) was developed in an Excel spreadsheet VBA Macro (Visual Basic Application) to estimate the anchor capacity taking into account the soil-chain interaction effects. The LEM model was used to produce the probability densities of anchor capacities. A generic semisubmersible platform was modelled in the Caspian Sea using the Orcaflex software package. 3D coupled finite

element analyses were conducted to obtain the characteristic mean and maximum dynamic line tensions for 100 years return period sea states, as well as the design line tension and corresponding line angle at mudline. Samples of drag anchor capacity were generated at mudline and shank padeye using calibrated closed form solution (Silva-Gonzalez et al., 2013).

Undrained shear strength at mudline, gradient of shear strength with depth, fluke and shank bearing capacity factors, anchor geometrical configurations, line tension angle at mudline, and side friction factor were the key parameters involved in estimation of anchor capacities. The mean and expected maximum dynamic line tensions were expressed as functions of uncertain metocean variables using response surfaces. First order reliability method (FORM) was applied to assess the reliability of anchors connected to the catenary mooring line. Partial design factors on mean and maximum dynamic line tensions and capacities were extracted from the DNV design code (Det Norske Veritas, 2012).

3.4. Modelling Drag Embedment Anchors

Drag embedment anchors are commonly used with chains. The chain is connected to the end of mooring line and transfers the tension load to anchor at shank padeye. Soil resistance against anchor itself and the frictional capacity of the chain provides the ultimate anchor capacity, which can be a major component in overall system behaviour (Taylor and Valent, 1984; Fulton and Stewart, 1994; Wang et al., 2010; Ozmutlu, 2012; Tian and Randolph, 2015). In this study, a stud chain was used and the effect of soil-chain interaction was accounted for to ensure a sufficient certainty in proper calculation of overall holding capacity and consequent reliability.

3.4.1. Soil-chain Interaction

The analysis of soil-chain interaction is important, first, because of the chain frictional capacity, and second, the angle which is subtended at the attachment point on the anchor. The simplified closed form solution proposed by Neubecker and Randolph (1995(b)) was used to implement the soil-chain interaction effects. The model uses the force equilibrium in a segment of embedded anchor chain as shown in Figure 3-2, where T is the line tension, θ is the inclination from the horizontal, F is the friction force, and Q is the normal soil reaction on chain segment.

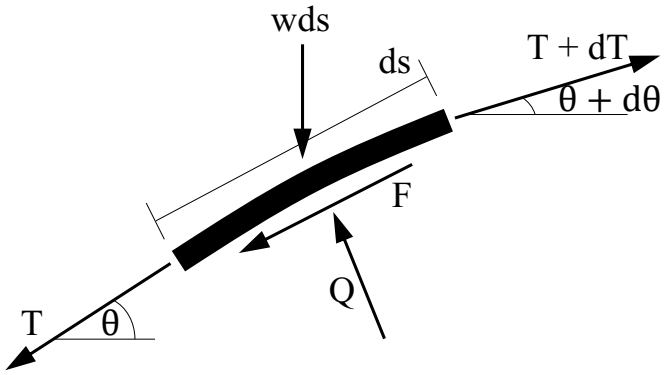

Figure 3-2. Force equilibrium of chain element embedded in soil.

Neubecker and Randolph (1995(b)) developed following sets of equations to calculate the frictional capacity of embedded anchor chain for a general soil strength profile given as:

$$s_u = s_{ug}.z^{\alpha} \quad (1)$$

where s_u is undrained shear strength; s_{ug} is gradient of shear strength with depth; z is depth; and α is soil profile index. The anchor self-weight has been eliminated for simplicity.

Chain tension-inclination compatibility: $$\frac{T_a\theta_a^2}{2} = d_a\bar{Q} \quad (2)$$

where T_a is chain tension at anchor; θ_a is chain inclination at anchor; d_a is depth of chain attachment point; and $\overline{Q}$ is average normal resistance of chain over embedment depth.

Frictional development along chain: $$\frac{T_o}{T_a} = e^{\mu(\theta_a - \theta_o)} \quad (3)$$

where T_o is chain tension at mudline; μ is chain-soil friction coefficient; and θ_o is chain inclination at mudline.

Chain profile in soil with $\alpha = 1$: $$z^* = e^{-x^*\theta_a} \quad (4)$$

where z* is depth normalized by d_a and x* is horizontal distance normalized by d_a.

In order to obtain higher accuracy, Nubecker and Randolph (1995) incorporated the self-weight of anchor chain to the general tension capacity equationgiven as:

$$T = T_a e^{\mu(\theta_a - \theta)} + \mu w s \quad (5)$$

where w is chain self-weight per unit length; s is length of chain; and θ is the chain angle in any given point.

Figure 3-3 shows the verification of the model against the centrifuge tests conducted by Bissett (1993). The centrifuge tests were performed in dense sand with a model chain consisting of four separate strands of wire plaited together. The model chain was attached at depths ranging from 50 mm to 200 mm and had an approximate diameter of 3 mm (Neubecker and Randolph (1995(b)). The exponential curve proposed by Neubecker and Randolph (1995(b)) is a good approximation to a real chain profile, where the bearing resistance is approximately proportional to depth.

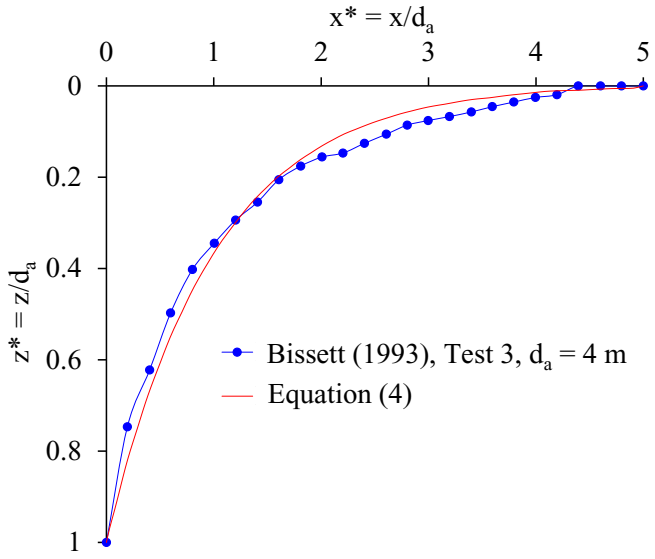

Figure 3-3. Comparison of chain profile in sand.

3.4.2. Ultimate Anchor Response

In this study, a rigorous prediction method using fundamental principles of soil mechanics and a yield envelope approach proposed by O'Neill et al. (2003) was used to calculate the ultimate holding capacity of the anchor in clay. As a drag embedment anchor approaches its ultimate capacity in soft undrained soils, failure of the soil consists of localized plastic flow around the anchor fluke and shank. The behaviour of the anchor will be largely independent of the orientation of the anchor with respect to the soil surface. The plastic yield locus of the anchor expresses the combination of vertical (V), horizontal (H), and bending moment (M) loads that result in failure of the anchor. For a given geometry and set of soil conditions, the locus can be expressed as a mathematical function of V, H, and M:

$$f\ (V, H, M) = 0 \tag{6}$$

Considering a simplified weightless drag anchor deeply embedded in undrained soil, a chain load, T_a, on the anchor padeye can be expressed in terms of forces parallel (H) and perpendicular (V) to the top face of the fluke and (negative) moment (M) about a particular reference point on the fluke, as shown in Figure 3-4. The anchor failure will occur under the combinations of these three loads (H, V, and M) and the anchor will move parallel (δh) and perpendicular (δv) to the fluke and rotationally (δψ) about the same fluke reference point. The failure of the soil around the deeply embedded anchor will remain local to the anchor fluke. Therefore, the failure loads will be independent of anchor orientation. In addition, the soil remains in contact with fluke, and the plastic fluke displacements are governed by normality to the failure locus, f (H, V, M). The normality condition (or associated flow) due to which the gradient of the yield locus determines the ratio of plastic displacement at failure, holds for undrained failure conditions when the soil remains attached to the anchor s (O'Neill et al., 2003).

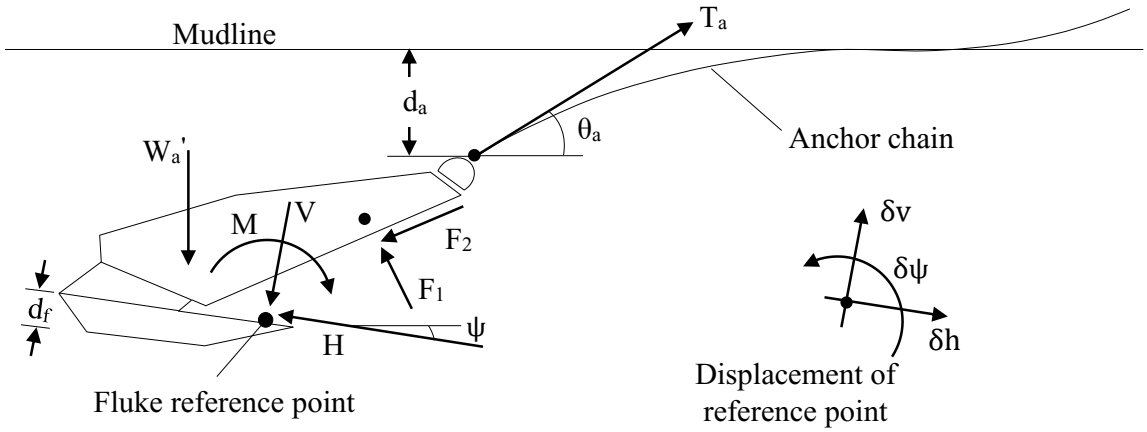

Figure 3-4. Loading mechanism and resulting displacements of a drag anchor at failure.

O'Neill et al. (2003) proposed a single mathematical curve fit in the V-H-M space:

$$f = \left(\frac{V - V_1}{V_{max} - V_1}\right)^q - 1 + \left[\left(\frac{M - M_1}{M_{max} - M_1}\right)^m + \left(\frac{H - H_1}{H_{max} - H_1}\right)^n\right]^{\frac{1}{p}} \quad (7)$$

where the offset load values V_1, M_1, and H_1, as well as the maximum load values V_{max}, M_{max}, and H_{max}, were obtained from the FE analyses, and were normalized by the fluke length, L_f and the undrained shear strength, s_u.. In order to achieve a best-fit solution, the curve fitting exponents m, n, p, and q were determined using a least-squares regression method. Table 3-1 summarizes the resulting values of model parameters for the wedge fluke yield loci.

Table 3-1. Curve fitting parameters for yield loci (O'Neill et al., 2003).

Parameter	Value
m	2.37
n	2.14
p	0.93
q	3.41
$H_1/(L_f s_u)$	0
$V_1/(L_f s_u)$	−1.25
$M_1/(L_f^2 s_u)$	−0.57
$H_{max}/(L_f s_u)$	3.34
$V_{max}/(L_f s_u)$	11.53
$M_{max}/(L_f^2 s_u)$	1.60

Figure 3-5 illustrates the yield locus obtained from the full set of wedge fluke displacement probes performed by different combinations of horizontal, δh, vertical, δv, and rotational, δψ, displacement. The dimensionless final load points are shown in M-H, M-V, and V-H space, taking a slice through the yield loci at the offset value of the third load component (V_1, H_1, and M_1).

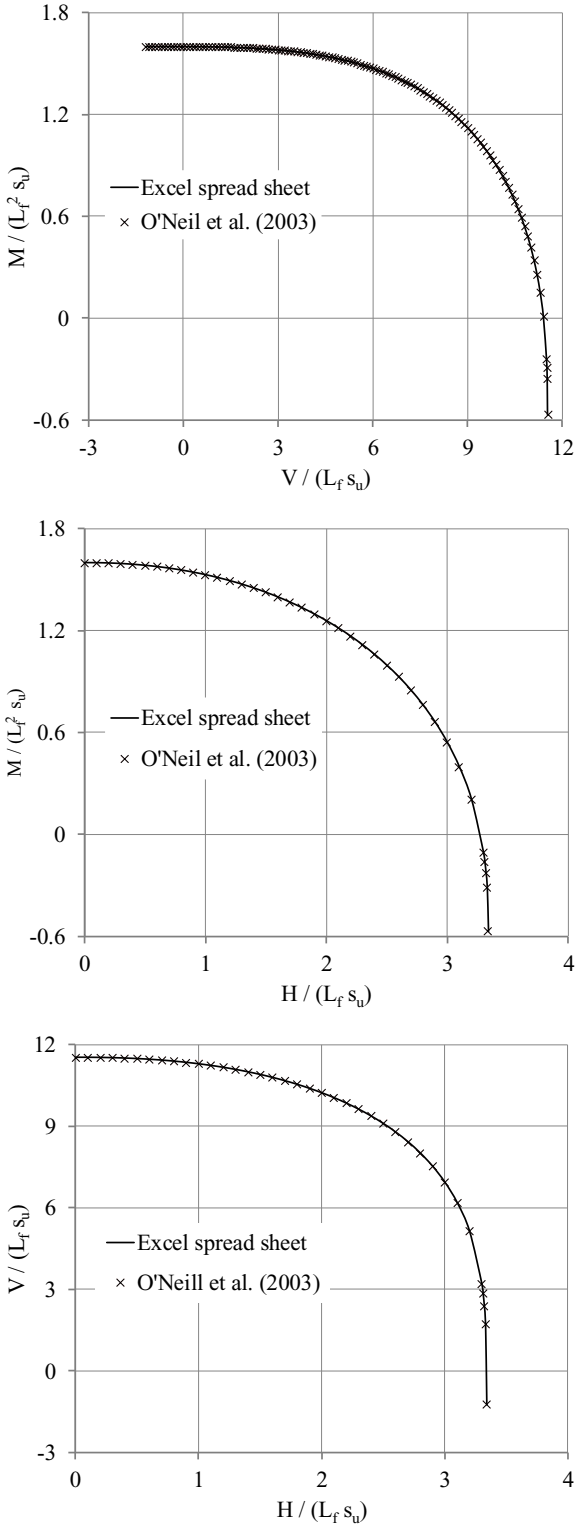

Figure 3-5. Yield locus in H-V-M space.

3.4.3. Developing Macros for Simulation of Anchor Response

The kinematic analysis to obtain the anchor trajectory, final embedment and the ultimate anchor capacity was conducted using limit equilibrium solution and the curve fit of the yield loci proposed by O'Neill et al. (2003). This model was used as a strong analytical tool for computations of the ultimate capacity for the purpose of probabilistic characterization of anchor capacity.

The effects of soil-chain interaction were taken into account as a key player in overall anchor system behaviour. VBA macros were coded and embedded into an Excel spreadsheet to obtain the static and kinematic response of drag embedment anchor in cohesive soil.

An idealized fluke of length L_f, thickness d_f, and width b_f, was assumed. The shank was modelled as a single flat plate of length L_s, width b_s (into the page), and inclined to the top face of the fluke at the fluke-shank angle, θ_{fs}. The soil was assumed to have surface undrained shear strength, s_{u0}, and an undrained shear strength gradient with depth, s_{ug}. As outlined in Figure 3-4, the anchor padeye was at an embedment depth, d_a, below the soil surface, and the top face of the fluke was inclined at an angle, ψ, to the horizontal. The anchor chain of effective width, b_c, was connected to the padeye at an inclination to the horizontal, θ_a, and under a tension, T_a. The shank resistance was assumed to have two components that limited the normal and shear strength of the shank. The normal shank force, F_1, acting normal to the shank axis, was obtained by multiplying the bearing capacity factor, $N_c = 9$, by the shank area perpendicular to the shank and the undrained shear strength. The sliding shank force, F_2, was obtained from the undrained shear strength

multiplied by the shank surface area, and was assumed to act parallel to the shank axis. The chain angle at the padeye was calculated using an expanded form of an equation by Neubecker and Randolph (1996) ignoring the effects of chain self-weight:

$$\theta_a = \left[\frac{2\, b_c\, N_c\, d_a\left(s_{u0} + 0.5\, s_{ug}\, d_a\right)}{T_a}\right]^{0.5} \quad (8)$$

After calculation of the normal and sliding shank forces, F_1 and F_2, a value of the chain tension at padeye, T_a, was assumed. By obtaining θ_a from equation (8), the force and moment equilibrium were used (taking into account F_1, F_2, T_a, and W_a') to calculate the fluke loads H, V, and M. In order to examine that the fluke loads were on the plastic yield locus, a check i.e. f (H, V, M) = 0 was implemented, and the value of T_a was changed and the process repeated until the requirement was satisfied. The incremental displacements of the fluke parallel (δh) and perpendicular (δv) to the fluke face and rotationally ($\delta\psi$) about the fluke reference point were calculated based on formulations in O'Neill et al. (2003). Figure 3-6 shows the preceding description of the analysis procedure.

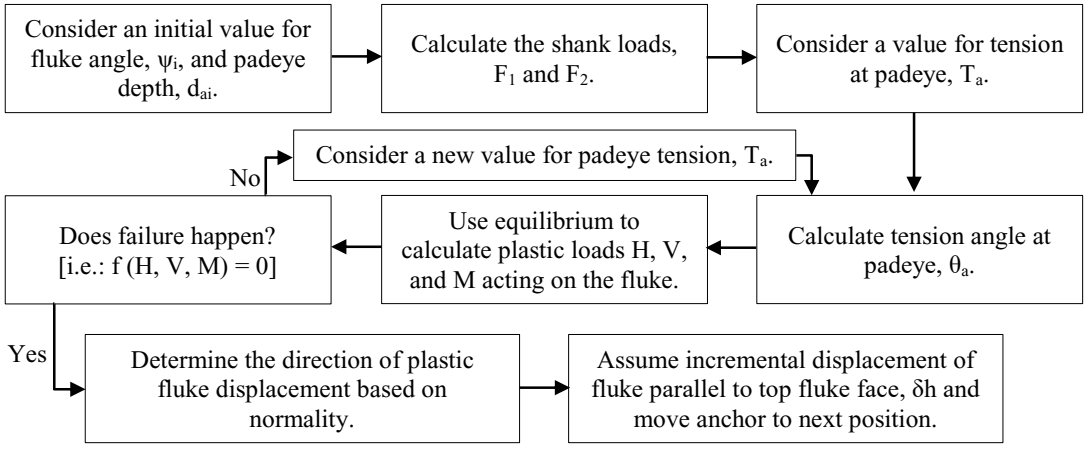

Figure 3-6. Analysis flowchart for kinematic anchor simulation using yield locus.

The developed Excel spreadsheet was validated against the results of finite element analysis (O'Neill et al., 2003), test results (Neubecker and Randolph, 1996), and practical anchor design charts (Figure 3-7 and Figure 3-8). The anchor efficiency η_a is the holding force divided by the dry weight of the anchor. The Neubecker and Randolph model (1996) is based on form factor f = 1.5, and resultant angle $\theta_w = 31°$. Form factor (dimensionless) converts the rectangular fluke area to true fluke area. The results from the developed Excel spreadsheet are in perfect agreement with the finite element analysis results. There are slight differences between the predictions made by the developed Excel spreadsheet and the test results that are because of the simplified geometries used in analytical models. The input parameters of the validation case study for a 32 tonne (t) MK5 Stevpris anchor are given in Table 3-2.

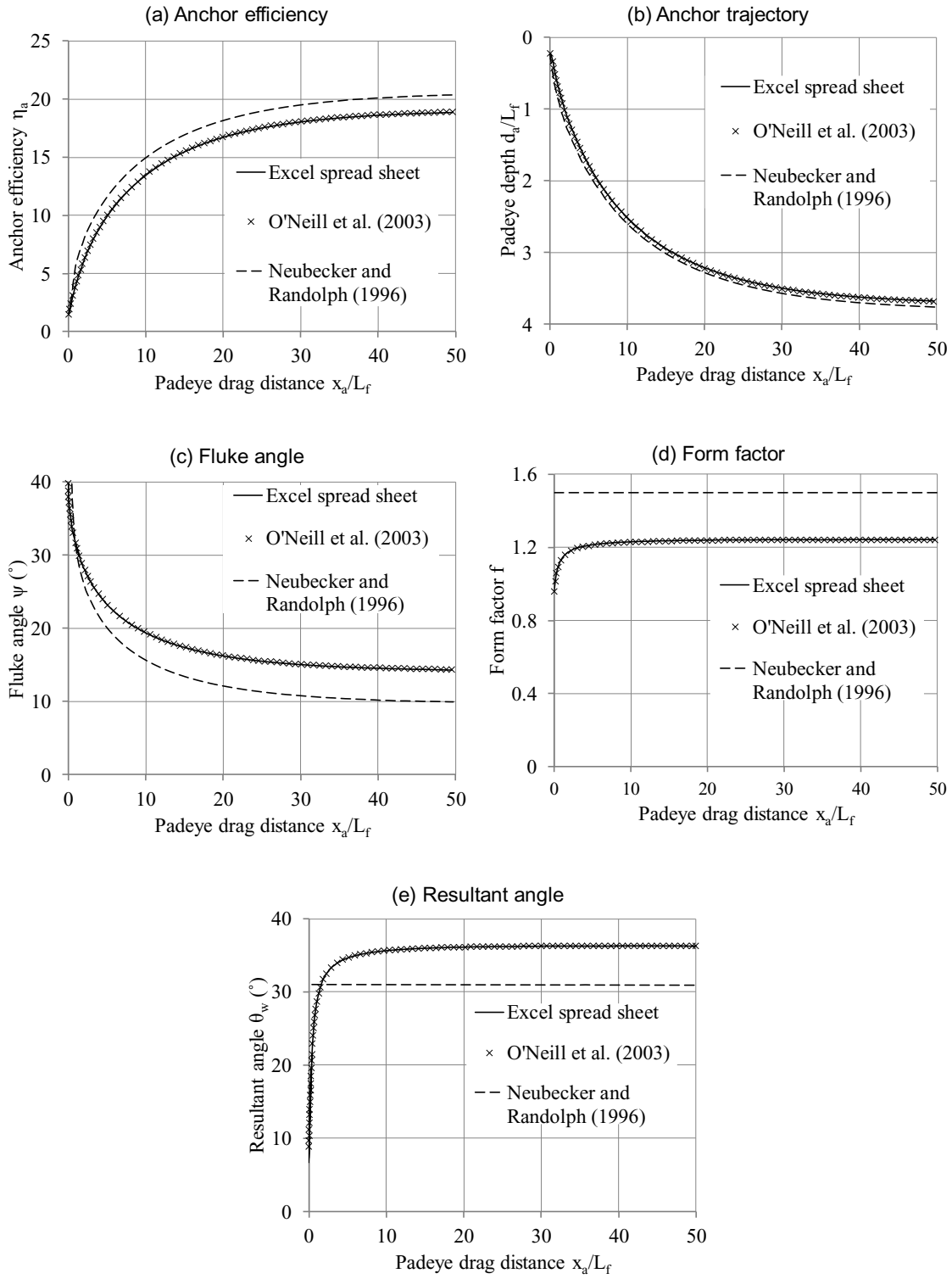

Figure 3-7. Comparison of result for Vryhof Stevpris anchor 32 t.

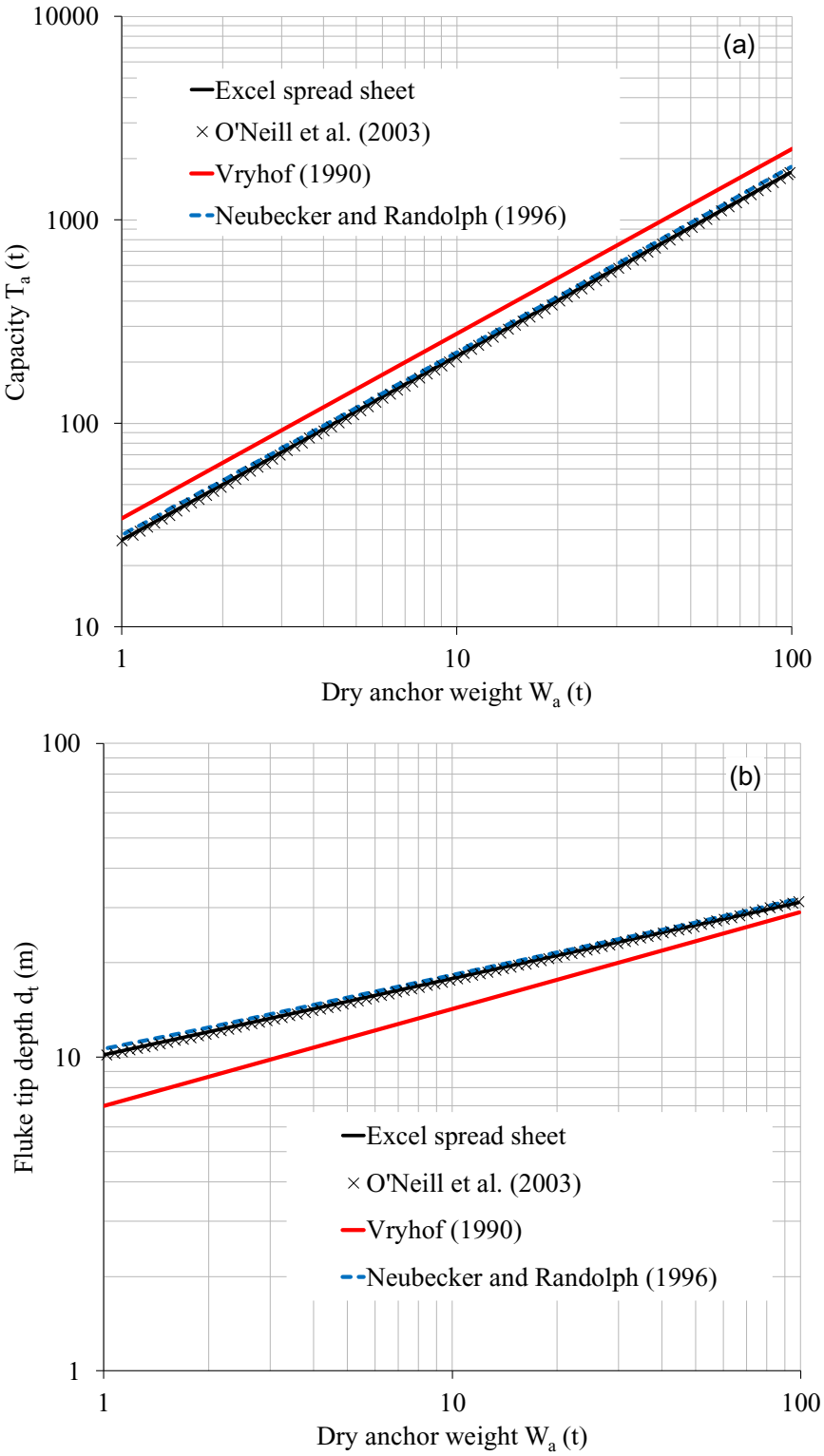

Figure 3-8. Comparison of result for anchors in soft clay: (a) anchor holding capacity, (b) fluke tip depth.

Table 3-2. Anchor and soil parameters used in yield locus analysis of 32 t 50° anchor (O'Neill et al., 2003).

Parameter	Value
Anchor submerged weight, W_a' (kN)	274
Fluke length, L_f (m)	4.97
Fluke width, b_f (m)	4.23
Fluke thickness, d_f (m)	0.71
Fluke-shank angle, θ_{fs} (˚)	41.2
Shank length, L_s (m)	8.34
Shank width, b_s (m)	1.63
Chain self-weight, w_c (kN/m)	2.0
Effective chain width, b_c (m)	0.24
Chain-soil friction coefficient, μ	0.4 (Neubecker and Randolph, 1995b)
Bearing capacity factor, N_c	9
Undrained shear strength at mudline, s_{u0} (kPa)	0
Undrained shear strength gradient, s_{ug} (kPa/m)	1.5

3.5. Reliability Analysis

First order reliability method (FORM) was used through an iterative procedure to obtain the probabilistic results. The uncertainties of the seabed soil properties and environmental loads were accounted for. The probabilistic modelling of anchor capacity was conducted by using plastic yield loci characterizing the fluke failure states. The embedded profile and the frictional capacity of the anchor chain at the seabed were also considered in the calculation of ultimate holding capacity. A semisubmersible platform comprising catenary mooring system was simulated through fully coupled time domain analysis. Three hours

simulations were run to obtain the time history of catenary line responses for proposed wave spectrums. The uncertainties of the environmental loads, metocean variables including significant wave height, spectral peak period and wind velocity, and consequently the stress distribution throughout the catenary lines were accounted for by using the response surface method and appropriate probability density functions. The target annual probability of failure was assumed to be 10E-5 for consequence class 2 based on DNV (Det Norske Veritas, 2012). The full process will be discussed in coming sections.

3.5.1. Anchor-seabed Interaction Parameters

The drag anchor was designed based on the recommendations provided by DNV (Det Norske Veritas 2012). Two groups of Stevpris Mk5 and Mk6 anchors with L_f/d_f ratios of 6.67 and 3.09 were used to calculate the holding capacity as popular anchors in deepwater mobile and permanent mooring solutions. Figure 3-9 illustrates the main dimensions of a typical drag anchor, where F represents the fluke thickness (d_f). Table 3-3 summarizes the characteristics of the anchors.

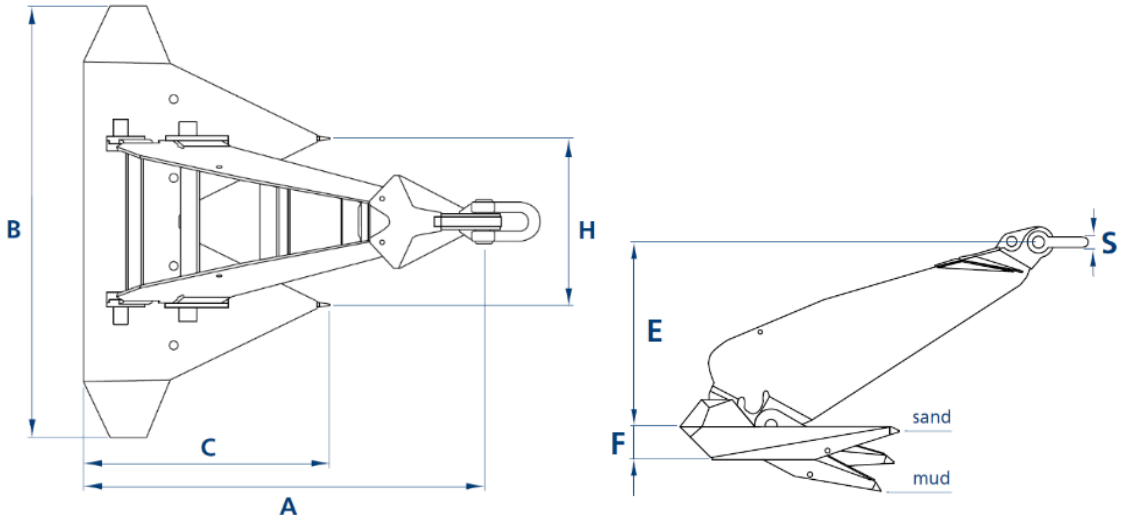

Figure 3-9. Schematic presentation of a drag anchor dimensions (Anchor manual, 2010).

An average characteristic linear profile of s_u given by a value of 0.67 kPa at mudline and a gradient of 1.50 kPa/m was employed to represent clayey soils in the Caspian Sea. Table 3-4 shows the fluke lengths (L_f), fluke thickness (d_f), design tensions at the padeye, $T_{d,a}$, design resistances at the padeye, $R_{d,a}$, and the corresponding line tension angles at the padeye, θ_a.

Table 3-3. Main dimensions for 20 t anchors (Anchor manual, 2010).

	Mk5 ($L_f/d_f = 6.67$)	Mk6 ($L_f/d_f = 3.09$)
A	7004 mm	6631 mm
B	7550 mm	7368 mm
C (L_f)	4297 mm	4696 mm
E	3569 mm	3132 mm
F (d_f)	644 mm	1520 mm
H	2917 mm	2890 mm
S	190 mm	180 mm
Fluke-shank angle (θ_{fs})	50˚	50˚

The chain-soil frictional load has a significant contribution to the ultimate holding capacity and the net load transferred to anchor padeye. However, the way it is considered in reliability analysis can seriously affect the degree of complexity. If the limit state function is formulated at the padeye, the complexity of the reliability analysis would be significantly increased, since the statistical dependence between the applied load and the anchor capacity would have to be accounted for.

Table 3-4. Drag anchor models.

Anchor type	L_f/d_f	L_f (mm)	d_f (mm)	$T_{d,a}$ (kN)	$R_{d,a}$ (kN)	θ_a (˚)
Mk5	6.67	4297	644	2234.67	2275.56	13.03
Mk6	3.09	4534	1468	2238.71	2267.14	12.91

In addition, the current study is further focused on uncertainties existed in evaluation of anchor capacity rather than the chain capacity. As an alternative approach, to prevent an extreme complexity in reliability analysis, properly incorporate the contribution of chain to the ultimate capacity and ignore the uncertainties of chain capacity for a reasonable simplification, the limit state function was formulated at mudline, and the chain-soil interaction effects were considered only in calculation of the ultimate holding capacity. A similar approach has been used before in reliability analysis of suction anchors in the literature (Choi, 2007; Silva-Gonzalez et al., 2013). This facilitated the reliability analysis assuming that the line tensions and the anchor capacity are statistically independent variables at the mudline.

3.5.2. Finite Element Modelling of Floating System

A generic semisubmersible platform with catenary spread mooring system was analysed in this study. The mooring system consists of eight lines that each has a chain/wire-rope/chain configuration. The upper and lower parts of mooring line are chain, while the mid part is wire rope. The platform was assumed to be in a depth of 700 m in the Caspian Sea. A finite element analysis (FEA) model was developed in OrcaFlex software to apply the environmental loads on platform and obtain the resultant tension loads in the mooring lines touchdown point (TDP). The platform was modeled as a rigid body with attachment points

for mooring lines. The motions of the platform were prescribed through the Response Amplitude Operator (RAO). Each mooring line was modeled using line elements attached to the platform at the top, and terminated at the anchor location on the seabed. The most heavily loaded line was determined for 100 year return period sea state with H_s = 9.5 m, T_p = 12.8 seconds, and U_{10} = 29 m/s, through generating 3 hour time histories at TDP. Figure 3-10 shows the applied RAO of the platform for head sea.

The key results of mooring analysis including the design line tension, T_d, and the line angle at mudline, θ_o, along with the characteristic mean tension, $T_{mean\text{-}C}$, and characteristic mean maximum dynamic tension, $T_{dyn,max\text{-}C}$, for 100 year return period sea states have been summarized in Table 3-5. See later discussion of equation (10) for calculation of the design line tension.

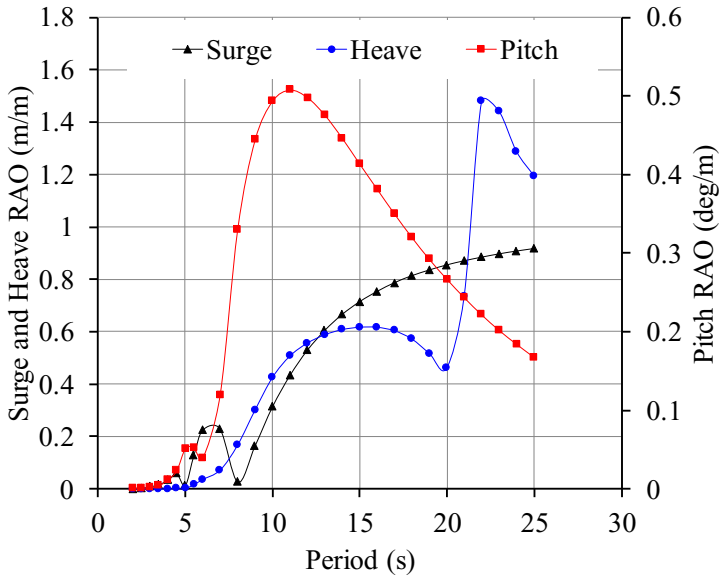

Figure 3-10. Semisubmersible RAO, head sea.

Table 3-5. Characteristic and design tensions for the catenary mooring system.

H_s (m)	T_p (s)	U_{10} (m/s)	$T_{mean\text{-}C}$ (kN)	$T_{dyn,max\text{-}C}$ (kN)	T_d (kN)	θ_o (˚)
9.5	12.8	29	846	623	2493	1.3

3.5.3. Limit State Function

The limit state function is set in terms of the anchor holding capacity and the mooring line tensions at the mudline (Det Norske Veritas, 2012):

$$M = R_d - T_d \tag{9}$$

where R_d is the design anchor and chain system capacity at mudline.

The design line tension at mudline, T_d, can be expressed as the sum of the characteristic mean line tension, $T_{mean\text{-}C}$, due to pretension and mean environmental loads, and the characteristic dynamic line tension, $T_{dyn,max\text{-}C}$, due to low frequency and wave frequency motions at that point, multiplied by their respective partial safety factors γ_{mean}, γ_{dyn}:

$$T_d = T_{mean-C} \cdot \gamma_{mean} + T_{dyn-C} \cdot \gamma_{dyn} \tag{10}$$

where γ_{mean} is the partial safety factor on mean line tension, and γ_{dyn} is the partial safety factor on dynamic line tension. For consequence class 2 and the dynamic analysis, the values of γ_{mean} and γ_{dyn} are 1.40 and 2.10, respectively (Det Norske Veritas, 2012). Both $T_{mean\text{-}C}$ and $T_{dyn,max\text{-}C}$ are expressed at the mudline as functions of the significant wave height (H_s), peak period (T_p), and wind velocity (U_{10}) representing an extreme sea-state. Therefore the limit state function can be written as:

$$M\left(R, H_s, T_p, U_{10}\right) = R_d - T_{mean-C} \cdot \gamma_{mean} - T_{dyn,max-C} \cdot \gamma_{dyn} \tag{11}$$

The anchor capacity and load tensions are evaluated in the direction of the mooring line at dip-down point, where the anchor line starts to embed (i.e. at an angle θ_o with the horizontal). The probability of failure p_F during a given extreme sea state can be expressed as:

$$p_F = P\left[M\left(R, H_s, T_p, U_{10}\right) \leq 0\right] \quad (12)$$

The annual probability of failure p_{Fa} can be written as an exponential function of the probability of failure p_F, using a Poisson model for the occurrence of extreme sea states (Silva-Gonzalez et al., 2013):

$$p_{Fa} = 1 - exp(-\lambda p_F) \quad (13)$$

where λ is defined as the ratio of number of extreme sea states to their observation period (in years); for small values of λp_F, the annual probability of failure is $p_{Fa} \approx \lambda p_F$.

3.5.4. Probabilistic Modelling of Anchor Capacity

The anchor holding capacity at mudline was obtained through combining the anchor capacity at shank padeye, and the limit equilibrium state model developed by Neubecker and Randolph (1995(a)) for chain-soil interaction effect. This method serves as an efficient analytical tool for intensive computations of probabilistic anchor capacities. More recent studies have been conducted on prediction of the ultimate holding capacity of drag embedment anchors (i.e., Lai et al., 2020). Figure 3-11 shows capacity interaction diagrams in V-H space at the padeye and the mudline. The vertical and horizontal loads at mudline are the vertical and horizontal components of mooring line tension, respectively; while the vertical and horizontal loads at padeye are the load components normal and parallel to the top face of the inclined fluke, respectively. Figure 3-11 shows that for intermediate ratios

of H/V, the padeye capacity slightly exceeds the mudline capacity. This could be related to the different failure mechanism observed by O'Neill et al. (2003) for wedge and rectangle flukes. As example, the wedge fluke can be sustained along with a negative V under particular translations. O'Neill et al. have observed the same effect for another case when the wedge fluke was released vertically and rotationally, and was loaded horizontally to a failure point, where the fluke was forced by the soil to move upwards and rotate anticlockwise. This suggests that under particular circumstances the wedge fluke moves parallel to the bottom fluke face and shift the yield locus. This highlights the asymmetric and complex kinematics of the wedge fluke.

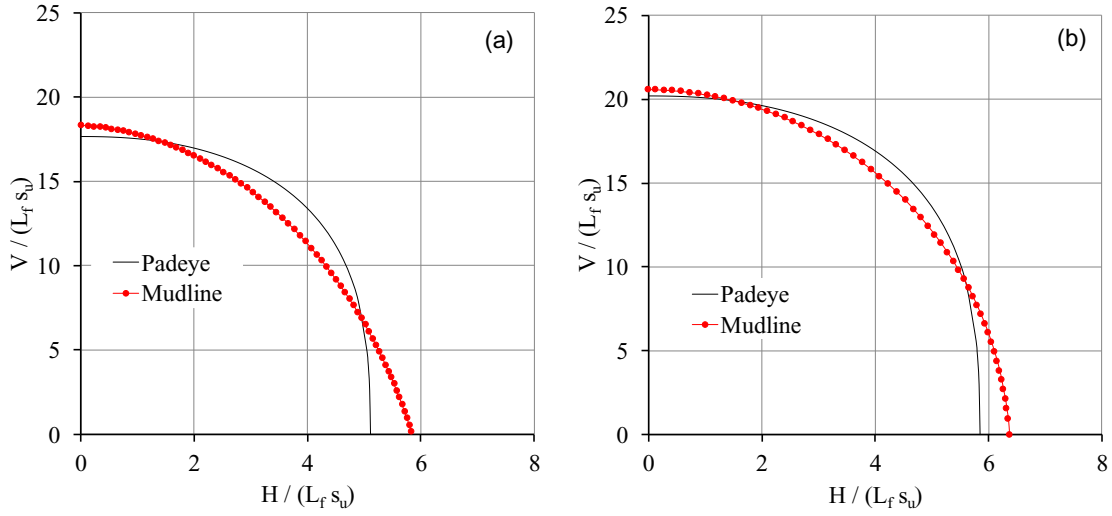

Figure 3-11. Capacity components at the padeye and mudline: (a) $L_f/d_f = 6.67$, $L_f = 4.297$ m, (b) $L_f/d_f = 3.09$, $L_f = 4.534$ m.

The key parameters of anchor-seabed interaction including the undrained shear strength gradient (s_{ug}), the side shear factor (α_s), the fluke bearing factor (N_c), and the line tension angle at the padeye (θ_a) were used to construct the samples of anchor capacities. A lognormal distribution (Silvia-Gonzalez et al., 2013) was assumed for s_{ug}, with mean value

of 1.5 kPa/m and coefficient of variation δs_{ug} = 0.20 to consider the uncertainty due to systematic test variations and spatial variation of the soil properties. The intercept undrained shear strength at mudline is s_{u0} = 0.00 kPa. The fluke bearing and side friction factor were represented by a bivariate lognormal distribution, with mean values $\mu_{\alpha s}$ = 0.7 and μ_{Nc}= 9, which calibrated the plasticity model, coefficients of variation $\delta_{\alpha s}$ = 0.2 and δ_{Nc} = 0.25, and correlation coefficient $\rho = -0.8$ (El-Sherbiny, 2005; Luke et al., 2003; Najjar, 2005). Since a given load capacity can be explained by different combinations of α_s and N_c, and considering that capacity increases with any of them, hence α_s and N_c are negatively correlated. The load angle at the padeye was modeled as $\theta_a = \mu_{\theta a} + \Delta\theta_a$, where $\Delta\theta_a$ is a zero-mean normal random variable with standard deviation equal to 2 (Gilbert, 2010), and the mean value $\mu_{\theta a}$ was estimated as the load angle obtained from the design of the anchor models. An extensive number of 5000 simulations were conducted to construct the sample of anchor capacities with undisturbed and remolded soil conditions using the parameters s_{ug}, α_s, N_c and θ_a. The histograms and the fitted distribution functions of anchor capacities at mudline are illustrated in Figure 3-12.

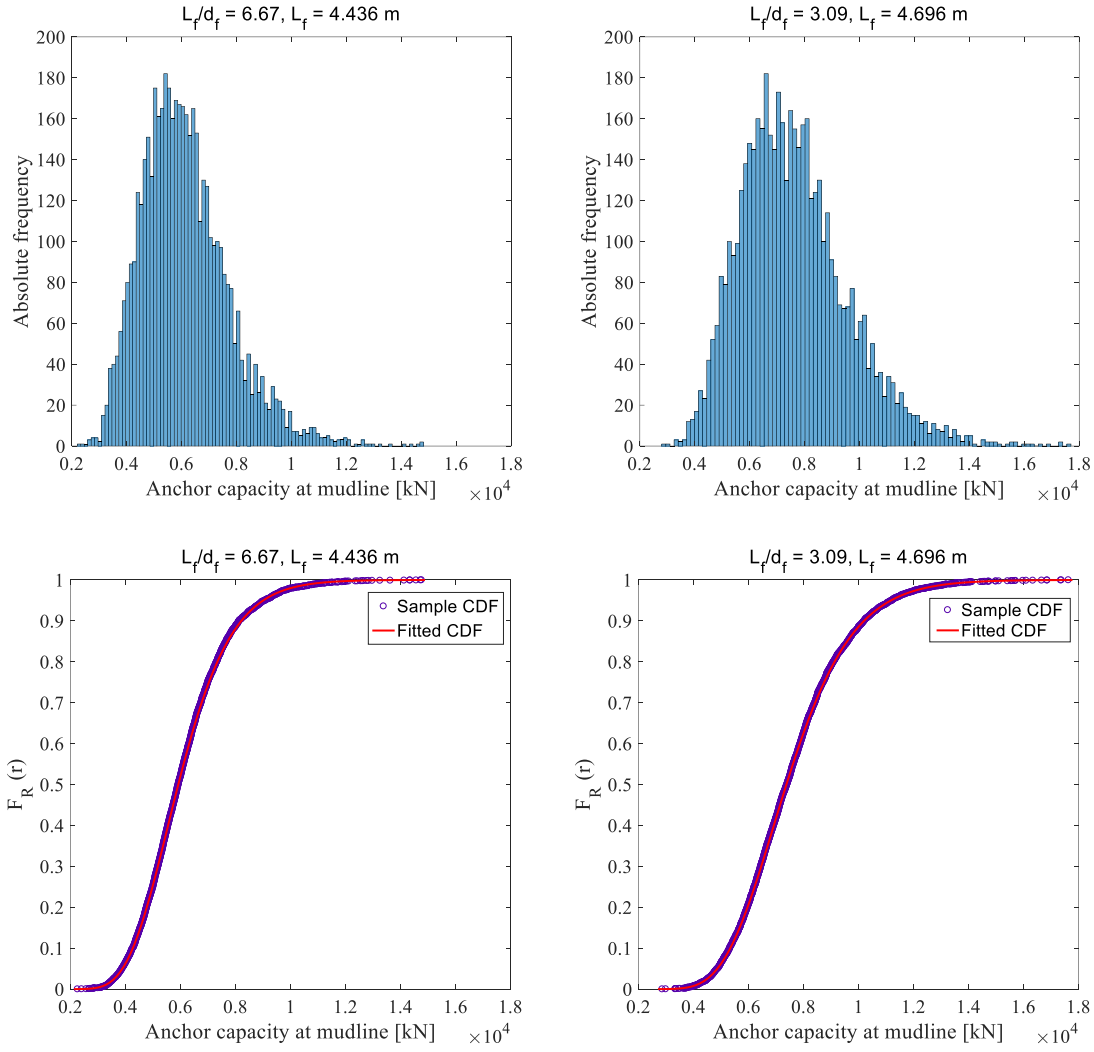

Figure 3-12. Histograms of simulated and fitted capacities at mudline for undisturbed soil.

Table 3-6 shows the mean (μ), standard deviation (σ), median value (m), and coefficient of variation (δ) of anchor capacities at padeye and mudline for some of the anchor models. The mean capacity at padeye is 7 – 10% less than at the mudline. In each anchor model, the differences in capacity at padeye and at mudline decrease slightly as the fluke length and fluke thickness increase. The same conclusion can be drawn for median capacities at padeye and at mudline. The coefficients of variation of the capacity at padeye and mudline are about 26% for both anchor models.

Table 3-6. Statistical properties of anchor capacity at padeye and mudline; undisturbed soil.

Model	L_f/d_f	L_f(m)	Padeye				Mudline				μ_{Ra}/μ_R
			μ_{Ra} (kN)	σ_{Ra} (kN)	δ_{Ra}	m_{Ra} (kN)	μ_R (kN)	σ_R (kN)	δ_R	m_R (kN)	
Mk5	6.67	4.149	4684.8	1221.9	0.261	4533.1	5184.0	1352.1	0.261	5016.2	0.90
Mk5	6.67	4.629	6347.5	1659.6	0.261	6141.0	6853.2	1791.9	0.261	6630.4	0.93
Mk6	3.09	4.267	4859.4	1257.1	0.259	4704.5	5416.8	1401.3	0.259	5244.1	0.90
Mk6	3.09	4.848	7049.6	1835.0	0.260	6822.2	7681.8	1999.6	0.260	7434.0	0.92

The strength of remolded soil can be used in capacity analyses to estimate the lower bound of axial capacity component (Najjar, 2005). Samples of anchor capacity were generated considering a remolded shear strength profile given by a lognormal gradient with mean value 0.45 kPa/m and coefficient of variation $\delta s_{ug} = 0.05$ (Silvia-Gonzalez et al., 2013). The value of shear strength at mudline was assumed $s_{u0} = 0.00$ kPa. Table 3-7 shows the mean, standard deviation, and coefficient of variation of capacities for some anchor models. The results showed that the mean capacity at the padeye is 3 – 5% less than mudline. There is no significant difference between the coefficients of variation of capacity at padeye and mudline (about 18% for both anchor models).

Table 3-7. Statistical properties of anchor capacity at padeye and at mudline; remolded soil.

Model	L_f/d_f	L_f(m)	Padeye			Mudline			μ_{Ra}/μ_R
			μ_{Ra}(kN)	σ_{Ra}(kN)	δ_{Ra}	μ_R(kN)	σ_R(kN)	δ_R	
Mk5	6.67	4.149	1709.0	298.4	0.175	1785.1	311.7	0.175	0.96
Mk5	6.67	4.629	2315.6	405.3	0.175	2390.1	418.3	0.175	0.97
Mk6	3.09	4.267	1772.2	318.2	0.180	1857.1	333.4	0.180	0.95
Mk6	3.09	4.848	2571.0	464.4	0.181	2673.6	482.9	0.180	0.96

A truncated lognormal distribution was used to account for the lower bound capacity. This lower bound value was defined as the anchor capacity related to the remolded shear strength. In order to consider the probability of capacity being less than its lower bound, a finite mass probability was added to the truncated distribution (Najjar, 2005). Table 3-8 shows that the lower bound capacity is about 35 – 36 % of median capacity at mudline.

In order to obtain the capacity distribution, square polynomials were fitted for the mean and standard deviations of anchor capacity as a function of anchor fluke length for each group of models. The variation of mean and standard deviations of anchor capacity at padeye and mudline for anchors with L_f/d_f = 6.67 is shown in Figure 3-13. Similar curve fits were obtained for anchor capacities in remolded soil condition and then probability distributions of load capacity were developed as a function of anchor fluke length for varying L_f/d_f ratios.

Table 3-8. Ratio of lower bound capacity to median capacity at mudline.

Model	L_f/d_f	L_f(m)	μ_R/m_R
Mk5	6.67	4.149	0.36
Mk5	6.67	4.297	0.36
Mk5	6.67	4.436	0.36
Mk5	6.67	4.629	0.36
Mk6	3.09	4.267	0.35
Mk6	3.09	4.534	0.36
Mk6	3.09	4.696	0.36
Mk6	3.09	4.848	0.36

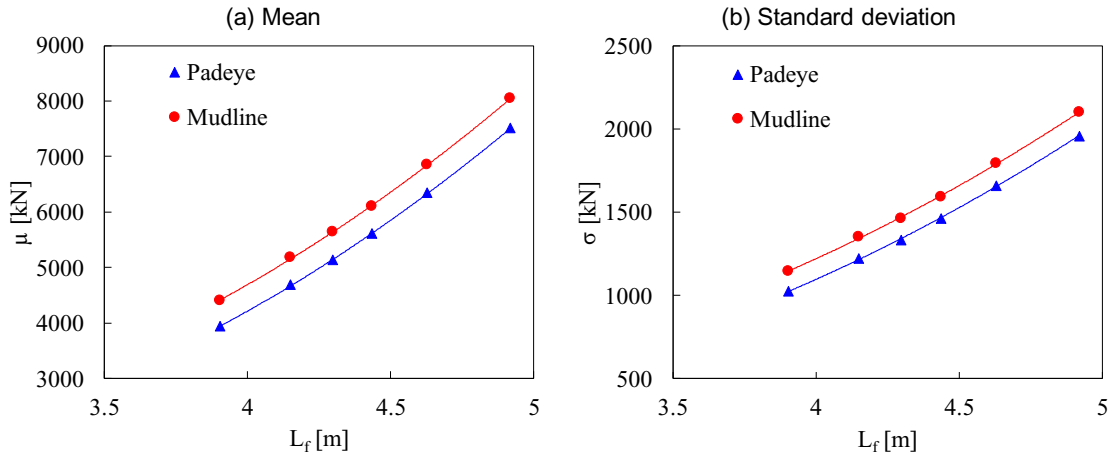

Figure 3-13. Mean and standard deviation of anchor capacity versus fluke length; L_f/d_f = 6.67.

3.5.5. Probabilistic Modelling of Line Tension

Response surfaces were developed using a similar methodology proposed by Silva-Gonzalez et al. (2013). The dynamic tension in mooring line assumed to be a Gaussian process (Choi, 2007; Sarkar and Eatock Taylor, 2000). The model proposed by Davenport

(Davenport, 1964) was used to express the expected maximum dynamic line tension within an extreme sea state of duration Δt:

$$\mathrm{E}\left[T_{dyn,max}\right]_{\Theta} = \mu_{Tdyn,max} = \left[\sqrt{2\ln(\nu_{\Theta}\Delta t/2)} + \frac{0.5772}{\sqrt{2\ln(\nu_{\Theta}\Delta t/2)}}\right]\sigma_{T,\Theta} \quad (14)$$

A random vector of r uncertain environmental variables (Θ) represents the extreme sea state. The standard deviation and the mean crossing rate of the dynamic tension are shown by $\sigma_{T,\Theta} = \sigma(\Theta)$, and $\nu_{\Theta} = \nu(\Theta)$. Second order polynomial expansions given in equation (15) were used in developing the Response surfaces to express the mean line tension T_{mean} and the expected maximum dynamic line tension at mudline $T_{dyn,max}$ in terms of Θ:

$$Y(\Theta) = c + a^{T}\Theta + \Theta^{T}b\Theta \quad (15)$$

where Y(Θ) is the response of interest, and Θ is the vector of environmental variables of order r ×1. The parameters c, a(r ×1) and b(r ×r) are the unknown coefficients to be determined from response analysis. The response of mooring system to seven key environmental parameters from Sardar-e-Jangal gas field in the Caspian Sea was examined to develop the response surfaces. A database of 8100 combinations of environmental variables was made using significant wave height (H_s), wave direction (d_w), peak period (T_p), wind velocity (U_{10}), wind direction (d_{ww}), surface current velocity (U_c), and current direction relative to wave direction (d_{wc}). The mooring line with the highest load was considered to obtain the response surfaces. The response surfaces for mean and maximum expected dynamic line tension are illustrated in Figure 3-14 for domains of significant wave height and peak wave period.

Extreme sea states are identified within a storm event. A clustering and de-clustering time window are defined around the peak period (t_{peak} - $\Delta T_{cluster}$, t_{peak} - $\Delta T_{cluster}$). The significant

wave height of a sea state at t_{peak} shall be higher than a threshold value ($H_s \geq H_s^{th}$) within the defined window to be considered as extreme sea state. The other environmental variables are determined as those occurring at time t_{peak}. The extreme values of environmental variables for the Caspian Sea were determined based on three-hour time series provided by metocean studies over a 24 years observation period (Private communications with Field operator).

The Peaks over Threshold method was used to generate the marginal probability distributions of $\Theta = [H_s, T_p, U_{10}]^T$ according to a set of 24 extreme sea states during the hindcast time series. The mean annual rate λ is 30/24 = 1.25 per year based on maximum likelihood estimate. Table 3-9 and Table 3-10 show the fitted marginal distributions, the parameters from maximum likelihood estimates, and correlation coefficients for environmental variables.

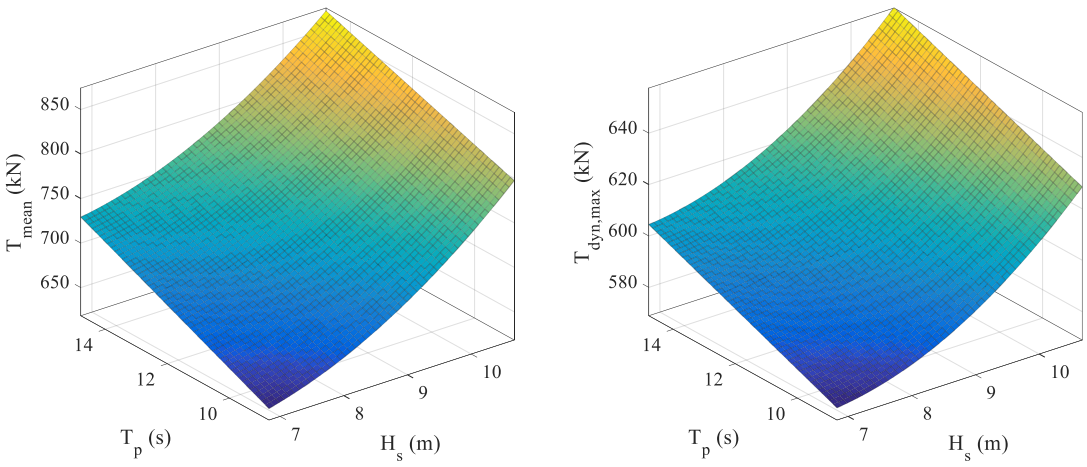

Figure 3-14. Response surfaces for T_{mean} and $T_{dyn,max}$.

Table 3-9. Distribution parameters of environmental variables.

Variable	Probability distribution	Distribution parameters	
H_s	Weibull	Scale	9.5351
		Shape	10.1552
T_p	Lognormal	$\mu_{\ln T_p}$	2.4966
		$\sigma_{\ln T_p}$	0.1196
U_{10}	Lognormal	$\mu_{\ln U_{10}}$	3.4827
		$\sigma_{\ln U_{10}}$	0.1095

Table 3-10. Estimated correlation coefficients.

	H_s	T_p	U_{10}
H_s	1	0.9728	0.9905
T_p	0.9728	1	0.9935
U_{10}	0.9905	0.9935	1

3.5.6. Results of Reliability Analysis

Reliability analyses were conducted using first order reliability method (FORM.) A narrow and appropriately weighted Gaussian distribution was used to model the finite probability at the lower bound capacity to ignore the convergence problems in FORM (Melchers, 2003). The variation of the annual reliability index as a function of dry anchor weight and fluke length is shown in Figure 3-15. It should be noted that each point in Figure 3-15 (a) corresponds to a specific point in Figure 3-15 (b), and vice versa. For example, point 5 represents a Mk5 anchor with L_f = 4.629 m and W_a = 25 t with annual reliability index 4.12. Figure 3-15 shows that a target reliability level can be achieved by different anchor

models with similar fluke length and different weights. As instance, for a desired reliability index $\beta_{annual} = 4.6$, either $L_f/d_f = 6.67$ with $L_f = 4.919$ m and $W_a = 30$ t (point 6), or $L_f/d_f = 3.09$ with $L_f = 4.848$ m and $W_a = 22$ t (point 10) can be used. This shows that in spite of excessive difference between anchor weights, the reliability levels are very close because of almost identical fluke lengths. For target failure probabilities between 10^{-4} and 10^{-5}, the available weight and fluke length for $L_f/d_f = 6.67$ vary from 22 t and 4.436 m to 25 t and 4.629 m; they vary from 18 t and 4.534 m to 20 t and 4.696 m for $L_f/d_f = 3.09$. This range of target failure probabilities is usually used for the ultimate limit state design of offshore systems (Det Norske Veritas, 2010(a), 2010(b), 2012, and 2013) and corresponds to reliability indices between 3.72 and 4.26. The results illustrated in Figure 3-15 also show that two different anchor models of the same weight and different fluke length can give different reliability levels. As instance, for a given weight i.e. 18 t, changing the value of L_f/d_f from 6.67 (point 2) to 3.09 (point 8), the value of L_f changes from 4.149 m to 4.534 m, and the annual reliability index increases from 3.06 to 3.92. This means a reduction by two orders of magnitude in annual failure probability from 1.11×10^{-3} to 4.46×10^{-5}. These results indicate that the anchor weight is not of great importance for capacity of deeply buried drag anchors in soft clay and their reliability is significantly affected by the fluke length. Based on the results in Figure 3-15, the logarithm of failure probability was related to fluke length and anchor weight for each anchor model. Figure 3-16 shows the variation of log (p_{Fa}) versus fluke length and anchor weight. For each L_f/d_f, a linear relationship was obtained between log (p_{Fa}) and fluke length/anchor weight. The slope of curve defines the required increment in fluke length and anchor weight to reduce the probability of failure by a factor of 10 (a magnitude of one order). This can be used in a life cycle cost-benefit

analysis, where the modeling initial cost is required as a function of probability of failure. The initial cost can increase by increasing material mass and volume, which are associated with anchor weight and fluke length, and therefore deduction in failure probability. It can be concluded from Figure 3-16 that the slopes for $L_f/d_f = 6.67$ are higher than for $L_f/d_f = 3.09$. The required increasing rate of the fluke length and anchor weight for $L_f/d_f = 6.67$ are 0.272 m and 4.03 t, respectively. The magnitude of these parameters for $L_f/d_f = 3.09$ are slightly less i.e. 0.254 m and 3.46 t, respectively. Therefore, for reliability indices between 3.72 and 4.26, the required length and weight increase to reduce the failure probability by 10 are in the order of 6% and 20%, respectively.

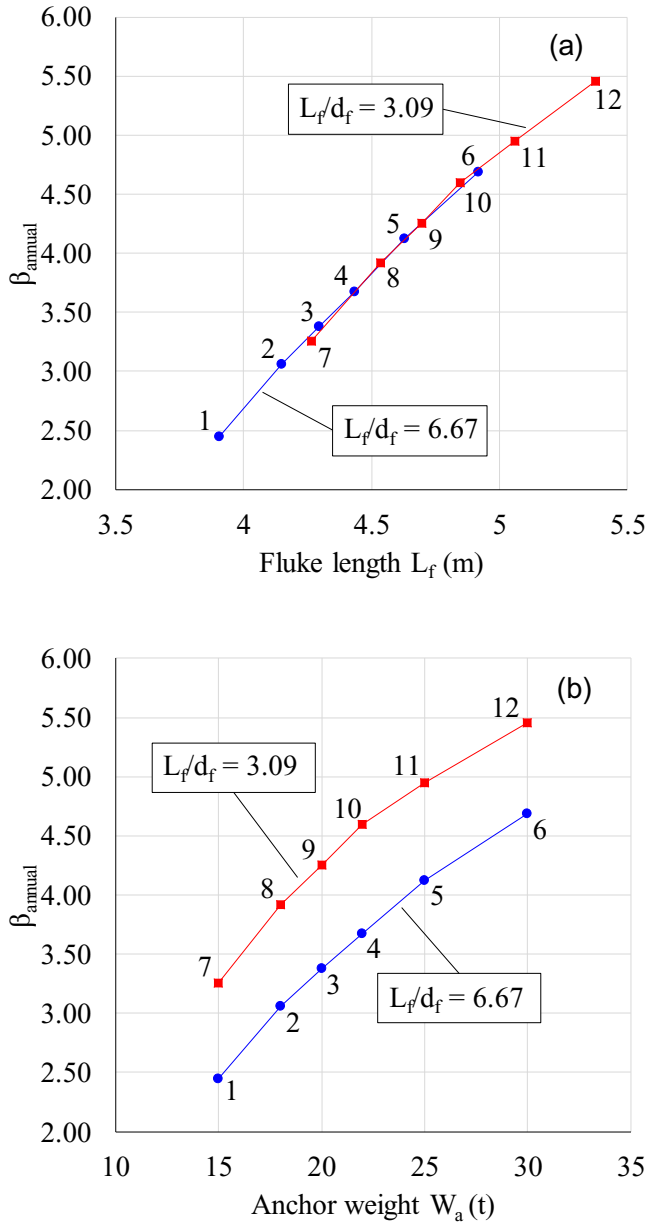

Figure 3-15. Annual reliability index versus (a) fluke length, and (b) anchor weight.

3.5.7. Relative Reliability of Drag Embedment Anchors and Suction Caissons

It is worth quantifying the relative reliability of drag anchors presented in this study and suction anchors in previous studies. In order to conduct a precise and reliable comparison, the value of all input parameters i.e. line tensions acting on the anchor at mudline and soil

properties should be the same for both anchors. An alternative way of examining the relative reliability for different line tensions and soil properties is to define a constant load to capacity ratio for both anchors and determine their reliability index for the given ratio. Table 3-11 shows a comparison between the reliability indices of a suction caisson model from Silvia-Gonzalez et al. (2013) with a drag anchor determined in this paper. The suction caisson has a length to diameter ratio 6 and is designed for a catenary mooring system. For each anchor, the characteristic mean maximum dynamic line tension ($T_{dyn,max\text{-}C}$) during 100 year return period sea states, and the mean ultimate anchor capacity at mudline (μ_R) are given in Table 3-11. For a given ratio $T_{dyn,max\text{-}C}/\mu_R$ = 10.2%, the annual reliability indices for suction caisson and drag anchor are about 5.3 and 3.6, respectively. This is a four order of magnitude reduction in annual failure probability from 1.59×10^{-4} to 5.79×10^{-8}. It can be concluded, from this comparison, that a suction caisson has a higher reliable performance rather than a drag embedment anchor in soft clay.

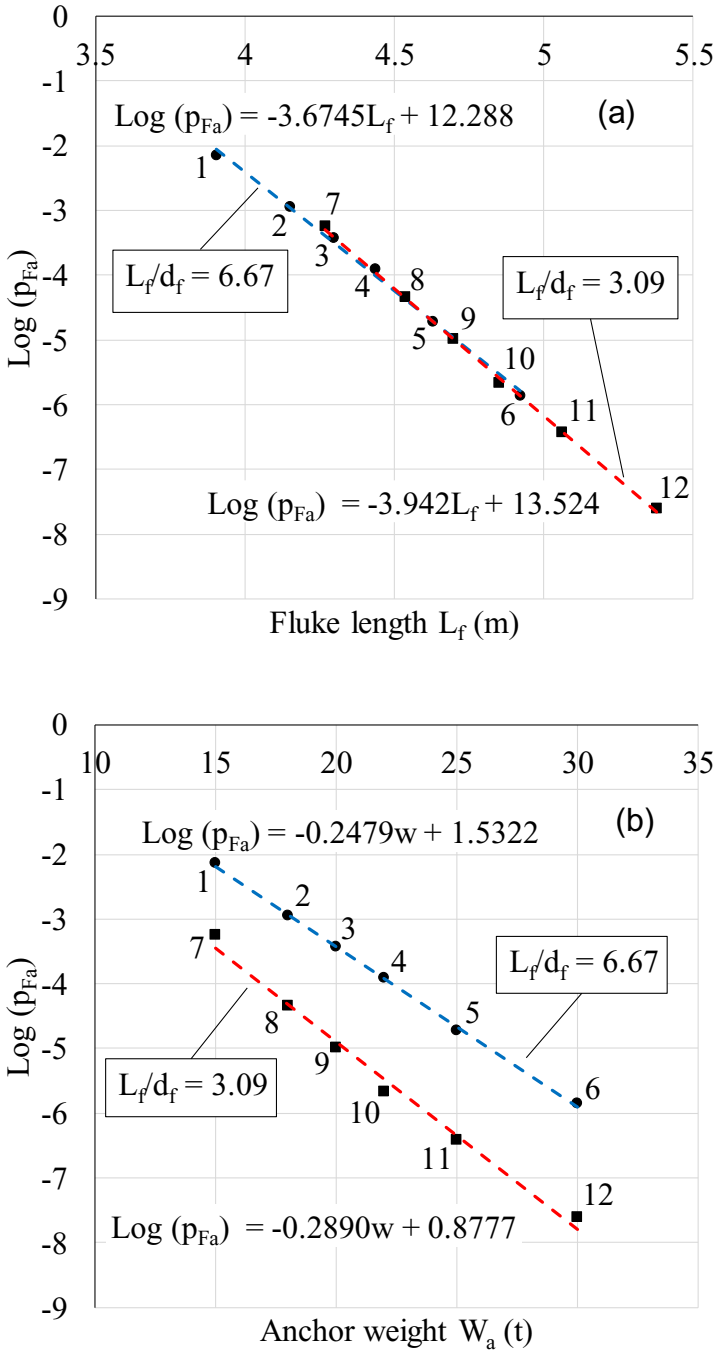

Figure 3-16. Logarithm of failure probability versus (a) fluke length, and (b) anchor weight.

Table 3-11. Comparison of annual reliability index of drag embedment anchor with Silvia-Gonzalez et al. (2013) suction caisson.

Anchor model	L_f (m)	$T_{dyn,max-C}$ (kN)	μ_R (kN)	$T_{dyn,max-C}/\mu_R$	β_a
Drag anchor	4.436	623	6103.6	0.102	3.6
Suction caisson	23.2	2277	22325.53	0.102	5.3

3.6. Conclusions

The reliability of drag embedment anchors for catenary mooring systems was assessed using FORM. Two models of drag embedment anchors with fluke length-fluke thickness ratio equal to 6.67 and 3.09 were used for reliability analyses. The limit state function was formulated at mudline, taking into account the uncertainties in seabed soil properties and metocean variables. A fully coupled time domain analysis was conducted to calculate the catenary mooring line tensions in a semisubmersible platform. Response surface method was used to express the line tensions at mudline. An Excel spreadsheet VBA Macro was developed based on a limit equilibrium model to estimate the anchor capacities, considering the embedded profile and the frictional capacity of the anchor chain at the seabed. The developed spreadsheet was validated against the FEA results, test results, and practical design charts. Lognormal distributions were fitted to generated capacities as function of fluke length and the ratio of fluke length to fluke thickness. Statistical properties of anchor capacities such as mean, standard deviation, coefficient of variation and median were calculated at mudline and padeye. The anchor models with reliable performance were determined based on the target failure probability of 10E-05. Annual reliability indices were expressed as function of fluke length and dry anchor weight, using linear expressions

for logarithm of failure probability, and a comprehensive parametric study was conducted. The results provided an important insight into the reliability based design of drag embedment anchors.

The study revealed that the anchor geometry has a significant impact on reliability indices as the major contributor to the ultimate anchor capacity. However, an identical curve fit was obtained for reliability index of the anchors with different ratios of fluke length to fluke thickness. The chain-soil interaction is the secondary influential parameter that needs to be studied in future works. It was observed that reliability index depends on the fluke length and is largely irrelevant to the anchor weight. For a given anchor weight, the reliability index was increased by increasing the fluke length. This showed that keeping a constant anchor weight, a larger fluke length provides higher reliability index. In order to reduce the failure probability by a factor of 10 (i.e. one order of magnitude), the fluke length and anchor weight shall be increased by 6% and 20%, respectively. This in turn shows the significant impact of the fluke length on reliability as the primary influential anchor parameter in comparison with anchor weight.

In addition, the mean and median capacities at padeye were found to be 7 – 10% less than those at mudline, proving the importance of frictional capacity of the chain as the secondary influential parameter. A close coefficient of capacity variation at padeye and mudline (about 26%) was observed for both anchor groups. The ratio of the lower bound capacity to median capacity at mudline was also 35 – 36 %. However, the fluke length was remained as the primary influential parameter. As the fluke length and thickness increase in each group of anchors, the difference between the capacity at padeye and mudline decreases, which shows the dominancy of anchor geometry relative to the chain-soil interaction.

Overall, the level of the reliability indices obtained for drag embedment anchors were found to be lower than the other anchoring solutions such as suction caissons. This indeed gets back to the theoretical basis developed for calculation of holding capacities. In case of the suction anchors, the simple anchor geometry, well-developed soil failure mechanisms, pre-defined depth of installation and soil properties, and an accurate calculation of anchor capacity are all contributing to a higher level of reliability. Neither of these advantages is completely achievable in case of drag embedment anchors. Complicated geometry, uncertain trajectory and final embedment depth, uncertain soil properties and oversimplified failure mechanisms and capacity calculation are all resulting in lower level of reliability. However, this is a compromise between the cost and the risk and many of these uncertainties in response of drag embedment anchors are mitigated with relatively low-cost field trials and holding capacity tests. In other words, the real reliability levels of drag anchors (i.e. through field trials) are much higher than the reliabilities the can be obtained through computational works. This shows that improving the computational reliability indices needs developing more sophisticated theoretical models for estimation of the ultimate anchor capacities, that in turn can result is lowering the construction expenses through eliminating the anchor field trials.

3.7. Acknowledgments

The authors gratefully acknowledge the financial support of this research by Memorial University of Newfoundland through VP start-up fund.

References

Anchor manual 2010. Vryhof anchors BV Netherland. The Guide to Anchoring 2010.

Aubeny C, Han SW, Murff JD, 2003(c). Suction caisson capacity in anisotropic, purely cohesive soil. Int. J. Geomech. 3(2):225-35. doi: 10.1061/~ASCE!1532-3641~2003!3:2~225!

Aubeny CP, Han S, Murff JD, 2003(a). Refined model for inclined load capacity of suction caissons. Proceedings of OMAE 22nd International Conference on Offshore Mechanics and Arctic Engineering; June 8-13; Cancun, Mexico. doi:10.1115/OMAE2003-37502

Aubeny CP, Han SW, Murff JD, 2003(b). Inclined load capacity of suction caissons. Int. J Numer. Anal. Methods Geomech. 27(14):1235-54. doi:10.1002/nag.319

Bissett MJ, 1993. Soil resistance to chain anchor movement [dissertation]. Univ. of Western Australia.

Choi YJ, 2007. Reliability assessment of foundations for offshore mooring systems under extreme environments [dissertation]. The University of Texas at Austin.

Clukey E, Banon H, Kulhawy F, 2000. Reliability assessment of deepwater suction caissons. Proceedings of Offshore Technology Conference OTC 12192; May 1-4; Houston, Texas. https://doi.org/10.4043/12192-MS

Davenport AG, 1964. Note on the distribution of the largest value of a random function with applications to gust loading. Proceedings of the Institution of Civil Engineers, London, England 28(2):187–96. doi: https://doi.org/10.1680/iicep.1964.10112

Det Norske Veritas, 2010(a). Position Mooring. Offshore Standard DNV-OS-E-301.

Det Norske Veritas, 2010(b). Dynamic Risers. Offshore Standard DNV-OS-F201.

Det Norske Veritas, 2012. Design and Installation of Fluke Anchors. Offshore Standard DNV-RP-E301.

Det Norske Veritas, 2013. Submarine Pipeline Systems. Offshore Standard DNV-OS-F101.

El-Sherbiny R, 2005. Performance of suction caisson anchors in normally consolidated clay [dissertation]. The University of Texas at Austin.

Fulton TM, Stewart WP, 1994. Vertical Loads on Drag Embedment Anchors. Proceedings of Offshore Technology Conference OTC 7491; May 2-5; Houston, Texas. doi: https://doi.org/10.4043/7491-MS

Gilbert R, 2010. FORM analysis for suction caisson anchor [dissertation]. University of Texas at Austin.

Lai Y, Zhu B, Huang Y, Chen C, 2020. Behaviors of drag embedment anchor in layered clay profiles. Applied Ocean Research 101, 102287, https://doi.org/10.1016/j.apor.2020.102287.

Luke AM, Rauch AF, Olson RE, Mecham EC, 2003. Components of suction caisson capacity measured in axial pullout tests. Proceedings of international symposium on deepwater Mooring Systems.

Ma KT, Duggal A, Smedley P, L'Hostis D, Shu H., 2013 A historical review on integrity issues of permanent mooring systems. Proceedings of Offshore Technology Conference OTC 24025; May 6-9; Houston, Texas. https://doi.org/10.4043/24025-MS

Melchers RE, Ahammed M, Middleton C, 2003. FORM for discontinuous and truncated probability density functions. Struct. Saf. 25(3):305-13. doi: https://doi.org/10.1016/S0167-4730(03)00002-X

Najjar SS, 2005. The Importance of lower-bound capacities in geotechnical reliability assessments [dissertation]. The University of Texas at Austin.

Neubecker SR, Randolph MF, 1995(a). Performance of embedded anchor chains and consequences for anchor design. Proceedings of Offshore Technology Conference OTC 7712; 1995 May 1-4; Houston, Texas; pp. 191–200. https://doi.org/10.4043/7712-MS

Neubecker SR, Randolph MF, 1995(b). Profile and frictional capacity of embedded anchor chains. J. Geotech. Eng. 121(11):797-803. doi: https://doi.org/10.1061/(ASCE)0733-9410(1995)121:11(797)

Neubecker SR, Randolph MF, 1996. The performance of drag anchor and chain systems in cohesive soil. Mar. Georesources Geotechnol 14(2):77-96. doi: http://dx.doi.org/10.1080/10641199609388305

O'Neill MP, Bransby MF, Randolph MF, 2003. Drag anchor fluke-soil interaction in clays. Can. Geotech. J. 40(1):78–94. doi: 10.1139/T02-096

Ozmutlu S, 2012. The use of drag embedment anchors in offshore mooring systems. Vryhof anchors BV Netherlands. OTEO International Conference on Offshore Renewable Energy.

Private communications with Field operator.

Sarkar A, Eatock Taylor R, 2000. Effects of mooring line drag damping on response statistics of vessels excited by first- and second-order wave forces. Ocean Eng. 27(6):667-86. doi: https://doi.org/10.1016/S0029-8018(99)00014-1

Silva-Gonzalez F, Heredia-Zavoni E, Valle-Molina C, Sanchez-Moreno J, Gilbert RB, 2013. Reliability study of suction caissons for catenary and taut-leg mooring systems. J. Struct. Saf. 45:59–70. doi: http://dx.doi.org/10.1016/j.strusafe.2013.08.011

Taylor R, Valent P, 1984. Design guide for drag embedment anchors.

Tian Y, Randolph MF, Cassidy MJ, 2015. Analytical solution for ultimate embedment depth and potential holding capacity of plate anchors. Géotechnique 65(6):517–30. doi: https://doi.org/10.1680/geot.14.P.228.

Valle-Molina C, Heredia-Zavoni E, Silva-González FL, 2008. Reliability analysis of suction caissons for FPSO systems. Proceedings of the ASME 27th International Conference on Offshore Mechanics and Arctic Engineering OMAE 57140; June 15-20; Estoril, Portugal; pp. 1–6.

Wang LZ, Guo Z, Yuan F, 2010. Quasi-static three-dimensional analysis of suction anchor mooring system. Ocean Eng 37(13):1127–38. doi:10.1016/j.oceaneng.2010.05.002

4. Chapter 4

Nonlinear Integrated Dynamic Analysis of Drill Strings under Stick-Slip Vibration

Mohammad Javad Moharrami[1], Clóvis de Arruda Martins[2], Hodjat Shiri[3]

1: Department of Civil Engineering
Memorial University of Newfoundland
e-mail: mjmoharrami@mun.ca

2: Department of Mechanical Engineering
University of São Paulo, Brazil
e-mail: cmartins@usp.br

3: Department of Civil Engineering
Memorial University of Newfoundland
e-mail: hshiri@mun.ca

This chapter was published as a journal paper in Applied Ocean Research.

Abstract

Stick-slip torsional vibration raising from bit-formation contact is a catastrophic dynamic phenomenon occurring in deep-water oil and gas drilling systems. The torsional vibrations can result in premature fatigue failure of drilling equipment and reduce drilling efficiency. Thus, studying the dynamics of the system is a vital key to identify the roots of the vibration and establish appropriate mitigation and remediation methods. In this paper, an efficient approach for finite element (FE) modeling of stick-slip vibrations of the full drill strings was proposed. The model was developed based on a rate-dependent formulation of bit-rock interaction, for which the cutting process is integrated through the frictional contact. The nonlinear effects of large rotations and the geometrically nonlinear axial-torsional coupling were taken into account. The effect of energy dissipation due to the presence of drill mud along the drill pipes and drill collars was incorporated through Rayleigh viscous damping. The performance of the developed numerical model was verified through comparisons with a lumped-parameter model. The conducted research work resulted in a robust and practical integrated FE model to simulate the entire drill string and mimic the drill string system dynamics under torsional vibrations.

Keywords: Drill string dynamics; Nonlinear vibrations; Stick-slip; Bit-rock interaction; Rayleigh viscous damping; Finite element modeling.

4.1. Introduction

A drill string is an essential component of rotary drilling systems employed in deep-water oil and gas extraction. The main function of the drill string is to transfer the surface rotary motion from the drive system to the drill bit, as well as to provide the axial force, known as weight-on-bit (WOB), for an efficient cutting process in the borehole (Jansen and van den Steen, 1995). Figure 4-1 illustrates an offshore drilling platform and its drill string system comprising mainly of thin-walled drill pipes screwed together by threaded joints, followed by thick-walled drill collars, and drill bit.

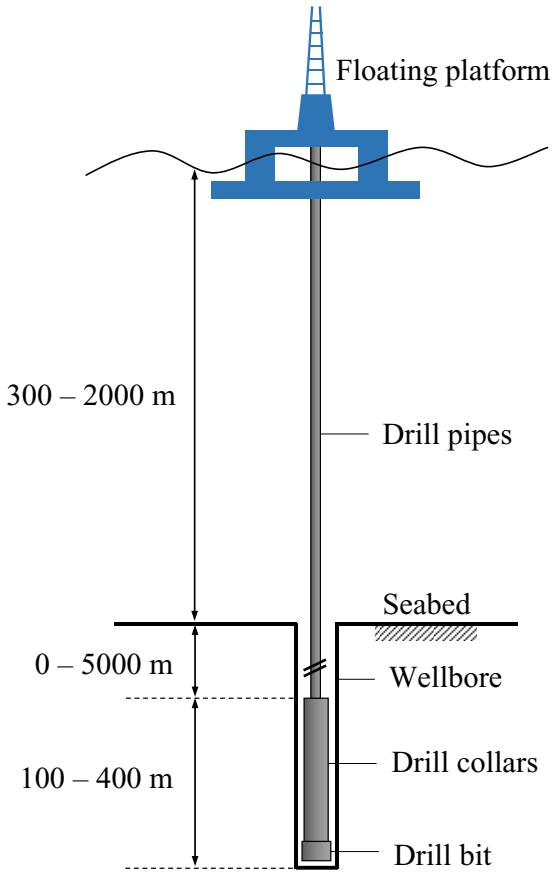

Figure 4-1. Schematic view of an offshore drilling rig and the corresponding drill string

Drill pipes constitute a significant length of the drill string and transfer the applied rotary motion at the surface to the drill bit. The lower end of the drill string is composed of various components, such as drill collars and stabilizers, collectively called the bottom-hole assembly (BHA) (MacDonald and Bjune, 2007). Drill collars are run in compression and are responsible for providing the desired weight-on-bit and facilitating straight drilling (Chevallier, 2001). The drill string length varies between 0 and 5 km, with a collar section of a few hundred meters (Jansen and van den Steen, 1995). This extreme slenderness of the drill string makes it prone to different nonlinear dynamical phenomena leading to costly field failures (MacDonald and Bjune, 2007).

The stick-slip vibration is a catastrophic type of torsional oscillations, which in particular, leads to failure of drill pipes, bit, and downhole electronic devices (Jansen and van den Steen, 1995). This type of vibration lies within the broad class of self-excited vibrations, in which the rotary motion of the bit provides an exciting torque-on-bit (TOB), and thus, no external force is required to maintain the oscillation (Finnie and Bailey, 1960; Rao, 2011). The frictional force acting on the bit, stemming from a highly nonlinear bit-rock interface, has been identified as the leading cause of the stick-slip phenomenon (Halsey et al., 1988; Brett, 1992; Jansen and van den Steen, 1995; Gourdon and Israelachvili, 2003). The stick-slip vibration involves cyclic fluctuations in the bit angular velocity, varying from near zero up to more than twice the measured drive velocity at the surface (Chen et al., 2002).

Studying the drill string dynamics under the nonlinear vibration modes is a fundamental step to reveal the origins of the dangerous dynamical phenomena and control the harmful oscillations. Over the past decades, analytical (e.g., Lin and Wang, 1991; Brett, 1992;

Jansen and van den Steen, 1995; Richard et al., 2007; Navarro-López and Cortes, 2007; Liu et al., 2013) and numerical (e.g., Axisa and Antunes, 1992; Sampaio et al., 2007; Khulief et al., 2007; Ritto et al., 2009; Germay et al., 2009; Ghasemloonia et al., 2013; Liu et al., 2014; Kapitaniak et al., 2015) studies have been conducted to model the characterization of drill string dynamics. However, the complex nonlinear nature of the drill string-wellbore interaction and the consequent vibration modes have imposed extreme difficulties against proposing a simplified and robust solution for integrated dynamic system analysis of the entire drill string.

In this paper, a numerical model was developed by incorporation of the highly non-linear bit-rock contact boundary condition, and a proper quantification of the viscous mud damping. A computationally efficient approach was proposed to model the contact at the bit-rock interface and capture the cutting and friction effects. The alternative approach was developed based on the velocity-weakening behavior of the torque-on-bit that is observed in the published data. A modal analysis was conducted to estimate the eigenfrequencies and mode shapes of the drill string using a linear perturbation frequency analysis. A procedure was presented for proper selection of the Rayleigh damping coefficients in order to retain the effect of higher vibration modes. Also, a five degree-of-freedom lumped-parameter model was developed and the results of the torsional vibrations obtained from both numerical and analytical models were compared. The dynamics of the drill pipes, drill collars, and drill bit, were considered in the lumped-parameter model, and the bit-rock interaction and the equivalent mud damping were incorporated. The bit-rock contact was modeled as a combination of the Karnopp model (at zero angular velocity) and the Stribeck friction, through a switching model.

The FEM models which have addressed the torsional stick-slip vibration of the full-scaled drill string, has used different approach, and ignored one or more aspects of the problem such as shear deformations (e.g., Khulief et al., 2007; Sampaio et al., 2007; Germay et al., 2009), damping (e.g., Khulief et al., 2007), and geometric coupling between the axial and torsional vibrations (e.g., Germay et al., 2009). On the other hand, the behavior of the drill pipes as an extremely slender structure has been less explored in the literature due to the complex nonlinear nature of the drill string-wellbore interaction and the resultant vibration modes. Furthermore, the external parameters, i.e., operational conditions, can affect the nonlinear dynamical behavior of the drill string structure. The current study simultaneously addressed the significance of the aforementioned aspects, through developing an innovative FEA model. It was observed that the developed numerical model was in great qualitative agreement with field and experimental observations regarding stick-slip vibrations. The results showed that for certain operational parameters, the torsional stick-slip vibrations can occur at frequencies different than the first natural frequency of the system. Field test results and numerical simulations using the models developed in Sections 2 and 3 were compared to verify the predictions. The study showed that the developed numerical model along with the proposed procedure is a robust tool that can be used for accurate and cost-effective analysis of the drill string stick-slip vibration.

4.2. Developing the FEM Model

FEM has been extensively used in the dynamic analysis of drill string systems (e.g., Axisa and Antunes, 1992; Sampaio et al., 2007; Khulief et al., 2007; Ritto et al., 2009; Germay et al., 2009; Ghasemloonia et al., 2013; Liu et al., 2014; Kapitaniak et al., 2015). The

advantage of the FEM over the analytical methods (i.e., lumped-parameter models) lies within appropriate treatment of the complicated boundary conditions and forces, such as fluid-drill string interaction, drill string-wellbore contact, and bit-rock interaction, as well as the interplay between different vibration modes. Moreover, evaluating the equivalent system properties and the coding of the lumped-parameter models is quite intricate, and the verification of the predicted results is often challenging.

In this paper, a global three-dimensional FEM model of the drill string was developed in ABAQUS/Explicit. The geometrical nonlinearity of the deformable model, i.e., the nonlinear effects due to the large rotational displacements, as well as the axial-torsional geometrical nonlinear coupling were considered. The consideration of geometrical nonlinearities is vital in dynamics of structures and drill string systems (Banerjee and Dickens, 1990; Trindade and Sampaio, 2002; Sampaio et al., 2007). Figure 4-2. shows the overall configuration and the characteristics of the modeled drill string, where *x*, *y*, and *z* are the translational degrees of freedom, whereas ϕ_x, ϕ_y, and ϕ_z are the rotational degrees of freedom around *x*, *y*, and *z* axes, respectively.

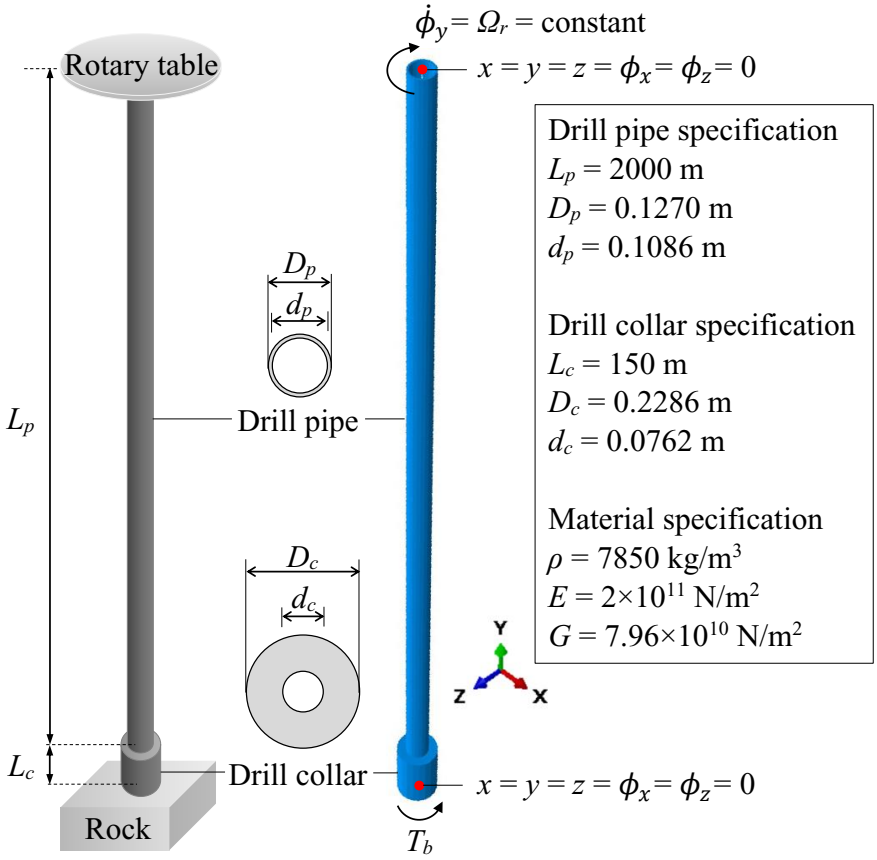

Figure 4-2. Illustration of the realistic drill string (left) and the corresponding FEM model developed in ABAQUS with boundary conditions at the surface and the bit (right)

A slenderness (diameter divided by length) ratio of less than 0.1 indicates that the three-dimensional continuum drill string can be abstracted to a one-dimensional beam model (Vlasov, 1961). Therefore, the two-node linear interpolation beam element, B31, (Timoshenko beam) was selected from the ABAQUS element library to model both the drill pipes and the drill collars. Timoshenko beam (in which the beam section remains planar but not necessarily perpendicular to the neutral axis, i.e., shear effects) was used because (i) it incorporates the Euler-Bernoulli theory (which ignores the shear effects by assuming that the beam section remains planar and perpendicular to the neutral axis), and

(ii) it considers shear effects and has superior application in dynamic analysis of drill string with respect to shear stresses (Ritto et al., 2009). The B31 is a one-dimensional line element in three-dimensional space that has stiffness associated with axial deformation, bending, and torsion (ABAQUS/Explicit User's Manual, 2017). Each node has six degrees-of-freedom; three translational and three rotational. Using the beam elements in modeling the drill string significantly reduces the computational time and cost of the simulation, yet providing a good approximation of the model response.

4.2.1. Bit-Rock Contact Boundary Condition

Appropriate contact modeling at the bit level is a crucial aspect of nonlinear dynamic analysis of drill string. The torque-on-bit at the bit-rock interface consists of cutting and friction components between the drill-bit and the rock (Detournay and Defourny, 1992; Richard et al., 2007; Detournay et al., 2008). Conventionally, under a constant weight-on-bit, the bit-rock interaction law is characterized by a frictional contact with a nonlinear coefficient of friction decreasing with the bit angular velocity (Richard and Detournay, 2000). The nonlinear velocity-weakening behavior that has been observed in the field and laboratory drilling experiments (Brett, 1992; Pavone and Desplans, 1994; Abbassian and Dunayevsky, 1998), is often the major cause of the drill bit stick-slip phenomenon. Accurate prediction of contact and friction effects is thus vital in investigation of the torsional behavior of the drill string.

ABAQUS/Explicit employs the kinematic and penalty contact models. These models, however, require defining the contact surfaces, i.e., modeling the bit and the rock bodies through two- or three-dimensional finite elements, which in turn, leads to computational

challenges and convergence issues due to the inherent nonlinearity of the contact interface. As an alternative approach, to prevent an extreme complexity in contact analysis, and efficiently employ the beam elements to minimize the computational cost, the frictional contact at the bit-rock interface was modeled using an equivalent frictional moment. The normal and tangential force components at the contact surface were related by using the Coulomb model. The tangential force component was transformed to the external moment by means of the geometric relation *external moment = tangential force component × bit radius* (Vlajic et al., 2014b). Then, the frictional torque-on-bit T_b can be expressed as follows (ABAQUS/Explicit User's Manual, 2017):

$$T_b = \begin{cases} M, & if\ |M| < T_0 \text{ (stick mode)}, \\ M_{sl}, & otherwise \text{ (slip mode)}. \end{cases} \quad (1)$$

where M is the magnitude of all frictional moments acting on the bit (drill collar's end) about the longitudinal axis (tangent to the bit-rock contact surface), $T_0 = \mu_s R_b W_b$ is the break-away moment (maximum static friction torque), $M_{sl} = \mu(\dot{\phi}_b) R_b W_b$ is the sliding friction moment about the longitudinal axis, R_b is the bit radius, $W_b > 0$ is the weight-on-bit, and $\mu(\dot{\phi}_b)$ is the Static-Kinetic Exponential Decay friction formulation (see Figure 4-3.) defined as follows:

$$\mu(\dot{\phi}_b) = \left[\mu_c + (\mu_s - \mu_c) e^{-\gamma|\dot{\phi}_b|}\right] \quad (2)$$

where $\dot{\phi}_b = \Omega_b$ is the bit angular velocity, μ_c and μ_s are the kinetic (Coulomb) and static friction coefficients, respectively, and $\gamma > 0$ is the constant decay coefficient. The friction coefficients play a key role in determining the tangential force and have been shown to be influential on system dynamics (Liao et al., 2012). It is noted that μ_s can be greater than one depending on the surfaces, while $\mu_c \in (0, 1)$ and $\mu_s > \mu_c$.

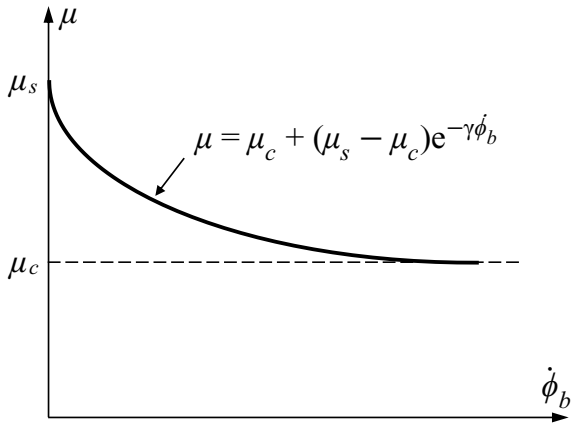

Figure 4-3. Exponential decay friction coefficient used in the ABAQUS model

The alternative approach allowed for accurate and effective capturing of the frictional contact at the bit-rock interface, preventing in particular, the extra difficulties in contact analysis, and rather modeling the bit and rock bodies using the FEM mesh.

4.2.2. Mesh Sensitivity Analysis

The mesh density (element size) can significantly affect the computational effort, convergence, and solution accuracy. The large elements will reduce the precision of the results for both low- and high-frequency responses of the system. Also, small elements will provoke unrealistically high-frequency vibrations into the system, and prohibit the convergence of the solution. Special attention thus must be paid to the appropriate selection of the element size. A preliminary mesh sensitivity analysis was conducted by varying different mesh densities in the drill pipe and drill collar sections. The element size on the collar section was set to be smaller than the pipe section to ensure a denser element distribution on the drill collars, where the stick-slip response of the drill bit due to frictional contact was of particular interest. Figure 4-4 compares the results of mesh sensitivity analysis and its impact on prediction of the angular velocity of the bit.

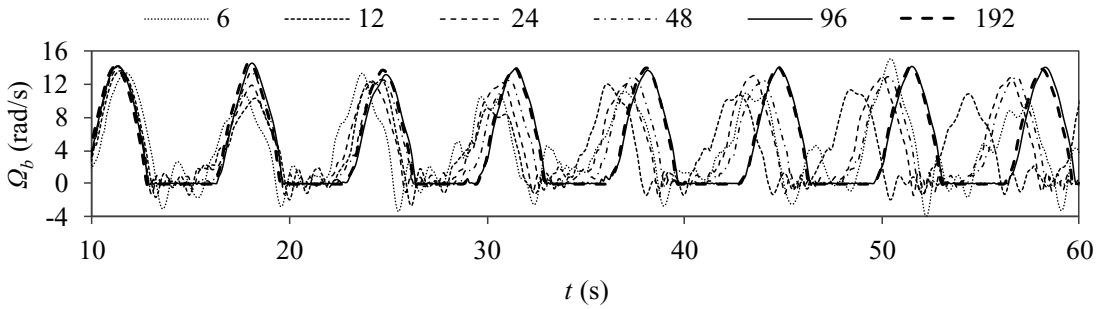

Figure 4-4. Time-series of the bit stick-slip vibration for varying mesh density for Ω_r = 4.19 rad/s (4.19 × 60/2π = 40 rpm). The numbers on the plot indicate the number of elements in each FEM mesh

As the result of mesh sensitivity analysis, a mesh of 96 elements (64 on the pipe, and 32 on the collar section) with a uniform discretization was used to achieve a balance between the computational effort and the precision.

4.2.3. Modal Analysis

Modal analysis was conducted to identify the inherent dynamic characteristics of the system, i.e., natural frequencies, mode shapes, and damping. The natural modes of vibration are affected by the boundary conditions and the material properties including inertia, stiffness, and damping (Fu and He, 2001). To that end, the first 500 undamped natural frequencies and the corresponding mode shapes of the drill string were determined by the Lanczos eigenvalue extraction method in a linear perturbation frequency analysis. The criterion for extraction of 500 natural modes was to establish at least ten natural frequencies for torsional vibration. The stationary behavior of the rotating drill string is equivalent to the dynamics of the same structure fixed at the surface and free at the bit (Challamel et al., 2000). Thus, the boundary condition at the top end of the drill string

(rotary table) was completely fixed, while the lower end (bit) was fixed in all directions except the rotation about the longitudinal axis of the string.

The modal analysis resulted in a total effective mass of 433.43 kgm^2 for the first 500 modes. This was about 87% of the total real mass moment of inertia of the drill string ($J_{string} = 4 \times J_p + J_c = 186.5753 + 311.7961 = 498.3714$ kgm^2). Table 4-1 shows the natural frequencies and the corresponding effective masses for the first ten torsional modes of the drill string.

Table 4-1. Torsional natural frequencies and modal effective masses of the drill string

Mode number	Natural frequency	Natural frequency	Modal effective mass moment of inertia	Modal mass moment of inertia participation ratio	Normalized natural frequency
n	ω_n (rad/s)	f_n (Hz)	(kgm^2)	(%)	ω_n/ω_1
113 (1)	1.206	0.192	380.31	87.74	1.00
142 (2)	5.264	0.838	30.94	7.14	4.37
148 (3)	10.022	1.595	8.90	2.05	8.31
153 (4)	14.876	2.368	4.06	0.94	12.34
159 (5)	19.749	3.143	2.30	0.53	16.38
165 (6)	24.621	3.919	1.48	0.34	20.42
168 (7)	29.484	4.693	1.02	0.24	24.46
174 (8)	34.330	5.464	0.75	0.17	28.48
178 (9)	39.156	6.232	0.57	0.13	32.48
181 (10)	43.956	6.996	0.45	0.10	36.46

As shown in Table 4-1, the ratio of the effective mass to the total modal mass for the first torsional mode is 380.31/433.43 = 87.74%, which verifies the significant contribution of this mode to the system response. The fundamental natural frequency (ω_1) is 1.2056 rad/sec (f_1 = 0.19188 Hz) which is associated with the most significant modal effective mass of 380.31 kgm^2. The cumulative effective mass for the first ten modes is 430.77941 kgm^{2,} which indicates these modes retain 99.38% of the total modal mass of the system and perfectly capture its dynamics. Figure 4-5(a) shows the result of the convergence study for the first ten torsional natural frequencies with different mesh densities. It was observed that the natural frequencies obtained from 96 elements had less than 0.7% difference with those obtained from 192 elements. This negligible difference validates the accuracy of the mesh with 96 elements over the dominant modes. The first four torsional mode shapes are also illustrated in Figure 4-5(b). Also, a convergence study based on natural frequencies has been conducted by Vlajic et al. (2014a).

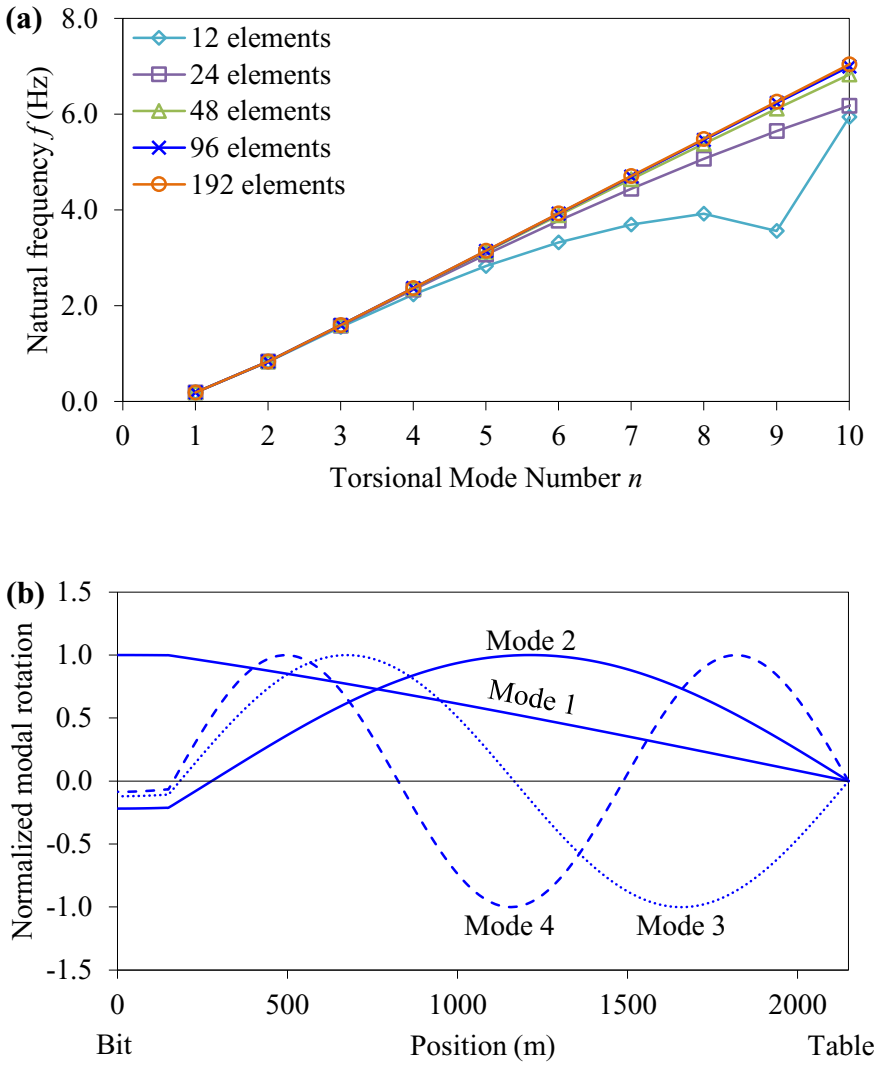

Figure 4-5. Results of modal analysis. (a) Variation of the natural torsional frequency with number of elements, and (b) torsional mode shapes obtained from the mesh of 96 elements

4.2.4. Damping Effect

Mud-drill string interaction is an important aspect of the drill string dynamical behavior, which can impose further complexities into the problem. Furthermore, the inclusion of damping due to the presence of surrounding mud leads to more realistic modeling and is

essential for satisfactory results. The viscous damping effect has been modeled in different ways, such as an empirical function of vibration frequency and mud density (e.g., Spanos et al., 1997), Rayleigh damping proportional to mass (e.g., Sampaio et al., 2007; Ghasemloonia et al., 2013) or stiffness (e.g., Germay et al., 2009), hydrodynamic drag force (velocity-squared proportional) (e.g., Jansen, 1991; Christoforou and Yigit, 1997), and a combination of steady-state friction force and Basset (history) force accounting for the acceleration rate of the drilling fluid particles (e.g., Hovda, 2018).

The most common way of treating viscous damping effects, i.e., drilling mud, in numerical simulations is the frequency-dependent Rayleigh damping. The standard form of the Rayleigh damping matrix is defined as a linear combination of the mass and stiffness matrices, M and K, respectively, that is (Rayleigh, 1945; Chopra and McKenna, 2016):

$$C = \alpha M + \beta K \tag{3}$$

where α and β are the mass and the stiffness proportional coefficients, respectively. The damping ratio of mode n associated with natural frequency ω_n (rad/s) is (Chopra and McKenna, 2016):

$$\xi_n = \frac{\alpha}{2\omega_n} + \frac{\beta\omega_n}{2} \tag{4}$$

The coefficients α and β are evaluated from the two modal damping ratios ξ_i and ξ_j corresponding to the i-th and j-th natural modes of the system. Rewriting Eq. (4) in matrix form for modes i and j lead to a set of two algebraic equations as follows:

$$\frac{1}{2}\begin{bmatrix} 1/\omega_i & \omega_i \\ 1/\omega_j & \omega_j \end{bmatrix}\begin{Bmatrix} \alpha \\ \beta \end{Bmatrix} = \begin{Bmatrix} \xi_i \\ \xi_j \end{Bmatrix} \tag{5}$$

Assuming $\xi_i = \xi_j = \xi$ in Eq. (5), the coefficients α and β are computed as:

$$\alpha = \xi \frac{2\omega_i \omega_j}{\omega_i + \omega_j}, \beta = \xi \frac{2}{\omega_i + \omega_j} \quad (6)$$

The impact of the drill string-drilling fluid interaction on the system dynamics can be modeled by more sophisticated approaches (e.g., Païdoussis and Semler, 1998; Escudier et al., 2000; Escudier et al., 2002; de Pina and Carvalho, 2006; Païdoussis et al., 2008). However, the incorporation of damping effect was not a primary objective of the current study. Simultaneous incorporation of shear deformations, damping, geometric coupling between the axial and torsional vibrations, and the nonlinear drill string-wellbore interaction and the resultant vibration modes required a less complicated damping model to enable convergence of the numerical model. There the Rayleigh damping was adapted in the current study. Rayleigh damping is relatively straightforward due to its mathematical convenience. However, special care must be taken when implementing this method in practical problems. A drawback of Rayleigh damping is that the obtained damping ratio changes with response frequency; which means it is less than the target damping ratio ξ for frequencies between ω_i and ω_j, while increases rapidly for frequencies lower than ω_i and higher than ω_j. Therefore, ω_i and ω_j should be assigned such that the damping ratios over the dominant modes come closer to the target damping. In addition, although existing studies have used a diversity of damping levels (e.g., Germay et al., 2009; Ritto et al., 2009; Bakhtiari-Nejad and Hosseinzadeh, 2017), no practical method has been addressed to form the physical damping matrix through finite element analysis (Liu and Gorman, 1995). The following procedure demonstrates the appropriate selection of mass and stiffness damping coefficients to form the Rayleigh damping matrix and minimize the frequency-dependent damping variations.

A preliminary study was carried out to determine ω_i and ω_j for which the constants α and β gave satisfactory damping ratio for all modes. For a target damping ratio $\xi = 0.02$, ω_i was set to be the first natural frequency ω_1, whereas ω_j was set to be about the second, the third, the fifth, and the tenth natural frequency of the drill string. The result of Rayleigh damping variations over the selected frequency ranges is illustrated in Figure 4-6..

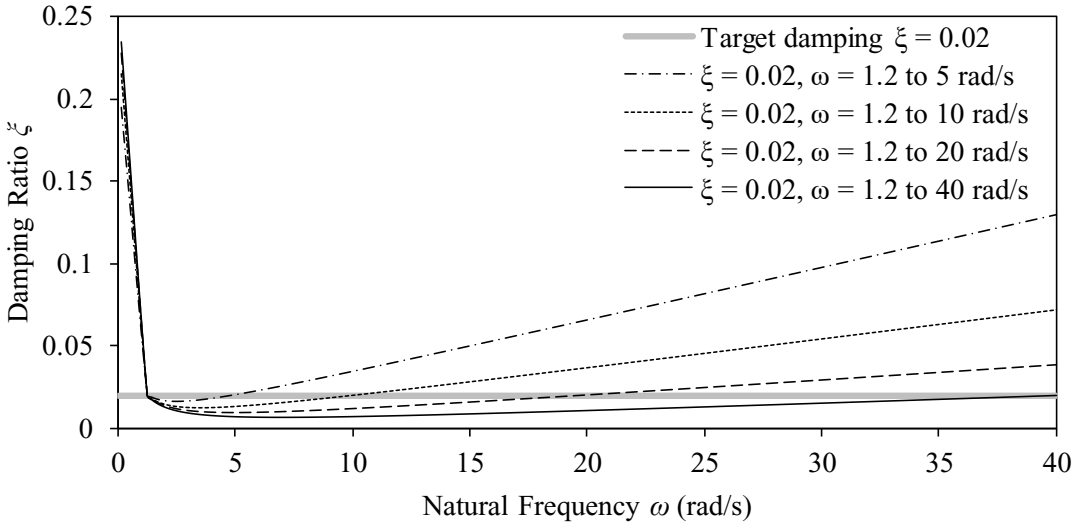

Figure 4-6. Variation of Rayleigh damping with frequency band

Figure 4-6 shows that choosing a narrow frequency band, i.e., $\omega_i = \omega_1$ and $\omega_j \approx \omega_2$, leads to damping ratios immensely larger than the target damping for high-frequency responses, the so-called de-amplification effect. However, picking a wide frequency band, i.e., $\omega_i = \omega_1$ and $\omega_j \approx \omega_{10}$, results in damping ratios smaller than the target damping for high-frequency responses. To avoid overdamping of the high-frequency torsional vibrations, which have been observed in previous field investigations (e.g., Germay et al., 2009; Nessjøen et al., 2011), α and β were determined by using $\omega_i = \omega_1$ and $\omega_j = \omega_{10}$ (see Table 4-1) in the rest of this study. This broad frequency band gave a conservative underdamped

system for intermediate modes, which is more favorable than a non-conservative overdamped system, particularly in fatigue assessment of the drill string system.

4.3. Developing Lumped-Parameter Model

One of the most commonly used lumped-parameter models is the torsional pendulum. In this model, the drill pipes are assumed as inertialess torsional springs, the twisting of the relatively rigid bottom-hole assembly (BHA) is neglected, and the rotary table velocity is constant. Several torsional pendulum models have been proposed in the literature to study the stick-slip vibration of the drill string (e.g., Lin and Wang, 1991; Brett, 1992; Jansen and van den Steen, 1995; Richard et al., 2007). Although the torsional pendulum models are easy to implement and provide useful information on the dynamics of BHA/bit, they are not able to consider two important characteristics of the drill string: (i) the increase in the length as the drilling operation proceeds, and (ii) the vibrations along the entire drill string, i.e., at drill pipes and drill collars. To overcome such shortcomings, multi degrees-of-freedom models of torsional vibration (Navarro-López and Cortes, 2007) as well as coupled axial-lateral-torsional vibrations (Liu et al., 2013) have been introduced.

In this section, a five degree-of-freedom lumped-parameter model was developed based on the generic lumped-parameter model of Navarro-López and Cortes (2007) to make comparisons with the numerical model (see Figure 4-7). The developed model is able to consider the vibrations along the entire drill string, i.e., drill pipes and drill collars, which are neglected in the torsional pendulum models. The key assumptions of the model are: (i) the drill string and the borehole are both straight and vertical, (ii) the drill pipes behave as torsional spring without structural damping, and the drill collars behave as a rigid body,

(iii) there are no bit lateral motions, (iv) the frictional contact in the pipe threaded connections, and between the pipes and the borehole are ignored, (v) the orbital motion of the drilling mud is laminar, i.e., without turbulences, (vi) the energy dissipation effect of the drilling mud is modeled by lumped viscous damping, (vii) the motor dynamic is not considered, (viii) the drive system rotates at a constant and positive speed, and (ix) the weight-on-bit is constant during operation (Navarro-López and Cortes, 2007).

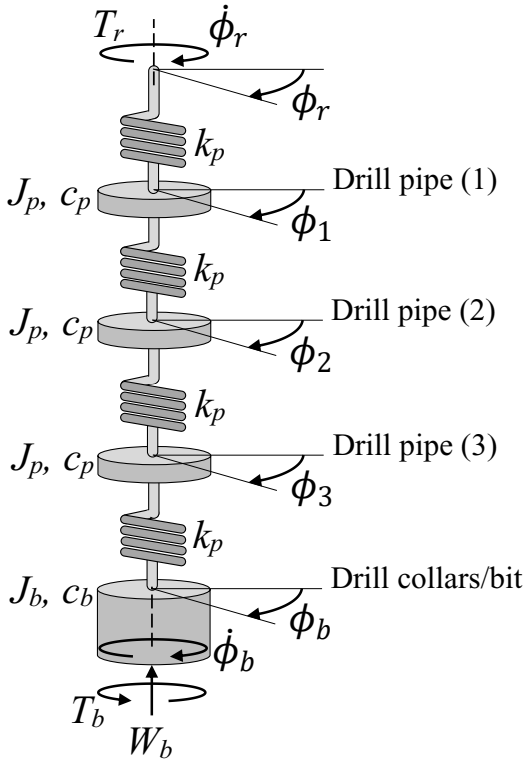

Figure 4-7. Lumped-parameter model representation of the drill string

Under the above assumptions, the bit behavior and the forces acting on the bit was computed by setting the boundary condition at the surface (rotary table), the mechanical properties of the drill string, and the bit-rock interface law representing the boundary condition at the lower end of the drill string (Richard et al., 2007). Based on prior works

(e.g., Jansen and van den Steen, 1995; Navarro-López and Cortes, 2007), the corresponding set of motion equations can be written as follows:

$$\begin{cases} k_p(\phi_r - \phi_1) - T_r = 0 \\ J_p\ddot{\phi}_1 + c_p\dot{\phi}_1 + k_p(\phi_1 - \phi_r) + k_p(\phi_1 - \phi_2) = 0 \\ J_p\ddot{\phi}_2 + c_p\dot{\phi}_2 + k_p(\phi_2 - \phi_1) + k_p(\phi_2 - \phi_3) = 0 \\ J_p\ddot{\phi}_3 + c_p\dot{\phi}_3 + k_p(\phi_3 - \phi_2) + k_p(\phi_3 - \phi_b) = 0 \\ J_b\ddot{\phi}_b + c_b\dot{\phi}_b + k_p(\phi_b - \phi_3) + T_b = 0 \end{cases} \tag{7}$$

where ϕ_r, ϕ_1, ϕ_2, ϕ_3, ϕ_b are the angular displacements of, respectively, the rotary table, drill pipe 1, drill pipe 2, drill pipe 3, and drill collars/bit, $T_r = k_p(\phi_r - \phi_1)$ is the torque delivered by the rotary table to the drill string ($T_r > 0$), and T_b is a nonlinear function representing the frictional torque-on-bit, which is discussed in detail in Section 4.3.1. Following prior studies (e.g., Jansen and van den Steen, 1995), the model parameters can be obtained as follows:

$$J_p = \rho I_p(L_p/4), \quad J_c = \rho I_c L_c, \quad J_b = J_c + J_p/2, \quad k_p = GI_p/(L_p/4) \tag{8.1}$$

with

$$I_p = (\pi/32)(D_p^4 - d_p^4), \quad I_c = (\pi/32)(D_c^4 - d_c^4) \tag{9.2}$$

where J_p, J_c, and J_b are the mass moment of inertia of the drill pipe, the drill collar, and the drill bit, respectively, k_p is the torsional stiffness of the drill pipe, and I_p and I_c are the polar moments of inertia of the drill pipe and the drill collar section, respectively. The equivalent viscous damping coefficients of drill pipe c_p, and drill collars/bit c_b, are given by:

$$c_p = \hat{c}(L_p/4), \quad c_b = \hat{c}(L_p/8) \tag{10.3}$$

where $\hat{c}$ is the viscous damping coefficient per unit length of the drill pipe.

By defining the system state-space vector as:

$$X = \left[\phi_r, \dot{\phi}_r, \phi_1, \dot{\phi}_1, \phi_2, \dot{\phi}_2, \phi_3, \dot{\phi}_3, \phi_b, \dot{\phi}_b\right]^T = [x_1, x_2, x_3, x_4, x_5, x_6, x_7, x_8, x_9, x_{10}]^T \quad (9)$$

then, the set of second-order differential equations of motion of the drill string system can be expressed as a set of ten first-order equations in terms of the state variables as follows:

$$\dot{X} = AX + T \quad (10)$$

where A and T are given by:

$$A = \begin{bmatrix} 0 & 1 & 0 & 0 & 0 & 0 & 0 & 0 & 0 & 0 \\ 0 & 0 & 0 & 0 & 0 & 0 & 0 & 0 & 0 & 0 \\ 0 & 0 & 0 & 1 & 0 & 0 & 0 & 0 & 0 & 0 \\ \frac{k_p}{J_p} & 0 & -\frac{2k_p}{J_p} & -\frac{c_p}{J_p} & \frac{k_p}{J_p} & 0 & 0 & 0 & 0 & 0 \\ 0 & 0 & 0 & 0 & 0 & 1 & 0 & 0 & 0 & 0 \\ 0 & 0 & \frac{k_p}{J_p} & 0 & -\frac{2k_p}{J_p} & -\frac{c_p}{J_p} & \frac{k_p}{J_p} & 0 & 0 & 0 \\ 0 & 0 & 0 & 0 & 0 & 0 & 0 & 1 & 0 & 0 \\ 0 & 0 & 0 & 0 & \frac{k_p}{J_p} & 0 & -\frac{2k_p}{J_p} & -\frac{c_p}{J_p} & \frac{k_p}{J_p} & 0 \\ 0 & 0 & 0 & 0 & 0 & 0 & 0 & 0 & 0 & 1 \\ 0 & 0 & 0 & 0 & 0 & 0 & \frac{k_p}{J_p} & 0 & -\frac{k_p}{J_p} & -\frac{c_b}{J_b} \end{bmatrix}$$

and

$$T = [0, 0, 0, 0, 0, 0, 0, 0, 0, -T_b/J_b]^T \quad (11)$$

To solve the set of motion equations, the nonlinear torque-on-bit T_b was modeled through a variable structure as described in the following section.

4.3.1. The Nonlinear Bit-Rock Interaction

Several modeling approaches have been used in the literature to characterize the frictional torque-on-bit, i.e., Coulomb model (see, e.g., Jansen and van den Steen, 1995), velocity-weakening model (e.g., Brett, 1992; Leine et al., 2002; Mihajlovic et al., 2004; Yigit

Christoforou, 2006), and their combination with zero velocity band friction (e.g., Navarro-López and Cortes, 2007). These models are based on experimental results (Brett 1992; Pavone and Desplans, 1994), which indicate a decrease in the torque-on-bit for increasing angular velocity. As shown in Figure 4-8, to prevent the numerical instabilities during the switchover from stick to slip friction, and achieve high computing efficiency, the bit-rock contact was modeled as a combination of the Karnopp model (Karnopp, 1985) and the Stribeck effect (negatively sloped friction at the slip phase).

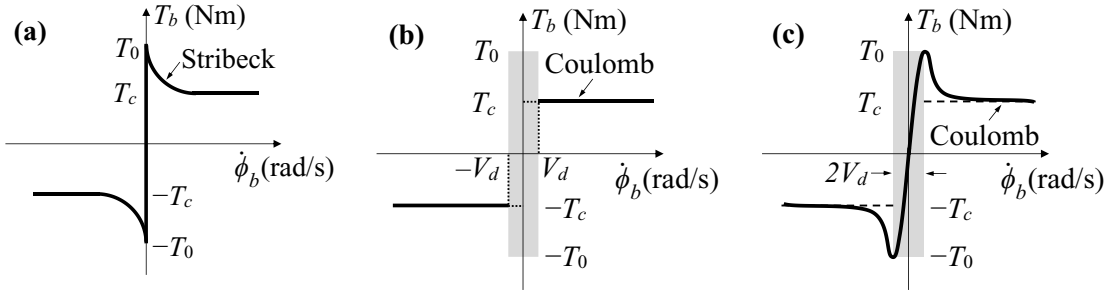

Figure 4-8. Friction models: (a) Stribeck model, (b) Karnopp model, (c) switch model (enhanced Karnopp friction model) + Stribeck model

Further details on the variable structure can be found in Sepehri et al. (1996) and Leine et al. (1998). The frictional torque-on-bit is thus computed as follows:

$$T_b = \begin{cases} T_{st}\,, if\ \left|\dot{\phi}_b\right| < V_d\ \ and |T_{st}| \le T_0 \text{ (stick mode)}, \\ T_0 sgn(T_{st})\,, if\ \left|\dot{\phi}_b\right| < V_d\ \ and\ |T_{st}| > T_0 \text{ (transition from stick to slip)}, \\ T_{sl} sgn\left(\dot{\phi}_b\right), if\ \left|\dot{\phi}_b\right| \ge V_d \text{ (slip mode)}. \end{cases} \tag{1211}$$

with

$$T_{st} = -c_b\dot{\phi}_b - k_p(\phi_b - \phi_3), T_0 = \mu_s R_b W_b, T_{sl} = \mu(\dot{\phi}_b) R_b W_b \tag{13}$$

where $V_d > 0$ is the threshold velocity, T_{st} is the reaction torque during the stick phase that must overcome the break-away torque to make the bit move, T_0 is the break-away torque (maximum static friction torque), T_{sl} is the sliding friction torque, R_b is the bit radius, $W_b > 0$ is the weight-on-the bit, and $\mu(\dot{\phi}_b)$ is the bit exponential-decay friction coefficient defined in Eq. (2). The exponential decaying behavior of the torque-on-bit (Stribeck effect) is in agreement with the field and experimental observations (Brett, 1992; Pavone and Desplans, 1994; Abbassian and Dunayevsky, 1998), as discussed in Section 4.2.1. It is noted that $-k_p(\phi_b - \phi_3)$ is always positive.

The implemented approach to model the bit-rock contact is in accordance with the FEM contact modeling. Additionally, it is possible to use the rate-independent bit-rock interaction models (Detournay and Defourny, 1992; Detournay et al., 2008), in which the torque-on-bit and weight-on-bit are decomposed into pure cutting and frictional contact components, and are related to the depth of cut.

4.3.2. Eigen Frequency Extraction

The natural frequencies were calculated analytically by assuming a fixed and a free boundary condition at the surface and the bit, respectively. The set of equations of motion of such a system is as follows:

$$\begin{cases} J_p\ddot{\phi}_1 + k_p(\phi_1) + k_p(\phi_1 - \phi_2) = 0 \\ J_p\ddot{\phi}_2 + k_p(\phi_2 - \phi_1) + k_p(\phi_2 - \phi_3) = 0 \\ J_p\ddot{\phi}_3 + k_p(\phi_3 - \phi_2) + k_p(\phi_3 - \phi_b) = 0 \\ J_b\ddot{\phi}_b + k_p(\phi_b - \phi_3) = 0 \end{cases} \tag{14}$$

By using the characteristic equation method, the characteristic determinant was calculated as follows:

$$\det(K - \omega^2 J) = 0 \tag{15}$$

where ω is the natural frequency, and K and J are the torsional stiffness and mass moment of inertia matrices, respectively, given by:

$$K = \begin{bmatrix} 2k_p & -k_p & 0 & 0 \\ -k_p & 2k_p & -k_p & 0 \\ 0 & -k_p & 2k_p & -k_p \\ 0 & 0 & -k_p & k_p \end{bmatrix}, J = \begin{bmatrix} J_p & 0 & 0 & 0 \\ 0 & J_p & 0 & 0 \\ 0 & 0 & J_p & 0 \\ 0 & 0 & 0 & J_b \end{bmatrix} \tag{16}$$

Solving Eq. (15), the first four natural torsional frequencies of the system can be obtained using the corresponding mechanical characteristics.

4.4. Results and Discussions

4.4.1. Numerical Results

The full drill string configuration given in Figure 4-2. was numerically studied assuming Ω_r = 2.09 rad/s (2.09 × 60/2π = 20 rpm), W_b = 40 kN, and ξ = 0.03 (α = 0.070416 1/s and β = 0.001321 s). Figure 4-9 shows the simulation results over 60 s for which the drill string exhibits steady-state stick-slip vibrations. The first 10 s of the analysis was the ramping-up of the rotary velocity from zero to the desired value, which is not displayed in the time-series.

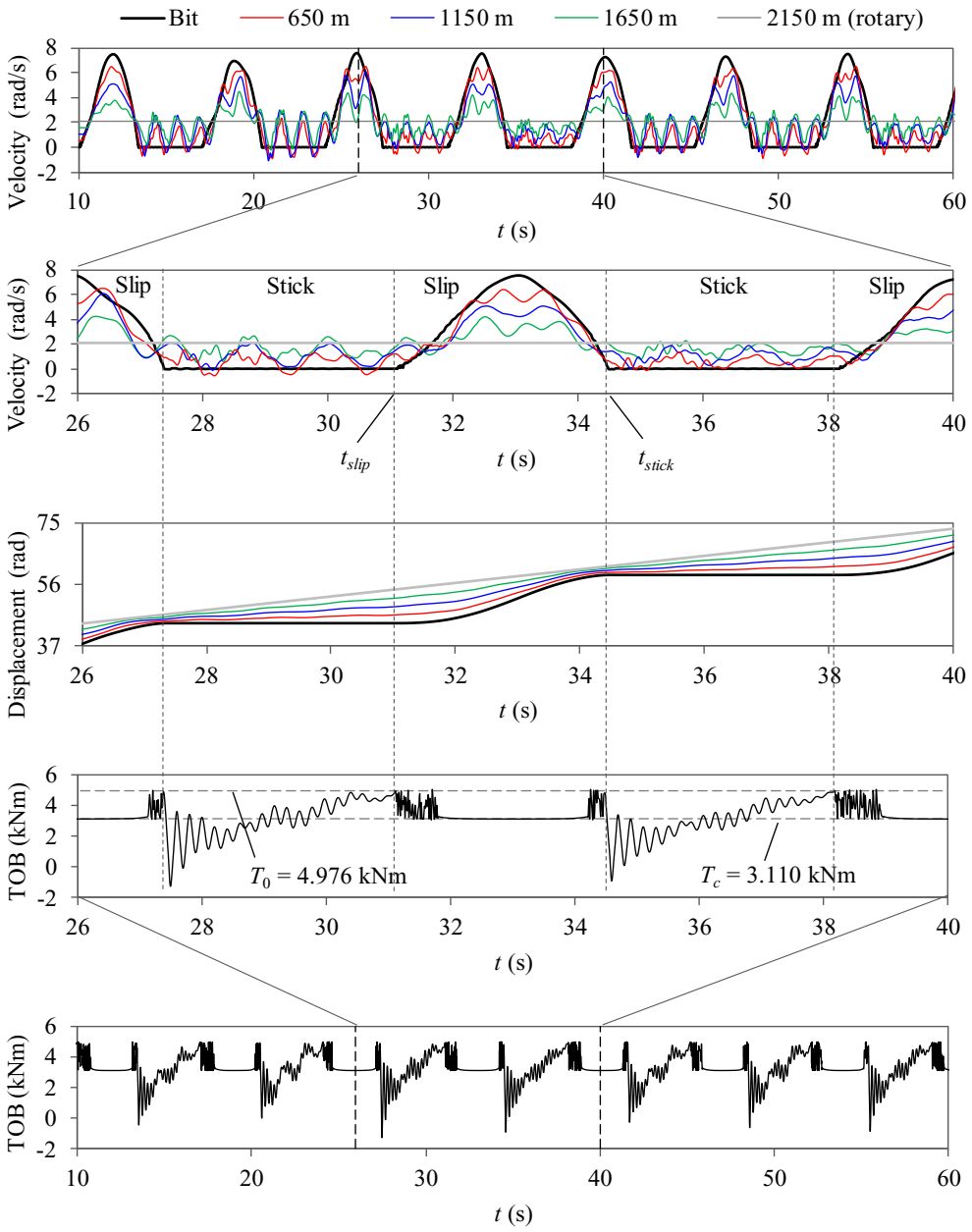

Figure 4-9. Stick-slip slip time-series obtained from FEM model for Ω_r = 2.09 rad/s (2.09 × 60/2π = 20 rpm), W_b = 40 kN, and ξ = 0.03 with α = 0.070416 1/s and β = 0.001321 s. Time-series of the angular velocities are for the drill bit in black, 650 m above the bit in red, 1150 m above the bit in blue, 1650 m above the bit in green, and 2150 m above the bit (rotary table) in gray

As depicted in Figure 4-9, the angular displacement of the rotary table was increased linearly with a constant slope, which corresponds to the constant angular velocity criterion of the rotary table. The dynamic response of the drill bit, however, was identified by steady-state oscillations, representing the stick-slip limit cycles. The limit cycling behavior is in agreement with the field and experimental results of drill string rotation during drilling process (e.g., Jansen and van den Steen, 1995; Kapitaniak et al., 2015). Each limit cycle was characterized by one stick and one slip phase, during which the angular velocity of the drill bit was varying between zero and a maximum value of about 7.5 rad/s, while the angular velocity at the rotary table remained at 2.09 rad/s. This is in agreement with the field results, where the bit angular velocity is about three times larger than the rotary table velocity (Jansen and van den Steen, 1995; Chen et al., 2002). In the time interval t_{slip} = 31.1501 $\leq t < t_{stick}$ = 34.4876 s, the angular velocity of the drill bit is positive, and thus, the system operates under the slip mode. Due to the change in the magnitude of the angular velocity, two distinct motions were observed during the slip mode. The accelerating motion, i.e., $t_{slip} \leq t \leq$ 33.051 s, where the angular acceleration is positive, and hence, in direction to the angular velocity; and the decelerating motion, i.e., 33.051 < $t < t_{stick}$, where the angular acceleration is negative, and therefore, opposite in direction to the angular velocity. During the stick phase, i.e., in the time interval t_{stick} = 34.4876 $\leq t < t_{slip}$ = 38.1626 s, the bit was fully stopped (zero angular velocity), while the rotary table rotated at a constant velocity. This caused an incremental twisting of the drill string, and thus, the reaction torque, i.e., the instantaneous torque applied by the drill string onto the drill bit, developed due to the increasing elastic energy stored in the drill pipes. During this time interval, the value of torque-on-bit T_b was calculated based on Newton's third law, for

which the reaction torque adjusts itself with all the frictional moments in the connector; see Eq. (1). The stick is maintained until the break-away torque value $T_0 = \mu_s R_b W_b$ is reached at $t = t_{slip}$. The oscillations observed in the time-series of the torque-on-bit at the transition between stick to slip phase can be related to the transition from the static coefficient of friction μ_s, to the kinetic coefficient of friction μ_c, inherent to the physical phenomenon of friction. Likewise, the stick regime can be interpreted considering the lumped-parameter model, in which the value of the reaction torque $T_{st} = -c_b\dot{\phi}_b - k_p(\phi_b - \phi_3)$ increases due to the raising elastic energy ($\approx k_p\phi_3 > 0$) in the torsional spring. Eventually, the value of reaction torque reaches the break-away torque, T_0 at $t = t_{slip}$, where the system switches to the slip mode; see Eq. (12).

Figure 4-10 presents the variation of the torque-on-bit T_b with the bit angular velocity Ω_b during one stick-slip limit cycle, computed for Ω_r = 2.09 rad/s, W_b = 40 kN, and ξ = 0.03 (α = 0.070416 1/s and β = 0.001321 s).

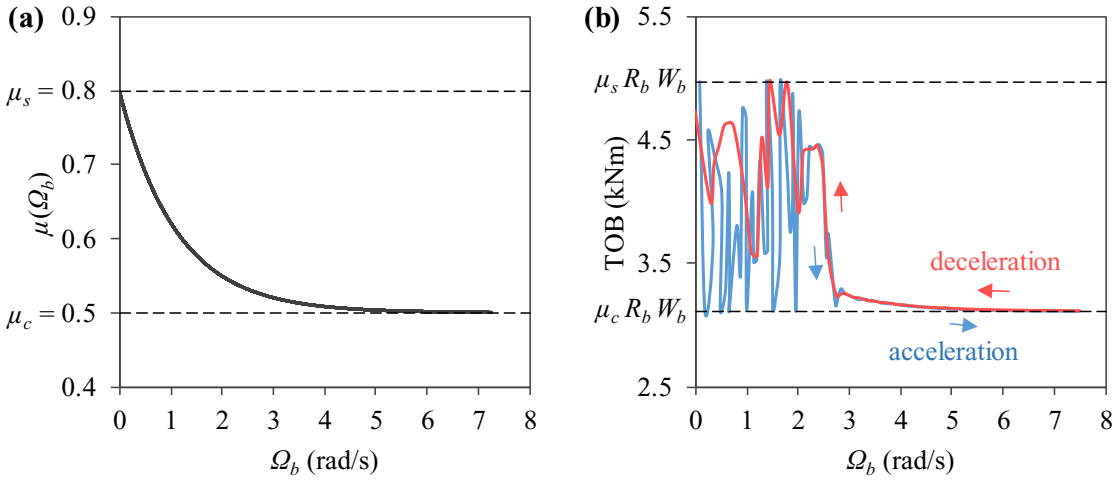

Figure 4-10. Evolution of (a) the exponential decaying coefficient of friction $\mu(\Omega_b)$ and (b) the torque-on-bit T_b with bit angular velocity Ω_b obtained from FEM model

As shown in Figure 4-10, apart from the oscillations at low velocities due to the transition from static to kinetic coefficient of friction, the torque-on-bit decreases with increasing Ω_b and vice versa. The observed velocity-weakening response of the torque-on-bit is in agreement with the published field and experimental results (Brett, 1992; Pavone and Desplans, 1994; Abbassian and Dunayevsky, 1998).

4.4.2. Comparison between the FEM and Lumped-Parameter Models

The results obtained from numerical model were compared with lumped-parameter model to have a comparative evaluation of the models' performance. The model parameters are given in Table 4-2, and the key values of the model are: Ω_r = 2.09 rad/s, W_b = 40 kN, and ξ = 0.03. The equations of motion (Eqs. (7) and (12)) were numerically integrated using the 4th-5th order Runge-Kutta method with variable time steps through the built-in function 'ode45' in MATLAB. The initial conditions for all state variables were taken as zero, except for Ω_r, which was taken as 2.09 rad/s. The viscous damping coefficient per unit

length of drill pipes, $\hat{c}$, was taken as 0.0378 Ns/rad corresponding to a damping ratio ξ = 0.03; this value was adopted from the study of Jansen and van den Steen (1995).

Table 4-2. Parameter values computed for the full drill string configuration given in Figure 4-2.

Quantity	Variable	Value	Unit
Mass moment of inertia of drill pipe	J_p	46.644	kgm^2
Mass moment of inertia of bit	J_b	335.118	kgm^2
Torsional stiffness of drill pipe	k_p	1891.897	Nm/rad
Equivalent viscous damping coefficient for drill pipe	c_p	18.9	Nms/rad
Equivalent viscous damping coefficient for drill collars/bit	c_b	9.45	Nms/rad
Bit radius	R_b	0.1555	m
Static friction coefficient	μ_s	0.8	–
Kinetic (Coulomb) friction coefficient	μ_c	0.5	–
Decay coefficient	γ	0.9	–
Threshold velocity	V_d	1×10^{-6}	–

Figure 4-11 presents a comparison between the system response computed with the FEM and lumped-parameter model. The responses are in good agreement with each other. For the FEM model, there is a variation in the amplitude of stick-slip oscillations of the bit, whereas the response of the lumped-parameter model is almost of constant amplitude. As the bit is about to fully stop, it may rotate backwards for short time intervals. The backward

rotations cause negative values of the torque-on-bit as seen in the FEM time-series (Figure 4-11(a)), which is in close qualitative agreement with field observations (e.g., Halsey et al., 1988; Jansen, L. van den Steen, 1995). Despite slight differences between the analytical and numerical responses, there is excellent agreement between their phase trajectories and frequency components.

Another characteristic of the dynamical behavior of the drill bit is related to the transition phase; that is, the way the phase trajectories enter and leave the stick phase. For the FEM model, there is a gradual and continuous decrease in the value of the instantaneous torque-on-bit when the bit enters the stick phase, rather the sudden drop (discontinuity) observed in the torque-on-bit computed with the lumped-parameter model; see Figure 4-11(a). Nevertheless, at this moment, due to the sudden drop of the angular acceleration from a negative value to zero in both models, the velocity is not differentiable, and thus, the phase trajectories exhibit identical behavior at the transitioning from slip to stick phase. On the other hand, when the system leaves the stick phase, the torque-on-bit computed with the FEM model exhibits oscillations at the very beginning of the transition phase, causing a variant acceleration, and thus, a singular velocity. However, the torque-on-bit computed with the lumped-parameter model shows a smooth transition between the static and kinetic values, and hence, the acceleration, due to which the velocity is differentiable. Therefore, the ways the phase trajectories leave the stick phase are different between FEM and lumped-parameter model.

To determine the frequency components of the bit response under stick-slip condition, a spectral analysis was carried out using FFT method for both FEM and lumped-parameter model responses, as depicted in Figure 4-11(c). The results revealed that the torsional

(stick-slip) limit cycles of the bit exhibit polychromatic contents with dominant frequency of $f_D/f_1 = 0.14/0.192 = 0.73$ and $f_D/f_1 = 0.13/0.178 = 0.73$ for the FEM and lumped-parameter model, respectively. This indicates that the stick-slip vibrations can occur at frequencies different (lower) than the first torsional natural frequency of the drill string depending on the operational conditions. It is worth noting that stick-slip vibrations at natural frequencies different to the fundamental one have been observed in field operations, as reported in previous investigations (Germay et al., 2009; Nessjøen et al., 2011). The difference between the dominant frequency and the first natural frequency of the system in both models corresponds to the nonlinear frictional torque-on-bit arising from the bit-rock interaction. It is noted that the amplitude of zero frequency components of the response spectra corresponds to the twice of the mean angular velocity of the bit, i.e., 4.28 rad/s and 4.10 rad/s computed with the FEM and lumped-parameter model, respectively.

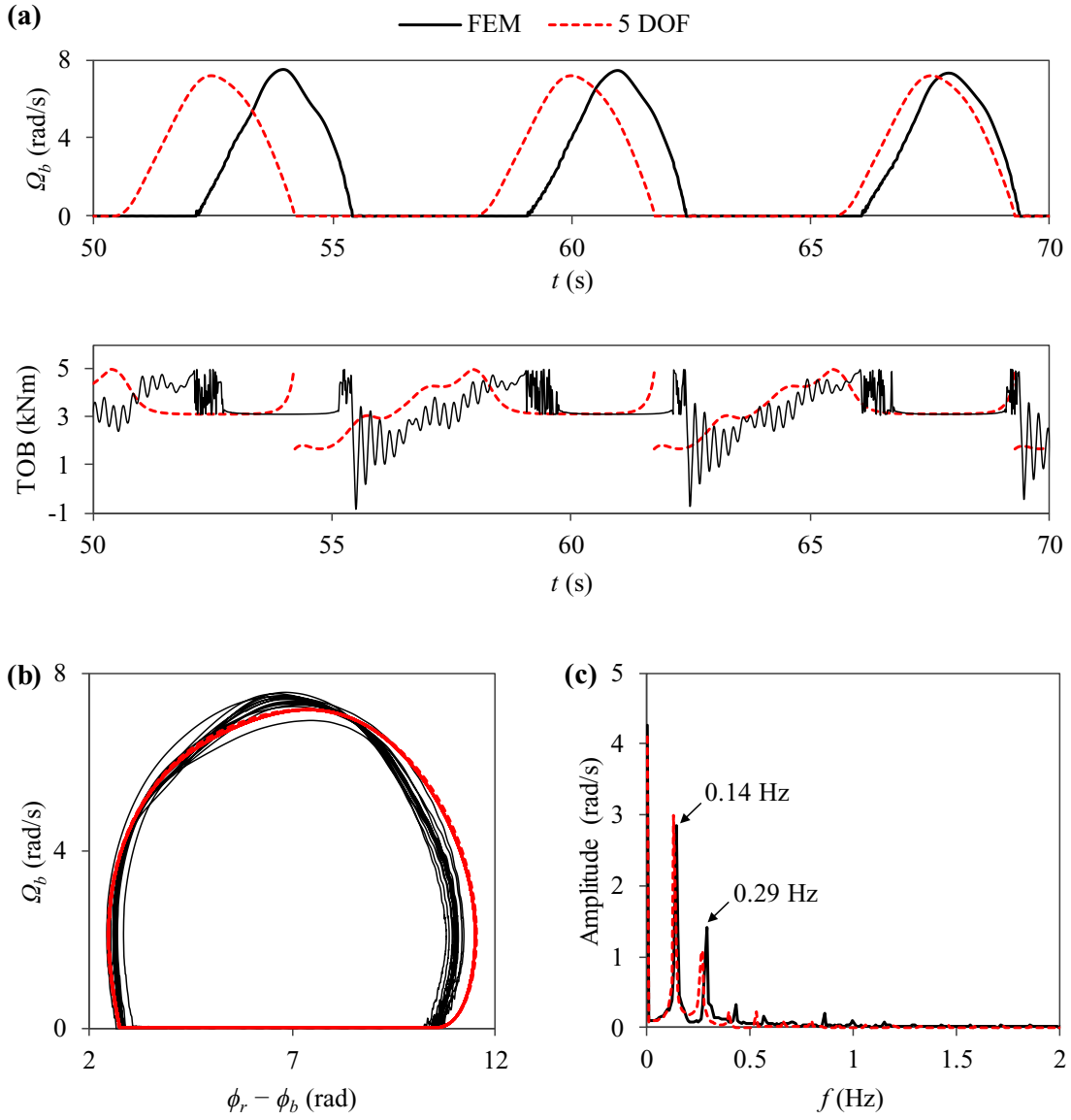

Figure 4-11. Example stick-slip response obtained from the FEM model (solid lines), and the lumped-parameter model using Eqs. (7) and (12) with parameter values given in Table 4-2 (dashed lines). Ω_r = 2.09 rad/s, W_b = 40 kN, and ξ = 0.03. (a) Time-series, (b) phase-planes, and (c) amplitude spectra corresponding to the angular velocities shown in (a)

The natural frequencies of the drill string system obtained from the FEM and the five degrees-of-freedom lumped-parameter model in the present study were compared with those given in Jansen and van den Steen (1995), as illustrated in Table 4-3.

Table 4-3. Comparison between the torsional natural frequencies of the drill string obtained from the lumped-parameter and the FEM model

Natural frequencies	2 DOF lumped-parameter model (Jansen and van den Steen, 1995)	5 DOF lumped-parameter model	FEM model
f_1 (Hz)	0.178	0.178	0.192
f_2 (Hz)	−	0.815	0.838
f_3 (Hz)	−	1.447	1.595
f_4 (Hz)	−	1.876	2.368

The eigenvalues of the lumped-parameter model were extracted by solving Eq. (15) using MATLAB command '*d = eig(K,M)*' for the parameter values given in Table 4-2. The good agreement between the natural frequencies confirms the structural characteristics of the five degrees-of-freedom lumped-parameter model proposed in this study.

4.4.3. Field Test Verification

In this section, the FEM and lumped-parameter models developed in the present study were verified against the field test data published in Kyllingstad and Nessjøen (2009). The investigated system was a realistic drill-string model equipped with a proportional-integral (PI) speed controller, which effectively dampens the torsional oscillations at the stick-slip frequency. The drill string was approximately 3200 m long consisting of 2300 m drill pipe

with (D_p, d_p) = (0.1397, 0.1214) m, 800 m drill pipe with (D_p , d_p) = (0.127, 0.1086) m, and 100 BHA with (D_c, d_c) = (0.2032, 0.0635) m. The desired angular velocity was approximately 9.42 rad/s (9.42 × 60/2π = 90 rpm).

Figure 4-12 shows comparison between the simulation results and the field drilling test. It is noted that the time interval $0 \leq t \leq 40$ s in the pots represents the time interval $4200 \leq t \leq 4240$ s in Kyllingstad and Nessjøen (2009) corresponding to steady-state stick-slip oscillations of the field test. According to the figure, the maximum peak-to-peak angular velocity obtained from the lumped-parameter model, the FEM model, and the field test was 19.74, 21.50, and 21.67 rad/s, respectively. This indicates that the FEM response comes closer in agreement with the field/experimental results, which has been also reported in previous investigations (e.g., Kapitaniak et al., 2015). The agreement between performed simulations and field test was further confirmed by spectral analysis of the bit angular velocity using FFT for these cases. The stick-slip frequency obtained from both the FEM and the lumped parameter models was 0.2 Hz (5 s), which was in good agreement with the stick-slip frequency of the field test 0.189 Hz (5.3 s) for this particular drill string.

It is important to note that, although differences were observed, a fairly good match was achieved between the simulation results and the field test. The difference between simulation results and field test may be related to the bit-rock interface parameters. Due to the restriction on the availability of only surface measurements (Vromen et al., 2017), these parameters were obtained from other studies (e.g., Navarro-López and Cortes, 2007). A better agreement between the simulation results and the field test can be obtained if the bit-rock related parameters are validated based on downhole field measurements.

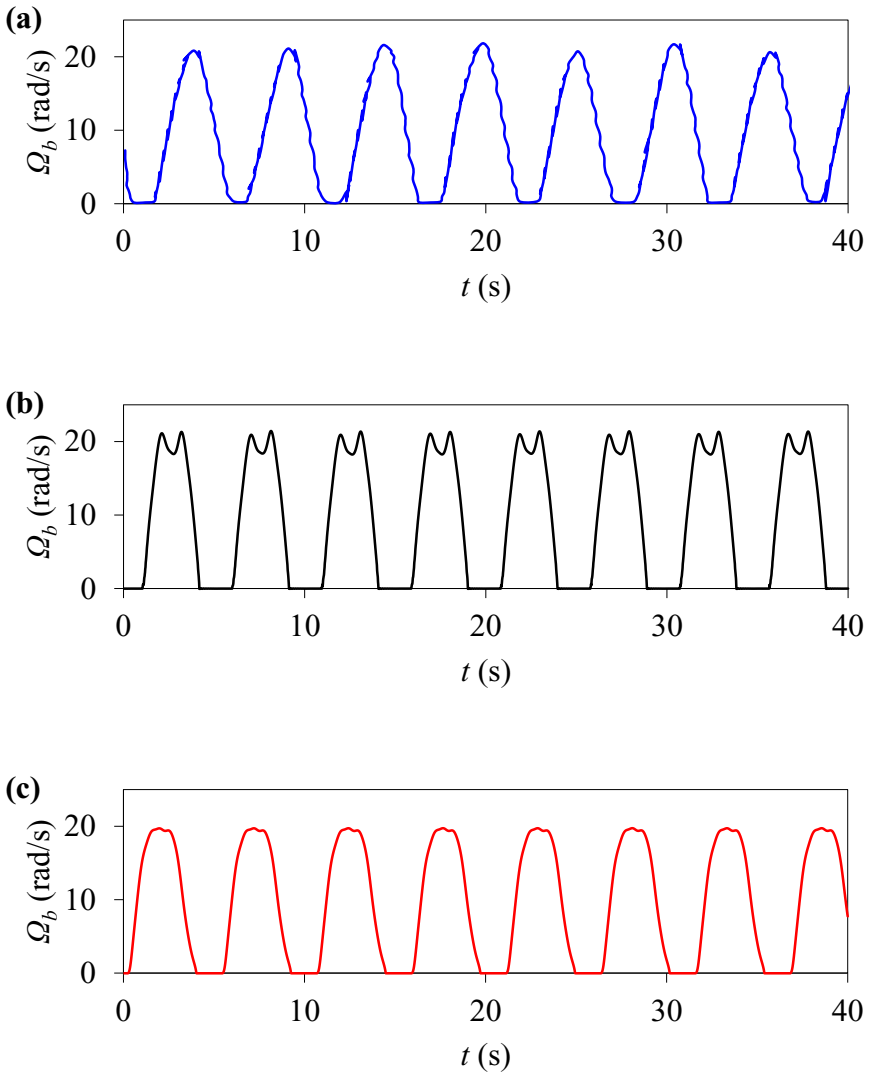

Figure 4-12. Example of stick-slip vibration occurring in the field test under constant rotational velocity Ω_r = 9.42 rad/s. (a) Field test result from Kyllingstad and Nessjøen (2009), (b) FEM simulation, and (c) 5 DOF lumped-parameter model

4.5. Summary and Conclusion

In this paper, an efficient approach of three-dimensional, nonlinear FE modeling was developed to predict the vibrations of full drill string. The torsional behavior of the entire drill string was efficiently captured by incorporation of the highly nonlinear bit-rock interaction and the viscous mud damping effect along the drill pipes and drill collars. An alternative approach was proposed based on the velocity-weakening response of the torque-on-bit that has been observed in the published data. The contact at the bit-rock interface was modeled, and the effect of cutting and friction was captured. A modal analysis was conducted to estimate the eigenfrequencies and the mode shapes of the drill string system using a linear perturbation frequency analysis. A procedure was proposed for proper selection of Rayleigh damping coefficients in order to retain the effect of higher vibration modes of the drill string. A nonlinear torsional lumped-parameter model of the full drill string was adopted considering the dynamics of the drill pipes, the drill collars, and the drill bit, accounting for the bit-rock interaction and the equivalent mud damping. The performance of the developed FEM model was compared with the lumped-parameter model. It was observed that the numerical stick-slip simulation was in close agreement with field and experimental observations. The developed model properly captured the limit cycling behavior of the stick-slip vibrations, the torque-on-bit reduction with bit angular velocity, and the backward rotations of the bit. The analysis identified a self-excited torsional vibration at a fundamental frequency of 0.14 Hz, which is much lower than the first natural torsional frequency of the drill string, i.e., 0.192 Hz. For certain operating

parameters, the proposed lumped parameter model could predict the dynamic characteristics of the system under stick-slip vibrations.

To verify the accuracy of the developed models in this study, a comparison was made between the field test example of stick-slip oscillation and the numerical results obtained from the FEM and the lumped-parameter models. It was shown that the FEM model provided good quantitative and qualitative agreements with the field test both in terms of the amplitude and the frequency of stick-slip vibration.

The study showed that the developed numerical model is computationally efficient, accurate, and robust tool to assess the response of the entire drill string system under different operational conditions.

4.6. Acknowledgment

The authors gratefully acknowledge the financial support of this research by the Tourism, Culture, Industry and Innovation (TCII) of NL, Canada, through the Ignite funding program, the Memorial University of Newfoundland through VP start-up funding support, and the Mitacs though Globalink funding program.

References

ABAQUS/Explicit User's Manual, 2017. SIMULIA.

Abbassian, F., Dunayevsky, V.A., 1998. Application of stability approach to torsional and lateral bit dynamics. SPE Drilling Completion. 13(2), 99–107. https://doi.org/10.2118/30478-PA

Axisa, F., Antunes, J., 1992. Flexural vibration of rotors immersed in dense fluids: part I – theory. J. Fluids Struct. 6(1), 3–21. https://doi.org/10.1016/0889-9746(92)90052-5

Bakhtiari-Nejad, F., Hosseinzadeh, A., 2017. Nonlinear dynamic stability analysis of the coupled axial-torsional motion of the rotary drilling considering the effect of axial

rigid–body dynamics. Int. J. Non-Linear Mech. 88, 85–96. https://doi.org/10.1016/j.ijnonlinmec.2016.10.011

Banerjee, A.K., Dickens, J., 1990. Dynamics of an arbitrary flexible body in large rotation and translation. J. Guid. Control Dyn. 13 (2), 221–7. https://doi.org/10.2514/3.20540

Brett, J. F., 1992. The Genesis of Bit-Induced Torsional Drillstring Vibrations. Society of Petroleum Engineers. https://doi.org/10.2118/21943-PA

Challamel, N., Sellami, H., Chenevez, E., Gossuin, L., 2000. A Stick-slip Analysis Based on Rock/Bit Interaction: Theoretical and Experimental Contribution. Society of Petroleum Engineers. https://doi.org/10.2118/59230-MS

Chen, S.L., Blackwood, K., Lamine, E., 2002. Field investigation of the effects of stick-slip, lateral and whirl vibrations on roller-cone bit performance. SPE Drilling and Completion. 17 (1), 15–20. https://doi.org/10.2118/76811-PA

Chevallier, A.M., 2001. Nonlinear stochastic drilling vibrations. Diss., Rice University. https://hdl.handle.net/1911/17946

Chopra, A.K., McKenna, F., 2016. Modeling viscous damping in nonlinear response history analysis of buildings for earthquake excitation. Earthq. Eng. Struct. Dyn. 45, 193–211. https://doi.org/10.1002/eqe.2622

Christoforou, A.P., Yigit, A.S., 1997. Dynamic modeling of rotating drillstrings with borehole interactions. J. Sound Vib. 206(2), 243–260. https://doi.org/10.1006/jsvi.1997.1091

de Pina, E.P.F., Carvalho, M.S., 2006. Three-Dimensional Flow of a Newtonian Liquid Through an Annular Space with Axially Varying Eccentricity. ASME. J. Fluids Eng. 128 (2), 223–231. https://doi.org/10.1115/1.2170126

Detournay, E., Defourny, P., 1992. A Phenomenological Model for the Drilling Action of Drag Bits. Int. J. Rock Mech. Min. Sci. Geomech. Abstr. 29, 13–23. https://doi.org/10.1016/0148-9062(92)91041-3

Detournay, E., Richard, T., Shepherd, M., 2008. Drilling Response of Drag Bits: Theory and Experiment. Int J. Rock Mech. Min. Sci. 45(8), 1347–1360. https://doi.org/10.1016/j.ijrmms.2008.01.010

Escudier, M.P., Gouldson, I.W., Oliveira, P.J., Pinho, F.T., 2000. Effects of inner cylinder rotation on laminar flow of a Newtonian fluid through an eccentric annulus. Int. J. Heat Fluid Flow. 21 (1), 92–103. https://doi.org/10.1016/S0142-727X(99)00059-4

Escudier, M.P., Oliveira, P.J., Pinho, F.T., 2002. Fully developed laminar flow of purely viscous non-Newtonian liquids through annuli, including the effects of eccentricity and inner-cylinder rotation. Int. J. Heat Fluid Flow. 23(1), 52–73. https://doi.org/10.1016/S0142-727X(01)00135-7

Finnie, I., Bailey, J.J., 1960. An experimental study of drill-string vibration. ASME J. Eng. Ind. 82 (2), 129–135. https://doi.org/10.1115/1.3663020

Fu, Z.F., He, J., 2001. Modal Analysis, Elsevier Science & Technology.

Germay, C., Denol, V., Detournay, E., 2009. Multiple mode analysis of the self-excited vibrations of rotary drilling systems. J. Sound Vib. 325(1–2), 362–81. https://doi.org/10.1016/j.jsv.2009.03.017

Ghasemloonia, A., Geoff Rideout, D., Butt, S.D., 2013. Vibration Analysis of a Drillstring in Vibration-Assisted Rotary Drilling: Finite Element Modeling With Analytical Validation. ASME. J. Energy Resour. Technol. 135(3): 032902. https://doi.org/10.1115/1.4023333

Gourdon, D., Israelachvili, J.N., 2003. Transitions between smooth and complex stick-slip sliding of surfaces. Phys. Rev. E 68, 021602. 10.1103/PhysRevE.68.021602

Halsey, G.W., Kyllingstad, A., Kylling, A., 1988. Torque Feedback Used to Cure Slip-Stick Motion. Society of Petroleum Engineers. https://doi.org/10.2118/18049-MS

Hovda, S., 2018. Automatic detection of abnormal torque while reaming. J. Pet. Sci. Eng. 166, 13–24. https://doi.org/10.1016/j.petrol.2018.02.050

Jansen, J.D., 1991. Nonlinear rotor dynamics as applied to oil well drillstring vibrations. J. Sound Vib. 147 (1), 115–135. https://doi.org/10.1016/0022-460X(91)90687-F

Jansen, J.D., van den Steen, L., 1995. Active damping of self-excited torsional vibrations in oil well drillstrings. J. Sound Vib. 179 (4), 647–668. https://doi.org/10.1006/jsvi.1995.0042

Kapitaniak, M., Vaziri Hamaneh, V., Chávez, J.P., Nandakumar, K., Wiercigroch, M., 2015. Unveiling complexity of drill-string vibrations: experiments and modelling. Int. J. Mech. Sci. 101–102, 324–337. https://doi.org/10.1016/j.ijmecsci.2015.07.008

Karnopp, D., 1985. Computer simulation of stick–slip friction in mechanical dynamic systems. ASME J Dyn Syst Meas Control. 107(1), 100–103. https://doi.org/10.1115/1.3140698

Khulief, Y.A., Al-Sulaiman, F.A., Bashmal, S., 2007. Vibration analysis of drillstrings with self-excited stick–slip oscillations. J. Sound Vib. 299, 540–558. https://doi.org/10.1016/j.jsv.2006.06.065

Kyllingstad, A., Nessjøen, P.J., 2009. A New Stick-Slip Prevention System. Society of Petroleum Engineers. https://doi.org/10.2118/119660-MS

Leine, R.I., van Campen, D.H., de Kraker, A., van den Steen, L., 1998. Stick–slip vibrations induced by alternate friction models. Nonlinear Dyn. 16, 41–54. https://doi.org/10.1023/A:1008289604683

Leine, R.I., van Campen, D.H., Keultjes, W.J.G., 2002. Stick–slip whirl interaction in drill–string dynamics. J Vib. Acoust. 124 (2), 209–220. https://doi.org/10.1115/1.1452745

Liao, C.M., Vlajic, N., Karki, H., Balachandran, B., 2012. Parametric studies on drill-string motions. Int. J. Mech. Sci. 54 (1), 260–268. https://doi.org/10.1016/j.ijmecsci.2011.11.005

Lin, Y.Q., Wang, Y.H., 1991. Stick-slip vibration of drillstrings. ASME J. Eng. Ind. 113 (1), 38–43. https://doi.org/10.1115/1.2899620

Liu, M., Gorman, D.G., 1995. Formulation of Rayleigh damping and its extensions. Computers and Structures. 57 (2), 277–285. https://doi.org/10.1016/0045-7949(94)00611-6

Liu, X., Vlajic, N., Long, X., Meng, G., Balachandran, B., 2013. Nonlinear motions of a flexible rotor with a drill bit: stick-slip and delay effects. Nonlinear Dyn. 72 (1–2), 61–77. https://doi.org/10.1007/s11071-012-0690-x

Liu, X., Vlajic, N., Long, X., Meng, G., Balachandran, B., 2014. State-Dependent Delay Influenced Drill-String Oscillations and Stability Analysis. ASME. J. Vib. Acoust. 136 (5): 051008. https://doi.org/10.1115/1.4027958

MacDonald, K.A., Bjune, J.V., 2007. Failure analysis of drill strings. Eng. Fail. Anal. 14, 1641–1666. https://doi.org/10.1016/j.engfailanal.2006.11.073

Mihajlovic, N., van Veggel, A.A., van de Wouw, N., Nijmeijer, H., 2004. Analysis of friction-induced limit cycling in an experimental drill-string system. ASME J. Dyn. Syst Meas Control. 126, 709-720. https://doi.org/10.1115/1.1850535

Navarro-López, E.M., Cortes, D., 2007. Avoiding harmful oscillations in a drillstring through dynamical analysis. J. Sound Vib. 307, 152–171. https://doi.org/10.1016/j.jsv.2007.06.037

Nessjøen, P.J., Kyllingstad, A., Dambrosio, P., Fonseca, I.S., Garcia, A., Levy, B., 2011. Field Experience with an Active Stick-Slip Prevention System. Society of Petroleum Engineers. https://doi.org/10.2118/139956-MS

Oden, J.T., Martins, J.A.C., 1985. Models and computational methods for dynamic friction phenomena. Computer Methods in Applied Mechanics and Engineering, 52 (1–3), 527–634. https://doi.org/10.1016/0045-7825(85)90009-X

Païdoussis, M.P., Luu, T.P., Prabhakar, S., 2008. Dynamics of a long tubular cantilever conveying fluid downwards, which then flows upwards around the cantilever as a confined annular flow, J. Fluids Struct. 24 (1), 111–128, https://doi.org/10.1016/j.jfluidstructs.2007.07.004

Païdoussis, M.P., Semler, C., 1998. Non-linear dynamics of a fluid-conveying cantilevered pipe with a small mass attached at the free end. Int. J. Non Linear Mech. 33 (1) 15–32, https://doi.org/10.1016/S0020-7462(97)00002-4

Pavone, D.R., Desplans, J.P., 1994. Application of high sampling rate downhole measurements for analysis and cure of stick–slip in drilling. Society of Petroleum Engineers. https://doi.org/10.2118/28324-MS

Rao, S.S., 2011. Mechanical vibrations, fifth ed., Pearson.

Rayleigh, L., 1945. Theory of Sound, 1. Dover: New York, NY.

Richard, T., Detournay, E., 2000. Stick-Slip Vibrations of PDC Bits. American Rock Mechanics Association.

Richard, T., Germay, C., Detournay, E., 2007. A simplified model to explore the root cause of stick-slip vibrations in drilling systems with drag bits. J. Sound Vib. 305 (3), 432–56. https://doi.org/10.1016/j.jsv.2007.04.015

Ritto, T.G., Soize, C., Sampaio, R., 2009. Non-linear dynamics of a drill–string with uncertain model of the bit–rock interaction. Int. J. Non-Linear Mech. 44, 865–76. https://doi.org/10.1016/j.ijnonlinmec.2009.06.003

Sampaio, R., Piovan, M.T., Lozano, G.V., 2007. Coupled axial/torsional vibrations of drill-strings by means of non-linear model. J. Mech. Res. Commun. 34, 497–502. https://doi.org/10.1016/j.mechrescom.2007.03.005

Sepehri, N., Sassani, F., Lawrence, P.D., Ghasempoor, A., 1996. Simulation and experimental studies of gear backlash and stick-slip friction in hydraulic excavator swing motion. ASME J Dyn. Syst. Meas. Control. 118, 463–467. https://doi.org/10.1115/1.2801168

Spanos, P.D., Payne, M.L., Secora, C.K., 1997. Bottom-hole assembly modeling and dynamic response determination. ASME J. Energy Resour. Technol. 119(3), 153–158. https://doi.org/10.1115/1.2794983

Trindade, M., Sampaio, R., 2002. Dynamics of beams undergoing large rotations accounting for arbitrary axial rotations. J. Guid. Control Dyn. 25 (4), 634–43. https://doi.org/10.2514/2.4957

Vlajic, N., Fitzgerald, T., Nguyen, V., Balachandran, B., 2014a. Geometrically exact planar beams with initial pre-stress and large curvature: Static configurations, natural frequencies, and mode shapes. Int. J. Solids Struct. 51 (19–20), 3361–3371. https://doi.org/10.1016/j.ijsolstr.2014.05.026

Vlajic, N., Liu, X., Karki, H., Balachandran, B., 2014b. Torsional oscillations of a rotor with continuous stator contact. Int. J. Mech. Sci. 83, 65–75. https://doi.org/10.1016/j.ijmecsci.2014.03.025

Vlasov, V.Z., 1961. Thin Walled Elastic Beams, second ed., National Science Foundation, Washington, DC, Israel Program for Scientific Translation, Jerusalem, Israel [First edition – Stroizdat (in Russian) Moscow, 1940].

Vromen, T., van de Wouw, N., Doris, A., Astrid, P., Nijmeijer, H., 2017. Nonlinear output-feedback control of torsional vibrations in drilling systems. Int. J. Robust Nonlinear Control. 27, 3659– 3684. https://doi.org/10.1002/rnc.3759

Yigit, A.S., Christoforou, A.P., 2006. Stick-Slip and Bit-Bounce Interaction in Oil-Well Drillstrings. ASME J. Energy Resour. Technol. 128 (4), 268–274. https://doi.org/10.1115/1.2358141

5. Chapter 5

Numerical Investigation of the Nonlinear Drill String Dynamics under Stick-Slip Vibration

Mohammad Javad Moharrami[1], Hodjat Shiri[2], Clóvis de Arruda Martins[3]

1: Department of Civil Engineering
Memorial University of Newfoundland
e-mail: mjmoharrami@mun.ca

2: Department of Civil Engineering
Memorial University of Newfoundland
e-mail: hshiri@mun.ca

3: Department of Mechanical Engineering
University of São Paulo, Brazil
e-mail: cmartins@usp.br

This chapter is an under-review (revision submitted) journal manuscript.

Abstract

This paper presents a comprehensive analysis of the influence of the field operating parameters on the structural dynamic response of the full-scaled drill string under stick-slip vibration. The analysis allows for studying the qualitative and quantitative variation of the stick-slip response of the drill pipes and bottom-hole assembly (BHA) under varying rotational velocity, weight-on-bit, and viscous damping. To achieve this goal, a robust and practical finite element (FE) model of the full-scaled drill string was developed based on a velocity-weakening formulation of the nonlinear bit-rock interaction. The nonlinear Timoshenko beam (shear deformable) was used to model both drill pipes and drill collars. The model accounts for the nonlinear effects of large rotational displacements, the geometrically nonlinear axial-torsional coupling effects, as well as the axial and torsional stiffness of the drill pipes and drill collars. The effect of fluid damping acting along the drill pipes and drill collars was modeled using the Rayleigh method. A detailed investigation of damping parameters was carried out. Parametric studies on the stick-slip response of the entire drill string under different field operational conditions were conducted. The dynamical time-series of the system response were analyzed in terms of the response spectra and descriptive statistics of the drill pipes and drill collars. Comparisons were made between the developed numerical model and a lumped-parameter model. The conducted research work revealed new dynamic characteristics of the entire drill string with regard to stick-slip vibration, providing insight into the behavior of the drill pipes and drill collars under different operating conditions.

Keywords: Drill string dynamics; Nonlinear vibrations; Stick-slip; Bit-rock interaction; Rayleigh viscous damping; Finite element modeling, Spectral analysis.

5.1. Introduction

Rotary drilling system is used in deep-water oil and gas extraction. The essential part of such a system is called drill string, compromising mainly of thin-walled drill pipes, thick-walled drill collars, and the drill bit (Jansen and van den Steen, 1995; Nandakumar, M. Wiercigroch, 2013). The main function of the drill string is to transfer the surface rotary motion from the drive system to the drill bit, as well as to provide the axial force, known as weight-on-bit (WOB), for an efficient cutting process in the borehole (Jansen and van den Steen, 1995). Figure 5-1. shows an offshore drilling vessel and the basic components of the drill string.

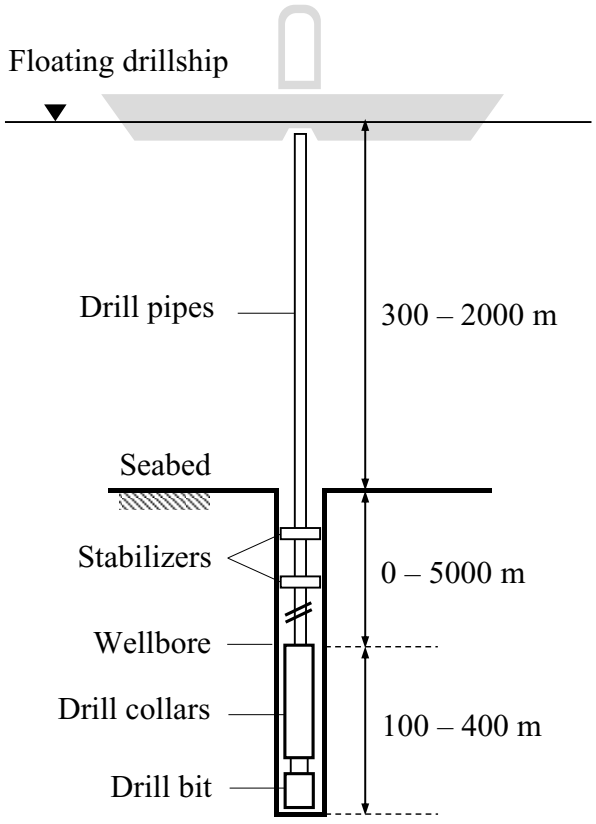

Figure 5-1. Schematic of a typical offshore drilling system

The length of the drill string inside the wellbore can be of several kilometers (Jansen and van den Steen, 1995). A significant length of the drill string is made of the drill pipes, which are under tension and transfer the top rotary motion to the drill bit. The lower end of the drill string called the bottom-hole assembly (BHA), is composed of various components, such as drill collars and stabilizers (MacDonald and Bjune, 2007). Drill collars are under compression and provide the required weight-on-bit to facilitate straight drilling (Chevallier, 2001). Due to its extreme slender structure, the drill string is vulnerable to destructive dynamical vibrations, which can result in fatigue damage and catastrophic field failures (MacDonald and Bjune, 2007). Raising from nonlinear bit-formation contact (Jansen and van den Steen, 1995; Brett, 1992; Halsey, 1988), the stick-slip vibration is the most severe type of torsional oscillation, detrimental to the life of drill string and downhole equipment (Jansen and van den Steen, 1995). These vibrations involve fluctuation in the bit angular velocity, ranging from zero up to twice the rotary table velocity (Chen et al., 2002). On the one hand, the high bit angular velocities during the slip phase can induce severe axial and lateral vibrations in the BHA, leading to excessive wear and even failure of the drill bit (Khulief et al., 2007). On the other hand, the high levels of torque-on-bit during the stick phase, varying between 500 and 10000 Nm, can twist the drill string for several turns (Jansen and van den Steen, 1995). The consequent large torsional deformation during the twisting can cause failure of the drill pipes or the threaded connections (MacDonald and Bjune, 2007).

Over the past decades, different modeling techniques have been used to investigate the distinct aspects of stick-slip vibration of the drill string and BHA. These techniques include lumped-parameter (Jansen and van den Steen, 1995; Yigit and Christoforou, 1998; Richard

et al., 2007; Navarro-López, D. Cortes, 2007; Liu et al., 2013), continuous-parameter (Cosserat theory of rods) (Tucker and Wang, 1999; Silveira, 2011), and FEM models (Khulief et al., 2007; Sampaio et al., 2007; Germay et al., 2009). The advantage of the FEM over the analytical models lies within appropriate treatment of complicated boundary conditions and forces, incorporating the geometrical nonlinearities inherent to the drill string structure, as well as considering the interplay between different vibration modes.

On the one hand, regarding the FEM models which have addressed the torsional stick-slip vibration of the full-scaled drill string, each author has used different approach, and ignored one or more aspects of the problem. The models of (Khulief et al., 2007; Sampaio et al., 2007; Germay et al., 2009) are based on linear Euler-Bernoulli beam, which does not account for the shear deformation. The model of (Khulief et al., 2007) does not account for damping, while the model of (Germay et al., 2009) neglects the geometric coupling between the axial and torsional vibrations. It is worth emphasizing that a detailed analysis of the damping in conjunction with FEM formulation is not considered in any of the above works. On the other hand, the majority of these studies have analyzed the dynamics of the drill string through the vibrations of the BHA. Even though BHA has a significant influence on the overall dynamic response of the system, the behavior of the drill pipes as an extremely slender structure has been extensively neglected in the literature and is yet to be understood. This is due to the complex nonlinear nature of the drill string-wellbore interaction and the resultant vibration modes, which impose further difficulties against proposing a simplified and robust solution for integrated dynamic system analysis of the entire drill string, incorporating both the drill pipes and drill collars.

Furthermore, the external parameters, i.e., operational conditions, can affect the nonlinear dynamical behavior of the drill string structure. Therefore, in order to predict the drilling performance under different operating conditions, a parametric study can be essential. Also the parametric study provides some insight into the field operating range of external parameters in order to avoid the harmful vibration modes, and obtain reliable and efficient drilling operation. One of the first attempts to investigate the drill string vibrations under varying operating conditions was presented in (Dareing and Livesay, 1968). The study, however, included uncoupled longitudinal vibration along the drill string in the absence of bit-rock excitation and contact forces. Parametric studies of the rotor-stator system behavior with regard to initial conditions (unbalanced mass, friction coefficient, and drive speed) was also presented in (Liao et al., 2012).

To that end, this paper analyzes the effect of rotary table velocity, weight-on-bit, and viscous mud damping on the torsional stick-slip vibration along the drill pipes and drill collars using a robust and efficient FE model. Due to the vital role of the viscous damping in the overall response of the system, special attention is paid to detailed analysis of damping.

In this paper, a comprehensive analysis of the dynamical behavior of the drill pipes and drill collars under different operating conditions was carried out, with particular attention to the drill pipe section. The investigation was performed under torsional stick-slip vibration. An integrated nonlinear numerical model was developed to obtain the dynamic responses along the drill string, taking into account the highly nonlinear bit-rock contact boundary condition. A computationally efficient approach was used to model the rate-dependent bit-rock contact interface and capture the cutting and friction effects. The

nonlinear Timoshenko beam was applied to model the drill string accounting for shear deformation, as well as axial and torsional stiffness of the drill pipes and drill collars. The axial and torsional vibrations were geometrically coupled, and the nonlinear effects of large rotations were taken into account. A linear perturbation frequency analysis was performed to estimate the eigenfrequencies of the drill string. A procedure was proposed for proper quantification of the Rayleigh damping coefficients to maintain the effect of higher vibration modes. The performance of the numerical model was verified against a five degree-of-freedom lumped parameter model. The developed lumped parameter model involved the dynamics of the drill pipes, drill collars, and drill bit, as well as the nonlinear bit-rock interaction and the equivalent mud damping along the string. The effect of rotary velocity, weight-on-bit, and damping ratio on the dynamical behavior of the entire drill string was examined. The dynamical response of the drill pipes was analyzed, quantitatively and qualitatively. The spectral analyses were carried out to determine the effect of operating parameters on the stick-slip frequency of the system. The descriptive statistics, i.e., mean, amplitude, and standard deviation of angular velocities along the drill string were computed for varying operational conditions. It was observed that the stick-slip frequency decreased with decreasing rotary velocity. The results indicated that the amplitude, mean, and standard deviation of the angular velocity of the drill pipes and drill collars/bit under stick-slip occurrence were largely related to the rotary velocity and its threshold value. Also the dominant frequency of stick-slip vibration was dependent on the rotary velocity. The results showed that the drill pipes can be excited at frequencies higher than the second natural vibration mode of the system, with noticeable amplitudes.

The results were in close qualitative agreement with field and experimental observations under stick-slip oscillation. The outcomes revealed new features of the overall torsional dynamics of the drill string as an integrated system.

5.2. Developing the FEM Model

A global three-dimensional FEM model was developed in ABAQUS/Explicit. The overall configuration and material properties were taken from a drill string structure as given in Table 5-1. The slenderness feature of the drill string, that is, the ratio diameter divided by length less than 0.1 (Vlasov, 1961), implies that the three-dimensional continuum drill string can be modeled using one-dimensional beam elements. Thus, the two-node linear interpolation beam element B31 (Timoshenko beam) (ABAQUS, 2017) was employed to model both the drill pipes and drill collars. The B31 is a one-dimensional line element in three-dimensional space that has stiffness associated with axial deformation, bending, and torsion (ABAQUS, 2017). Each node has six degrees-of-freedom; three translational and three rotational. Using the beam elements in modeling the drill string leads to a significant reduction in the computational time and costs of the simulation, yet maintaining a good accuracy of the model response. As the tool joints have negligible effect on the axial and torsional vibrations (Bradbury and Wilhoit, 1963), the drill pipe was modeled with a uniform cross-sectional area. The consideration of geometrical nonlinearities is vital in dynamics of structures and drill string systems (Sampaio et al., 2007; Trindade and Sampaio, 2002; Banerjee and Dickens, 1990). Therefore, the effect of geometric nonlinearities, i.e., large rotational displacements and geometric coupling between the axial and torsional vibration modes, were taken into account. Figure 5-2. shows the overall

configuration of the modeled drill string, where x, y, and z are the translational degrees of freedom, whereas ϕ_x, ϕ_y, and ϕ_z are the rotational degrees of freedom around x, y, and z axes, respectively.

Table 5-1. Geometry and material properties of the drill string (Jansen and van den Steen, 1995)

Parameter	Variable	Value	Unit
Drill pipe specification			
Drill pipe length	L_p	2000	m
Drill pipe outer diameter	D_p	0.1270	m
Drill pipe inner diameter	d_p	0.1086	m
Drill collar specification			
Drill collar length	L_c	150	m
Drill collar outer diameter	D_c	0.2286	m
Drill collar inner diameter	d_c	0.0762	m
Material specification			–
Steel density	ρ	7850	kg/m^3
Young´s modulus	E	2×10^{11}	N/m^2
Shear modulus	G	7.96×10^{10}	N/m^2

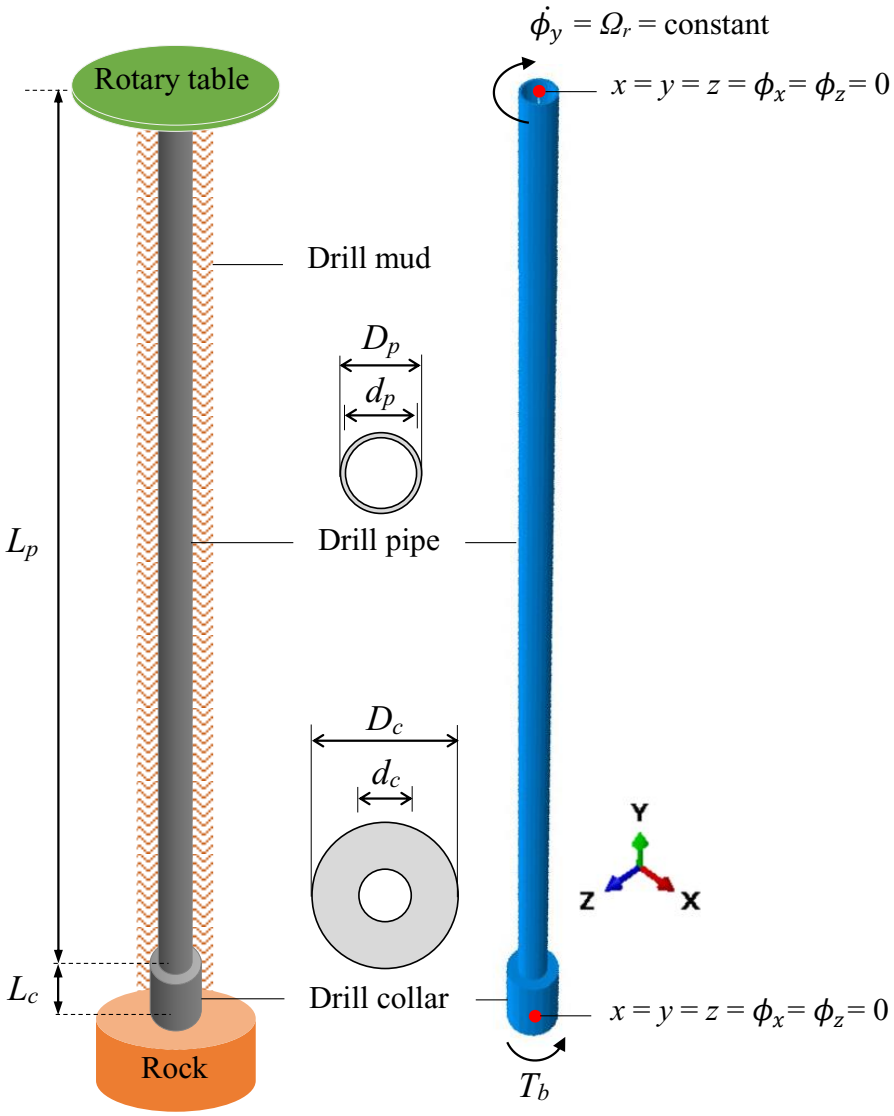

Figure 5-2. A sketch of the considered full drill string (left) and the corresponding FEM model developed in ABAQUS with boundary conditions at the surface and the bit (right), where ϕ_x, ϕ_y, and ϕ_z denote the rotational degrees of freedom around x, y, and z axes, respectively

Classically, for a static weight-on-bit, the bit-rock contact interface is characterized by a frictional torque decreasing with the bit angular velocity (Richard and Detournay, 2000). The nonlinear velocity-weakening behavior of the torque-on-bit has been observed in the

field and laboratory drilling experiments (Brett, 1992; Abbassian and Dunayevsky, 1998; Pavone and Desplans, 1994), and is often considered as the primary cause of the drill bit stick-slip oscillations. ABAQUS/Explicit provides the kinematic and penalty contact models. However, the inherent nonlinearity of the contact interface leads to computational challenges and convergence issues. As an alternative approach, to avoid extreme difficulties in contact analysis, and efficiently employ the beam elements to minimize the computational cost, the frictional contact at the bit-rock interface was modeled through an equivalent frictional moment. The normal and shear force components at the contact interface were described using the Coulomb friction model. The frictional torque-on-bit T_b was then expressed as follows:

$$T_b = \begin{cases} M, & if\ |M| < T_0 \text{ (stick mode)}, \\ M_{sl}, & otherwise \text{ (slip mode)}. \end{cases} \quad (1)$$

where M is the magnitude of all frictional moments acting on the bit (drill collar's end) about the longitudinal axis (tangent to the bit-rock contact surface), $T_0 = \mu_s R_b W_b$ is the break-away moment (maximum static friction torque), $M_{sl} = \mu(\dot{\phi}_b) R_b W_b$ is the sliding friction moment about the longitudinal axis, R_b is the bit radius, $W_b > 0$ is the weight-on-bit, and $\mu(\dot{\phi}_b)$ is the Static-Kinetic Exponential Decay friction formulation defined as follows:

$$\mu(\dot{\phi}_b) = \left[\mu_c + (\mu_s - \mu_c) e^{-\gamma|\dot{\phi}_b|}\right] \quad (2)$$

where $\dot{\phi}_b = \Omega_b$ is the bit angular velocity, μ_c and μ_s are the kinetic (Coulomb) and static friction coefficients, respectively, and $\gamma > 0$ is the constant decay coefficient. It is noted that μ_s can be greater than one depending on the surfaces, while $\mu_c \in (0, 1)$ and $\mu_s > \mu_c$.

A mesh of 96 elements (64 on the pipe and 32 on the collar section) with a uniform discretization was used. To accurately capture the stick-slip vibration due to bit-rock contact, the element size on the collar section was set to be smaller than the pipe section. The selection of the mesh size was based on a mesh sensitivity analysis, which confirmed convergence of the solution and satisfactory accuracy of the numerical results for the entire drill string.

The first 500 undamped natural frequencies and the corresponding mode shapes of the drill string were extracted using the Lanczos linear perturbation method (ABAQUS, 2017). The criterion of extracting 500 natural modes was to obtain at least ten natural torsional frequencies of the drill string. The boundary condition at the upper end (rotary table) was completely fixed, while the lower end (bit) was only free to rotate about the longitudinal axis of the string. The obtained natural frequencies of the system are given in Table 5-2.

Table 5-2. Torsional natural frequencies of the drill string

Mode number	Natural frequency	Natural frequency,	Normalized natural frequency
n	ω_n (rad/s)	f_n (Hz)	ω_n/ω_1
1	1.206	0.192	1.00
2	5.264	0.838	4.37
3	10.022	1.595	8.31
4	14.876	2.368	12.34
5	19.749	3.143	16.38
6	24.621	3.919	20.42
7	29.484	4.693	24.46
8	34.330	5.464	28.48
9	39.156	6.232	32.48
10	43.956	6.996	36.46

The viscous damping stemming from drill mud has a crucial role in the drill string dynamics. The fundamental frequency of the self-excited torsional vibration has been shown to change due to the presence of internal/external mudflow (Ritto et al., 2009). Also, increasing the torsional damping has been found to disfavor the stick-slip oscillation (Jansen and van den Steen, 1995; Dawson et al., 1987; Kyllingstad and Halsey, 1988), and extend the upper boundary of the stable operating region of the drill string (Nandakumar and Wiercigroch, 2013; Zamanian et al., 2007; Liu et al., 2014; Bakhtiari-Nejad and Hosseinzadeh, 2017). Therefore, proper modeling of viscous damping is essential to the dynamical behavior of the system and more realistic results. Obtaining the actual mud damping, however, is a challenging process. Moreover, no practical method has been

addressed to form the physical damping matrix through finite element analysis (Liu and Gorman, 1995).

In this paper, the viscous mud damping was modeled using the frequency-dependent Rayleigh damping, which is the most common way of incorporating viscous damping effects in numerical models. The standard form of the Rayleigh damping is defined as a linear combination of mass matrix M and stiffness matrix K, as follows (Rayleigh, 1945; Chopra and McKenna, 2016):

$$C = \alpha M + \beta K \tag{3}$$

where the constant values α and β are the mass proportional and the stiffness proportional coefficients, respectively. The coefficients α and β are evaluated from the two target frequencies ω_i and ω_j corresponding to the i-th and j-th natural modes of the system, respectively, and the prescribed modal damping ratio ξ, as follows:

$$\alpha = \xi \frac{2\omega_i \omega_j}{\omega_i + \omega_j}, \beta = \xi \frac{2}{\omega_i + \omega_j} \tag{4}$$

where $\omega = 2\pi f$.

A disadvantage of the Rayleigh damping is that the achieved damping ratio varies with response frequency. Therefore, in order to at least minimize the variation of the damping ratio over the intermediate modes, a preliminary study was carried out to determine the appropriate target frequencies. Figure 5-3. shows the result of Rayleigh damping variation over different frequency bands (i.e., 0.19 – 0.80 Hz, 0.19 – 1.59 Hz, 0.19 – 3.18 Hz, and 0.19 – 6.37 Hz).

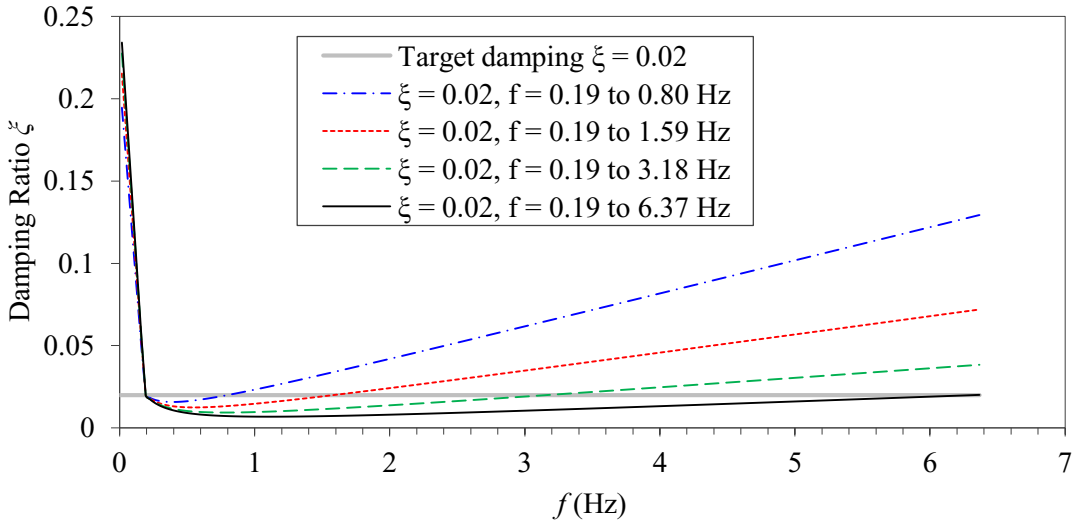

Figure 5-3. Effect of frequency band on the Rayleigh damping variations

The results indicate that choosing a narrow frequency band (i.e., 0.19 – 0.80 Hz) leads to damping ratios immensely larger than the target damping for high-frequency responses, the so-called de-amplification effect. However, picking a wider frequency band results in damping ratios smaller than the target damping for high-frequency modes. Thus, α and β were determined by using f_1 and f_{10} (see Table 5-2.) as the target frequencies in order to minimize the frequency-dependent damping variations, as well as to maintain the high-frequency torsional vibration, which has been reported in previous investigations (Germay et al., 2009; Nessjoen et al., 2011). This broad frequency band gave a conservative underdamped system for intermediate modes, which is more favourable than a non-conservative overdamped system, particularly in fatigue assessment of the drill string system.

5.3. Model Validation

The five degrees-of-freedom lumped-parameter model shown in Figure 5-4. was used to make comparisons with the numerical model. The model is capable of capturing the vibrations along the entire drill string, namely, drill pipes and drill collars. The corresponding set of equations of motion are as follows:

$$\begin{cases} k_p(\phi_r - \phi_1) - T_r = 0 \\ J_p\ddot{\phi}_1 + c_p\dot{\phi}_1 + k_p(\phi_1 - \phi_r) + k_p(\phi_1 - \phi_2) = 0 \\ J_p\ddot{\phi}_2 + c_p\dot{\phi}_2 + k_p(\phi_2 - \phi_1) + k_p(\phi_2 - \phi_3) = 0 \\ J_p\ddot{\phi}_3 + c_p\dot{\phi}_3 + k_p(\phi_3 - \phi_2) + k_p(\phi_3 - \phi_b) = 0 \\ J_b\ddot{\phi}_b + c_b\dot{\phi}_b + k_p(\phi_b - \phi_3) + T_b = 0 \end{cases} \quad (5)$$

where ϕ_r, ϕ_1, ϕ_2, ϕ_3, ϕ_b are the angular displacements of the rotary table, drill pipe 1, drill pipe 2, drill pipe 3, and drill collars/bit, respectively, $T_r = k_p(\phi_r - \phi_1)$ is the torque delivered by the rotary table to the drill string ($T_r > 0$), and T_b is a nonlinear function representing the frictional torque-on-bit. The model parameters J_p, J_c, J_b, are the mass moments of inertia of drill pipe, drill collar, and drill bit, respectively, and k_p is the torsional stiffness of drill pipe, given by:

$$J_p = \rho I_p(L_p/4), J_c = \rho I_c L_c, J_b = J_c + J_p/2, k_p = GI_p/(L_p/4) \quad (6)$$

with

$$I_p = (\pi/32)(D_p^4 - d_p^4), I_c = (\pi/32)(D_c^4 - d_c^4) \quad (7)$$

where I_p and I_c are the polar moments of inertia of the drill pipe and the drill collar section, respectively. c_p and c_b are the equivalent viscous damping coefficients of drill pipe and drill collars/bit, respectively, given by:

$$c_p = \hat{c}(L_p/4), c_b = \hat{c}(L_p/8) \quad (8)$$

where $\hat{c}$ is the viscous damping coefficient per unit length of the drill pipe.

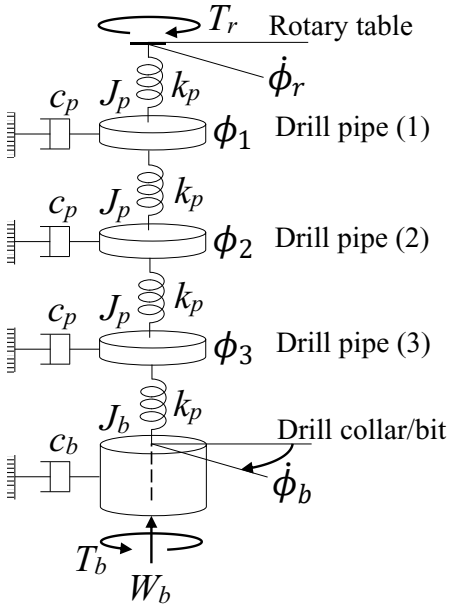

Figure 5-4. Lumped-parameter model representation of the drill string

The frictional torque-on-bit T_b was modeled as a combination of the Karnopp model (Karnopp, 1985) and the Stribeck effect (negatively sloped friction at the slip phase), through a variable structure proposed in Refs. (Navarro-López and Cortes, 2007; Sepehri et al., 1996; Leine et al., 1998); see Figure 5-5.. Thus,

$$T_b = \begin{cases} T_{st}\,, if\ \left|\dot{\phi}_b\right| < V_d\ \ and |T_{st}| \le T_0 \text{ (stick mode)}, \\ T_0 sgn(T_{st})\,, if\ \left|\dot{\phi}_b\right| < V_d\ \ and\ |T_{st}| > T_0 \text{ (transition from stick to slip)}, \\ T_{sl} sgn\left(\dot{\phi}_b\right), if\ \left|\dot{\phi}_b\right| \ge V_d \text{ (slip mode)}. \end{cases} \tag{9}$$

with

$$T_{st} = -c_b\dot{\phi}_b - k_p(\phi_b - \phi_3),\ T_0 = \mu_s R_b W_b,\ T_{sl} = \mu\left(\dot{\phi}_b\right) R_b W_b \tag{10}$$

where $V_d > 0$ is the threshold velocity, T_{st} is the reaction torque during the stick phase that must overcome the break-away torque to make the bit move, T_0 is the break-away torque (maximum static friction torque), T_{sl} is the sliding friction torque, R_b is the bit radius, $W_b >$

0 is the weight-on-the bit, and $\mu(\dot{\phi}_b)$ is the bit exponential-decay friction coefficient defined in Eq. (2). The exponential decaying behavior of the torque-on-bit (Stribeck effect) is in agreement with the field and experimental observations (Brett, 1992; Abbassian and Dunayevsky, 1998; Pavone and Desplans, 1994).

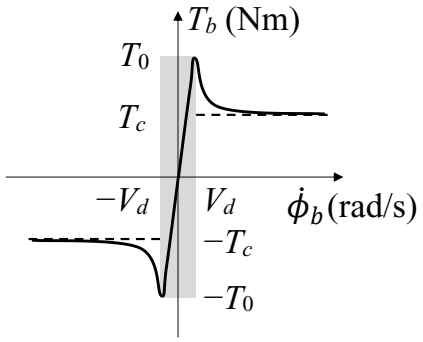

Figure 5-5. Friction model at the bit: switch friction model (enhanced Karnopp friction model) + Stribeck model

The drill string vibration obtained from the numerical model was compared with the lumped-parameter model. The simulations were carried out for Ω_r = 7.33 rad/s (7.33 × 60/2π = 70 rpm), which is within the common field operating range, W_b = 40 kN, and ξ = 0.03. The model parameters are given in Table 5-3. The equations of motion (Eqs. (5) and (6)) were numerically integrated using the 4th-5th order Runge-Kutta method with variable time steps through the built-in function 'ode45' in MATLAB. The initial condition for all state variables (except Ω_r), was taken as zero. To achieve damping ratio ξ = 0.03, the viscous damping coefficient per unit length of drill pipes $\hat{c}$ = 0.0378 Ns/rad was used (adapted from Jansen and van den Steen, 1995).

Table 5-3. Model parameters computed for the full drill string configuration given in Table 5-1

Quantity	Variable	Value	Unit
Mass moment of inertia of drill pipe	J_p	46.6438	kgm^2
Mass moment of inertia of bit	J_b	335.1180	kgm^2
Torsional stiffness of drill pipe	k_p	1891.8971	Nm/rad
Equivalent viscous damping coefficient for drill pipe	c_p	18.9	Nms/rad
Equivalent viscous damping coefficient for drill collars/bit	c_b	9.45	Nms/rad
Bit radius	R_b	0.1555	m
Static friction coefficient	μ_s	0.8	–
Kinetic (Coulomb) friction coefficient	μ_c	0.5	–
Decay coefficient	γ	0.9	–
Threshold velocity	V_d	1×10^{-6}	–

Figure 5-6. presents the comparative evaluation between the models' performance under stick-slip condition. There is an excellent agreement between the results. The FEM model exhibits variations in the stick-slip amplitude, while the lumped-parameter model shows oscillations with almost constant amplitude. This indicates that that the FEM response comes closer in agreement with the field and experimental results, as reported in previous investigations (see, e.g., Kapitaniak et al., 2015).

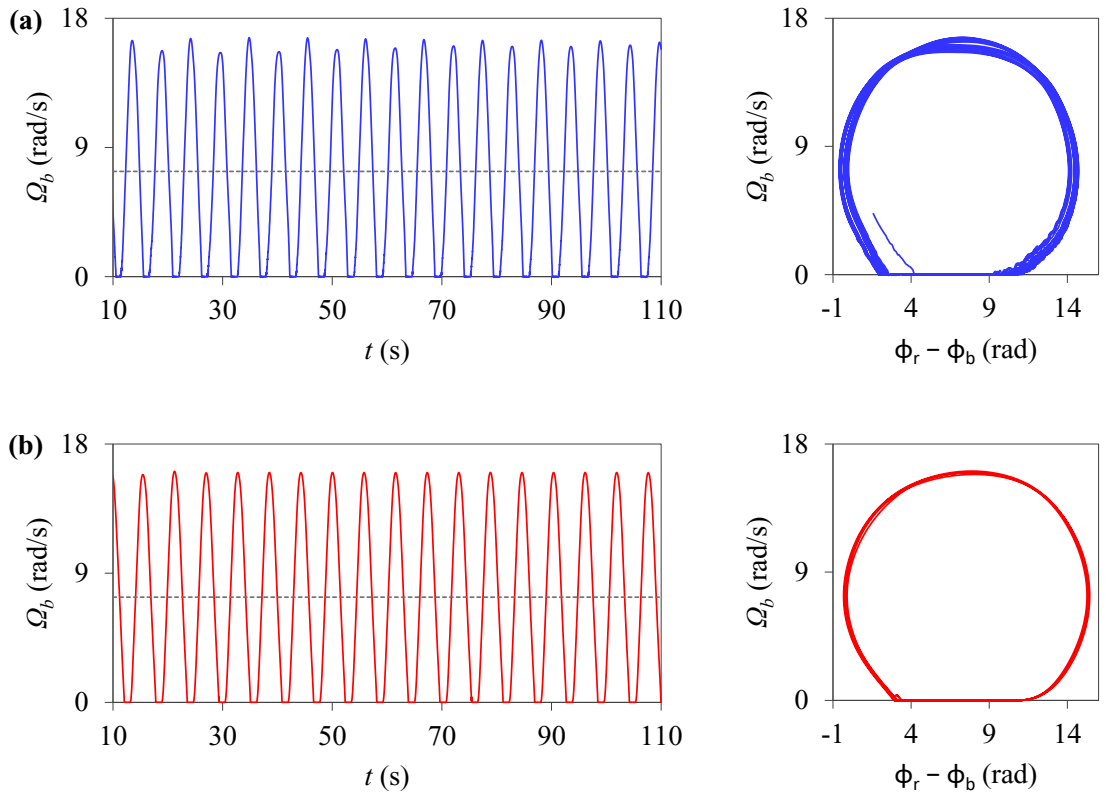

Figure 5-6. Example stick-slip time-series and phase planes of the bit angular velocity obtained from (a) the FEM model, and (b) the lumped-parameter model using Eqs. (5) and (6) with parameter values given in Table 5-3. Ω_r = 7.33 rad/s, W_b = 40 kN, and ξ = 0.03 (with α = 0.070416 1/s and β = 0.001321 s). Dashed lines indicate the rotary velocity Ω_r

During the slip phase, the angular velocity of the drill bit initially increases. After reaching a velocity up to more than twice the rotary velocity at the surface, the drill bit velocity decreases. Eventually, the bit comes to a full stop (zero angular velocity), while the rotary table maintains a constant velocity. The incremental twisting of the drill string leads to an increase of the elastic energy stored in the drill pipes during which the reaction torque, namely, the instantaneous torque applied by the drill string onto the drill bit, builds up.

During that time, the value of torque-on-bit T_b is computed based on Newton's third law, for which the reaction torque adjusts itself with all the frictional moments acting on the bit; see Eq. (1). Finally, the reaction torque overcomes the break-away torque value $T_0 = \mu_s R_b W_b$, and the bit starts to rotate, resulting in a continuation of the stick-slip cycle. The limit cycling behavior is in agreement with field and experimental measurements (Jansen and van den Steen, 1995; Mihajlovic et al., 2004).

5.4. Results and Discussion

The numerical model was used for parametric studies. The level of rotary table velocity Ω_r, weight-on-bit W_b, and damping ratio ξ were varied to investigate their effect on the drill string vibration and the existence of stick-slip. Only one variable was changed at each simulation to assess its individual influence. The time-series of angular velocities were obtained for observation nodes along the drill string over 110 s, during which the first 10 s was the ramping-up of the rotary velocity from zero to the desired level.

For each simulation, the peak-to-peak angular velocity of the observation nodes was calculated from $t = 70$ s to $t = 90$ s. Figure 5-7. demonstrates the response amplitude of the drill pipe mid-point (1150 m above the bit) and the drill bit under stick-slip oscillations. The observed torsional oscillations of the drill string under stick-slip condition were limit cycles (bounded periodic vibrations); see Section 5.3. Therefore, the considered time duration covered at least one full cycle of the velocity oscillation for each node, and the calculated amplitudes represented the absolute amplitude of the whole simulation for that node. Furthermore, the apparent oscillations of the peak-to-peak velocities under stick-slip situation were negligible and did not affect the calculated amplitudes significantly; see

Figure 5-7.. The statistical properties of the system response, such as mean and standard deviation of the angular velocities, were then evaluated at each node throughout the time-series from t = 10 s to t = 110 s. Adequate quantification of these statistical characteristics can be further used in fatigue analyses of the drill string system.

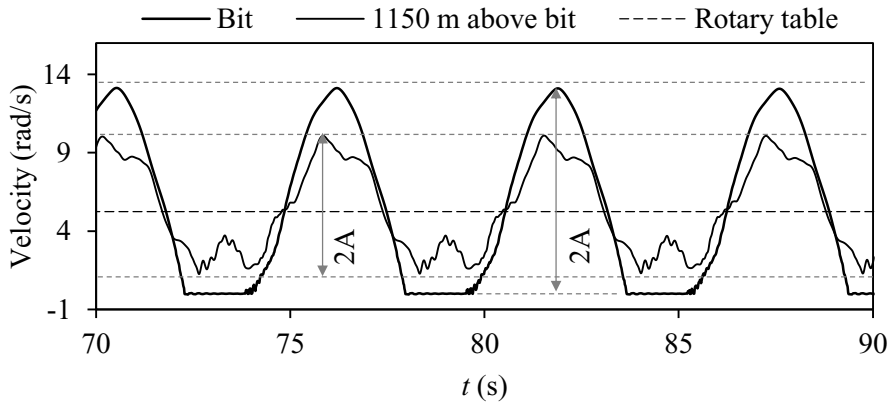

Figure 5-7. Definition of the peak-to-peak amplitude ($2A$) of angular velocity under stick-slip condition for Ω_r = 5.24 rad/s, ξ = 0.03, W_b = 40 kN

To gain more in-depth insight into the behavior of the drill string under steady-state stick-slip vibration, the frequency analyses of the numerically obtained angular velocities were carried out. The time-series of angular velocities along the drill string were treated using the fast Fourier transform (FFT). The obtained spectra indicated the discrete frequencies and amplitudes of the angular velocities that contributed to the stick-slip response of the system. The time-series from t = 10 s to t = 110 s were sampled at a frequency of 80 Hz (Nyquist frequency 40 Hz) to achieve high-resolution spectra. The resolution of the obtained spectra was 0.01 Hz, therefore the results were quantitative representation of the contributing frequencies. It is worth noting that the amplitude of zero frequency components of the response spectra corresponds to twice the mean angular velocities,

which are not represented in the plots. Also, it is noted that the ordinate in each spectrum plot represents the normalized amplitude, that is, the amplitude of each frequency divided by the amplitude of the dominant frequency.

5.4.1. Effect of Rotary Velocity Ω_r

Four different levels of rotary velocity Ω_r = 2.09, 5.24, 7.33, and 11.52 rad/s were considered. The weight-on-bit W_b and damping ratio ξ were fixed at 40 kN and 0.03, respectively, with α = 0.070416 1/s and β = 0.001321 s.

For rotary velocities smaller than a particular threshold value, i.e., 2.09, 5.24, and 7.33 rad/s, the drill pipes experience normal periodic torsional vibration, whereas the drill bit undergoes periodic stick-slip vibration; see plots (a) – (c) in Figure 5-8. and Figure 5-9.. This situation can be identified by the closed trajectories of the phase planes representing ceaseless torsional oscillation. As the rotary velocity increases up to a certain threshold value, the duration of the stick phase is decreased, while the amplitude of the vibration is increased. This agrees with field and experimental observations (see, e.g., Kyllingstad and Halsey, 1988; Liu et al., 2017). For higher rotary velocities, i.e., 11.52 rad/s, which exceed the threshold value, the torsional vibration at both drill pipes and drill collars gradually damps out, and the drill string performs at stable condition with a velocity close to the rotary velocity; see plot (d) in Figure 5-8. and Figure 5-9.. The suppression of stick-slip oscillation by increasing the rotary velocity beyond the threshold value is in agreement with field observations (see, e.g., Jansen and van den Steen, 1995; Dawson et al., 1987; Kyllingstad and Halsey, 1988).

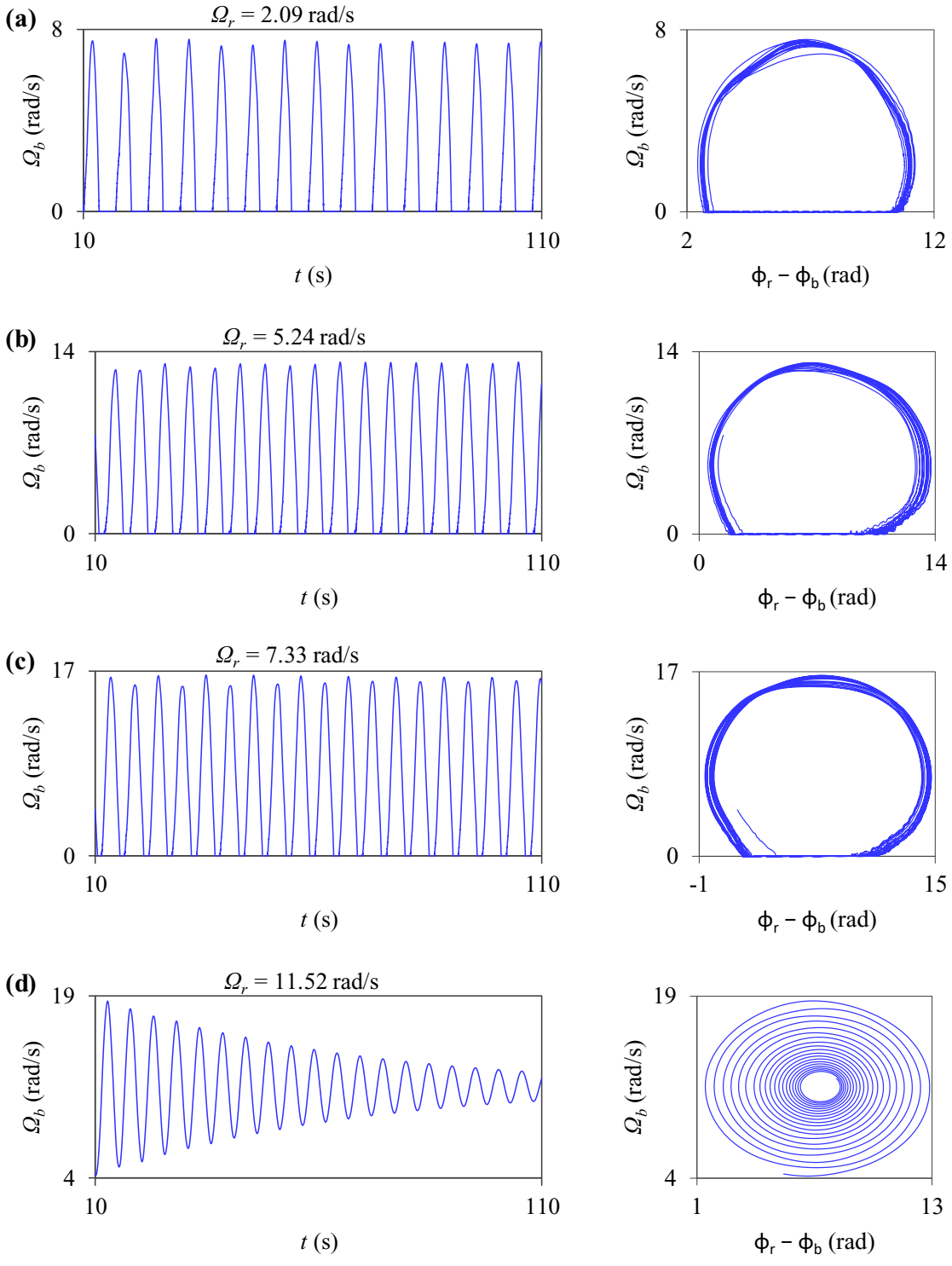

Figure 5-8. Time- series and phase planes of the angular velocity at the drill bit for W_b = 40 kN, ξ = 0.03, and Ω_r of (a) 2.09 rad/s, (b) 5.24 rad/s, (c) 7.33 rad/s, and (d) 11.52 rad/s

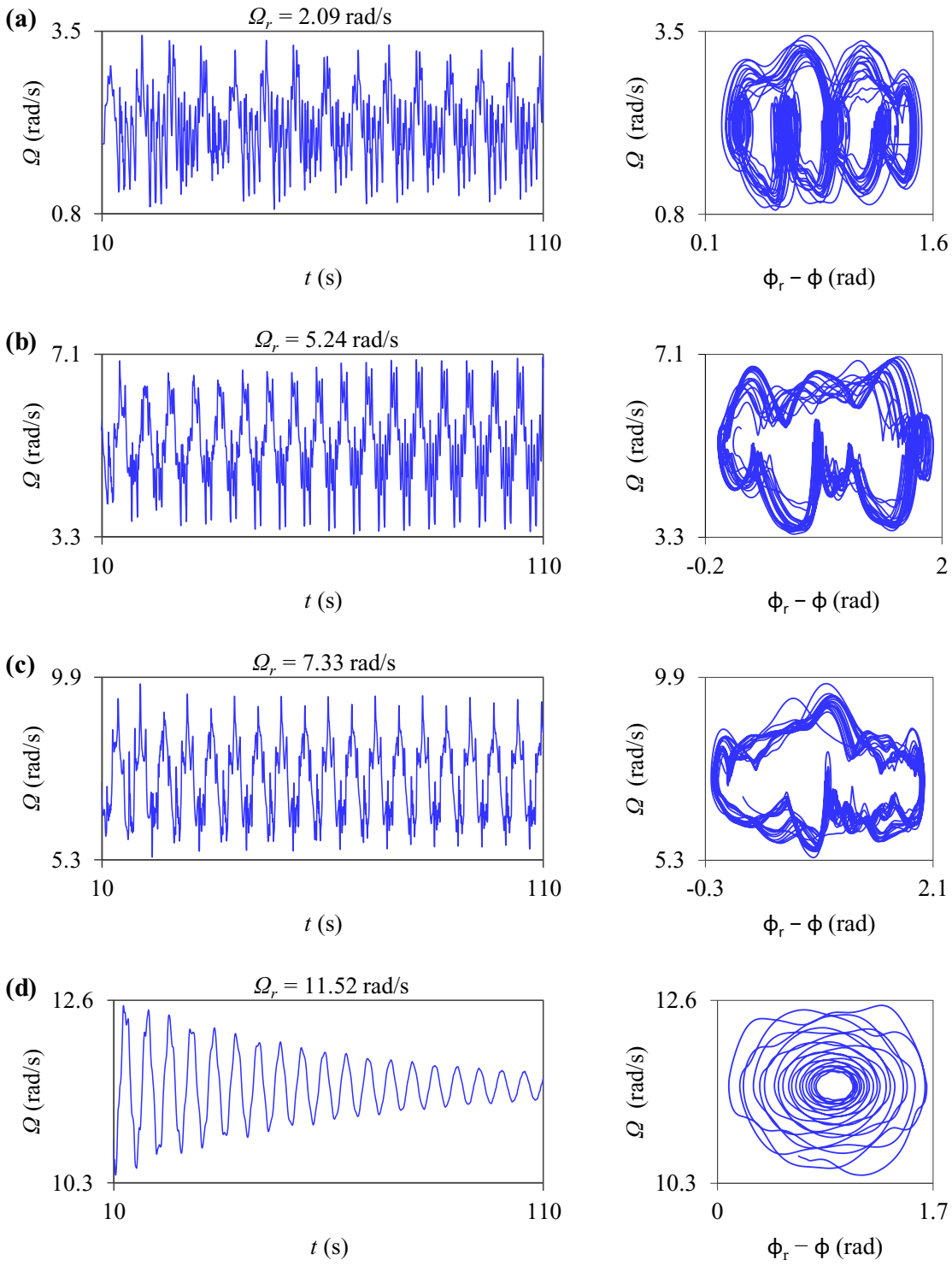

Figure 5-9. Time-series and phase planes of the angular velocity at 1900 m above the drill bit for W_b = 40 kN, ξ = 0.03, and Ω_r of (a) 2.09 rad/s, (b) 5.24 rad/s, (c) 7.33 rad/s, (d) 11.52 rad/s

Table 5-4 presents the calculated mean angular velocity along the drill string for varying Ω_r. Under each rotary velocity, the mean angular velocity of the drill pipes and drill collars along the drill string is in the vicinity of the rotary velocity. This indicates that the mean velocity of the drill string is directly related to the rotary velocity at the surface.

Table 5-4. Mean angular velocity μ (rad/s) at different points along the drill string for W_b = 40 kN, ξ = 0.03, and varying Ω_r

Distance above the bit (m)	Ω_r = 2.09 rad/s	Ω_r = 5.24 rad/s	Ω_r = 7.33 rad/s	Ω_r = 11.52 rad/s
2150	2.09	5.24	7.33	11.52
1900	2.10	5.23	7.33	11.52
1650	2.10	5.21	7.32	11.51
1400	2.11	5.20	7.32	11.51
1150	2.11	5.19	7.31	11.50
900	2.12	5.18	7.31	11.50
650	2.12	5.16	7.31	11.50
400	2.13	5.15	7.30	11.49
150	2.14	5.15	7.30	11.49
112.5	2.14	5.15	7.30	11.49
75	2.14	5.15	7.30	11.49
37.5	2.14	5.15	7.30	11.49
0	2.14	5.15	7.30	11.49

Figure 5-10. presents the amplitude spectra of angular velocities at the drill bit and 1900 m above the bit under stick-slip vibration for different Ω_r. For low rotary velocity, i.e., 2.09 rad/s, the dominant frequency f_D = 0.14 Hz of both drill pipes and drill collars/bit is significantly smaller than the first torsional natural frequency of the system f_1 = 0.19188 Hz. (f_D/f_1 = 0.73); see Figure 5-10.(a). This indicates that stick-slip vibration can occur at frequencies lower than the first natural frequency of the drill string. This is an interesting finding which agrees with published field observations (Kyllingstad and Halsey, 1988). For higher rotary velocities, i.e. 5.24 and 7.33 rad/s, the dominant frequency of both drill

pipes and drill collars f_D = 0.18 ~ 0.19 Hz is slightly smaller than the first torsional natural frequency of the system; see Figure 5-10.(b) and (c). The difference between the dominant frequencies and the first natural frequency of the system corresponds to the nonlinear frictional torque arising from the bit-rock interaction.

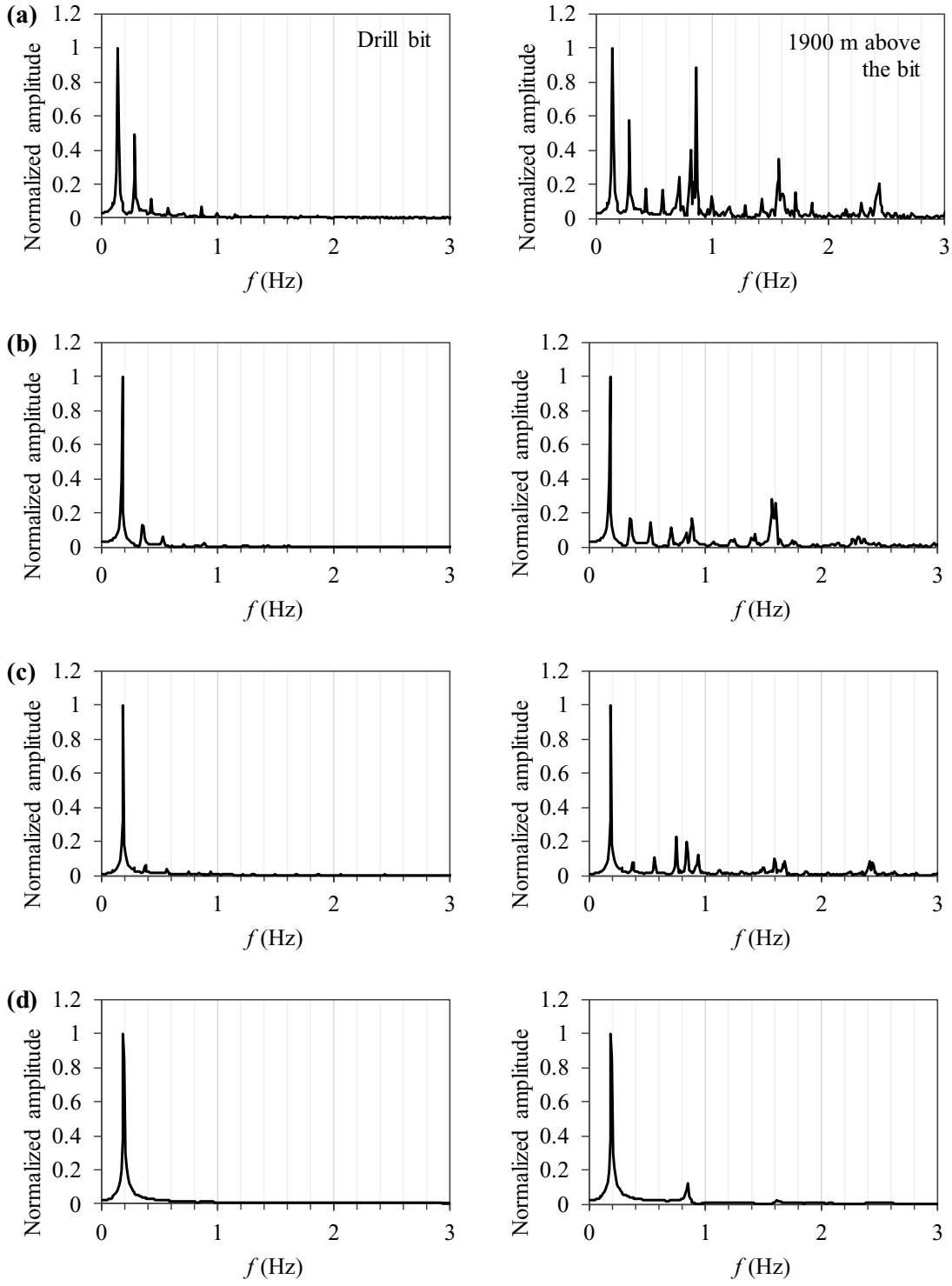

Figure 5-10. Response spectra of angular velocity at the drill bit (left) and 1900 m above the bit (right) with W_b = 40 kN, ξ = 0.03, and Ω_r of (a) 2.09 rad/s, (b) 5.24 rad/s, (c) 7.33 rad/s, (d) 11.52 rad/s

According to Figure 5-10.(a) – (c), the amplitude decreases with frequency at the drill bit, that is, the higher harmonics have a smaller contribution to the stick-slip vibration of drill collars/bit, especially for higher rotary velocities. In contrast, the contribution of higher harmonics is significant in the drill pipes, especially for lower rotary velocities. For instance, in Fig. 9(a) corresponding to the point 1900 m above the bit, the peak frequencies are 0.29, 0.86, 1.58, and 2.44 Hz, which the three latter are related to the second (0.838 Hz), third (1.595 Hz), and fourth (2.368) natural torsional frequency of the system, respectively (see Table 5-2.). From these results, it can be concluded that under a stick-slip vibration, the contribution of higher frequencies in the response of drill pipes is more noticeable than drill collars/bit. This can be related to the smaller cross-sectional area and longer length of the drill pipe section compared to the drill collar section.

5.4.2. Effect of Weight-on-Bit W_b

Simulations were carried out using four different values of weight-on-bit W_b = 10, 30, 40, and 50 kN. The criteria of choosing 50 kN as the largest weight-on-bit was to approximately limit its value to the total weight of the drill collar section (≈ 43 kN). The rotary velocity Ω_r and damping ratio ξ were considered to be fixed at 6.3 rad/s and 0.03, respectively, with α = 0.070416 1/s and β = 0.001321 s.

Figure 5-11. and Figure 5-12. show the time-series and the corresponding phase planes of angular velocity at the bit and 1650 m above the bit, respectively, for varying W_b. For levels of weight-on-bit smaller than a certain threshold value, i.e., 10 kN, no stick-slip vibration is observed, and the torsional vibration at both drill pipes and drill collars gradually disappears; see plot (a) in Figure 5-11. and Figure 5-12.. As the W_b increases and exceeds

the threshold value, i.e., 30, 40, and 50 kN, the drill bit exhibits periodic stick-slip vibration, resulting in periodic torsional vibration at drill pipes; see plots (b) – (d) in Figure 5-11. and Figure 5-12.. This indicates that increasing the W_b gives rise to more severe stick-slip vibration with larger amplitude, whereas decreasing the W_b can diminish the stick-slip condition. This is in accordance with field measurement data (see, e.g., Brett, 1992).

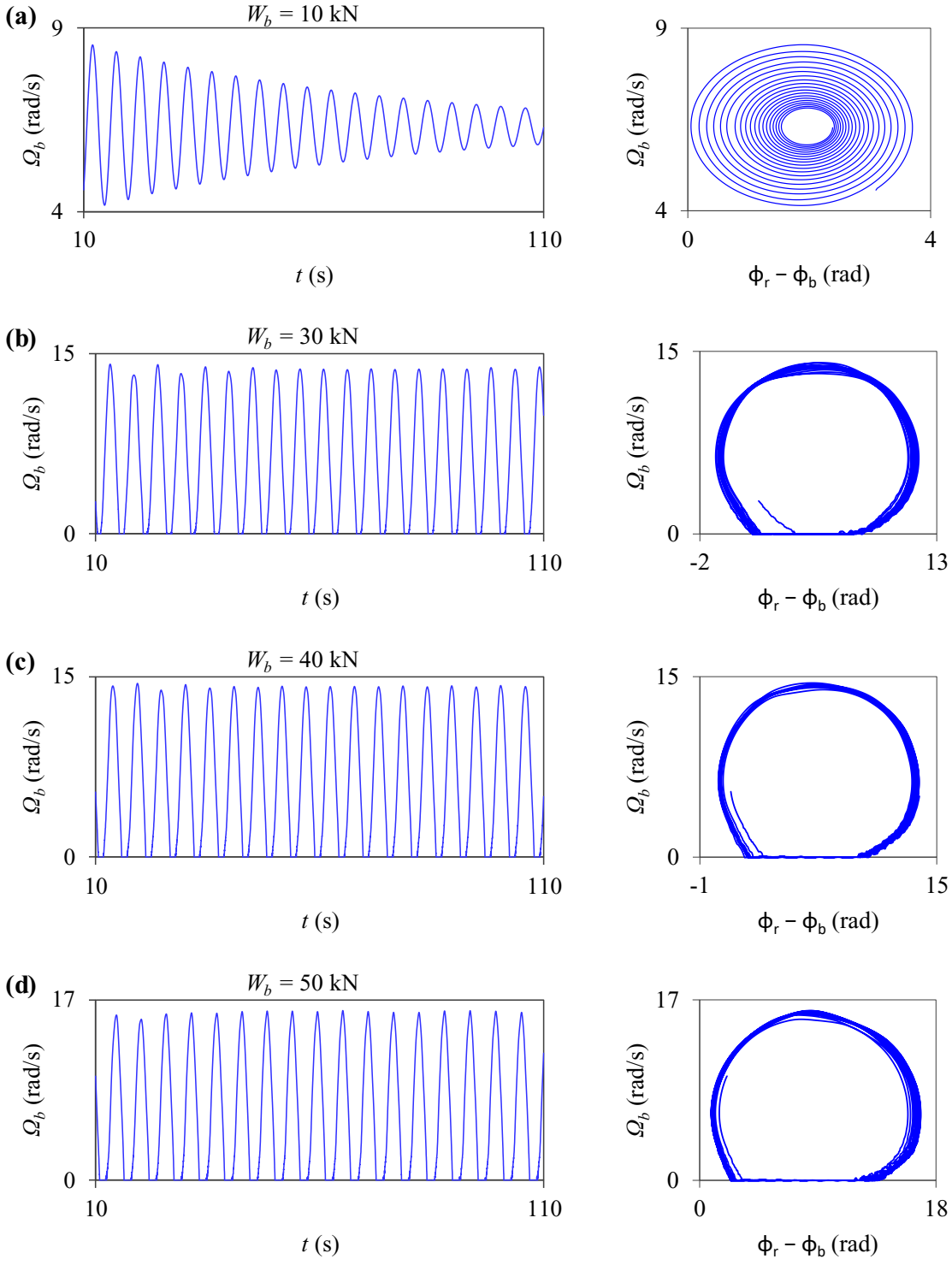

Figure 5-11. Time-series and phase planes of the angular velocity at the bit for Ω_r = 6.3 rad/s, ξ = 0.03, and W_b of: (a) 10 kN, (b) 30 kN, (c) 40 kN, (d) 50 kN

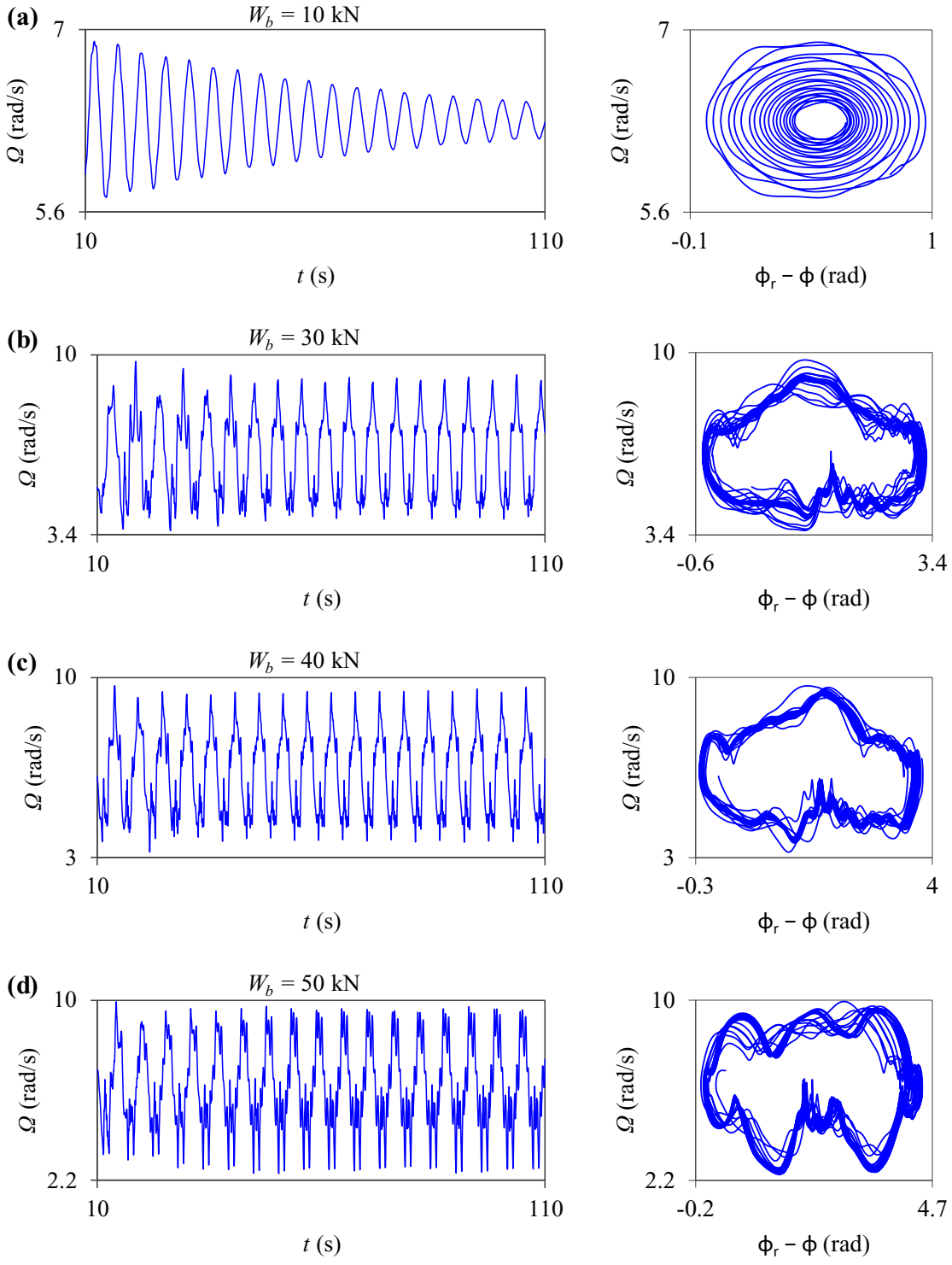

Figure 5-12. Time-series and phase planes of the angular velocity at 1650 m above the bit for Ω_r = 6.3 rad/s, ξ = 0.03, and W_b of: (a) 10 kN, (b) 30 kN, (c) 40 kN, (d) 50 kN

Table 5-5 shows the calculated mean angular velocity along the drill string. For small levels of weight-on-bit with no stick-slip vibration, i.e., W_b = 10 kN, the mean angular velocity of the entire drill string is equal to the rotary velocity. As the weight-on-bit increases and exceeds the threshold value, the mean angular velocity along the drill string becomes different from the rotary velocity. The difference between the rotary velocity and the mean angular velocity along the drill string indicates continuous twist, and thus, torsional instability in the drill string during stick-slip vibration.

Table 5-5. Mean angular velocity μ (rad/s) at different points along the drill string for Ω_r = 6.3 rad/s, ξ = 0.03, and varying W_b

Distance above the bit (m)	W_b = 10 kN	W_b = 30 kN	W_b = 40 kN	W_b = 50 kN
2150	6.300	6.3000	6.3000	6.3000
1900	6.301	6.3024	6.2816	6.2807
1650	6.302	6.3048	6.2631	6.2619
1400	6.302	6.3072	6.2450	6.2441
1150	6.303	6.3096	6.2282	6.2274
900	6.304	6.3119	6.2129	6.2117
650	6.305	6.3142	6.1986	6.1968
400	6.306	6.3164	6.1853	6.1826
150	6.306	6.3185	6.1728	6.1694
112.5	6.306	6.3185	6.1727	6.1693
75	6.306	6.3185	6.1726	6.1692
37.5	6.306	6.3185	6.1726	6.1692
0	6.306	6.3185	6.1726	6.1693

Figure 5-13. illustrates the response spectra of the angular velocities for varying W_b. According to this figure, the stick-slip dominant frequency f_D ~ 0.19 Hz is slightly smaller than the first torsional natural frequency of the system 0.19188 Hz for different levels of W_b. This implies that the dominant frequency depends mainly on the angular velocity of the rotary table. It is noted that increasing the weigh-on-bit has been shown to increase the

frequency of the stick-slip limit cycle depending on the operating parameter (Germay et al., 2009). Moreover, it is observed that larger W_b can excite higher frequency components in the drill pipes; see Figure 5-13..

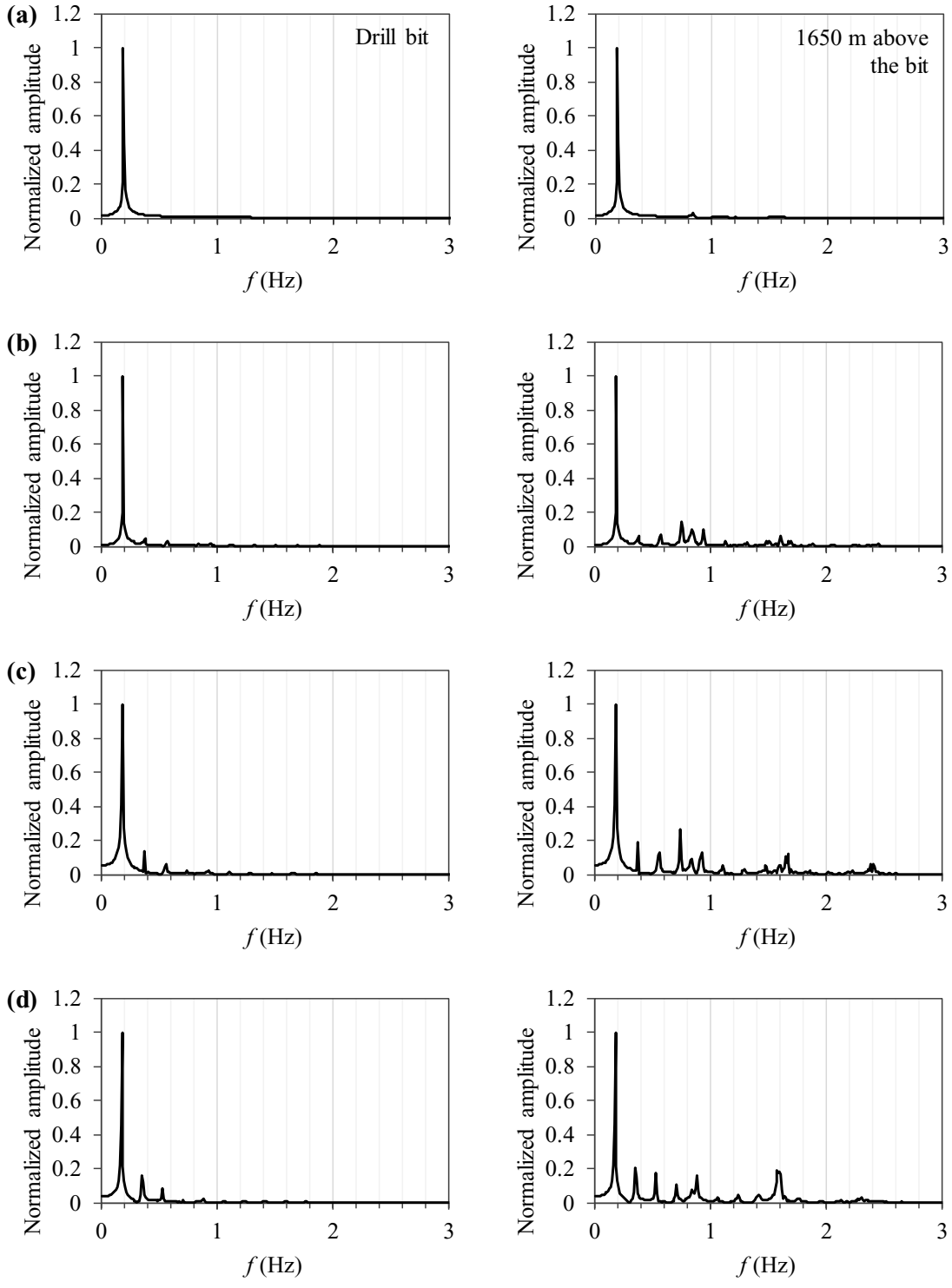

Figure 5-13. Response spectra of angular velocity at the drill bit (left) and 1650 m above the bit (right) for Ω_r = 6.3 rad/s, ξ = 0.03, and W_b of (a) 10 kN, (b) 30 kN, (c) 40 kN, (d) 50 kN

The increase of weight-on-bit is associated with a rise in the break-away torque; $T_0 = \mu_s R_b W_b$, which is accompanied by a prolonged stick phase and a larger slip amplitude. This can be described in terms of the physical phenomenon as follows: if the weight-on-bit is increased, it will produce a greater frictional torque that needs to be overcome in order to enter the slip phase. This, in turn, requires a larger twisting of the drill string to accumulate reaction torque in the bit until it reaches the frictional torque. Therefore, the duration of the stick phase under fully developed stick-slip condition is more extended for larger W_b; see Figure 5-11.(b) – (d).

5.4.3. Effect of Damping Ratio ξ

To conduct a detailed investigation of the effect of Rayleigh damping on stick-slip vibration of the drill string, nine values of damping ratio were considered, as given in Table 5-5. For each damping ratio, the corresponding α and β were calculated using Eq. (4) with $\omega_1 = 1.2056$ rad/s and $\omega_{10} = 44.2$ rad/s. The rotary velocity Ω_r and weight-on-bit W_b were fixed at 5.24 rad/s and 40 kN, respectively.

Table 5-6. Damping ratio ξ and corresponding values for α and β coefficients

ξ	α	β
	(1/s)	(s)
0.03	0.070416	0.00132142
0.05	0.117361	0.00220237
0.07	0.164305	0.00308332
0.10	0.234721	0.00440474
0.15	0.352082	0.00660711
0.20	0.469442	0.00880948
0.25	0.586803	0.01101185
0.27	0.633747	0.01189280
0.30	0.704164	0.01321422

Figure 5-14. and Figure 5-15. illustrate the time-series and phase planes of the angular velocity at the bit and 1400 m above the bit, respectively, for different damping ratios. For damping ratios smaller than a certain value, i.e., ξ = 0.05, 0.10, and 0.20, the drill string responses with periodic torsional vibration at the drill pipes and stick-slip at the drill bit; see plots (a) – (c) in Figure 5-14. and Figure 5-15.. It can be seen that increasing the damping ratio decreases the duration of the stick phase, as well as the amplitude of torsional vibration at both drill pipes and drill bit. For damping ratios higher than a particular threshold value, i.e., 0.27, the stick-slip vibration is removed, and thus, the angular velocity of the drill pipes and drill collars/bit come close to the rotary velocity; see plot (d) in Figure 5-14. and Figure 5-15.. The loss of stick-slip vibration above the threshold damping is in agreement with previous observations (see, e.g., Jansen and van den Steen, 1995; Dawson et al., 1987; Kyllingstad and Halsey, 1988).

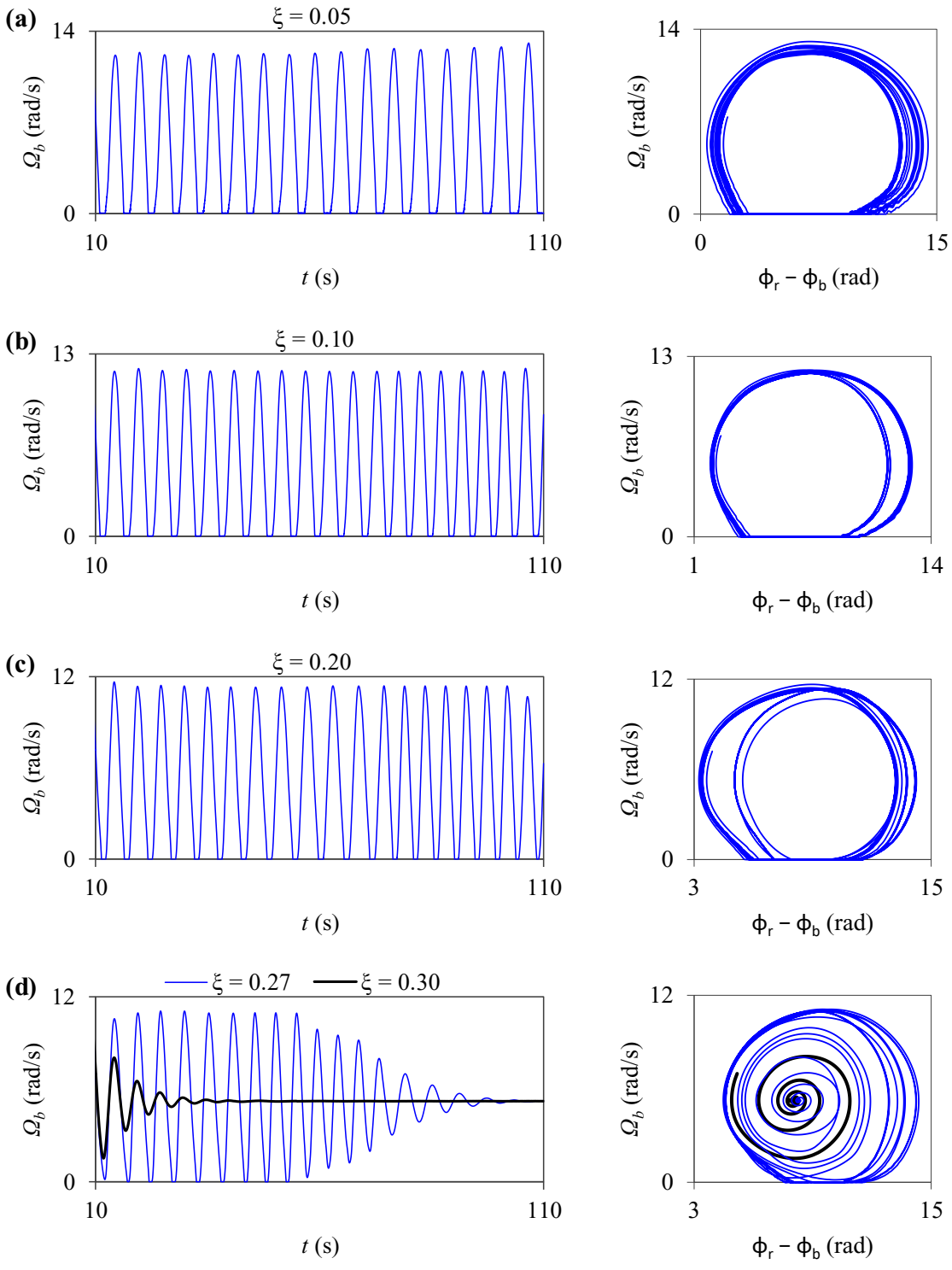

Figure 5-14. Time-series and phase planes of the angular velocity at the bit for Ω_r = 5.24 rad/s, W_b = 40 kN, and ξ of: (a) 0.05, (b) 0.10, (c) 0.20, (d) 0.27 and 0.30

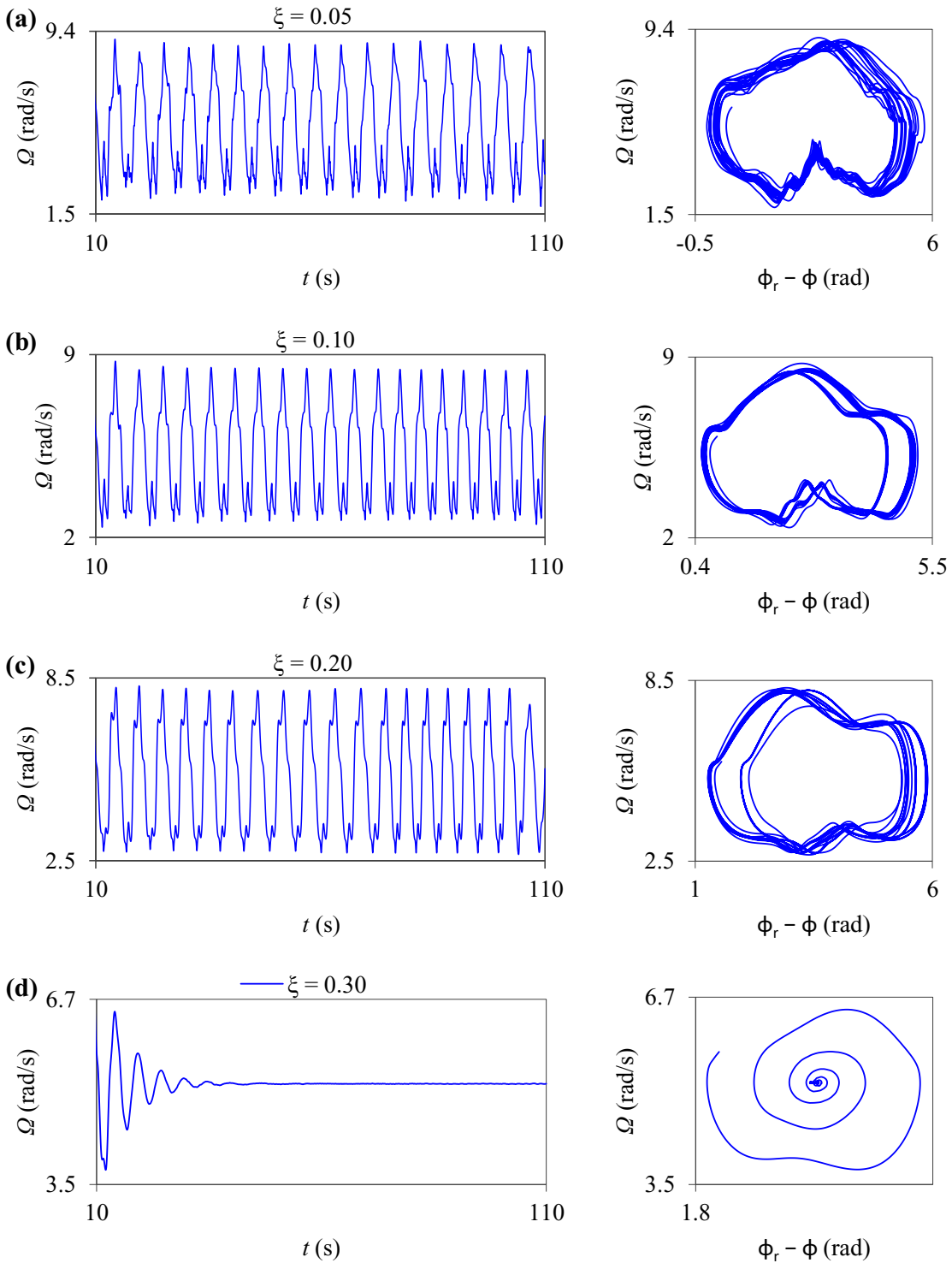

Figure 5-15. Time-series and phase planes of the angular velocity at 1400 m above the bit for Ω_r = 5.24 rad/s, W_b = 40 kN, and ξ of: (a) 0.05, (b) 0.10, (c) 0.20, (d) 0.30

Table 5-7 shows the mean angular velocity along the drill string under different damping ratios. By increasing the damping ratio, the mean angular velocity along the drill string does not change significantly and remains in the vicinity of the rotary velocity.

Table 5-7. Mean angular velocity (μ) at different points along the drill string for Ω_r = 5.24 rad/s, W_b = 40 kN, and varying ξ

Distance above the bit (m)	ξ = 0.05	ξ = 0.10	ξ = 0.20	ξ = 0.27
2150	5.24	5.24	5.24	5.24
1900	5.23	5.23	5.23	5.24
1650	5.22	5.22	5.21	5.23
1400	5.21	5.21	5.20	5.23
1150	5.20	5.20	5.19	5.22
900	5.19	5.19	5.18	5.22
650	5.18	5.18	5.17	5.21
400	5.18	5.17	5.16	5.21
150	5.17	5.15	5.15	5.20
112.5	5.17	5.15	5.15	5.20
75	5.17	5.15	5.15	5.20
37.5	5.17	5.15	5.15	5.20
0	5.17	5.15	5.15	5.20

Figure 5-16. shows the response spectra of the angular velocities for varying damping ratio ξ. According to this figure, the dominant frequency of the stick slip vibration f_D = 0.18 ~ 0.19 Hz for varying damping ratio remains close to, i.e., slightly smaller than, the first natural torsional frequency of the system 0.19188 Hz. Although the influence of viscous mud damping on the dominant frequency might be negligible, it introduces a ragged behavior in the spectra.

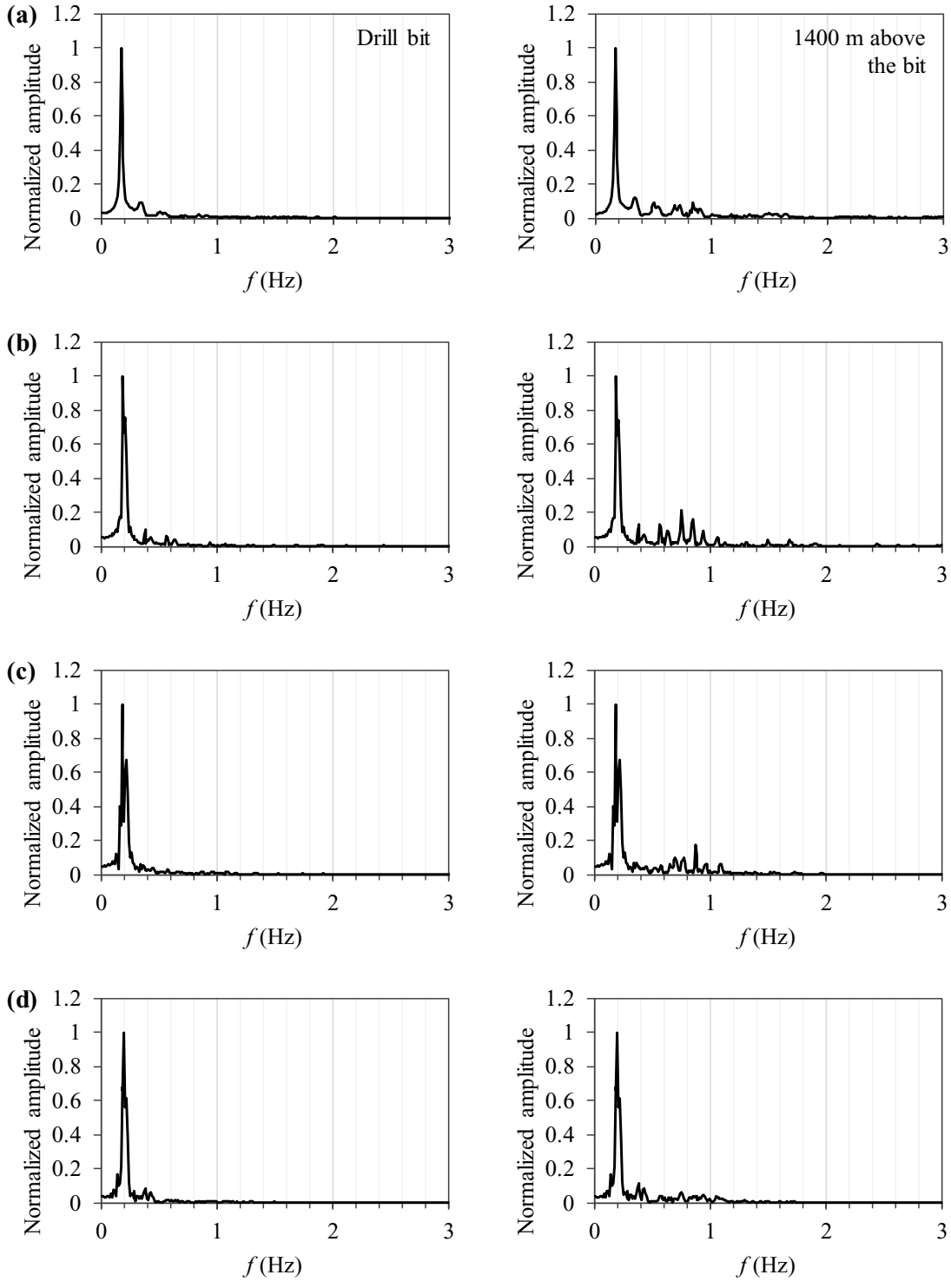

Figure 5-16. Response spectra of angular velocity at the drill bit (left) and 1400 m above the bit (right) for Ω_r = 5.24 rad/s, W_b = 40 kN, and ξ of: (a) 0.05, (b) 0.10, (c) 0.20, (d) 0.27

The comparison between the stick-slip response predicted by the analytical model (presented in Section 5.3) and numerical model when varying damping ratio shows a noticeable difference between their threshold values of damping. Figure 5-17. demonstrates the result of the comparison. For damping ratios up to $\xi = 0.10$, both the lumped-parameter and FEM model predict a steady-state stick-slip vibration; see Figure 5-17.(a). By reaching $\xi = 0.13$, however, the stick-slip is eliminated in the lumped-parameter model, whereas the FEM model shows a continuous stick-slip oscillation; see Figure 5-17.(b). The difference in the threshold value of the damping ratio between the numerical and analytical models may be related to the Rayleigh damping model that does not guarantee an equal value of damping coefficient for all the modes.

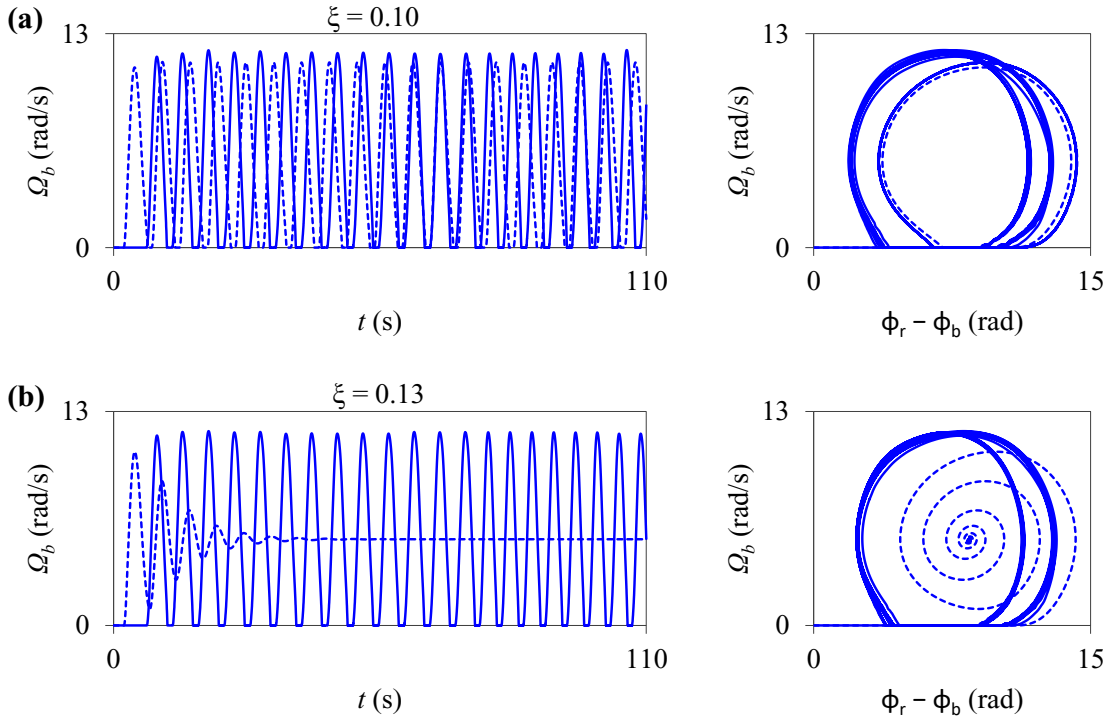

Figure 5-17. Time-series (left) and phase planes (right) of the bit response obtained from FEM model (solid lines) and lumped-parameter model (dashed lines) for $\Omega_r = 5.24$ rad/s, $W_b = 40$ kN, and ξ of (a) 0.10, (b) 0.13

To gain a better understanding of the dynamical behavior of the entire drill string, the variation of the amplitude and standard deviation of angular velocity along the drill string with Ω_r, W_b, and ξ is shown in Figure 5-18. and Figure 5-19., respectively.

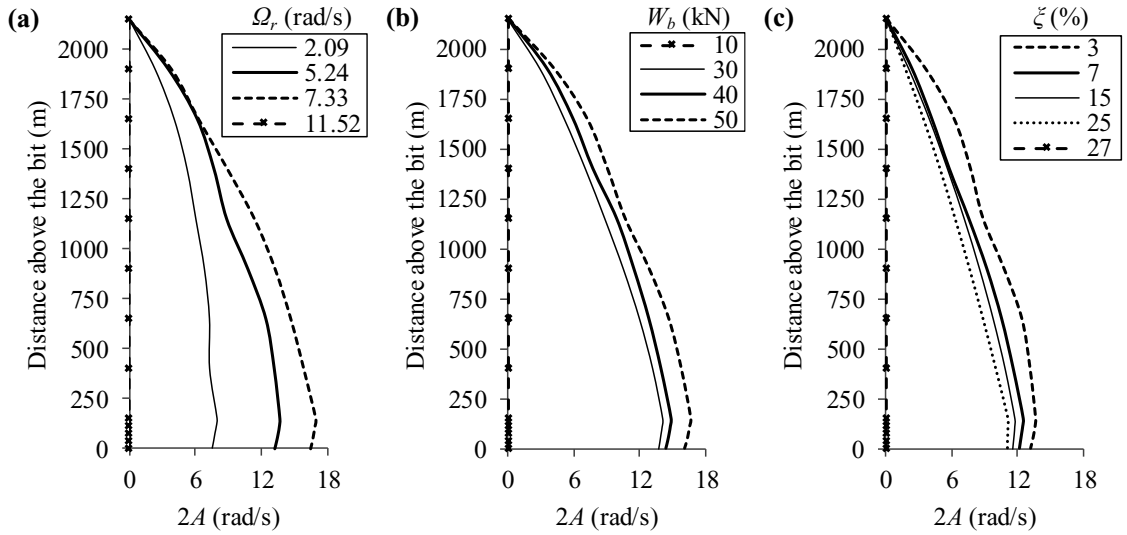

Figure 5-18. Variation of the peak-to-peak amplitude of angular velocity along the drill string under different stick-slip conditions. (a) W_b = 40 kN and ξ = 0.03, (b) Ω_r = 6.3 rad/s and ξ = 0.03, (c) Ω_r = 5.24 rad/s and W_b = 40 kN

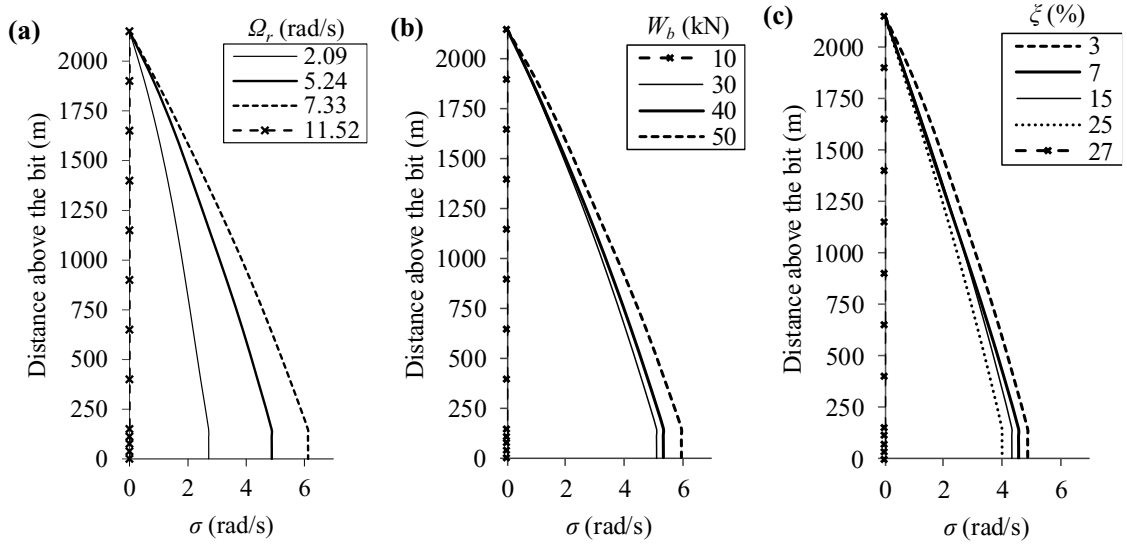

Figure 5-19. Variation of the standard deviation of angular velocity along the drill string under different stick-slip conditions. (a) W_b = 40 kN and ξ = 0.03, (b) Ω_r = 6.3 rad/s and ξ = 0.03, (c) Ω_r = 5.24 rad/s and W_b = 40 kN.

Under each stick-slip condition, the vibration amplitude A and standard deviation σ along the drill string increase rapidly from zero at the rotary table to the maximum at the top of the drill collars, and remain almost constant along the collar section. This shows that the torsional stick-slip oscillation of the drill collars/bit is more crucial than the drill pipes with regards to the intensity. The almost constant-amplitude torsional vibration along the drill collars is mainly due to the high torsional stiffness of the collar section, which makes it to behave as a rigid body.

The amplitude and standard deviation of the angular velocity of the drill pipes and drill collars/bit along the drill string under stick-slip oscillation increase with Ω_r and W_b, as depicted in plots (a) – (b) in Figure 5-18. and Figure 5-19., respectively, but decrease with ξ as depicted in plot (c) in Figure 5-18. and Figure 5-19., respectively. A rotary velocity or

damping ratio higher than a threshold value, or a weight-on-bit lower than a threshold value can remove the stick-slip oscillations. As the stick-slip is removed, the amplitudes and standard deviations of angular velocity of both drill pipes and drill collars/bit reach zero. It is noted that although stick-slip vibration can be reduced or even eliminated by increasing the rotary velocity above the threshold value, the vibration amplitudes and standard deviations along the drill string can be intensified before reaching the threshold velocity; see plot (a) in Figure 5-18. and Figure 5-19. This, in turn, can results in larger cyclic stresses in the drill pipes and drill collars, detrimental to the life of the system.

Varying the damping ratio does not significantly alter the stick-slip vibration; see plot (c) in Figure 5-18. and Figure 5-19.. For example, increasing the ξ from 0.07 to 0.10, which is an increase of 42.86%, decreases the standard deviation of the drill collar for only 3%. Similarly, increasing the ξ from 0.03 to 0.25, which is an increase of 833.33%, decreases the standard deviation of the drill collars/bit for 17.89%. Therefore, if Ω_r and W_b are to be kept constant, and the stick-slip is treated only by altering the viscous damping, then a large Rayleigh damping ratio should be considered for mitigation. It is noted that although viscous damping can reduce the amplitude of torsional vibration along the drill string or even remove the stick-slip vibration, the realistic damping value may be too small to eliminate the oscillations at field operating condition.

The growth of the amplitude of the torsional vibration at each point along the drill string with regard to the stick-slip is significantly affected by the rotary velocity, rather the weight-on-bit and viscous damping.

5.5. Summary and Conclusion

In this chapter, a detailed numerical investigation on the drill string stick-slip motion was presented. Firstly, an efficient and robust nonlinear finite element (FE) model was developed to predict the vibrations of the full drill string. The stick-slip phenomenon was efficiently modeled by incorporation of the highly nonlinear bit-rock interaction and the viscous mud damping effect along the entire drill string. An alternative approach was presented based on the rate-dependant behavior of torque-on-bit that has been observed in the published data. The bit-rock contact was modeled, and the effect of cutting and friction was captured. The nonlinear Timoshenko beam (shear deformation) was implemented. The nonlinear effects of large rotational displacements, the geometrically nonlinear axial-torsional coupling effects, as well as the axial and torsional stiffness of the drill pipes and drill collars were considered in the model. A modal analysis was conducted to estimate the eigenfrequencies of the drill string system through a linear perturbation frequency analysis. A procedure was proposed to properly select the Rayleigh damping coefficients in order to minimize the variation of the frequency-dependent damping, as well as to retain the effect of higher vibration modes of the system. A nonlinear torsional lumped-parameter model of the full drill string was developed considering the dynamics of the drill pipes, drill collars, and drill bit, accounting for the bit-rock interaction and the equivalent mud damping. The performance of the developed FEM model was compared with the lumped-parameter model.

Secondly, the influence of operating parameters such as rotary velocity, weight-on-bit, and viscous mud damping on the system dynamics was investigated. Particular attention was

paid to the torsional behavior of drill pipes, rather focusing only on the BHA response. The time-series of angular velocities were obtained for different points along the drill pipes and drill collars under each operating condition. The mean, peak-to-peak amplitude, and standard deviation of the obtained velocity time-series under different operating conditions were computed and compared. Spectral analyses were carried out to determine the frequency components of the torsional vibration of the drill pipes and drill collars/bit.

The results showed that the mean angular velocity of each point along the drill string was independent of the weight-on-bit and damping ratio, but directly related to the rotational velocity at the surface. Variation of rotary velocity was more influential with regard to the growth of the amplitude and standard deviation of stick-slip vibration at each point along the drill string, compared to the weight-on-bit and damping ratio. The stick-slip dominant frequency was dependent mainly on the angular velocity of the rotary table and was decreased with decreasing the rotary velocity. Nevertheless, the dominant frequency appeared to be independent of the weight-on-bit and damping for the considered drill string and operating conditions. The contribution of higher frequencies to the torsional stick-slip response of the drill collars/bit was negligible. However, noticeable peaks at frequencies close to the higher natural vibration modes of the system were observed in the response spectra of drill pipes under low rotary velocities. The intensity of the higher frequency components in the response of drill pipes increased with decreasing the rotary velocity.

In summary, the study demonstrated new characteristics of the stick-slip motion of the entire drill string, provided the significant influence of the rotary table velocity on the self-excited torsional motions of the drill string. The results were in close qualitative agreement with published field and experimental data.

5.6. Acknowledgments

The authors gratefully acknowledge the financial support of this research by the Research and Development Corporation (RDC) (now TCII) through the Ignite funding program, the "Mitacs" through Globalink program, and the Memorial University of Newfoundland through VP start-up funding support.

References

ABAQUS (2017), ABAQUS/Explicit User's Manual, SIMULIA.

Abbassian F., Dunayevsky V.A. (1998), Application of stability approach to torsional and lateral bit dynamics, SPE Drilling Completion. 13(2) 99-107.

Bakhtiari-Nejad F., Hosseinzadeh A. (2017), Nonlinear dynamic stability analysis of the coupled axial-torsional motion of the rotary drilling considering the effect of axial rigid–body dynamics, Int. J. Non-Linear Mech. 88; 85–96.

Banerjee A.K., Dickens J. (1990), Dynamics of an arbitrary flexible body in large rotation and translation. J Guid Control Dyn; 13(2):221–7.

Bradbury R.E., Wilhoit J.C. (1963), Effect of Tool Joints on Passages of Plane Longitudinal and Torsional Waves Along a Drill Pipe, ASME. J. Eng. Ind. 85;156–162.

Brett J.F. (1992), The genesis of bit-induced torsional drillstring vibrations, SPE Drill. Eng. 7;168–174.

Chen S.L., Blackwood K., Lamine E. (2002), Field investigation of the effects of stick-slip, lateral and whirl vibrations on roller-cone bit performance, SPE Drilling and Completion. 17 (1) 15–20.

Chevallier A.M. (2001), Nonlinear stochastic drilling vibrations, Diss., Rice University. https://hdl.handle.net/1911/17946.

Chopra A.K., McKenna F. (2016), Modeling viscous damping in nonlinear response history analysis of buildings for earthquake excitation, Earthq. Eng. Struct. Dyn. 45;193–211

Dareing D.W., Livesay B.J. (1968), Longitudinal and angular drillstring vibrations with damping. ASME J. Manuf. Sci. Eng. 90;1–9.

Dawson R., Lin Y.Q., Spanos P.D., (1987). Drill-string stick-slip oscillations, In: Proceedings of the SEM Spring Conference on Experimental Mechanics. Houston, Texas.

Germay C., Denol V., Detournay E. (2009), Multiple mode analysis of the self-excited vibrations of rotary drilling systems, J. Sound Vib. 325(1–2) 362–81

Halsey G.W., Kyllingstad A., Kylling A., (1988). Torque feedback used to cure stick-slip motion, SPE Annual Tech. Conf. and Exhibition.

Jansen J.D., van den Steen L. (1995), Active damping of self-excited torsional vibrations in oil well drillstrings, J. Sound Vib. 179 (4) 647–668.

Kapitaniak M., Vaziri Hamaneh V., Chávez J.P., Nandakumar K., Wiercigroch M. (2015), Unveiling complexity of drill-string vibrations: experiments and modelling, Int. J. Mech. Sci. 101–102; 324-337.

Karnopp D. (1985), Computer simulation of stick–slip friction in mechanical dynamic systems, ASME J Dyn Syst Meas Control. 107(1) 100–103.

Khulief Y.A., Al-Sulaiman F.A., Bashmal S. (2007), Vibration analysis of drillstrings with self-excited stick–slip oscillations, J. Sound Vib. 299;540–558.

Kyllingstad A., Halsey G.W., (1988). A Study of Slip/Stick Motion of the Bit. Society of Petroleum Engineers. doi:10.2118/16659-PA.

Leine R.I., van Campen D.H., de Kraker A., van den Steen L. (1998), Stick–slip vibrations induced by alternate friction models, Nonlinear Dyn. 16;41–54.

Liao C.M., Vlajic N., Karki H., Balachandran B. (2012), Parametric studies on drill-string motions, Int. J. Mech. Sci. 54;260–268.

Liu M., Gorman D.G. (1995), Formulation of Rayleigh damping and its extensions, Computers and Structures. 57(2) 277–285

Liu X., Vlajic N., Long X., Meng G., Balachandran B. (2013), Nonlinear motions of a flexible rotor with a drill bit: stick-slip and delay effects, Nonlinear Dyn. 72 (1-2) 61-77.

Liu X., Vlajic N., Long X., Meng G., Balachandran B., (2014), Coupled axial-torsional dynamics in rotary drilling with state-dependent delay: stability and control, Nonlinear Dyn.

Liu, Y., Páez Chávez, J., De Sa, R. et al., (2017), Numerical and experimental studies of stick–slip oscillations in drill-strings. Nonlinear Dyn 90, 2959–2978. https://doi.org/10.1007/s11071-017-3855-9

MacDonald K.A., Bjune J.V. (2007), Failure analysis of drillstrings, Eng. Fail. Anal. 14;1641–1666.

Mihajlovic N., van Veggel A.A., van de Wouw N., Nijmeijer H. (2004), Analysis of friction-induced limit cycling in an experimental drill-string system, ASME J. Dyn. Syst Meas Control. 126;709-720.

Nandakumar K., Wiercigroch M. (2013), Stability analysis of a state dependent delayed, coupled two DOF model of drill–string vibration, J. Sound Vib. 332 (10) 2575–92.

Navarro-López E.M., Cortes D. (2007), Avoiding harmful oscillations in a drillstring through dynamical analysis, J. Sound Vib. 307; 152–171.

Nessjoen P.J., Kyllingstad A., Dambrosio P., Fonseca I.S., Garcia A., Levy B., (2011), Field Experience with an Active Stick-Slip Prevention System, Society of Petroleum Engineers.

Pavone D.R., Desplans J.P., (1994), Application of high sampling rate downhole measurements for analysis and cure of stick–slip in drilling, Society of Petroleum Engineers.

Rayleigh L. (1945), Theory of Sound, 1. Dover: New York, NY.

Richard T., Detournay E., (2000), Stick-Slip Vibrations of PDC Bits, American Rock Mechanics Association.

Richard T., Germay C., Detournay E. (2007), A simplified model to explore the root cause of stick-slip vibrations in drilling systems with drag bits, J. Sound Vib. 305 (3) 432–56.

Ritto T.G., Sampaio R., Soize C., (2009(a)). Drill-string nonlinear dynamics accounting for the drilling fluid, 30º CILAMCE-Iberian-Latin-American Congress on Computational Methods in Engineering, Armação dos Búzios, Rio de Janeiro, Brazil.

Sampaio R., Piovan M.T., Lozano G.V. (2007), Coupled axial/torsional vibrations of drill-strings by means of non-linear model. J. Mech. Res. Commun. 34; 497–502.

Sepehri N., Sassani F., Lawrence P.D., Ghasempoor A. (1996), Simulation and experimental studies of gear backlash and stick-slip friction in hydraulic excavator swing motion, ASME J Dyn Syst Meas Control. 118;463–467.

Silveira M. (2011), A comprehensive model of drill-string dynamics using Cosserat rod theory, (2011) Diss., University of Aberdeen.

Trindade M., Sampaio R. (2002), Dynamics of beams undergoing large rotations accounting for arbitrary axial rotations. J Guid Control Dyn; 25(4):634–43.

Tucker R.W., Wang C. (1999), An integrated model for drill-string dynamics, J. Sound Vib. 224;123–165.

Vlasov V.Z. (1961), Thin Walled Elastic Beams, second ed., National Science Foundation, Washington, DC, Israel Program for Scientific Translation, Jerusalem, Israel [First edition – Stroizdat (in Russian) Moscow, 1940].

Yigit A.S., Christoforou A.P (1998), Coupled torsional and bending vibrations of drillstrings subject to impact with friction. J. Sound Vib. 215;167–181.

Zamanian M., Khadem S.E., Ghazavi M.R., (2007), Stick-slip oscillations of drag bits by considering damping of drilling mud and active damping system. Journal of Petroleum Science and Engineering, 59;289–299.

6. Chapter 6

Fatigue Reliability Assessment of Drill String Due to Stick-Slip Vibrations and Wave-Frequency Vessel Motions

Mohammad Javad Moharrami[1], Hodjat Shiri[2]

1: Department of Civil Engineering

Memorial University of Newfoundland

e-mail: mjmoharrami@mun.ca

2: Department of Civil Engineering

Engineering, Memorial University of Newfoundland

e-mail: hshiri@mun.ca

This chapter is a conference paper to be presented in ISOPE2021, Greece.

Abstract

Fatigue damage is the most probable failure mechanism in the offshore drill strings. The major sources of fatigue damage include the mechanical vibrations due to nonlinear interaction of the drill string with wellbore, as well as the horizontal motions of the drilling vessel. The fatigue reliability assessment of drill string is a key component of the safe and cost-effective design of drill strings. This paper presents the fatigue reliability assessment of drill strings by using a coupled dynamic finite element (FE) model. The model incorporated the stick-slip vibration through a nonlinear bit-rock frictional contact, accompanied with horizontal offset and fluctuations of the drilling vessel using the response amplitude operator (RAO). The effect of mud damping, gravitational field, weight-on-bit, and nonlinear geometry, i.e., large rotational displacements and geometrical coupling between axial and torsional vibration modes were accounted for. The fatigue damage was calculated under different excitation scenarios imposed by the operating parameters and environmental conditions using the Goodman equation for mean stress, S-N curve (Wohler equation), and Miner rule. The reliability assessment was conducted by defining risk zones with normal, low, and high damage probabilities and consequences. The study showed that the first drill pipe at the top, the drill pipe passing through the BOP, and the lower drill pipe connected to dril lcollar are the crtitical regions of the drill string under combination of vibrations and vessel motions.

Keywords: Fatigue; Reliability; Endurance limit; Offshore drilling; Drill string dynamics; Nonlinear vibrations; Stick-slip; Bit-rock interaction; Rayleigh viscous damping; Finite element modeling; von Mises; Response amplitude operator (RAO)

6.1. Introduction

Offshore oil and gas drilling operations are extremely costly and impose further physical and functional challenges compared to onshore drilling. With a typical day-rate for deep-water drilling rig up to $600,000 to $800,000 in the offshore Gulf of Mexico (Amado, 2013), drill string failure will result in sever economic consequences (Macdonald and Bjune, 2007). Despite significant advances in manual and automated inspection techniques, as well as improved design codes and specifications, drill string failure due to fatigue phenomenon has raised concern in the industry. The analysis of 76 drill string failures across three continents from 1987 to 1990 indicated that fatigue was the primary cause in 65% of the failures (Hill et al., 1992). Fatigue is a progressive failure that primarily results from cyclic loading and/or corrosion, and initially appears in the form of microscopic cracks. The loading mechanisms responsible for drill string fatigue can be categorized as dog-legs, mechanical vibrations, and motions of drilling vessel in response to ocean waves (API 7G). Dog-legs are the curved regions of the wellbore due to which the rotating drill string is bent and subjected to fully-reversed alternating bending stresses. Mechanical vibrations, on the other hand, raise from the nonlinear impact and friction at the drill string-wellbore and bit-formation interfaces, resulting in considerable dynamic cyclic stresses (Christoforou and Yigit, 2003). These vibrations can exhibit in terms of axial, lateral, and torsional dynamic motions, which can exist separately or coupled together in a linear or nonlinear manner (Brett, 1992; Dunayevski et al., 1993). When drilling offshore from a floating vessel, the drill string is subjected to considerable cyclic bending stresses due to vessel motions (i.e., heave, roll, pitch, surge, and sway) in response

to ocean waves (Sarpkaya and Issacson, 1981). The cyclic stresses due to rotation of the drill string under bending and tension are detrimental to the fatigue of the drill pipes and should be avoided (API RP 7G). Hansford and Lubinski (1964) studied the effect of roll and pitch motions of the drilling vessel on the cumulative fatigue damage of the first joint of drill pipe at the upper extremity. Hansford and Lubinski (1970) defined the maximum permissible horizontal motion of the drilling vessel with regard to fatigue damage of the rotating drill string as a function of hookload. In the work of Patel, the excitation due to the bit-rock interaction was assumed as a prescribed function of time, i.e., a monochromatic harmonic excitation. The flex-joint above the subsea BOP stack is known as a severe dog-leg which experiences significant fatigue damage under vessel motions (Hansford and Lubinski, 1970). The low-frequency motions of the drilling vessel can induce large bending stress in the drill string and drilling riser structure, and when combined with the rotation, result in dynamic bending and shear stresses.

The key step to correctly predict the stress-state in a desired region of drill string is a robust and reliable mathematical model of the entire system. During the last decades, several techniques were proposed to model the drill string dynamical behavior in dog-legs or under mechanical vibration. In the present study, an integrated nonlinear dynamic FEM model of the coupled vessel-drill string system was developed to accurately estimate the stresses in the drill string under combined vessel motions and mechanical vibrations. The model accounts for viscous mud damping, gravitational field, weight-on-bit, nonlinear geometry, and geometrical coupling between axial and torsional vibration modes. A drawback of the proposed model is that the drill string-wellbore interaction is not considered. Moreover, the hydrostatic pressure of the drill mud acting on the collar section is ignored. These

effects, however, are not influential in accurate estimation of stresses in the regions of interest, and the proposed FEM model can be applied to the complex vessel-drill string system. In this study, the effect of heave motion of the drilling vessel is not considered. This is a legitimate assumption because the heave motions are typically isolated by means of heave compensator systems during drilling operation, resulting in an almost constant hook load and constant weight-on-bit. The interaction between the drill string and the riser was not considered in the model. It is believed the effect of this interaction on the drill pipe bending is small (Hansfor and Lubinski, 1970).

The efficiency and reliability of deep-water drilling system can be enhanced by predicting the dynamics of the drill string under vibrations and vessel induced responses. However, no mathematical and physical simulation methods have been proposed in the literature to consider the combination of such effects in a unified manner. This is due to (i) the complex nonlinear behavior of the drill string and the associated vibration modes, (ii) the complicated response of the vessel under random environmental loads, and (iii) the technical difficulties and costs of making full-scaled physical models incorporating the drill string both below and above the seabed. The primary contribution of this work lies within characterizing the relative and combined influence of vibrations and wave-induced vessel motions on the cyclic dynamic loading and the cumulative fatigue damage of the drill string and its reliable permormance with respect to fatigue failure.

6.2. Numerical Modeling

A global three-dimensional FEM model of the drill string was developed in ABAQUS/Implicit. The two-node linear interpolation Timoshenko beam element (B31)

was selected from the ABAQUS element library to model the slender drill pipes and drill collars. The B31 is a one-dimensional line element in three-dimensional space that has stiffness associated with axial deformation, bending, and torsion. Each node has six degrees-of-freedom; three translational and three rotational. Figure 6-1. shows the overall configuration of the modeled drill string, where x, y, and z are the translational degrees-of-freedom, whereas φ_x, φ_y, and φ_z are the rotational degrees-of-freedom around x, y, and z axes, respectively.

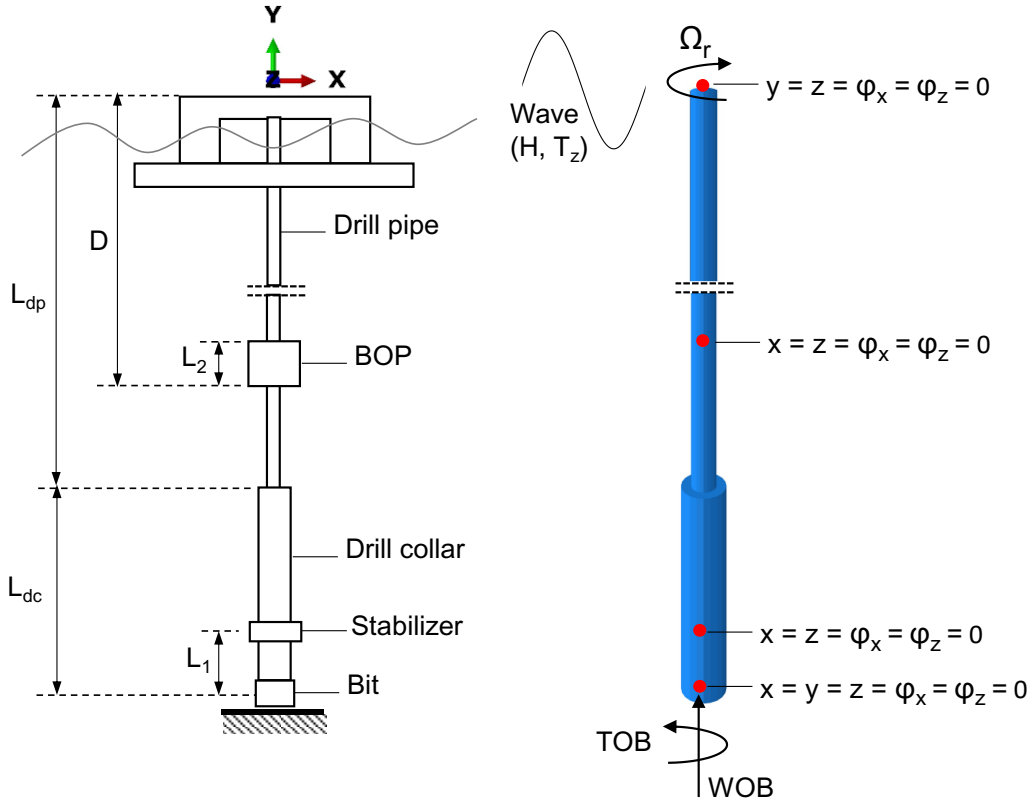

Figure 6-1. Illustration of the realistic drilling vessel and drill string under environmental loads (left) and the corresponding FEM model developed in ABAQUS with boundary conditions at the surface and the bit (right).

6.2.1. Fluid-Structure Interaction Model

The viscous damping effect due to drill mud was modeled using the frequency-dependent Rayleigh damping. The standard form of the Rayleigh damping matrix is defined as a linear combination of the mass and stiffness matrices, M and K, respectively, that is (Rayleigh, 1945; Chopra and McKenna, 2016):

$$C = \alpha M + \beta K \tag{1}$$

where α and β are the mass and the stiffness proportional coefficients, respectively.

6.2.2. Bit-Rock Interaction Model

The frictional contact at the bit-rock interface was modeled using an equivalent frictional torque-on-bit applied at the lower end of the collar section, given by:

$$TOB = \begin{cases} M, & if\ |M| < T_0 \text{ (stick mode)}, \\ M_{sl}, & otherwise \text{ (slip mode)}. \end{cases} \tag{2}$$

where M is the magnitude of all frictional moments acting on the lower end of the drill collar, $T_0 = \mu_s R_b W_b$ is the maximum static friction torque, $M_{sl} = \mu(\dot{\varphi}_b) R_b W_b$ is the sliding friction torque, R_b is the bit radius, $W_b > 0$ is the weight-on-bit, and $\mu(\dot{\varphi}_b)$ is the exponentially decaying friction coefficient given by (Oden and Martins, 1985):

$$\mu(\dot{\varphi}_b) = \left[\mu_c + (\mu_s - \mu_c) e^{-\gamma|\dot{\varphi}_b|}\right] \tag{3}$$

where $\dot{\varphi}_b = \Omega_b$ is the bit angular velocity, μ_c and μ_s are the kinetic (Coulomb) and static friction coefficients, respectively, and $\gamma > 0$ is the constant decay coefficient.

6.2.3. Gravitational Field and Boundary Conditions

An important aspect of drill string structure is the gravitational field due to which the drill pipes and drill collars operate under tension and compression, respectively. This behavior results from the combination of the static forces acting on the drill string, i.e., the gravity

force, the reactive weight-on-bit, and the hook load. To impose the gravitational field into the model, the drill string was subjected to self-weight and concentrated upward weight-on-bit during a static step. When the static equilibrium was achieved, the concentrated weight-on-bit was removed and replaced with a fixed boundary condition in longitudinal direction to maintain the tension and compression length changes in the pipe and collar sections, respectively. Then, the rotational motion of the drill string started about this pre-stressed equilibrium configuration.

Stabilizers are often placed at a prescribed distance from the bit to control the hole deviations and keep the drill collars centralized during drilling (Mitchell and Miska, 2011). Also, the lateral vibrations of the drill collar are decreased to a large extent. To model the effect of stabilizers on the collar section, that is decreasing the amplitude of lateral vibrations, a laterally-fixed boundary condition was considered at a distance of L_1 from the bit. It was assumed that during vessel drift and harmonic motion the WOB remained constant. However, note that the axial force in the bit varies when the vessel drifts.

Another important boundary condition is the flex joint placed above the subsea blowout preventer (BOP) stack. This point is known as a severe dog-leg where considerable reactive lateral forces are applied on the drill pipe due to horizontal offset of the drilling vessel (Hansford and Lubinski, 1970). To model this behavior, the lateral degrees-of-freedom in x and z direction and the rotational degrees-of-freedom about *x* and *z* were restrained at a distance of L_2 from the seabed.

6.2.4. Environmental Loads and Vessel Motions

A generic semisubmersible drilling vessel located at 700 m water depth was considered in this study. In design practice, the long-term environmental conditions are approximated by stationary Gaussian short-term sea-states. These sea-state are defined by significant wave height, peak period (or the zero up-crossing period), and probability of occurrence, and are represented in the form of scatter diagram (DNVGL-CG-0130). However, as the present work is intended to examine the coupled effect of vessel motions and dynamical vibrations on the fatigue trend along the rotating drill string, a single regular wave of height H = 7 m and zero up-crossing period T_z = 13.2 s equivalent to the most probable random sea-state was considered.

Vessel motions in regular waves can be defined by means of displacement response amplitude operators (RAOs). Displacement RAO relates the amplitude of the vessel motion to the amplitude of a particular wave with a unit height. According to Figure 6-2, the amplitude of surge response in a wave of period 13.2 s and height 7 m (and thus wave amplitude 3.5 m) is 3.5 m × 0.62 = 2.17 m.

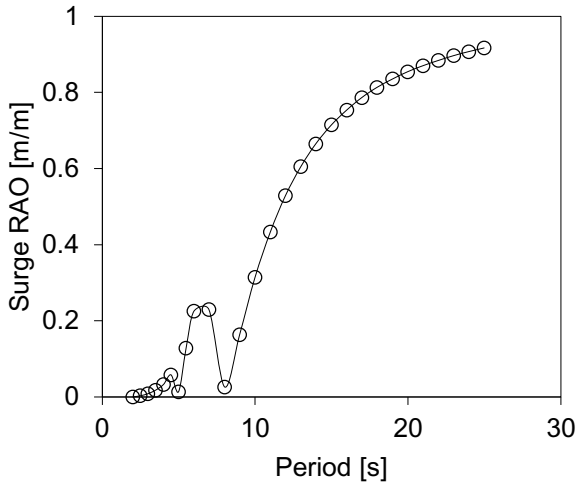

Figure 6-2. Response amplitude operator (RAO) of the semisubmersible drilling platform (Moharrami and Shiri, 2018)

6.3. Fatigue Reliability Calculations

To assess the reliable performance of drill string system, three constraints were considered following the work of Huang et al. (2019).

The first constraint was the maximum stress value that the structure may resist. If the applied stress is greater than the ultimate tensile strength, the structure fails.

The second constraint was the fatigue endurance limit which is an important material property for fatigue predictions. Endurance limit; the horizontal asymptote of the S-N curve, is defined as the alternating stress amplitude below which the fatigue test specimen can endure an infinite number of loading cycles without failure (Schijve, 2003). From an engineering perspective, the endurance limit is the highest stress amplitude for which no failure is observed after large number of loading cycles. For a given material, the endurance limit is obtained from closely controlled loading condition of the polished test specimen without geometric stress concentrations, which can significantly differ from the endurance

limit of the actual structural member. The difference depends on several factors, i.e., surface finish, size, reliability, and stress concentrations. The effect of these factors was quantified using the following equation (Stephens et al., 2001):

$$S_e = \frac{k_a k_b k_c}{k_f\, n} S'_e \tag{4}$$

where k_a is the surface condition modification factor, k_b is the size modification factor, k_c is the reliability factor, k_f is the stress concentration factor for fatigue, n is the factor of safety, S'_e is the test endurance limit, and S_e is the corrected endurance limit.

The third constraint was the reduced fatigue endurance limit due to mean stress. The drill string is subjected to high tensile stresses due to self weight which substantially influence the endurance limit. Considering that the fatigue tests are typically conducted at zero mean (fully reversed loading condition), Goodman rule (Hansford and Lubinski, 1964) was used to estimate the alternating stress S_a that causes crack initiation:

$$\frac{S_a}{S_e} + \frac{\sigma_m}{S_u} = 1 \rightarrow S_a = \left(1 - \frac{\sigma_m}{S_u}\right) S_e \tag{5}$$

where σ_m is the mean stress, S_u is the ultimate tensile strength of the material, and S_e is the corrected endurance limit.

The numerical simulations using beam elements in space give the axial stress components σ_{yy} (including bending) and the shear stress components τ caused by torsion. Application of the maximum-energy-of-distortion theory for this case gives the von Mises stress σ_{vM} as follows (Mitchell and Miska, 2011):

$$\sigma_{vM}(t) = \sqrt{(\sigma_{yy}(t))^2 + 3(\tau(t))^2} \tag{6}$$

Then, the Rainflow cycle counting method was used to extract the maximum von Mises stress amplitude, $\sigma_{a,max}$, and the mean von Mises stress, σ_m, from the variable amplitude stress time-series $\sigma_{vM}(t)$ in the time interval t = [600 to 700].

Eq. 9 summerizes the constraints used for fatigue reliability assessment of the drill string:

$$\begin{cases} \sigma_{a,max} \leq S_a;\ safe\ (infinite\ life) \\ S_a < \sigma_{a,max} \leq S_e;\ low\ risk\ (finite\ life) \\ S_e < \sigma_{a,max} \leq S_u;\ or\ \sigma_{a,max} > S_u;\ high\ risk \end{cases} \tag{7}$$

6.4. Cumulative Fatigue Damage Calculations

Structural resistance under fatigue loading is typically represented in terms of the number of cycles (N) to failure at a given stress amplitude (S), the so-called S-N curves. These data are derived from a collection of constant amplitude fatigue tests with zero mean stress. Because the von Mises stresses obtained from FEM model account for the mean effects, Goodman rule (Hansford and Lubinski, 1964) was used to calculate the equivalent alternate stress amplitude σ_{eq} that causes crack initiation at zero mean, as follows:

$$\frac{\sigma_a}{\sigma_{eq}} + \frac{\sigma_m}{S_u} = 1 \rightarrow \sigma_{eq} = \frac{\sigma_a}{1 - \frac{\sigma_m}{S_u}} \tag{8}$$

where σ_a is the alternating stress amplitude obtained from Rainflow counted cycle.

The equivalent stress (σ_{eq}) and the number of cycles to failure (N) were related using the Wohler equation, as follows:

$$N\sigma_{eq}^{m} = c \tag{9}$$

where m = 3 and c = 4.16 × 1011 are the positive constants (Netto et al., 2008) calculated for stress values in MPa. The cumulative fatigue damage was computed based on the Palmgren-Miner's (P-M) linear cumulative damage rule, given by:

$$D = \sum_{i=1}^{B} \frac{n_i}{N_i} \tag{10}$$

where B is the number of stress range blocks, n_i is the number of stress cycles in the ith stress block, N_i is the number of cycles to failure at constant stress range S_i according to the relevant S-N curve, and D is the damage ratio (equals 1 at failure).

6.5. Results and Discussions

A full drill string coupld with the lateral motions of the drilling vessel was modeled based on the numerical procedure presented in Section 6.2. The specifications of the modeld drill string are given in Table 6-1. It is noted that the distance between the stabilizer and the bit (L_1) is about the typical length of a triple stand (each stand is 30 ~ 31 ft).

Table 6-1. Geometry and material properties of the drill string

Parameter	Value
Drill string specification (Jansen and van den Steen, 1995)	
L_p = Drill pipe length [m]	2000
D_p = Drill pipe outer diameter [m]	0.1270
d_p = Drill pipe inner diameter [m]	0.1086
L_c = Drill collar length [m]	150
D_c = Drill collar outer diameter [m]	0.2286
d_c = Drill collar inner diameter [m]	0.0762
L_1 = Height from bit to stabilizer [m]	28.125
L_2 = Height from seabed to flex joint [m]	12.5
Material properties (Jansen and van den Steen, 1995)	
ρ = Steel density [kg/m^3]	7850
E = Young´s modulus [N/m^2]	2×10^{11}
G = Shear modulus [N/m^2]	7.96×10^{10}

The drill string was uniformly discretized with 128 and 64 elements on the pipe and collar sections, respectively. This number of elements was selected based on several mesh convergence experiments conducted for the maximum axial displacement y_{max}, the maximum rotational velocity Ω_{max}, and the maximum von Mises stress $\sigma_{vM,max}$, at the pipe-collar junction (where stress singularity exists due to the change in cross-sectional area). Table 6-2. shows the normalized results of the mesh convergence experiments with respect to the values predicted by the normal mesh. The results verified that the chosen mesh produced a good convergence. It is noted that the identical values of the maximum axial displacements as well as the maximum angular velocities in the pipe-collar junction confirms the compatibility condition. In order to integrate the equations of motion in the dynamic step, the Implicit time integration scheme was used with a fixed time step Δt = 0.01 s. This time step provided accurate time integration with regard to the system response under the applied excitations once the transients in the beginning of each step due to initial conditions were damped-out.

Table 6-2. Results of the mesh convergence experiments at the pipe-collar junction (150 m above the bit) from t = 80 to 120 s.

				Pipe cross-section			Collar cross-section		
	N_{dp}	N_{dc}	Δt	y_{max}	Ω_{max}	$\sigma_{vM,max}$	y_{max}	Ω_{max}	$\sigma_{vM,max}$
Normal	64	32	0.0125 s	1.0000	1.0000	1.0000	1.0000	1.0000	1.0000
Fine	128	64	0.01 s	1.0000	0.9922	0.9874	1.0000	0.9922	1.0008
Very fine	256	128	0.005 s	1.0000	0.9965	0.9861	1.0000	0.9965	1.0054

Numerical simulations were carried out under four scenarios, as follows: (A) stick-slip with rotary table velocity of Ω_r = 8.378 rad/s (80 RPM), (B) harmonic surge motion of the drilling vessel with peak-to-peak amplitude of 2.17 m and period of 13.2 s, and rotary table velocity of Ω_r = 20.94 rad/s (200 RPM), (C) static horizontal translation (drift) of the vessel equal to 1% of the water depth + scenario B, (D) scenario A + static horizontal translation of the vessel equal to 1% of water depth + harmonic surge motion of the vessel with peak-to-peak amplitude of 2.17 m and period of 13.2 s. In all the scenarios a constant weight-on-bit W_b = 90 kN was considered. This weight-on-bit was about 21.35% of the total weight of the collar section, which located the neutral point (the point with zero axial force) on the collar section at 32 m above the drill bit. Also, a damping ratio of 1% with α = 0.02347 1/s and β = 0.00044 s was assumed for all the scenarios. The following sections represent the results of the dynamic response analysis of the system under the prescribed scenarios. Figure 6-3 represents the prescribed angular velocity and horizontal motion at the top of drill string under different scenarios.

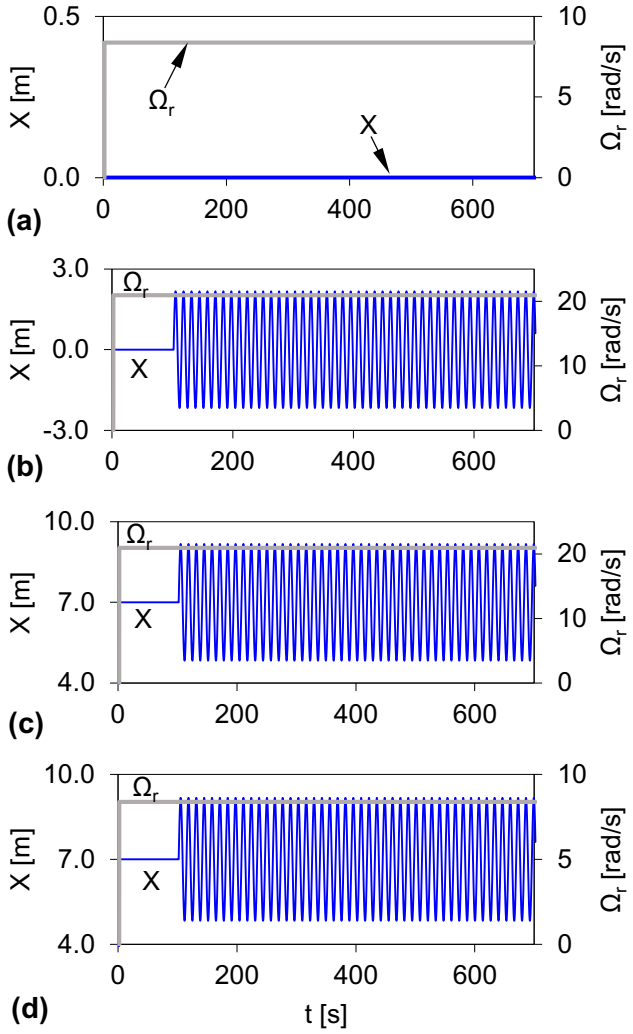

Figure 6-3. Excitations applied at the top of the drill string, where Ωr is the rotary table velocity and X is the horizontal motion of the drilling vessel. (a), (b), (c), and (d) represent the scenarios A, B, C, and D, respectively.

Scenario A

In this set of simulations, the system was excited by a constant rotary table velocity Ω_r = 8.378 rad/s (80 RPM). Under this excitation, the dynamical system experienced stick-slip vibrations due to the nonlinear bit-rock contact. As the axial and lateral degrees-of-freedom

were restrained at the bit, the forced dynamic response did not exhibit bit-bouncing or lateral vibrations, but axial and torsional vibrations were observed along the drill string owing to the geometric coupling between these vibration modes. Figure 6-4. shows the effect of stick-slip oscillations on the bit angular velocity, torque-on-bit (TOB), and torque at the rotary table (top torque).

Figure 6-5. a shows the time-series of axial, shear, and von Mises stresses at the top of the drill string. The value of axial stress is almost constant. The small oscillations about the mean value (static stress) are relatred to the axial-torsional geometrical coupling. The shear stress, however, exhibits large fluctuations with a frequency correponding to the stick-slip vibration. Note that without vessel motions, the axial stress is almost constant, and only the shear stress changes. Therefore, the variation of von Mises stress only due to the variation of shear stress originating from the stick-slip vibration.

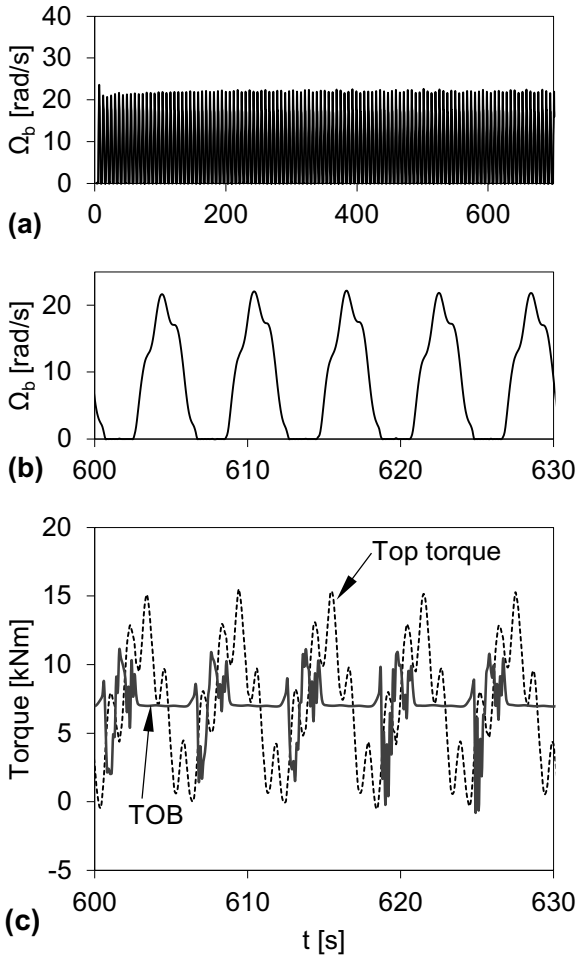

Figure 6-4. Effect of stick-slip vibration on the bit angular velocity, top torque, and TOB.

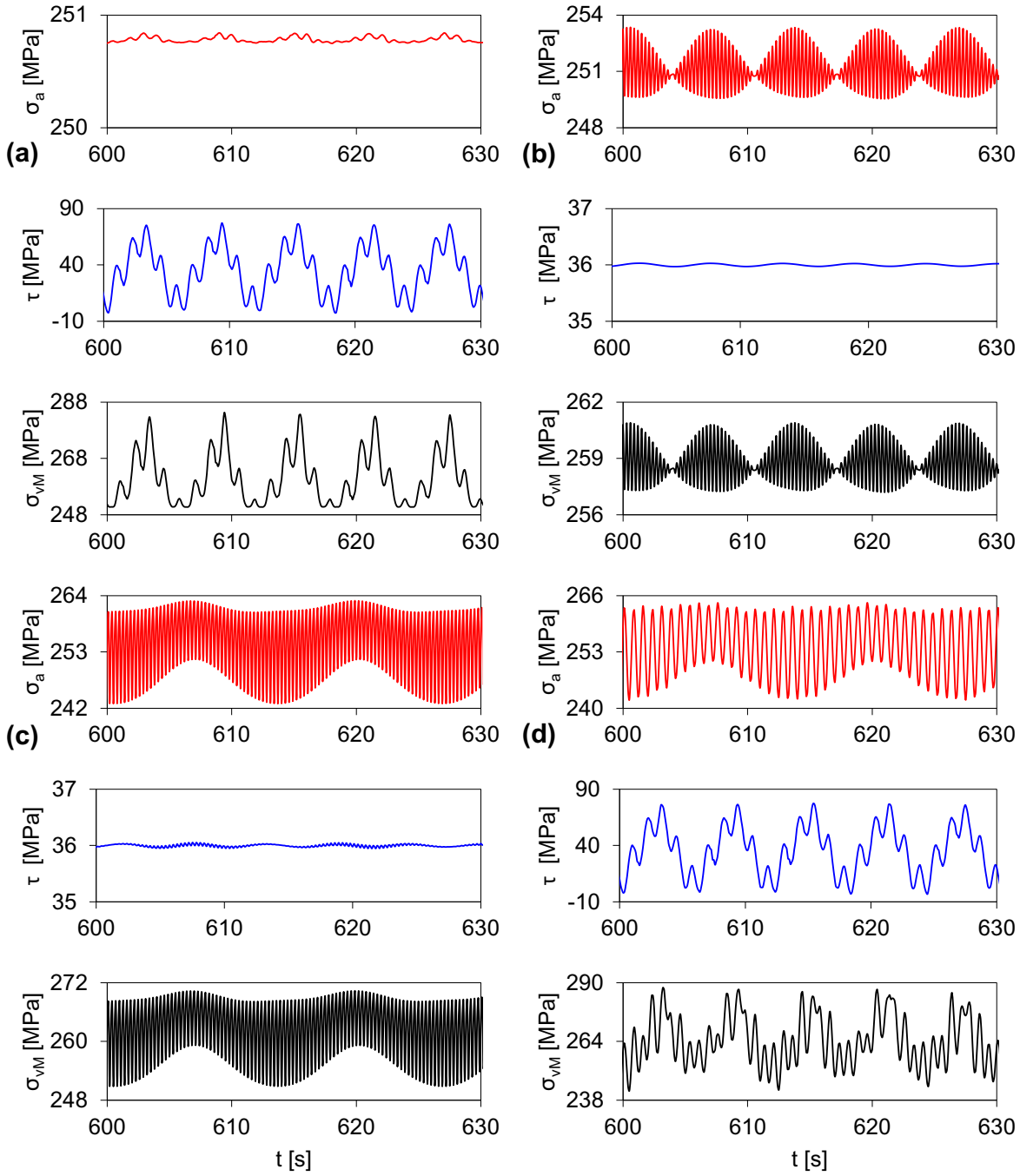

Figure 6-5. Stress time-series for the top-most drill pipe under: (a) stick-slip vibration, (b) vessel surge, (c) vessel drift + surge, (d) stick-slip + vessel drift and surge

Scenario B: In this set of simulations, the dynamic system was excited by a rotary table velocity Ω_r = 20.94 rad/s (200 RPM) and a harmonic surge motion with peak-to-peak amplitude of 2.17 m and period of 13.2 s (0.075 Hz) at the top (representing the surge motion of the drilling vessel). Figure 6-6. shows the bit angular velocity, TOB, and top torque. The increased rotary table velocity, which was beyond a threshold value, removed the stick-slip vibration and the bit velocity reached the value of rotary table velocity when the transient response due to initial conditions was damped-out. The stress time-series and the corresponding amplitude spectra of the axial, shear, and von Mises stresses for the top of the drill string are shown in Figure 6-5. b. The figure shows that the curved configuration of the drill pipe (due to vessel surge motions) combined with rotational velocity result in cyclic bending stresses, which are reflected in the axial stress.

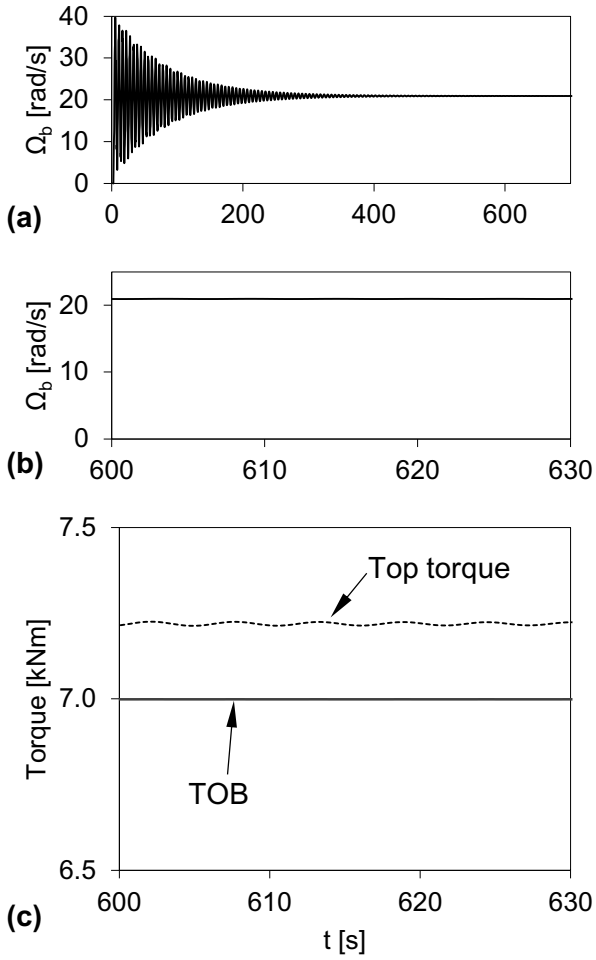

Figure 6-6. Time-series of bit angular velocity, top torque, and TOB without torsional stick-slip vibration.

Scenario C: In this set of simulations, a static horizontal offset equal to 1% of the water depth was applied to the top of the drill string to model the mean drift of the drilling vessel; and the dynamic system was excited similar to scenario B (a rotary table velocity Ω_r = 20.94 rad/s and a harmonic surge motion with peak-to-peak amplitude of 2.17 m and period of 13.2 s at the top). The time-series of stresses at the top of the drill string are shown in

Figure 6-5. c. It can be seen that the mean drift of the drilling vessel significantly increases the value of axial stress.

Scenario D: In this set of simulations, a static horizontal offset equal to 1% of the water depth was applied to the top of the drill string to model the mean drift of the drilling vessel; and the dynamic system was excited with a rotary table velocity Ω_r = 8.378 rad/s and a harmonic surge motion with peak-to-peak amplitude of 2.17 m and period of 13.2 s at the top. It is noted that this scenario involves the stick-slip vibration, as well as the mean drift and the harmonic surge motions of the drilling vessel. Figure 6-5. d shows the stress time-series and the corresponding amplitude spectra.

The amplitude spectra of von Mises stress at the top of the drill string associated with different excitations are illustrated in Figure 6-7. The spectral responses exhibit several peak frequency components which correspond to the frequency of the excitation loads. In the case of only torsional stick-slip vibrations; Figure 6-7. a, the major peak freqeuncy corresponds to the stick-slip frequency at f = 0.165 Hz; which is smaller than the first natural torsional frequency of the system (0.19 Hz). Other visible peaks are multiples of the major frequency, i.e., 0.83 Hz. When the top of drill string is excited by angular velocity and vessel motions; as showns in Figure 6-7. b and Figure 6-7. c, the response spectra involve a low-frequency peak related to the surge frequency, and some major peaks related to the rotary table velocity. Figure 6-7. d clearly shows that when the drill string is simultaneously subjected to stick-slip and vessel motions (drift + surge), the major peaks of the response spectrum are dominated by the stick-slip vibration and rotary table velocity, rather the vessel motions.

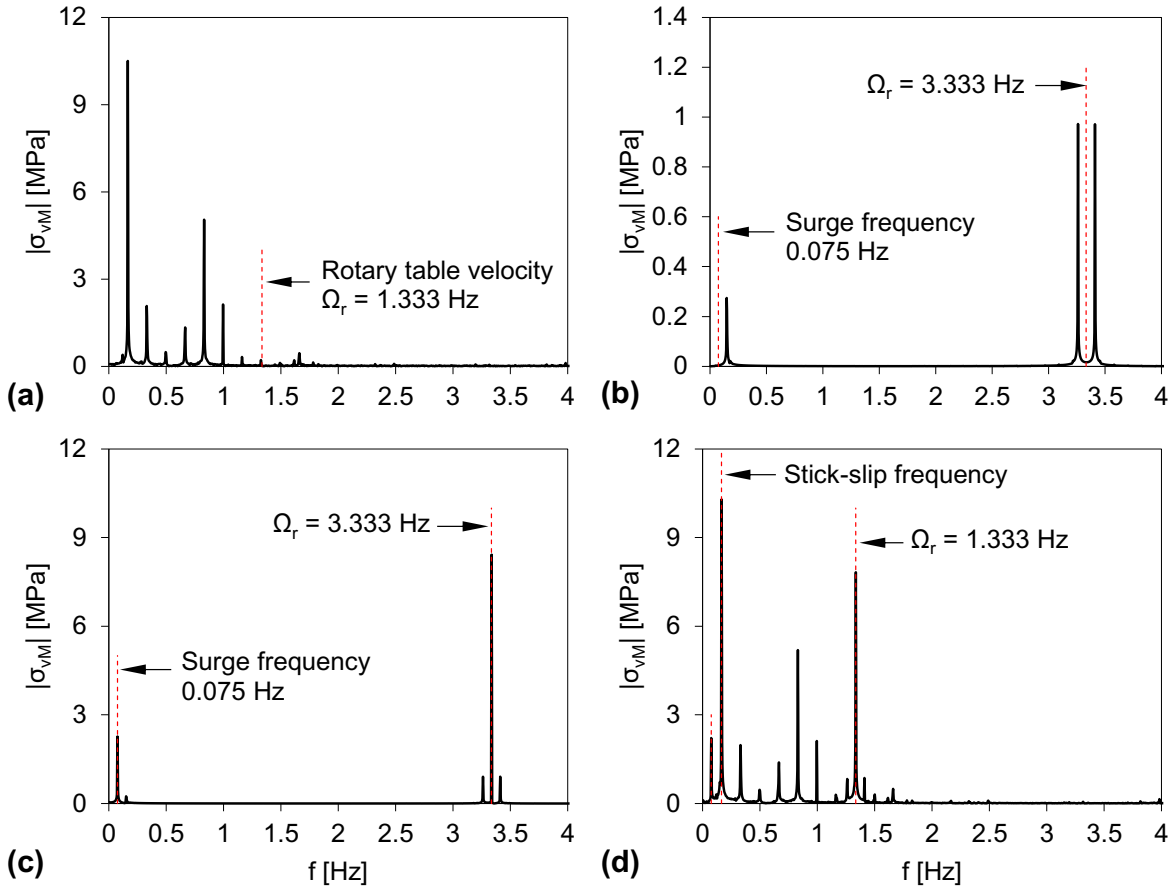

Figure 6-7. Fourier spectra of von Mises stress for the top-most drill pipe when the drill string is subjected to: (a) stick-slip vibration, (b) vessel surge motion, (c) vessel drift + surge motion, (d) stick-slip + vessel drift and surge motion. |σvM| denotes the amplitude of von Mises stress.

The trajectories of the drill pipe centre above the BOP stack under different scenarios are represented in Figure 6-8. It is clear from the figure that the lateral vibration of the drill pipes above the BOP stack follow the surge motion of the drilling vessel. The trajectories in x-z (horizontal) plane show that the combination of stick-slip vibration and vessel

motions increases the out-of-plane vibration of the drill pipe; see Figure 6-8. c. Indeed, analyzing the trajectory of the drill pipes below the BOP stack showed that their lateral motions were almost zero as they were decoupled from the lateral motions of the drilling vessel due to the presence of flex joint. The effect of excitation loads are also illustrated in phase-plane projections in Figure 6-9.

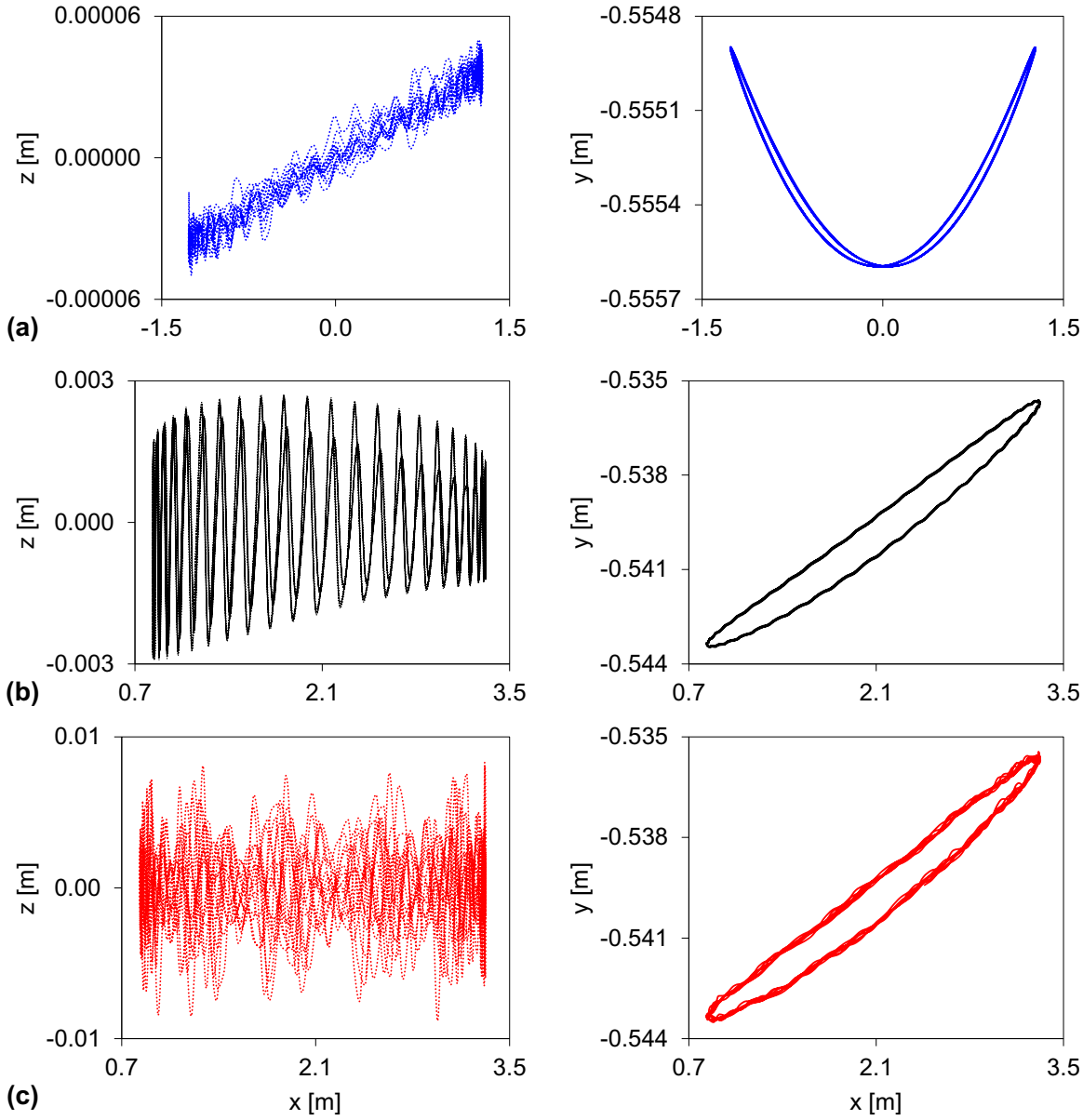

Figure 6-8. Horizontal (left) and vertical (right) trajectories of the centroid of rotating drill pipe above (-500 m) the BOP stack: (a), (b), and (c) correspond to scenarios B, C, and D, respectively. Note that for pipe cross-section, the beam axis passes though the centroid of the beam section.

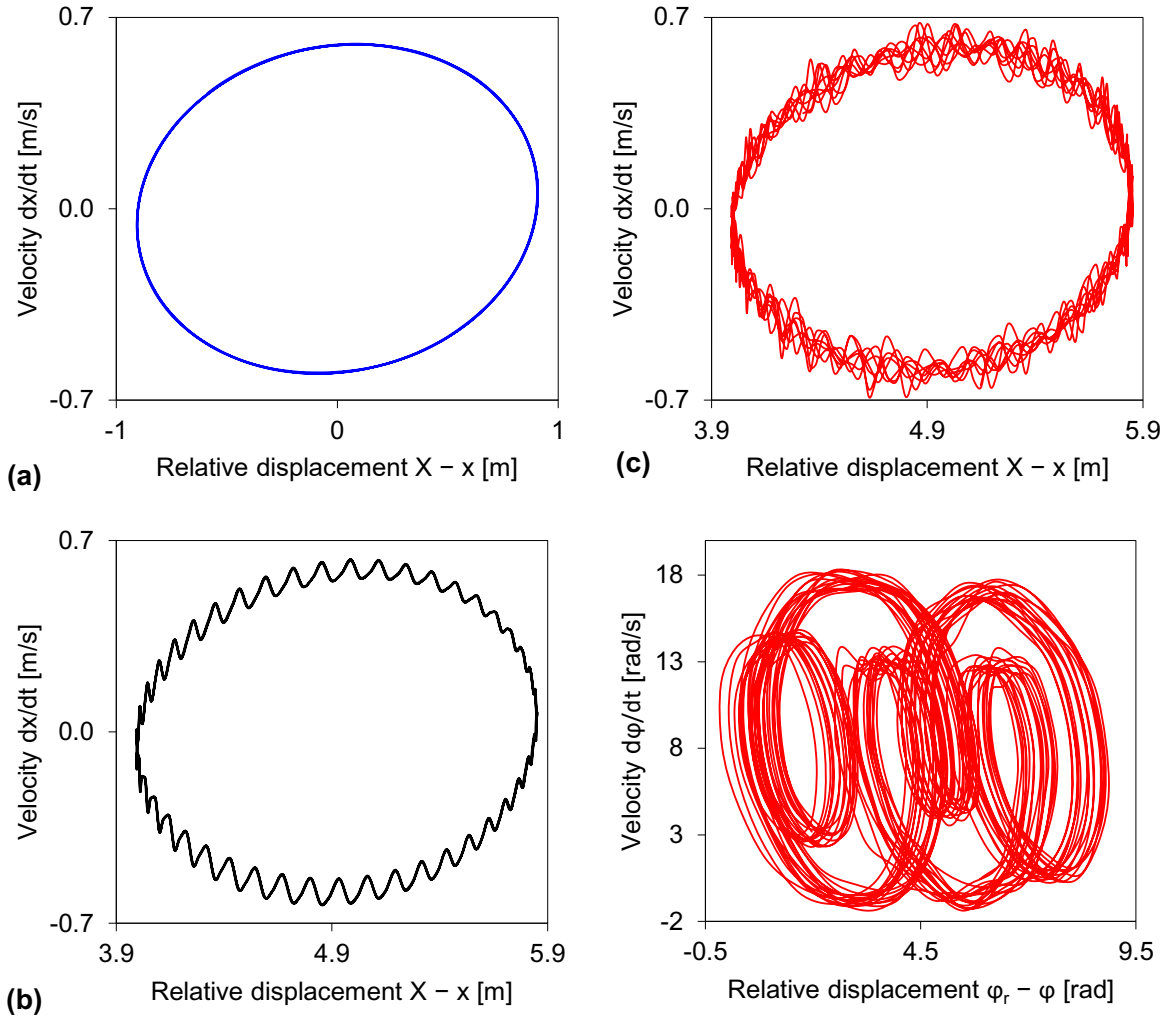

Figure 6-9. Phase-plane projections of drill pipe (-500 m) due to: (a) vessel surge motion, (b) vessel drift + surge motion, (c) stick-slip + vessel motion (drift + surge). X and x are the vessel and the drill pipe horizontal position, respectively; φ_r and φ are the rotary table and the drill pipe angular position, respectively.

6.5.1. Fatigue Reliability Assessment of Drill String

Fatigue reliability assessment of drill string was conducted based on the constraints and procedure established in Section 6.3. The values of von Mises stress were obtained along the drill string under different excitation scenarios including the stick-slip vibrations of the

dril string, the prescribed motions of the drilling vessel along with the drill string rotation, and the combination of both. The drilling vessel motions considered in this section included both the static drift and the harmonic surge. This criterion was chosen because the horizontal motions of the drilling vessel are most often a combination of harmonic surge (or sway) and drift (Hansford and Lubinski, 1970). Moreover, the mean and the alternating stress amplitudes of the drill string under the combined surge and drift were more severe than the pure harmonic surge; compare plot (b) with (c) in Figure 6-5 and Figure 6-7.

The drill pipes were assumed to be API E–75 grade, which is commonly used in offshore structure projects, with mechanical properties given in Table 6-3. To correct the endurance limit of the test specimen, the correction factors presented in Table 6-4 were used.

Figure 6-10. represents the variation of the corrected endurance limit, S_e, the alternating stress amplitude that causes crack initiation corrected for mean effects, S_a, and the maximum alternating stress amplitude due to excitation loading, σ_a.

Table 6-3. API E–75 mechanical properties

Mechanical property	Value
S_y = Minimum yield strength [MPa]	517
S_u = Minimum ultimate tensile strength [MPa]	690
S'_e = Minimum fatigue endurance limit for 10^6 cycles [MPa]	184

Table 6-4. Endurance limit correction factors; computed from Stephens et al. (2001)

Factor	Value
k_a (for machined surface finish)	0.798
k_b	0.706 for pipe section and 0.644 for collar section
k_c (corresponding to 8% standard deviation of the endurance limit)	0.868
k_f (for pipe section at the pipe-collar junction)	3
n	3

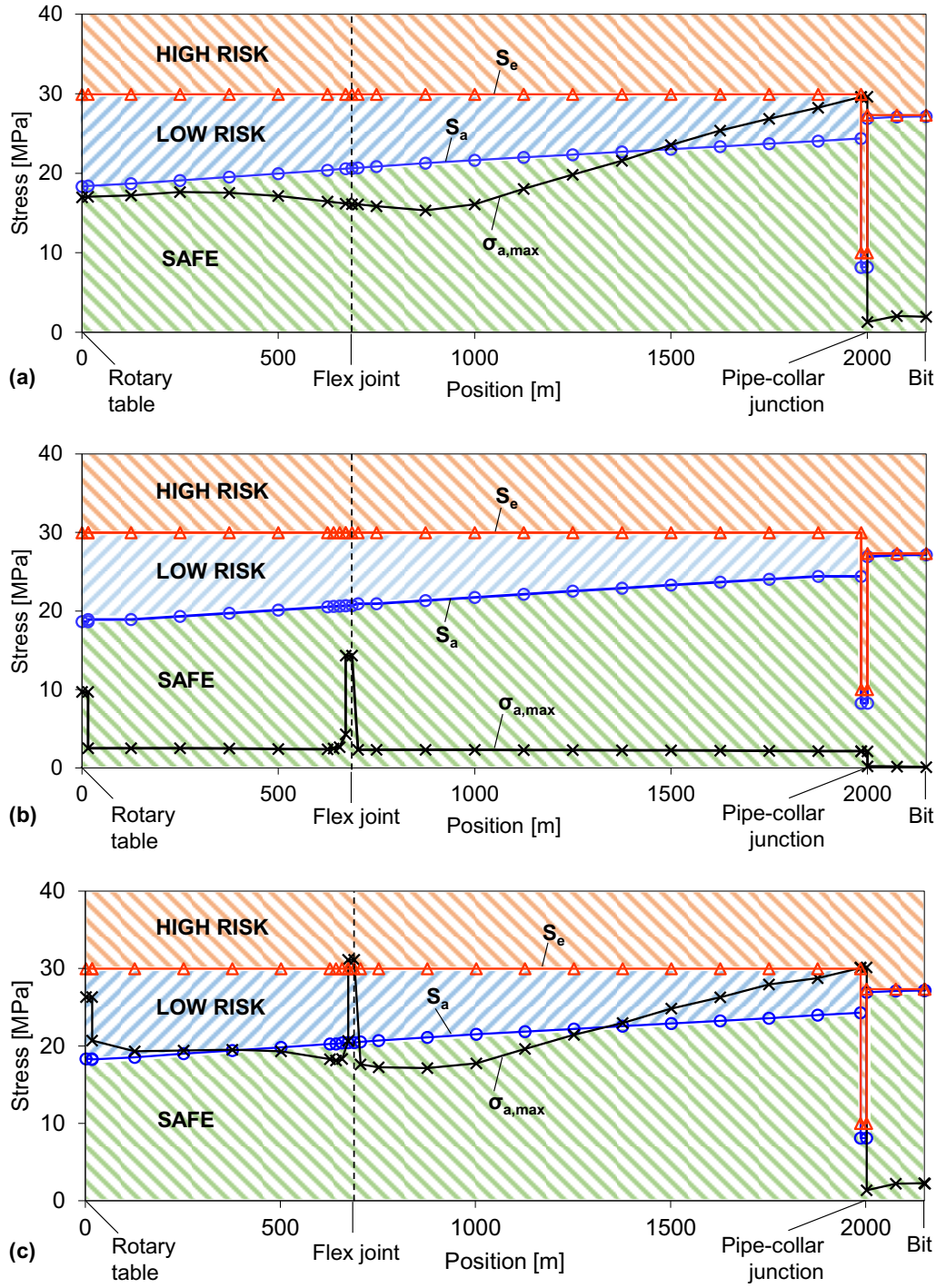

Figure 6-10. Illustration of the safe, low risk, and high risk zones along the drill string for three excitation scenarios computed for t = [600, 700] s: (a) torsional stick-slip without vessel motions, (b) vessel motions (harmonic surge + drift), and (c) stick-slip + vessel motions (harmonic surge + drift).

According to Figure 6-10. a, under torsional stick-slip vibrations, the drill pipes are subjected to higher alternating stresses compared to drill collars. This indicates that the stick-slip vibration is more exciting on the drill pipes fatigue than the drill collars. Also, it can be seen from the figure that the value of the induced alternating stress in the lower region of the drill pipe close to drill collar is three times greater than the endurance limit at the same region; $\sigma_{a,max}/S_e = 3$. Therefore, this region is in the high risk zone with the lowest reliability with respect to fatigue failure.

As illustrated in Figure 6-10. b, when the rotating drill string is subjected to the combined mean drift (1% of water depth) and wave-frequency motions of the drilling vessel, the maximum alternating stress amplitudes along the drill string are below the endurance limit. Therefore, the drill string operates in the safe region with respect to fatigue failure. The highest maximum alternating stresses occur in the upper region of the drill pipe close to the rotary table and in the area of BOP. This is due to sharp bending of the pipe in these regions, which exerts high-frequency cyclic stresses when combined with rotation. It is noted that the large alternating stresses in the drill pipe raise mainly from the drift of the drilling vessel, rather harmonic surge.

Figure 6-10. c shows the variation of alternating stress under simultaneous stick-slip vibration of the drill string and prescribed horizontal motions (drift + surge) of the drilling vessel. It can be seen that the maximum alternating stress in most of the drill pipes exceed S_a, which makes them vulnerable to fatigue damage. The critical regions of the drill pipe are the top segment connected to rotary table, the segment passing through the BOP, and the lowest segment connected to drill collar.

6.5.2. Cumulative Fatigue Damage Assessment

This section presents a quantitative comparison between the cumulative fatigue damage of the critical regions of the drill string under stick-slip vibration, vessel motions, and the combination of both. The cumulative fatigue damage under each excitation scenario was computed for the time interval t = [600, 700] s. This damage was then extrapolated to 1500 hour; which is a common frequency for drill pipes inspections (Ligrone et al., 1995), by multiplying it by 1500 hour × (3600 s/100 s). It is noted that this extrapolation method is valid due to limit cycling behaviour of the drill string under the excitation scenarios as depicted in Figure 6-9. Table 6-5 shows the computed fatigue damages.

Table 6-5. Fatigue damage at critical regions of drill string due to different excitation scenarios

Position	Stick-slip	Vessel motion (drift + surge)	Stick-slip + vessel motion (drift + surge)
0 m	4.82%	7.55%	16.24%
687.5 m	2.74%	14.46%	16.35%
2000 m (drill pipe end)	10.43%	0.00%	10.27%

6.6. Conclusions

Fatigue damage of deep-water offshore drill string occurs under mechanical vibrations, as well as horizontal movements of the drilling vessel from above the wellbore due to which the rotating drill pipe is bent. Despite numerous investigations with regard to modeling and

analyzing the mechanical vibrations, the behavior of drill string during deep-water drilling operations is yet to be understood. In this paper, the fatigue damage of an offshore drill string subjected to torsional stick-slip vibration and wave-induced motions of the drilling vessel was studied. A 3D FEM model of the drill string was developed using ABAQUS/Implicit package. The model accounted for the nonlinear bit-rock contact, horizontal motions of the drilling vessel, gravitational field, weight-on-bit, mud viscous damping (Rayleigh), and nonlinear geometry, i.e., large rotational displacement and geometric coupling between vibration modes. The reaction forces due to presence of the BOP stack and stabilizers were incorporated through appropriate boundary conditions. The stress time-series and the associated response spectra were analyzed. The cumulative fatigue damage and fatigue life were calculated along the drill string under different excitation scenarios.

The study showed that the mean drift of the drilling vessel had a great influence on the cyclic stresses, and thus fatigue damage, of the drill pipes at the top of the drill string and in the area of BOP. The effect of surge motion on the cyclic stresses of the drill pipes was negligible compared to mean drift offset. The results showed that the influence of stick-slip vibration on cyclic stresses of drill pipes was more severe compared to drill collars. The most vulnerable point of drill pipe under stick-slip vibration was at the pipe-collar junction.

The study showed that the coexistence of mechanical vibrations and wave-induced vessel motions is detrimental to reliable performance of the drill string, and can result in premature fatigue failure of some regions in the drill pipes. It was observed that the static translation of the drilling vessel dominates the maximum alternating stress amplitude of

the first drill pipe and the drill pipe at BOP area. Therefore, it is required to limit the allowable static translation to increase the fatigue life of the vulnerable drill pipes.

The FEM model and the methodology presented in this paper provides a novel and robust approach for dynamic analysis of drill string under coupled mechanical vibrations and drilling vessel motions. This methodology can be used for further investigation of dynamic response of drilling system during offshore operations.

6.7. Acknowledgments

The authors gratefully acknowledge the financial support of this research by Memorial University of Newfoundland through VP start-up fund.

References

Amado, L., 2013. Reservoir Exploration and Appraisal, Gulf Professional Publishing.

API Recommended Practice 7G, 1998. Recommended Practice for Drill Stem Design and Operating Limits, 16th ed. Washington DC, USA: American Petroleum Institute.

Brett, J. F., 1992. The Genesis of Bit-Induced Torsional Drillstring Vibrations. Society of Petroleum Engineers. https://doi.org/10.2118/21943-PA

Chopra, A.K., McKenna, F., 2016. Modeling viscous damping in nonlinear response history analysis of buildings for earthquake excitation. Earthq. Eng. Struct. Dyn. 45, 193–211. https://doi.org/10.1002/eqe.2622

Christoforou, A.P., Yigit, A.S., 2003. Fully coupled vibrations of actively controlled drillstrings. J. Sound Vib. 267 (5), 1029-1045, ISSN 0022-460X, https://doi.org/10.1016/S0022-460X(03)00359-6.

DNVGL-CG-0130, 2018 Edition, January 2018 - Wave loads

Dunayevsky, V.A., Abbassian, F., Judzis, A., 1993. Dynamic Stability of Drillstrings Under Fluctuating Weight on Bit. Society of Petroleum Engineers. doi:10.2118/14329-PA

Hansford, J. E., & Lubinski, A. 1964. Effects of Drilling Vessel Pitch or Roll on Kelly and Drill Pipe Fatigue. Society of Petroleum Engineers. doi:10.2118/696-PA

Hansford, J.E., Lubinski, A. 1970. Analysis of Some Factors Related to Permissible Horizontal Motions of a Floating Drilling Vessel. Society of Petroleum Engineers. doi:10.2118/2727-PA

Hansford, J.E., Lubinski, A., 1966. Cumulative Fatigue Damage of Drill Pipe in Dog-Legs. Society of Petroleum Engineers. doi:10.2118/1258-PA.

Hill, T.H., Seshadri, P.V., Durham, K.S., 1992. A Unified Approach to Drillstem-Failure Prevention. Society of Petroleum Engineers. doi:10.2118/22002-PA

Huang, L., Xue, Q., Liu, B., Yang, C., Wang, R., Han, L., 2019. Dynamic Reliability Analysis of Rotary Steering Drilling System, Mechanical Sciences 10 (1), 79–90. 10.5194/ms-10-79-2019

Jansen, J.D., van den Steen, L., 1995. Active damping of self-excited torsional vibrations in oil well drillstrings. J. Sound Vib. 179 (4), 647–668. https://doi.org/10.1006/jsvi.1995.0042

Ligrone, A., Botto, G., Calderoni, A. 1995. Reliability Methods Applied to Drilling Operations. Society of Petroleum Engineers. doi:10.2118/29355-MS

Macdonald, K.A., Bjune, J.V., 2007. Failure analysis of drillstrings. Engineering Failure Analysis, 14 (8), 1641-1666,

Mitchell, R.F., Miska, S., 2011. Fundamentals of Drilling Engineering. Society of Petroleum Engineers, Technology & Engineering

Moharrami, M.J., Shiri, H., 2018. Reliability assessment of drag embedment anchors in clay for catenary mooring systems. Marine Structures, 58, 342-360, ISSN 0951-8339,https://doi.org/10.1016/j.marstruc.2017.12.005.

Netto, T.A., Lourenco M.I., Botto, A., 2008. Fatigue performance of pre-strained pipes with girth weld defects: full-scale experiments and analysis. Int. J. Fatigue 30:767–778

Oden, J.T., Martins, J.A.C., 1985. Models and computational methods for dynamic friction phenomena. Computer Methods in Applied Mechanics and Engineering, 52 (1–3), 527–634. https://doi.org/10.1016/0045-7825(85)90009-X

Rayleigh, L., 1945. Theory of Sound, 1. Dover: New York, NY.

Sarpkaya, T., Issacson, M., 1981. Mechanics of Wave Forces on Offshore Structures. Van Nostrand Reinhold, NY.

Schijve, J., 2003. Fatigue of structures and materials in the 20th century and the state of the art. Int. J. Fatigue, 25(8), 679-702

Stephens, R,I., Fatemi, A., Stephens, R.R., Fuchs, H.O., 2001. Metal Fatigue in Engineering, 2nd ed. New York: Wiley.

7. Chapter 7

Conclusions and Recommendations

7.1. Conclusions

This research work resulted in important insight into the reliability floating offshore drilling platforms through tackling the drag acnhors and drill string as the key components of the system. The key findings can be summerized as follows:

- *Reliability of drag embedment anchor*
    - Anchor geometry, in particular, fluke length, is the primary influential parameter in reliability of drag embedment anchor with a significant contribution to the holding capacity, whereas anchor weight has almost no effect on the reliability of anchor.
    - Frictional capacity of chain is the secondary influential parameter in reliability of drag embedment anchor. The holding capacity at mudline is greater compared to holding capacity at padeye due to frictional soil-chain interaction.
    - In general, for a constant load to capacity ratio, the drag embedment anchors have a lower reliability index than suction anchors. This is due to complex geometry, uncertain installation trajectory and final embedment depth, uncertain soil properties and oversimplified failure mechanisms and capacity calculation of drag embedment anchors.
- *Drill string dynamics*

- The mean angular velocity of each point along the drill string is independent of the weight-on-bit and damping ratio, but directly related to the rotational velocity at the surface.
- Variation of rotary velocity is more influential with regard to the growth of the amplitude and standard deviation of stick-slip vibration at each point along the drill string, compared to the weight-on-bit and damping ratio.
- The stick-slip dominant frequency is dependent mainly on the angular velocity of the rotary table and decreases with decreasing the rotary velocity. Nevertheless, the dominant frequency appears to be independent of the weight-on-bit and damping for the considered drill string and operating conditions.
- Contribution of higher frequencies to the torsional stick-slip response of the drill collars/bit is negligible. However, noticeable peaks at frequencies close to the higher natural vibration modes of the system are observed in the response spectra of drill pipes under low rotary velocities. The intensity of the higher frequency components in the response of drill pipes increases with decreasing the rotary velocity.
- The mean drift of the drilling vessel is detrimental to fatigue life of the drill pipes at the top of the drill string and in the area of BOP due to sharp bending.
- The maximum alternating stress amplitude of drill pipes due to pure surge motion is considerably small compared to mean drift. Therefore, the static drift of the drilling vessel can be used for a conservative fatigue analysis of the drill pipes in the area of kelly and BOP stack.

- The torsional stick-slip vibrations significantly increase the magnitude of alternating stress amplitudes in drill pipes, especially in the lower region of the drill pipes close to drill collars. The large stress amplitude in this region is greater than the endurance limit of the material, and results in considerable fatigue failure risk. Although the risk of fatigue failure in drill collars is relatively small, the maximum fatigue damage in the collar section occurs around the bit.
- Combination of stick-slip vibration and vessel motions (drift + wave-frequency surge motion) is detrimental to reliable performance of the drill pipes. Under the combined loading, the drill pipes experience large amplitude cyclic shear (due to stick-slip vibration) and bending (due to vessel excursion) stresses, which result in equivalent stress amplitudes greater than the fatigue endurance limit.

7.2. Scientific/Engineering Contributions

This research work presented reliability assessment of drag embedment anchors using FORM, which has never been explored before. Almost all of the reliability analyses for anchors have focused on suction caissons.

Most of the FEM models addressing the torsional stick-slip vibration of the full-scaled drill string have ignored some important aspects of the problem, i.e., shear deformations, damping, and geometrical coupling between vibration modes. Furthermore, the behavior of the drill pipes as an extremely slender structure has been less explored in the literature. In this research work, the comprehensive dynamic analysis of the entire drill string using the developed FEM model provided insight into the stick-slip behavior of the drill pipes and drill collars under different operational conditions.

The problem of a rotating drill string under stick-slip vibrations coupled with the static and wave-frequency motions of the drilling platform is a gap of knowledge in the literature. The coupled FEM model of the drilling unit in this study provided basic building blocks for more comprehensive models, accommodating other dynamical phenomenon due to the drill string-wellbore interactions and the drilling platform motions. The fatigue reliability analysis of the drill string under both stick-slip and vessel motions resulted in identification of the risk zones of an offshore drill string during deep-water drilling operation.

7.3. Recommendations for Future Study

The ultimate holding capacity of a drag embedment anchor, and consequenctly the reliability index, are significantly affected by the soil properties and anchor geometry. Reliability analysis of these type of anchors in soil strata other than clay, i.e., sand and layered soil (clay over sand and sand over clay) is sugusted for future studies.

The use of First Order Reliability Method (FORM) for reliability analysis is a part of regular engineering analysis which provided scientifically contributory results in the present work. Other improved methods such as Second Order Reliability Method (SORM) could enhance the accuracy of the reliability results under the derived nonlinear limit state function, and are suggested for future studies.

The application of S-N curve for fatigue analysis is also part of routine engineering analysis which provides fatigue life of the structure without considering the inherent initial cracks. This means that a considerable portion of the estimated fatigue life is allocated to the crack initiation phase. Therefore, implementation of the fracture mehcnaics approach is suggested for fure works to account for the initial crack sizes on the drill string.

The axial, lateral, and torsional vibration modes of a drill string can be coupled. Dynamical behavior of the drill string under the coexistence of these vibrations is quite complex and can be further explored.

The consideration of drift (static) and wave-frequency surge motions of the floating platform combined with the stick-slip vibrations of the drill string provided insight into the response of the drill string during deep-water offshore drilling operations. In reality, the floating drilling platform experiences also vertical (heave) and rotational (i.e., roll and pitch) motions in response to the ocean waves. While during all operations, the heave motions are considerably isolated by using the heave compensator (HC) system installed on the top drive, the rotational motions of the platform can induce cyclic bending stresses in some areas of the rotating drill string. The coexistence of these cyclic stresses with those raising from vessel surge motions and stick-slip vibrations (presented in the current research work) are further detrimental to fatigue life of the drill string. The combination of these loading mechanisems could give more realistic estimation of the drill string's fatigue life, and is recommended for future studies.

Appendix A

Reliability of Drag Embedment Anchors for Applications in Canadian Deep Offshore

Mohammad Javad Moharrami[1], Hodjat Shiri[2]

1: Department of Civil Engineering

Memorial University of Newfoundland

e-mail: mjmoharrami@mun.ca

2: Department of Civil Engineering

Engineering, Memorial University of Newfoundland

e-mail: hshiri@mun.ca

This chapter was published in the conference proceedings of GeoEdmonton 2018.

Abstract

Reliability analysis was applied to calculate the failure probability of drag embedment anchors for intact catenary mooring lines (ULS). The probabilistic characterization of the seabed soil condition and environmental loading was associated to the Newfoundland and Labrador's (NL) deepwater sites (e.g. the Flemish Pass Basin). The ultimate holding capacity of the anchor was modeled using plastic yield loci incorporating the profile and frictional capacity of the embedded anchor chain. The dynamic line tensions were extracted from time domain analyses of a generic floating system subjected to environmental loadings. The reliability analysis was performed using First-order reliability method (FORM).

Résumé

Une analyse de fiabilité a été appliquée pour calculer la probabilité de défaillance des ancrages traînée pour les lignes caténaire intactes (ULS). La caractérisation probabiliste de l'état du sol du fond marin et de la charge environnementale a été associée aux sites d'eau profonde de Terre-Neuve-et-Labrador (TNL) (par ex. Le bassin du col Flemish). La capacité de rétention ultime de l'ancre a été modélisée en utilisant des locus de rendement en plastique incorporant le profil et la capacité de frottement de la chaîne d'ancrage intégrée. Les tensions de ligne dynamiques ont été extraites d'analyses temporelles d'un système flottant générique soumis à des charges environnementales. L'analyse de fiabilité a été effectuée en utilisant la méthode de fiabilité du premier ordre.

A.1. Introduction

Drag embedment anchors have been widely used in station-keeping systems of drilling and production vessels. These anchors are usually implemented along with catenary mooring lines, which arrive the seabed horizontally to withstand the large horizontal offsets of the floating unit due to the environmental loads. A drag anchor is mainly comprised of shank, fluke, padeye, and forerunner (the anchor chain embedded in the soil) and is pulled in to the seabed to reach its ultimate resistance. Several parameters such as anchor geometry, soil characteristics, applied loads, and type of mooring line can affect the performance and capacity of the drag anchor (Vryhof Anchors 2010). The uncertainties associated with these parameters, as well as difficulties in inspection and maintenance of embedded facilities in deepwater sites indicate the necessity of reliability based design and analysis of drag anchors.

A review of the previous studies shows that several researches have been conducted on reliability assessment of suction caissons both numerically and experimentally. Clukey et al. (2000) conducted the reliability analysis of suction caissons for catenary and taut-leg mooring systems for lateral and axial failure modes using FORM and SORM. Choi (2007) studied the reliability of suction caissons by estimating the caisson capacity at the padeye using the upper bound plastic limit equation proposed by Aubeny et al. (2003a) and considered the soil-chain interaction based on the Neubecker and Randolph (1995a) formulation. Valle-Molina et al. (2008) modeled the suction caisson capacity for a Floating Production Storage and Offloading (FPSO) vessel based on the plastic limit equations proposed by Aubeny et al. (2003a, 2003b, and 2003c) and applied Monte Carlo simulation

for reliability assessment. Silva-Gonzalez et al. (2013) evaluated the reliability of suction caissons using FORM through probabilistic modelling of caisson capacities and formulated a linear relationship between caisson height and probability of failure.

Despite suction caissons, there is a considerable gap in reliability assessment of drag embedment anchors and only one study has been conducted in this area. Moharrami and Shiri (2018) assessed the reliability of drag anchors for catenary mooring lines using FORM. The authors developed an Excel spreadsheet Visual Basic Application (VBA) Macro based on a limit equilibrium model proposed by Neubecker and Randolph (1995b) and a yield loci approach proposed by O'Neil et al. (2003) to calculate the anchor capacity taking into account the soil-chain interaction effect. They used response surface method to express the line tensions as a function of uncertain metocean variables and studied the relative reliability of drag anchors and suction caissons.

The present study deals with reliability analysis of drag embedded anchors used in the Flemish Pass Basin located in offshore Newfoundland and Labrador (NL), Canada. During past decades, offshore NL has been of great interest for oil and gas exploration and production projects. The unique metocean and geotechnical characteristics of this region, however, has caused further complexity to the design and installation of drilling and production facilities. Flemish Pass is a north-south trending, mid-slope basin with a water depth ranging from 500 to 1500 m located over 450 km off the east coast of NL between the Grand Banks and the Flemish Cap (Figure A-1). With an area of approximately 30,000 km2, the Flemish Pass is a region of active hydrocarbon exploration including three recent discoveries; Mizzen, Bay du Nord, and Harpoon. Based on geophysical studies, the seabed

of Flemish Pass Basin is mainly composed of large debris flow deposits (Brown et al. 2016).

Figure A-1. Location of the Flemish Pass Basin (image from http://www.ceaa-acee.gc.ca/050/evaluations/proj/80129)

A.2. Capacity Assessment

Simulations of anchor capacity were conducted at mudline using the Excel spreadsheet VBA Macro developed by Moharrami and Shiri (2018). The Excel spreadsheet estimates the anchor holding capacity based on a limit equilibrium model (LEM) originally proposed by Neubecker and Randolph (1995b) and a yield locus approach proposed by O'Neill et al. (2003).

The effects of soil-chain interaction were taken into account for two reasons. First, the friction between soil and the embedded chain will reduce the tension load transferred from mudline to the padeye and can have a slightly large contribution to the ultimate holding

capacity of the anchor. Neubecker and Randolph (1995b) developed the following equation to calculate the frictional capacity along the chain incorporating the self-weight of the chain into the total tension capacity:

$$T = T_a e^{\mu(\theta_a - \theta)} + \mu w s \tag{11}$$

where T is the tension in the chain, T_a is the chain tension at the anchor padeye, μ is the soil-chain friction coefficient, θ_a is the chain inclination at the anchor padeye, θ is the chain angle at any given point, w is the chain self-weight per unit length, and s is the length of the embedded chain.

The second reason for considering the soil-chain interaction is that it affects the loading direction at the padeye and consequently the holding capacity of the anchor. To calculate the loading angle at the padeye, an expanded form of the equation proposed by Neubecker and Randolph (1996) was used:

$$\theta_a = \left[\frac{2 b_c N_c d_a (s_{u0} + 0.5 s_{ug} d_a)}{T_a}\right]^{0.5} \tag{12}$$

where b_c is the effective width of the anchor chain, N_c is the bearing capacity factor, d_a is the padeye embedment depth, s_{u0} is the surface undrained shear strength, and s_{ug} is the undrained shear strength gradient with depth.

The anchor holding capacity and the fluke tip depth obtained from the developed Excel spreadsheet (Moharrami and Shiri 2018) were compared with those from finite element analysis (O'Neil et al. 2003), test results (Neubecker and Randolph 1996), and practical anchor design charts (Vryhof Anchors 1990) based on the input parameters given in Table A-1. Figure A-2 and Figure A-3 illustrate the results of comparisons.

Table A-1. Parameters used in yield locus analysis for a 32 t MK5 Vryhof Stevpris anchor (Moharrami and Shiri 2018)

Parameter	Value
Fluke length, L_f (m)	4.97
Fluke width, b_f (m)	4.23
Fluke thickness, d_f (m)	0.71
Bearing capacity factor, N_c	9
Undrained shear strength at mudline, s_{u0} (kPa)	0
Undrained shear strength gradient, s_{ug} (kPa/m)	1.5

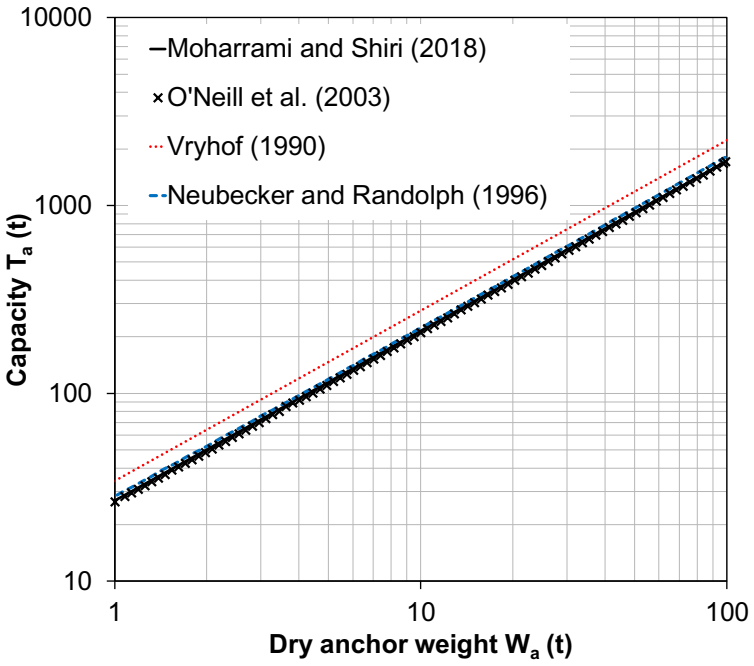

Figure A-2. Comparison of anchor capacity in soft clay

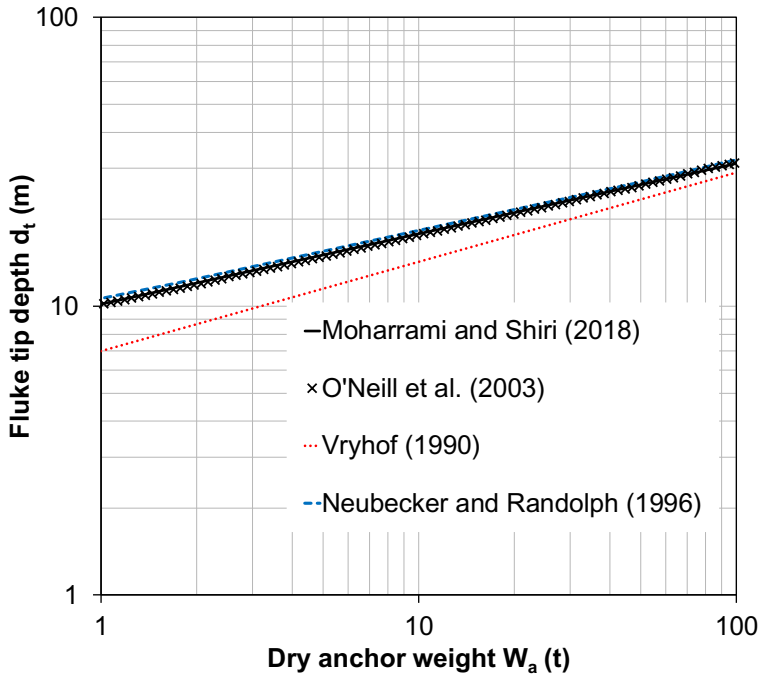

Figure A-3. Comparison of fluke tip depth in soft clay

A.3. Load Assessment

A semisubmersible platform with catenary mooring system was modeled using finite element analysis (FEA) to calculate the line tensions applied to the anchor. The mooring system consists of four (2×4) groups of lines as shown in Figure A-4. Each line has a combination of upper chain, middle wire, and bottom chain. The spacing between each group is 90 degrees and each line in the same group is separated by 45 degrees spacing. The extreme sea states of the Flemish Pass Basin with 100 years return period and a water depth of 700 m were considered to calculate the environmental loads on the platform and the resultant mooring line tensions.

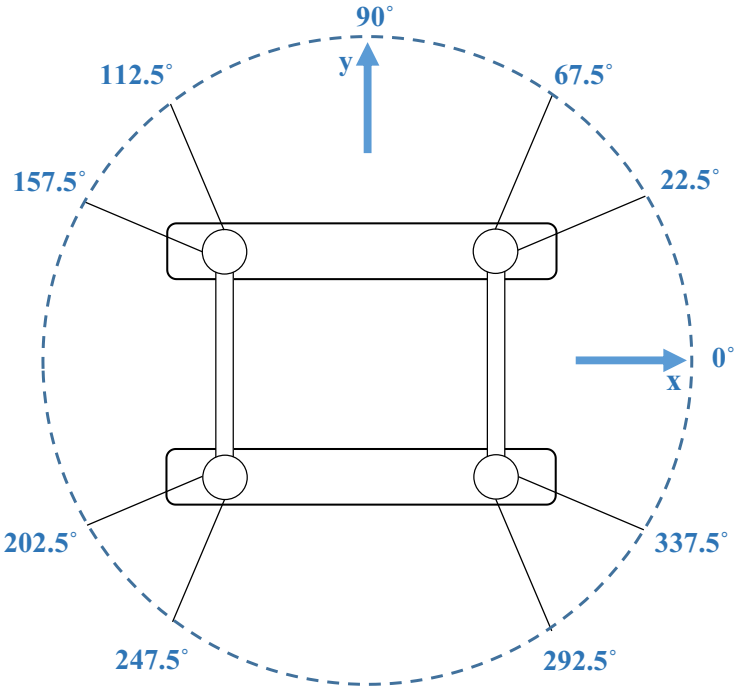

Figure A-4. Catenary mooring system pattern

The line tensions were estimated at touchdown point through 3 h time histories and were expressed in terms of mean and expected value of maximum dynamic tension. Assuming the dynamic tension as a Gaussian process, the expected maximum dynamic line tension was calculated based on the model proposed by Davenport (1964):

$$\mathrm{E}[T_{dyn,max}] = \left[\sqrt{2\ln(\nu\Delta t/2)} + \frac{0.5772}{\sqrt{2\ln(\nu\Delta t/2)}}\right]\sigma \tag{13}$$

where Δt is the duration of the extreme sea state, and σ and ν are the standard deviation and the mean-crossing rate of the dynamic tension, respectively

A.4. Reliability Analysis

Reliability analysis of drag embedment anchors was performed using FORM. In this method, the uncertainties associated with both environmental loadings and anchor capacity

are taken into account to determine the failure probability of drag anchor. The failure is related to exceeding a limit state i.e. line tension exceeding the anchor resistance.

The drag anchor was designed based on the recommended practice of Design and Installation of Fluke Anchors published by Det Norske Veritas, DNV-RP-E301 (DNV 2012). The holding capacities were calculated for four Mk5 Vryhof Stevpris anchors with a fluke length-fluke thickness ratio of 6.67. The main dimensions of a typical drag anchor are shown in Figure A-5, where F represents the fluke thickness. Table A-2 summarizes the characteristics of the anchor.

The limit state function was formulated at mudline, and the effects of soil-chain interaction were taken into account only in calculation of the ultimate holding capacity. In such case, the extreme complexity of reliability analysis due to the dependence between applied load and anchor capacity is neglected. Furthermore, the effect of frictional capacity of the embedded chain is properly associated with the ultimate holding capacity of the anchor, and the uncertainties of the chain are ignored. A similar method was used before in reliability assessment of suction anchors and drag embedment anchors (Choi 2007, Gonzalez et al. 2013, and Moharrami and Shiri 2018).

DNV (2012) presents two limit states to be considered for geotechnical design of fluke anchors:

1) Ultimate Limit State (ULS) to ensure that each mooring line can withstand the extreme environmental loads that it is subjected to. The ULS design requires individual mooring lines to be analyzed under extreme loading in the intact condition.

2) Accidental Limit State (ALS) to ensure that the mooring system can withstand the failure of one mooring line due to unknown reasons. The ALS design requires the analysis of damaged mooring system with one line removed.

Two failure consequence classes are possible for each limit state; consequence class 1 in which failure is unlikely to cause unacceptable consequences i.e. life lost, collision or uncontrolled oil and gas production, and consequence class 2 in which failure may cause unacceptable consequences. The target annual probability of failure for each limit state and consequence class is given in

Table A-3.

Based on DNV (2012), the limit state equation is expressed in terms of anchor holding capacity and mooring line tension at mudline:

$$G = R_d - T_d \tag{14}$$

where G is the limit state function, R_d is the design capacity of anchor-chain system at mudline, and T_d is the design line tension at mudline which can be expressed as follows:

$$T_d = T_{mean-C}\gamma_{mean} - T_{dyn-C}\gamma_{dyn} \tag{15}$$

where T_{mean-C} is the characteristic mean line tension due to pretension and mean environmental loads, $T_{dyn,-C}$ is the characteristic dynamic line tension due to low frequency and wave frequency motions, γ_{mean} is the load factor on the mean tension, and γ_{dyn} is the load factor on the dynamic tension. Table A-4 presents the load factors for ULS and ALS conditions.

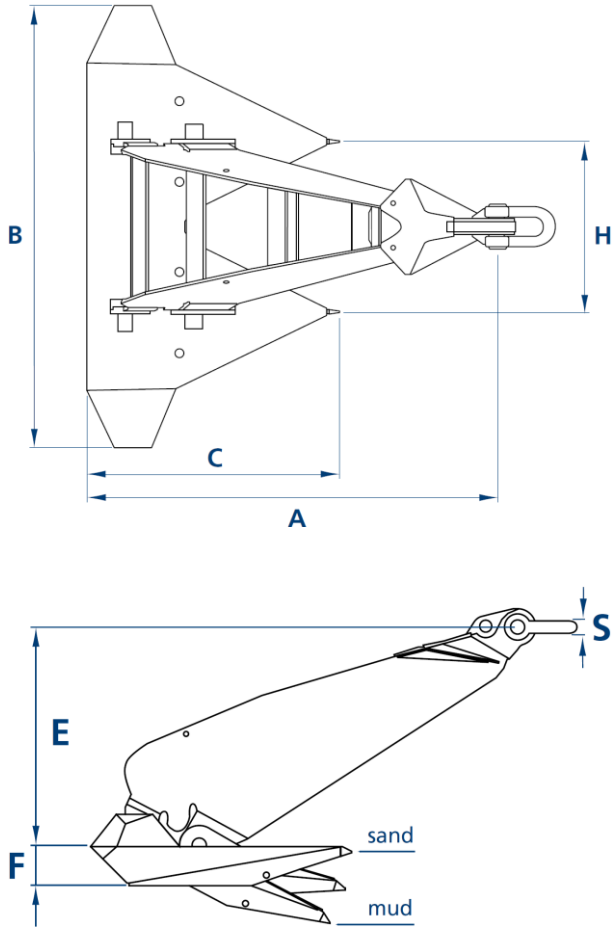

Figure A-5. Anchor dimensions (Vryhof Anchors 2010)

Table A-2. Main dimensions for Mk5 Vryhof Stevpris 22 t (Vryhof Anchors 2010)

Parameter	Value
A	7230 mm
B	7794 mm
C (L_f)	4436 mm
E	3684 mm
F (d_f)	665 mm
H	3011 mm
S	200 mm

Table A-3. Target annual probability of failure (DNV 2010a)

Limit state	Consequence class 1	Consequence class 2
ULS	10E-4	10E-5
ALS	10E-4	10E-5

Table A-4. Partial safety factors for dynamic analysis (DNV 2012)

Limit state	Consequence class	γ_{mean}	γ_{dyn}
ULS	1	1.10	1.50
ULS	2	1.40	2.10
ALS	1	1.00	1.10
ALS	2	1.00	1.25

The probability of failure is defined as the probability of design tension exceeding the design holding capacity of the anchor:

$$P_f = P(R_d < T_d) = P(G < 0) \tag{16}$$

A.5. Results

The results in this section are presented for reliability of drag embedment anchors in soft clay using FORM. Figure A-6 shows the annual reliability index for different anchor geometries as a function of fluke length. Based on the results illustrated in this figure, an average increase of 4.61% in fluke length, which corresponds to an average increase of 14.54% in anchor weight, can increase the reliability index about 11%. This indicates that the anchor weight does not have a significant contribution to the capacity of deeply buried drag anchors in soft clay, and their reliability is considerably affected by the fluke length. Figure A-7 shows the variation of annual probability of failure, p_{Fa}, versus fluke length.

Based on this figure, in order to achieve a target failure probability between 10^{-4} and 10^{-5}, either the 22 t anchor with a fluke length of 4.436 m, or the 25 t anchor with a fluke length of 4.629 m can be used. This range of target probability of failure is used for the ultimate limit state design of offshore systems (DNV 2010a, 2010b, 2012, and 2013), which corresponds to reliability indices between 3.72 and 4.26.

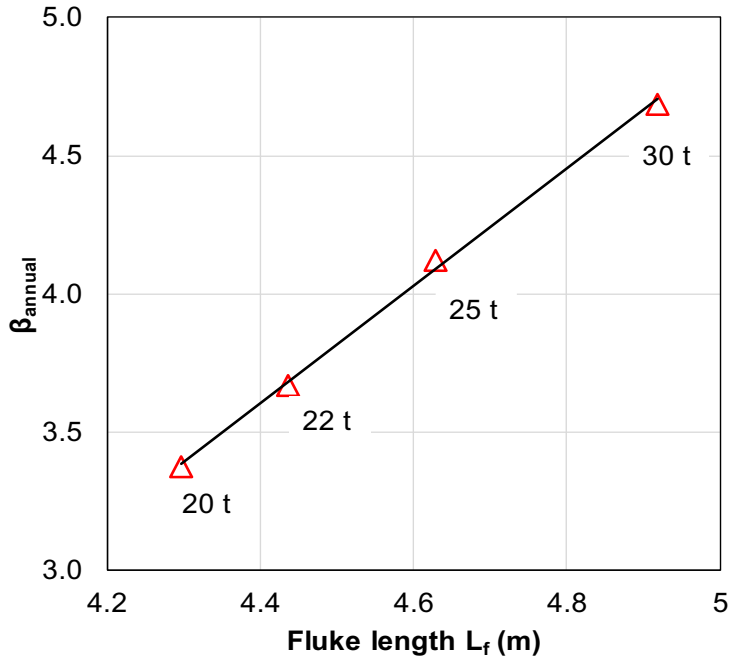

Figure A-6. Annual reliability index versus fluke length

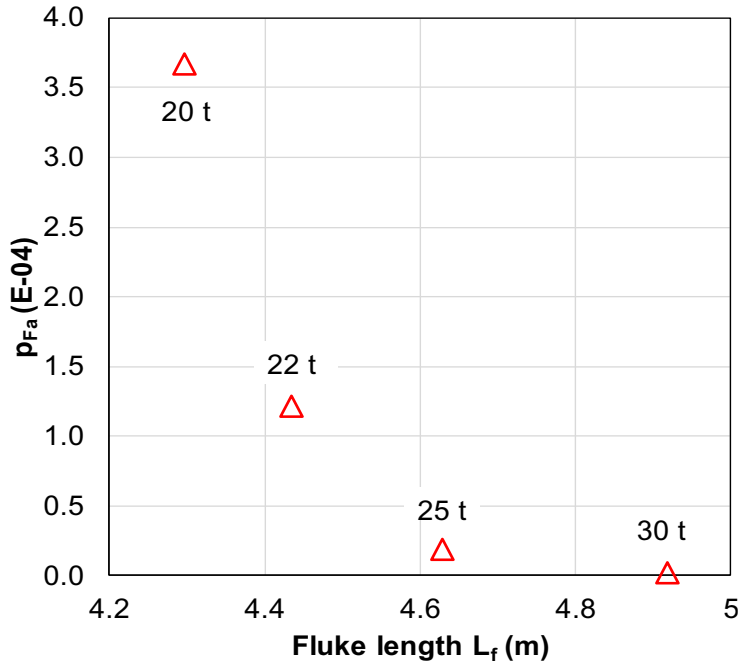

Figure A-7. Annual failure probability versus fluke length

A.6. Conclusion

In this study, the reliability of drag embedment anchors for catenary mooring systems was analyzed using FORM. The metocean characteristics and soil data of the Flemish Pass Basin in offshore Newfoundland and Labrador (NL), Canada, were used. Four drag anchors with a fluke length-fluke thickness ratio of 6.67 were analyzed. A fully coupled time domain analysis of a semisubmersible platform was performed to determine the line tensions at mudline. An Excel spreadsheet VBA Macro was implemented to estimate the anchor capacities at mudline considering the embedded profile of the chain and the soil-chain interaction. The ultimate limit state equation was formulated at mudline taking into account the uncertainties associated with the soil properties and metocean parameters. The anchor models with reliable performance were determined based on the target failure

probability of 10^{-5} for consequence class 2. Annual reliability indices and failure probabilities were expressed in terms of fluke length. The results show that the reliability index of drag anchors embedded in soft clay depends on the fluke length and is largely irrelevant to the anchor weight.

A.7. Acknowledgments

The authors gratefully acknowledge the financial support of this research by Memorial University of Newfoundland through VP start-up fund.

References

Aubeny, C., Han, S.W., Murff, J.D. 2003c. Suction caisson capacity in anisotropic, purely cohesive soil. Int. J. Geomech.

Aubeny, C.P., Han, S., Murff, J.D. 2003a. Refined model for inclined load capacity of suction caissons. Proceedings of OMAE 22nd International Conference on Offshore Mechanics and Arctic Engineering. Cancun, Mexico.

Aubeny, C.P., Han, S.W., Murff, J.D. 2003b. Inclined load capacity of suction caissons. Int. J Numer. Anal. Methods Geomech.

Brown, M., Power, D., King, T., McAffee, R., Dodge, K. 2016. Deepwater Newfoundland and Labrador; Technology Application and Opportunities for Exploration and Production, Proceedings of Arctic Technology Conference OTC 27468, St. John's, Newfoundland and Labrador.

Choi, Y.J. 2007. Reliability assessment of foundations for offshore mooring systems under extreme environments [dissertation]. The University of Texas at Austin.

Clukey, E., Banon, H., Kulhawy, F. 2000. Reliability assessment of deepwater suction caissons. Proceedings of Offshore Technology Conference OTC 12192, Houston, Texas.

Davenport, A.G. 1964. Note on the distribution of the largest value of a random function with applications to gust loading. Proceedings of the Institution of Civil Engineers, London, England, Volume 28, Issue 2, pp. 187-196

Det Norske Veritas. 2010a. Position Mooring. Offshore Standard DNV-OS-E-301.

Det Norske Veritas. 2010b. Dynamic Risers. Offshore Standard DNV-OS-F201.

Det Norske Veritas. 2012. Design and Installation of Fluke Anchors. Offshore Standard DNV-RP-E301.

Det Norske Veritas. 2013. Submarine Pipeline Systems. Offshore Standard DNV-OS-F101.

Moharrami, M.J. and Shiri, H. 2018. Reliability assessment of drag embedment anchors in clay for catenary mooring systems, Marine Structures, 58:342-360.

Neubecker, S.R. and Randolph, M.F. 1995a. Performance of embedded anchor chains and consequences for anchor design. Proceedings of Offshore Technology Conference OTC 7712, Houston, Texas.

Neubecker, S.R. and Randolph, M.F. 1995b. Profile and frictional capacity of embedded anchor chains. J. Geotech. Eng., Volume 121, Issue 11, p.p. 787-803

Neubecker, S.R. and Randolph, M.F. 1996. The performance of drag anchor and chain systems in cohesive soil. Mar. Georesources Geotechnol.

O'Neill, M.P., Bransby, M.F., Randolph, M.F. 2003. Drag anchor fluke-soil interaction in clays. Can. Geotech. J.

Silva-Gonzalez, F., Heredia-Zavoni, E., Valle-Molina, C., Sanchez-Moreno, J., Gilbert, R.B. 2013. Reliability study of suction caissons for catenary and taut-leg mooring systems. J. Struct. Saf.

Valle-Molina, C., Heredia-Zavoni, E., Silva-González, F.L. 2008. Reliability analysis of suction caissons for FPSO systems. Proceedings of the ASME 27th International Conference on Offshore Mechanics and Arctic Engineering OMAE 57140, Estoril, Portugal, pp. 1–6.

Vryhof Anchors. 1990. Anchor manual. Krimpen ad Yssel, The Netherlands.

Vryhof Anchors. 2010. Anchor manual. Krimpen ad Yssel, The Netherlands.

Appendix B

Analytical Modeling of Well-Conductor Seabed Interaction in Complex Layered Soil in Newfoundland Offshore

Etido Gideon Akpan[1], Xiaoyu Dong[2], Mohammad Javad Moharrami[3] & Hodjat Shiri[4], Hodjat Shiri[2]

1: Department of Civil Engineering

Memorial University of Newfoundland

e-mail: egakpan@mun.ca

2: Department of Civil Engineering

Engineering, Memorial University of Newfoundland

e-mail: xiaoyu.dong@mun.ca

3: Department of Civil Engineering

Memorial University of Newfoundland

e-mail: mjmoharrami@mun.ca

4: Department of Civil Engineering

Engineering, Memorial University of Newfoundland

e-mail: hshiri@mun.ca

This chapter was published in the conference proceedings of Geo St. John's 2019.

Abstract

This paper presents an analytical study of the well-conductor in complexly layered soil by providing a theoretical basis for the stability of wellhead. Arbitrary seabed soil stratum from Newfoundland deep offshore was considered, where the seabed sediments have distinct layers with varying properties and thickness which has a certain effect on the lateral loading capacity of the casing string. Considering the lateral loads on the top of the casing string, variable stiffness of casing string and the geomechanical characteristics of the soil layers, the differential equation of casing deflection and its solutions were established below the mudline, and the results of the modal analysis were obtained. The study revealed the importance of soil layers with different stiffness on the peak bending moment and deflection of the conductor system. The influence is more significant in the shallower layers closer to the sea bottom. It was observed that an in-depth knowledge about the geological data of the layered soil is of paramount importance for the accurate design of the conductor and surface casing. The analytical approach was found an appropriate system for early assessment of conductor system performance in layered soil condition.

RÉSUMÉ

Cet article présente une étude analytique du conducteur de puits dans un sol à couches complexes en fournissant une base théorique pour la stabilité de la tête de puits. On a examiné la couche de sol arbitraire des fonds marins de Newfoundland au large des côtes, où les sédiments des fonds marins ont des couches distinctes ayant des propriétés et une

épaisseur variables, ce qui a un effet certain sur la capacité de charge latérale de la colonne de cuvelage. Compte tenu des charges latérales au sommet du train de tassement, de la rigidité variable de celui-ci et des caractéristiques géomécaniques des couches de sol, l'équation différentielle de la flexion du tubage et ses solutions ont été établies sous la ligne de boue et les résultats de l'analyse modale ont été obtenus. L'étude a révélé l'importance de couches de sol de rigidité différente sur le moment de flexion maximal et la déflexion du système conducteur. L'influence est plus importante dans les couches moins profondes plus proches du fond de la mer. Il a été observé qu'une connaissance approfondie des données géologiques du sol stratifié était d'une importance primordiale pour la conception précise du conducteur et de la gaine. L'approche analytique s'est révélée être un système approprié pour l'évaluation précoce de la performance du système de conducteur dans des conditions de sol en couches.

B.1. Introduction

Typical offshore drilling operations are carried out using drilling risers and subsea Blowout Preventer (BOP) stacks deployed from drilling rigs. The BOP is placed on top of the subsea wellhead sometimes called the mudline wellhead which is located at sea bottom. While drilling the oil well, surface pressure control is provided by a blowout preventer (BOP).

If the pressure is not contained during drilling operations by the column of drilling fluid, casings, wellhead, and BOP, a well blowout could occur. Since the force transferred to wellhead through the bottom joint of the riser and the weights of BOP stack and all casing strings themselves have been undertaken by conductor and surface casing, vertical load-bearing capacity is important for determination of running depth of conductor and providing basis for prohibition of wellhead sinking (Guan et al., 2009).

However, conductor-seabed interaction plays a vital role in well integrity assessment in deep water drilling operation. Layered soil strata are often found in Newfoundland offshore. The ability to understand the interaction between the layered seabed and the casing string is essential for the accurate design and analysis of the conductor systems. Analytical solutions are very useful for the fast assessment of the riser performance at the early stages of design, prior to comprehensive numerical simulations. The seabed soil stratum is usually modeled with simplified homogeneous media represented by linear elastic springs. Variation of the soil stiffness through different soil layers may affect the structural response of the conductor system.

In this study, the differential equations proposed by Guan et al. (2009) were solved and the layered soil data from NL offshore was used to analytically investigate the lateral response of the well-conductor system.

B.2. Layered Seabed Soil in Newfoundland Offshore

Complex layered soil is quit common in NL offshore such as Flemish Pass Basin, 500 km away from St. John's coast line. The layered soil are also regularly observed in other Canadian offshore territories such as Beaufort Sea. Blasco et al. (1990) found that marine and continental regions are layered in Canadian Beaufort shelf. The overview of historical Beaufort Sea according to Timco and Frederking shows that the subsea sediments of Beaufort sea consist of 0.5m to 35m marine clays or silty clays.

In order to provide geotechnical engineering data for design of the conductor in the Jeanne d'Arc Basin, an investigation was done by Thompson et al. (1983). Sediments in this region consist of discontinues and thin layers of stiff clay.

Therefore; one of the most important parameters that may have influence on the mechanisms of the soil and soil deformation is the soil discontinuity such as soil layering. Many of the theoretical solutions have been developed for homogeneous seabed soil condition without considering the effect of different layers stiffness. This may have significant impact on system performance.

The layered soil properties that were used in the current study are given Table B-1 and Table B-2.

Table B-1. Layered soil properties in central FPB

components	depth (m)	initial modulus (kN/m3) undrained shear strength (MPa)	dry density (Mg/m3)	underwater bulk density (kN/m3)	at depth
very dense sand	0 7	14.7	1.676	6.63156	7
layered sands and clays	7 11	0.083	1.618	6.06258	63.3
very dense to dense sand	11 60	14.7	1.818	8.02458	18.33
hard silty clay	60 63	0.216	1.666	6.53346	61.6
layered sand, silt and clay	63 74.2	0.083	1.618	6.06258	63.3
hard silty clay	74.2 79	0.216	1.666	6.53346	61.6
layered sand, silt and clay	79 92	0.083	1.618	6.06258	63.3
hard silty clay	92 96	0.465	1.297	2.91357	95.4
layered sand, silt and clay	96 104	0.626	1.329	3.22749	95.5

Table B-2. Layered soil properties in Western FPB

components	depth (m)	initial modulus (kN/m3) undrained shear strength (MPa)	dry density (Mg/m3)	underwater bulk density (kN/m3)	at depth
very dense to dense sand	0 40.8	14.7	1.676	6.63156	26.35
hard silty clay	40.8 43	0.465	1.297	2.91357	95.4
dense sand	43 51.5	14.7	1.676	6.63156	7
hard clay	51.5 55.5	0.405	1.346	3.39426	54.4
layered sand, silt and clay	55.5 66.2	0.083	1.618	6.06258	63.3
hard silty clay	66.2 74	0.45	1.33	3.2373	71.4
layered sand, silt and clay	74 84	0.083	1.618	6.06258	63.3
hard silty clay	84 130	0.515 0.266	1.329 1.297	3.22749 2.91357	87.4 97.6

B.3. Analysis Model of Lateral Load-Bearing Capacity for Conductor in Layered Soil

The mechanical behaviour of structures that are in contact with the layered soil is affected by the interaction between the soil and the conductor. An analysis model of lateral load-bearing capacity suitable for conductor and surface casing for deep water is presented.

B.3.1. Force Analysis

Environmental forces from the ocean are transferred to the subsea wellhead from the riser. Theoretical analysis has proved that dynamics loads on the subsea wellhead transferred by the riser are the bending moment and vertical force.

Then, the deflection differential equation of pipe string under the interaction of transverse moment and vertical force of casing string below the mudline is obtained according to the mechanical equilibrium relationship.

$$\frac{d}{dx^2}\left[EI(x)\frac{d^2y}{dx^2}\right]+\frac{d}{dx}\left[N(x)\frac{dy}{dx}\right]+D(x)\cdot p(x,y)=0 \tag{1}$$

where: $EI(x)$ ($\mathrm{kN}\cdot m^2$) is the flexural rigidity changes along x axis, $N(x)$ (kN) is the axial force changes along x axis, $D(x)$ (m) is the variable outer diameter of the pipe string, $p(x,y)$ is the subgrade reaction per unit area: $p(x,y)=\bar{p}(x,y)/D(x)$ (kPa). Pipe strings above the mudline do not suffer from the subgrade reaction: $p(x,y)=0$.

B.3.2. Subgrade Reaction

According to different assumed conditions, the calculation methods of the subgrade reaction p can be divided into 3 kinds:

i. Limit of subgrade reaction method: Without considering the deformation of the foundation itself, p is the function of depth: $p = p(x)$;

ii. Elastic subgrade reaction method: Assuming that p is proportional to the nth power of the deflection of the pipe string: $p = kx^m y^n$, where k is a coefficient determined by the properties of the foundation which is also related to the choice of the exponential m $(m \geq 0)$, n $(0 < n \leq 1)$.

iii. Elastoplastic subgrade reaction method: Here, the plastic region is analyzed with limit of subgrade reaction method while the plastic region is analyzed with elastic subgrade reaction method. Then the transverse reaction can be solved with the continuous condition of the boundary of the elastic region and the plastic region. Since it can describe the nonlinear characteristics between pipe strings and the foundation, it is able to make more exact analysis on the lateral loading-bearing capacity with large displacement of pipe string comparing to other methods. It has been adopted in the API RP 2A named as $p - y$ curve method. When no experimental material is available, theoretical equations provided by the practice can be referred to for the calculation of the $p - y$ curve of clay and sandy soil.

Secant modulus of the subgrade reaction at depth x can be determined according to the $p - y$ curve $(E_s = p/y)$, and therefore p corresponding to different y can be determined $(p = E_s y)$

Substitute p with $p = E_s y$ in equation (1), we have:

$$\frac{d}{dx^2}\left[EI(x)\frac{d^2y}{dx^2}\right] + \frac{d}{dx}\left[N(x)\frac{dy}{dx}\right] + D(x) \cdot E_s y = 0 \qquad (2)$$

B.3.3. Forces

Risers in the deep-water conditions suffer from complex stress: the transverse component of the bottom tension, weight of the BOP and current force acting on it will render transverse moment M_t on the wellhead while the resultant force of the vertical component of the bottom tension and weight of the BOP is the vertical force N_t on the wellhead.

Axial force on the pipe string can be described as:

$$N(x) = \begin{cases} N_t + W(x) \cdot x & (x \le x_{\mathrm{ml}}) \\ N_t + W(x) \cdot x - F_f(x)(x - x_{\mathrm{ml}}) & (x > x_{\mathrm{ml}}) \end{cases} \quad (3)$$

where, x_{ml} is the length of the pipe string above the mudline (m), $W(x)$ is the weight of the pipe string per unit length (kN), $F_f(x)$ is the soil friction on the external wall of the pipe string per unit length (kN).

B.3.4. Flexural Rigidity

If there is a double layer casing pipe structure with cement sheath at the upper cementing segment of the combination pipe string, the equivalent flexural rigidity K_1 is:

$$K_1 = E_{st1}(I_{so} + I_{si}) + 0.6\, E_c I_c \quad (4)$$

where, E_{st1} is the modulus of elasticity of the steel of the pipe string (kPa), I_{so} is the moment of inertia of the surface casing (m^4), E_c is the modulus of elasticity of the cement sheath (kPa), I_c is the moment of inertia of the cement sheath (m^4).

If there is a double layer casing pipe structure at the upper segment of the combination pipe string without cement sheath, the equivalent flexural rigidity K_2 is:

$$K_2 = E_{st1}(I_{so} + I_{si}) \quad (5)$$

If it is a combination structure of cement sheath and surface casing rather than a conductor at the lower section of the combination pipe string, the equivalent flexural rigidity K_3 is:

$$K_3 = E_{st1}I_{si} + 0.8E_cI_c \tag{6}$$

B.4. Numerical Solution of the Analysis Model of Lateral Load-Bearing Capacity

In this paper, the effect of layered soil mechanical properties on the well conductor integrity is investigated using the analytical method.

Since the reaction between pipe string and the foundation is quite complex, the length L of the pipe string can be equally divided into n segments with difference method. The length of each segment is h. Set the top node of the pipe string as node 0 while the bottom node of the pipe string is node n. Prolonging the two ends and set virtual node -1, virtual node -2, virtual node n+1, and virtual node n+2 as shown in Figure B-1

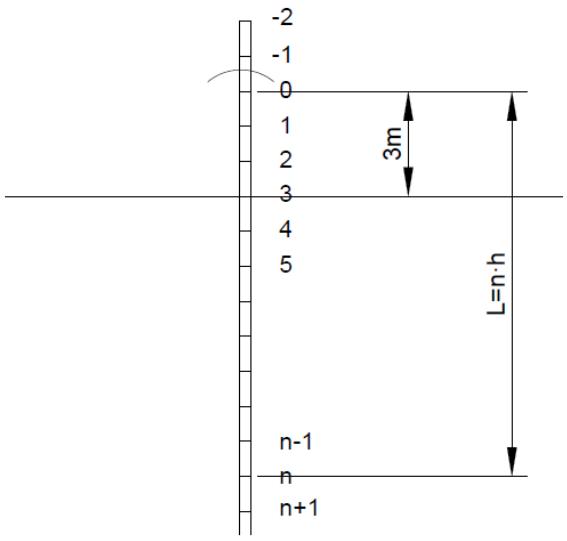

Figure B-1. Numerical grid of casing string

The derivative scheme in Eq. [2] can be approximately substituted by the difference scheme. Then Eq. [2] becomes (n+1) difference equations.

$$\begin{cases} a_i y_{i+2} + b_i y_{i+1} + c_i y_i + d_i y_{i-1} + e_i y_{i-2} = 0 \\ a_i = (EI)_{i+1} \\ b_i = -2(EI)_{i+1} - 2(EI)_i + N_i h^2 \\ c_i = (EI)_{i+1} + 4(EI)_i + (EI)_{i-1} - 2N_i h^2 + D_i (E_s)_i h^4 \\ d_i = -2(EI)_i - 2(EI)_{i-1} + N_i h^2 \\ e_i = (EI)_{i-1} \end{cases} \tag{7}$$

Boundary condition: when there is a moment M_t at node 0 on the top of the pipe string, internal force of the pipe string will have the same value as it but in opposite direction, that is: $M_0 = -M_t, Q_0 = 0$. As for the pipe string which dives relatively deep in to the soil, the node at the bottom end can be regarded as a free end, that is: $M_n = 0$, $Q_n = 0$.

Difference of boundary conditions gives 4 equations. Together with equation [7], there are n+5 equations to solve the variables in n+5 nodes. Since the poor precision of matrix expunction computation, Gleser method is generally used to get the expression of y_i $(i = -2, -1, \ldots, n+2)$ through transformation. Since $(E_s)_i$ varies nonlinearly, the calculation needs to be performed by iteration. Firstly, a group of $(E_s)_i^0$ are assumed. There is no subgrade reaction on the pipe string above the mudline: $E_s = 0$. A group of y_i^o will be obtained after solving them for once, with which a group of p_i^0 will be obtained according to the $p - y$ curve. Then according to $E_s = p/y$, a new group of $(E_s)_i^1$ can be obtained. Using the new $(E_s)_i^1$ to repeat the iteration process until $\left|(E_s)_i^0 - (E_s)_i^1\right| < \varepsilon$, where ε is the allowable accuracy condition. The deflection (transverse displacement) of

each node on the pipe string can be obtained, therefore rotation angle θ_i, moment M_i, shear Q_i, subgrade reaction p_i of each node can be calculated.

$$\begin{cases} \theta_i = -\dfrac{y_{i+1} - y_{i-1}}{2h} \\ M_i = -\dfrac{(EI)_i(y_{i+1} - 2y_i + y_{i-1})}{h^2} \\ Q_i = -\dfrac{(EI)_{i+1}y_{i+2} - [2(EI)_{i+1} - N_i h^2]y_{i+1}}{2h^3} + \\ \quad \dfrac{(EI)_{i+1}y_{i+2} - [2(EI)_{i+1} - N_i h^2]y_{i+1}}{2h^3} \\ P_i = (E_s)_i y_i \end{cases} \tag{8}$$

B.5. Example and Analysis of Influencing Factors

Parameters of a deepwater well in Newfoundland offshore area are:

Conductor: length 85 m, outer diameter 914.4 mm, wall thickness 25.4 mm, weight per unit length 7.8 kN/m.

Surface casing: length 650 m, outer diameter 508 mm, wall thickness 12.7 mm, weight per unit length 2.1 kN/ m, modulus of elasticity is 210 Gpa.

Cement sheath between two casing strings: Modulus of elasticity is 18 GPa, weight per unit length is 45 kN/m.

Length of pipe string above the mudline is 3m

Assuming in the adverse ocean environment maximum transverse moment conveyed to the wellhead is 3MN*m, vertical force is 1MN. To simplify the calculation, assuming it is clay layer from the mudline to 100 meters below it, of which the underwater bulk density is 7.0 kN/m^3 and the shear strength is 20 kPa.

The default input parameters are shown in Table B-3.

Table B-3.

Input Data				
Section	Characteristics		Value	Unit
wellhead	length of pipe string above mudline	xm1	3	m
	num transverse moment on the well	Mt	3	MN·m
	vertical force on the wellhead	N	1	MN
conductor	length	Lcd	85	m
	outer diameter	dcd	914.4	mm
	wall thickness	tcd	25.4	mm
	weight per unit length	Wcd	7.8	kN/m
surface casing	outer diameter	dsc	508	mm
	wall thickness	tsc	12.7	mm
	weight per unit length	Wsc	2.1	kN/m
	modulus of elasticity	Estl	210	Gpa
cement sheath between casings	modulus of elasticity	Ec	18	Gpa
	weight per unit length	Wc	45	kN/m
	return height		0	m
soil layer (Western Locatoin sheet)	depth range (under mudline)		130	m
	underwater bulk density		-	kN/m3
	initial modulus		-	kN/m3
Calculated Constants				
Section	Characteristics		Value	Unit
conductor	inertia moment of the conductor	Iso	0.00701	m-4
surface casing	inertia moment of the surface casing	Isi	0.00061	m-4
cement sheath	inertia moment of the cement sheath	Ic	0.02403	m-4
double layer casing pipe structure with cement sheath	equivalent flexural rigidity	K1	1.85981	GPa
cement sheath and surface casing	equivalent flexural rigidity	K3	0.47344	GPa

B.5.1. Effects of the Forces on the Wellhead

As shown in Figure B-2 to Figure B-6, an analysis was performed on the lateral load-bearing capacity of the combination pipe string under the interaction of different transverse moments and vertical forces.

The result shows that the transverse displacement, rotation angle, moment, shear, and subgrade reaction are almost zero when the depth goes over a certain value. That is, the forces on the wellhead only concentrate on a relatively short region at the upper pipe string and hardly bring any effects on the lower region.

Comparing the effects of different values of forces, the conclusion is that the transverse displacement on the top of pipe string has relatively obvious increase when the transvers moment is greater. Meanwhile, the moment and shear of the pipe string increase gradually with the increase of the transvers moment. Transverse displacement and moment become larger when there is a greater vertical force acting on the top of the pipe string. However, the effects of vertical force is not as obvious as the effects of the transverse moment. Forces undertaken by the subsea wellhead in deepwater drilling come from BOP stack above the wellhead, risers, drilling platform in the ocean environment. It's very important to reasonably control the drifting of the platform and the drilling ship and tension force on the top of the risers to guarantee the stability of wellhead and pipe strings.

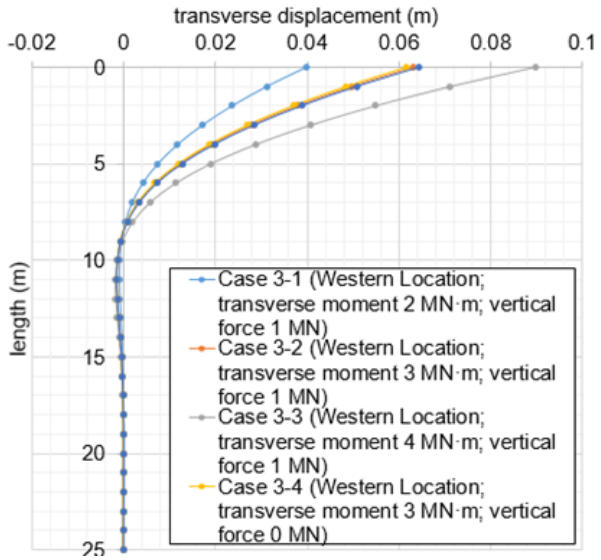

Figure B-2. Transverse displacement

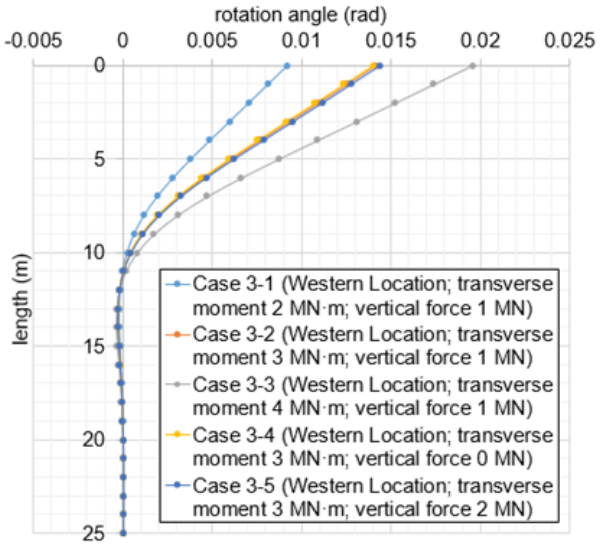

Figure B-3. Rotation angle

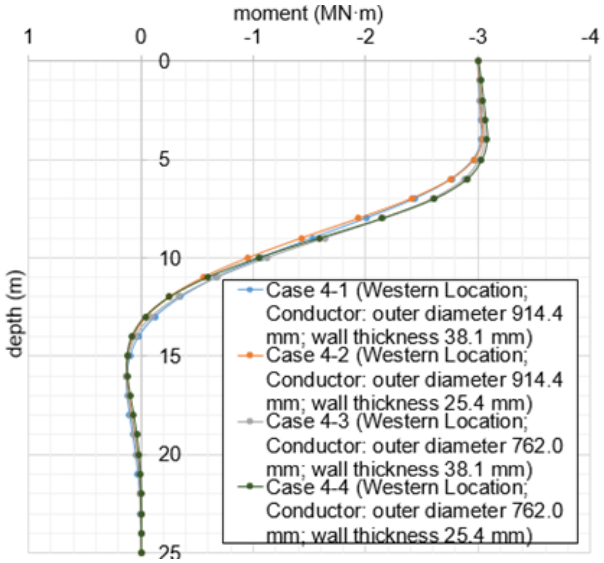

Figure B-4. Moment

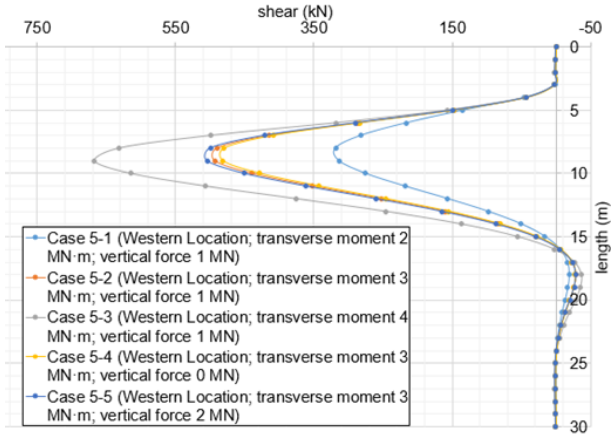

Figure B-5. Shear force

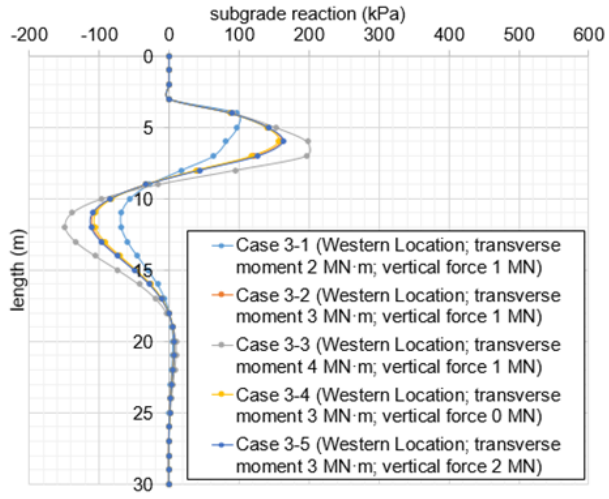

Figure B-6. Subgrade reaction

B.5.2. Effects of the Diameter and Wall Thickness of the Conductor

As shown in Figure B-7, analysis has been done on lateral load-bearing capacity of pipe string with different outer diameters and wall thicknesses.

The results illustrate that transverse displacement of the pipe string gradually decreases with increase diameter. Bending resistance of the pipe string increases with increase in the

wall thickness. When the value of loading is certain, diameter and wall thickness do not have great effects on the moment of the pipe string because the transverse displacement is relatively small.

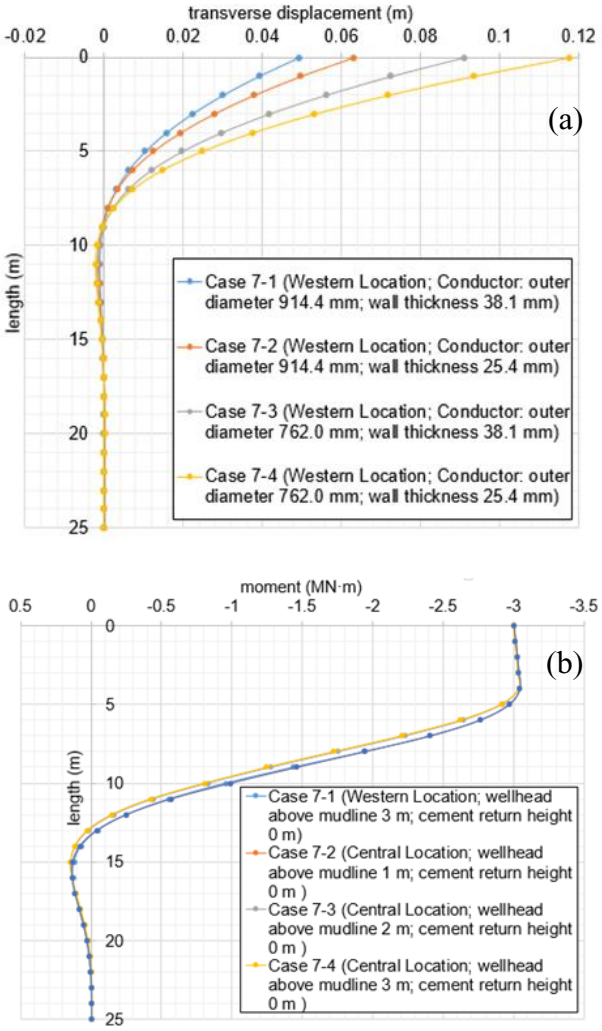

Figure B-7. a., Transverse displacement, b., Moment.

B.5.3. Effects of the Distance between Mudline and Wellhead, Cement Return Height, and Type of Foundation

Analysis was performed on lateral load-bearing capacity of pipe string while changing the distance between mudline and wellhead, the return height of the cement sheath on the surface casing, and the layered soil as shown in Figure B-8. The results illustrate that the larger distance is between the wellhead and mudline. However, scouring at the mudline has great effects on the lateral load-bearing capacity of the casing strings. Since relatively less contribution to the flexural rigidity of the combination pipe string has been made by the cement sheath, the return height of the surface casing does not have great effects on the transverse displacement and moment of the pipe string. When it is the sandy soil foundation, the transverse displacement and moment of the pipe string is smaller than those in the clayey soil foundation, meanwhile the length of the pipe being affected is also shorter (Guan et al., 2009).

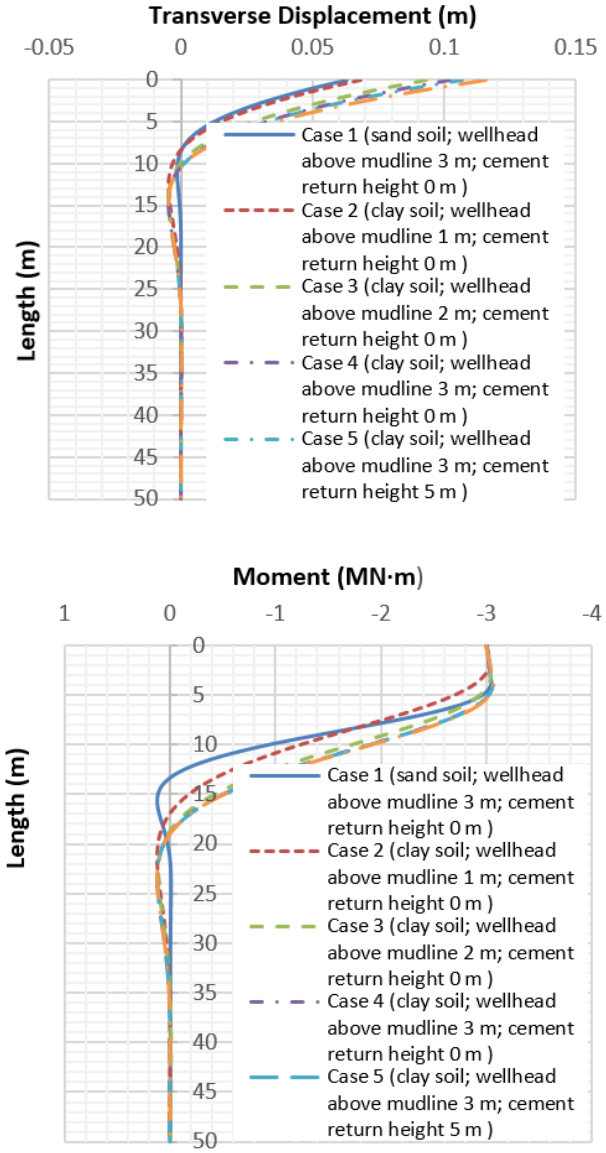

Figure B-8.

B.6. Conclusions

In this study the influence of well-conductor seabed interaction in a complexly layered soil in Newfoundland Offshore was investigated analytically. The dynamic differential equations of the casing deflection below the mud line and its numerical solutions were

established. It can be concluded that the seabed sediments have a certain effect on the lateral loading capacity of the casing string with a more significant effect in the shallower layers closer to the sea bottom. Distance between wellhead and mudline has relatively great effect on the lateral load-bearing capacity of the pipe string. Cementing sheath return height degree of the surface casing does not have great effect on the transverse displacement and moment of the pipe string. However, the diameter and the wall thickness of conductor also have effects on the bending moment of the pipe string. Hence, increase in wall thickness causes increasing the bending resistance of the pipe string.

B.7. Acknowledgements

The authors gratefully acknowledge the financial support of this research by the Research and Development Corporation (RDC) (now Innovate NL) through the ignite funding program and Memorial University of Newfoundland through VP start-up funding support.

References

API, (2011). "API Recommended Practice 2GEO/ISO 19901-4", Geotechnical and Foundation Design Considerations. 1st ed. American Petroleum Institute, Washington, DC.

Blasco, S., G. Fortin, P. Hill, M. O'Connor, and J. Brigham-Grette (1990). "The late Neogene and Quaternary stratigraphy of the Canadian Beaufort continental shelf in The Arctic Ocean Region."

Dong Y. Q. (1994) Vortex-induced nonlinear oscillation of TLP (tension-leg platforms) under combined wave-current. Acta Oceanologica Sinica, 16(3), 121-129

Guan, Z., Su, K., Su, Y. (2009). "Analysis on lateral load-bearing capacity of conductor and surface casing for deepwater drilling, College of Petroleaum Engineering, China University of Petroleum, Dongying, China

Jin, Y., Caihong L., Hanbin, L., Renjun, X., Shijing C. (2007). "Strength and Stability Analysis of Deep sea Drilling Risers," Beijing Key Laboratory of Urban Oil

and Gas Distribution Technology, China University of Petroleum, Beijing, China.

Kanhua S., Guan Z and Yinao S. (2008). "Mechanical Stability Analysis of Subsea Wellhead for Deepwater Drilling." Oil Drilling & Production Technology, Vol 30(6): pp 1-4.

Lanan, G.A., Cowin, T.G. & Johnston, D.K. 2011, "Alaskan Beaufort Sea Pipeline Design, Installation and Operation," Proceedings of the Arctic Technology Conference, February 7 - 9, 2011, 9p.

Matlock, H (1970). "Correlations for Design of Laterally Loaded Piles in Soft Clay." Proceedings of the 2nd annual Offshore Technology Conference, Paper No. OTC 1204.

Reese, L., Cox, W. and Koop F. (1974). "Analysis of Laterally Loaded Piles in Sand." Proceedings of the 6th annual Offshore Technology Conference, Paper No. OTC 2080.

Rohleder,S. A., Sanders, W. W. and Williamson, R. N. (2003). "Challenges of drilling an ultra-deep well in deepwater-spa prospect." SPE/IADC 79810

Y. Kim and S. Jeong (2011). "Analysis of Soil Resistance on Laterally Loaded Piles Based on 3D Soil–Pile Interaction." Computers and Geotechnics 38.2

Appendix C

Analytical Assessment of the Drilling Risers Stability in Newfoundland Deep Offshore

Etido Gideon Akpan[1], Xiaoyu Dong[2], Mohammad Javad Moharrami[3] & Hodjat Shiri[4], Hodjat Shiri[2]

1: Department of Civil Engineering

Memorial University of Newfoundland

e-mail: egakpan@mun.ca

2: Department of Civil Engineering

Engineering, Memorial University of Newfoundland

e-mail: xiaoyu.dong@mun.ca

3: Department of Civil Engineering

Memorial University of Newfoundland

e-mail: mjmoharrami@mun.ca

4: Department of Civil Engineering

Engineering, Memorial University of Newfoundland

e-mail: hshiri@mun.ca

This chapter was published in the conference proceedings of GeoEdmonton 2018.

Abstract

Marine drilling risers are amongst the key structural elements in deepwater oil and gas exploration projects. These risers are continuously subjected to dynamic environmental and operational loads. This has caused the drilling risers to be vulnerable against the fatigue loads. In this study, an analytical model was adopted by solving the governing differential equations to analyze the effect of Vortex-induced vibration (VIV) on the strength and stability of an arbitrary drilling riser operating in the Offshore Newfoundland. The case study showed that the amplitude of first-order dynamic oscillations is larger than that of higher-order responses. However, the higher-order responses can cause noticeable dynamic moment and shear force. The natural frequency of risers was found to decrease with increasing the water depth and increase for higher magnitudes of top tension. The analytical approach was found to be an appropriate solution for early assessment of the drilling riser fatigue life due to vortex induced vibration.

Résumé

Les colonnes montantes de forage font partie des éléments structurels essentiels des projets d'exploration pétrolière et gazière en eau profonde. Ces colonnes montantes sont continuellement soumises à des charges environnementales et opérationnelles dynamiques. Cela a rendu les colonnes de forage vulnérables aux charges de fatigue. Dans cette étude, un modèle analytique a été adopté en résolvant les équations différentielles régissant l'analyse des effets des vibrations induites par vortex (VIV) sur la résistance et la stabilité d'une colonne montante de forage arbitraire en exploitation au large de Newfoundland.

L'étude de cas a montré que l'amplitude d'oscillation dynamique du premier ordre est supérieure à celle des réponses en mode d'ordre supérieur. Il a également été observé que l'effet du moment dynamique et de la force de cisaillement des modes d'ordre supérieur pourrait être important. Il a été constaté que la fréquence naturelle des colonnes montantes diminuait avec l'augmentation de la profondeur de l'eau et augmentait lorsque les tensions maximales étaient plus élevées. L'approche analytique s'est avérée être une solution appropriée pour l'évaluation précoce de la durée de vie en fatigue du riser de forage due au vortex induit des vibrations.

C.1. Introduction

Marine drilling risers are the best solutions for oil and gas developments off the coast of Newfoundland and Labrador. For several decades and to the present day, new technologies have been adopted to reduce the fatigue of the drilling riser by carefully analyzing its strength and stability in deepwater drilling operations. The desire to drill in harsh, deepwater environments necessitates the need for riser strength and stability analysis. However, there is a requirement for more refined methods such as the use of finite element models to verify the strength and stability of the drilling riser system in extreme conditions. The challenges of deepwater oilfields and inter-continental gas transportation present the biggest opportunities for advancements in pipeline technology. At some fields, strong waves, currents, high pressures and high temperatures (HP/HT), sour reservoirs and deepwater conditions are pushing the limits of the marine riser. The hydrodynamic forces have a strong influence on the riser stability vis-a-vis its strength. Vortex induced vibration (VIV) is a major consideration in determining the stability of riser and should not be allowed to occur at any time during the design life of the riser system. As the water depth increases, the influence of VIV becomes crucial and poses more challenges to the overall system response. Therefore it is of great importance to investigate the dynamic behavior of risers under combined wave-current interaction in deepwater environments.

In this study the analytical method proposed by Jin et al. (2007) was adopted to assess the stability of a drilling riser in the Newfoundland offshore. Additional details on the derivation of the equations presented herein can be found in the work of Jin et al. (2007).

C.2. Nomenclature

V_c	Current velocity
L_w	Wavelength
ω_w	wave circular frequency
T_w	wave period
H	wave height
k	wave number
c	length of the riser
D	diameter of the riser
t_r	wall thickness
$\overline{m}$	mass per unit length
EI	flexural stiffness of the riser
T_0	top tension
ζ_s	damping ratio
ρ	density of the seawater
ω_s	vortex shedding frequency
C_L	lift coefficient
C_d	fluid damping coefficient
C_a	coefficient of additional mass
K_d	coefficient
m'	mass of adhered water per unit length

C.3. Vibration Equation of Marine Risers

A simplified analytical model has been established by Jin et al. (2007) to analyze the influence of VIV on the strength and stability of marine risers. A method for estimating vortex-induced dynamic response was developed. The riser is considered as a vertical beam with current and wave acting perpendicular to its undeflected longitudinal axis, as shown in Figure C-1.

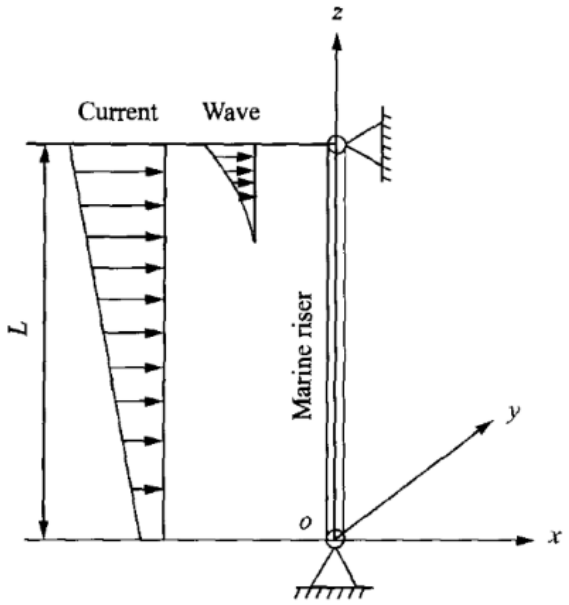

Figure C-1. Marine riser model (Jin et al, 2007)

Dong (1994) proposed an equation for the transverse motion of a marine riser under small-amplitude linear wave with the assumption of uniform cross section and mass distribution for the riser along z-direction. This equation is presented below:

$$EI.\frac{\partial^4 y}{\partial z^4} - T_0.\frac{\partial^2 y}{\partial z^2} + c.\frac{\partial y}{dt} + m.\frac{\partial^2 y}{\partial t^2} = F_y(z,t) \quad (1)$$

where, EI is the flexural stiffness of the riser [N.m^2]; To is the riser top tension [N]; c is the coefficient of viscous damping; m is the mass per unit length of the beam [kg/m]; and,

F_y (z, t) is the total external fluid force per unit length in the y-direction [N/m]:

$$F_y(z,t) = F_l(z,t) - F_r(z,t) \tag{2}$$

where, F_L (z, t) is the vortex lift force per unit length [N/m]; and, F_r (z, t) is the nonlinear fluid damping force. Both F_L (z, t) and F_r (z, t) are caused by the motions of riser in y-direction. F_L (z, t) can be expressed as follows:

$$F_L(z,t) = \frac{1}{2}\rho D(V_c + u)^2 C_L \cos(w_s t) = K_L(z).C_L \cos(w_s t) \tag{3}$$

where, ρ is the density of seawater [kg/m^3]; D is the external diameter of the riser [m]; C_L is the lift coefficient; ω_s is the frequency of vortex shedding [rad/s]; and, K_L is the lift force distribution coefficient [kg/s^2] which can be obtained as:

$$K_L(z) = \frac{1}{2}\rho D(V_c(z) + u)^2 \tag{4}$$

where, Vc is the current flow velocity and can be expressed as a linear function of water depth:

$$V_c(z) = a + bz \tag{5}$$

The horizontal propagation velocity of the linear wave, u, can be expressed as:

$$u = u(z,t) = \frac{\pi.H}{T_w} e^{k(z-1)} \cos(\omega_w t) \tag{6}$$

where, H is the wave height [m]; Tw is the wave period [sec]; □w is the wave circular frequency [rad/sec]; l is the length of the riser [m]; k is the wave number, k=2π/Lw; and, Lw is the wavelength [m].

Substituting Eq. [6] into Eq. [4], the lift force distribution coefficient is obtained as:

$$K_L(z) = \frac{1}{2}\rho D(V_c(z) + \frac{\pi.H}{T_w} e^{k(z-1)} \cos(\omega_w t))^2 \tag{7}$$

The nonlinear fluid damping force, Fr (z, t), can be defined using Morison Equation as follows:

$$F_r(z,t) = \frac{1}{2}\rho D C_d y'|y'| + C_a \rho \frac{\pi D^2}{4} = K_d C_d y'^2 sgn(y') + m' y'' \quad (8)$$

$$K_d = \frac{\rho D}{2}$$

$$m' = \frac{\rho C_a \pi D^2}{4}$$

where, C_d is the damping coefficient of water; m' is the added mass per unit length [kg/m]; and, C_a is the added mass coefficient.

C.4. VIV Assessment Approaches of Marine Risers

VIV has been a major concern for marine risers due to the potential to cause severe fatigue damage. In order to design marine risers, it is necessary to have good theoretical and analytical models for the prediction of VIV at the initial stage of design and prior to the development of a comprehensive numerical model, which is required in order to evaluate the problem and envisage solutions.

A simplified assessment of VIV is proposed in DNV-OS-F201. This simplified estimate of the induced fatigue damage is computed by conservatively assuming that 2D sheared current profiles are applied on the riser (e.g., unidirectional with a magnitude that varies with distance below the sea level). A lot of developments have been identified in this particular area. Software, such as SHEAR7 and VIVA by MIT and OrcaVIV by Orcina are now potentially suitable for handling VIV issues.

Jin et al. (2007), carried out some studies on the strength and stability analysis of deepwater marine drilling risers by analyzing the influence of VIV on the strength and stability of the

risers. They established a simplified analytical model and developed a method for calculating vortex induced dynamic response.

The VIV response of the riser is obtained by transforming the partial differential equation (PDE) of the transverse motion, Eq. [1], into a set of nonlinear ordinary differential equations (ODEs) using Galerkin method (Jin et al. 2007). The riser is assumed as a simply supported beam at both ends with the following boundary conditions:

$$y(0,t) = 0 \; \frac{\partial^2 y(0,t)}{\partial z^2} = 0 \qquad (9)$$

$$y(l,t) = 0 \; \frac{\partial^2 y(l,t)}{\partial z^2} = 0$$

The lateral displacement y(z, t) is given as a series of vibration mode shapes as follows:

$$y(z,t) = \sum_{n=1}^{\infty} y_n(t) \sin(\lambda_n z) \qquad (10)$$

$$\lambda_n = \frac{n\pi}{l}$$

The total external fluid force per unit length in the y-direction is then obtained by substituting Eq. [3], Eq. [8], and Eq. [10] into Eq. [2]. Also, by rearranging Eq. [1] via substituting Eq. [10] and [2] and applying the Galerkin method, we obtain:

$$\begin{aligned} y'' + \left[\lambda_{B_n}^2 + \lambda_{c_n}^2\right] + \frac{C_n}{\bar{m}} y_n' + \frac{2D_n}{l\bar{m}} &= \frac{2C_L}{\bar{m}l} \cos(\omega_s t) \int_0^1 K_l(z) \sin(\lambda_n z) dz \\ &= \frac{2C_L}{\bar{m}l} \cos(\omega_s t) \int_0^1 \left[\frac{1}{2} \rho D \left(V_c(z) \right.\right. \\ &\quad \left.\left. + \frac{\pi H}{T_w} e^{k(z-1)} \cos(\omega_w t)\right)^2\right] \sin(\lambda_n z) dz \\ &= A_c \cos(\omega_s t) + [A_w \cos(2\omega_w t) + 2A_{cw} \cos(\omega_w t)] \cos(\omega_s t) \end{aligned} \qquad (11)$$

$$\bar{m} = m + m'$$

$$\lambda_{B_n}^2 = \lambda_n^4 (EI/\bar{m})$$

$$\lambda_{C_n}^2 = \lambda_n (T_0/\bar{m})$$

$$C_n = 2\bar{m}(\lambda_{B_n}^2 + \lambda_{C_n}^2)^{1/2}\zeta_s$$

$$A_c = \begin{cases} \frac{\rho D C_L}{\bar{m} l}\left\{a^2\left(\frac{2l}{\pi}\right) + 2ab\left(\frac{l^2}{\pi}\right) + b^2\left[\frac{l^2}{\pi} - 4\left(\frac{l}{\pi}\right)^8\right]\right\}, n = 1,3 \\ -\frac{\rho D C_L}{\bar{m} l}\left\{ab\left(\frac{l^2}{\pi}\right) + b^2\left(\frac{l^3}{2\pi}\right)\right\}, n = 2,4 \end{cases}$$

$$A_w = \begin{cases} \frac{\rho D C_L}{\bar{m} l}\left(\frac{\pi H}{T_w}\right)^2 \frac{n\pi/l}{4k^2 + \left(n\pi/l\right)^2}(e^{-2kl} + 1), n = 1,3 \\ 0, n = 2,4 \end{cases}$$

$$A_{cw} = \begin{cases} \frac{\rho D C_L}{\bar{m} l}\left(\frac{\pi H}{T_w}\right)[aB_n(e^{-kl} + 1) + b(lB_n - 2k\bar{B}_n(e^{-kl} + 1))], n = 1,3 \\ -\frac{\rho D C_L}{\bar{m} l} b\left(\frac{\pi H}{T_w}\right) l\bar{B}_n, n = 2,4 \end{cases}$$

$$B_n = \frac{n\pi/l}{k^2 + \left(n\pi/l\right)^2}$$

$$\bar{B}_n = \frac{n\pi/l}{\left[k^2 + \left(n\pi/l\right)^2\right]^2}$$

where, $\bar{m}$ is the virtual mass of the riser per unit length, [kg/m]; $\lambda Bn2$ is the riser natural frequency for bending vibration; $\lambda Cn2$ is the riser natural frequency for for axial vibration; Cn is the viscous damping coefficient; ζs is the dimensionless damping ratio of the riser; Ac, Aw, Acw, Bn, and $\bar{Bn}$ are the coefficients; and Dn is obtained through a numerical algorithm (Jin et al. 2007):

$$D_j = K_d C_d \int_0^1 sgn(y') y'^2 \sin(\lambda_j z) dz, \qquad j = 1,2,3, \dots n \tag{12}$$

$$y' = y'(z,t) = \sum_{i=1}^{n} y_i'(t) \sin(\lambda_n z) \tag{13}$$

Solving this equation, the dynamic displacement of the riser, y (z, t), can be obtained using Eq. [10].

According to Ma et al. (2000), the dynamic moment is then given as:

$$M(z,t) = EI \frac{\partial^2 y}{\partial z^2} = EI \sum_{n=1}^{\infty} y_n^2 y_n(t) \sin(\lambda_n z) \tag{14}$$

The dynamic shearing force acting on the riser can be obtained from the following equation:

$$Q(z,t) = EI \frac{\partial^3 y}{\partial z^3} = EI \sum_{n=1}^{\infty} y_n^3 y_n(t) \cos(\lambda_n z) \tag{15}$$

C.5. Fatigue Analysis

Fatigue life assessments of drilling risers is a challenging aspect of the design due to contribution of several complex and interactive loading mechanisms such as operational vibrations, wave-induced oscillations, and vortex-induced vibrations (VIV).

Analytical solutions are adopted for the fast assessment of drilling riser performance at the early stages of design, prior to comprehensive numerical simulations of the complex loading conditions.

The total fatigue damage is assumed to be generated by the combined action of the following contributions:

- Mean motions of the vessel caused by the sequence of storms foreseen in the long-term environmental conditions.
- Slow-drift motions of the vessel inside each storm event.
- Wave-frequency motions of the vessel and hydrodynamic loads applied directly to the riser for each of the above events.
- Vortex induced vibration (VIV) effects in the length of riser exposed to high current profiles (e.g., first few 100 meters below the sea surface).
- Installation operations.

The admissible fatigue life is assumed to be equal to 10 times the design life for the entire pipe length. Suitable criteria will be defined to couple a particular environmental condition (wave and current) with the corresponding vessel offset. A time-domain approach will be followed to describe the dynamic response of the riser generated by the representative sea states of the long-term distribution. The total fatigue damage is then evaluated by means of a suitable procedure that shall be aligned with the solution approach, considering a reference S-N (stress range – number of cycles to failure) curve and the Palmgren-Miner law for summing the partial contributions.

The fatigue life of the marine riser can be estimated using Palmgren-Miner theory. Hence, the damage criterion is given by:

$$D_i = \sum_i \frac{n(\Delta\varepsilon_i)}{N(\Delta\varepsilon_i)} \tag{16}$$

where, $n(\Delta\varepsilon i)$ is the number of cycles of alternate strain that occurred in the range of $\Delta\varepsilon i$ and can as well be expressed as:

$$n(\Delta\varepsilon_i) = f_i t_i \tag{17}$$

fi is the frequency corresponding to the ith amplitude [rad/ses]; and ti is the vibration time [sec].

Similarly, the denominator in Eq. [16] can be obtained from the relevant S-N curve and it is related to the equation below:

$$N(\Delta\varepsilon_i) = c.(\Delta\varepsilon)^{-b} \tag{18}$$

where c and b are constants.

The symbol $\Delta\varepsilon$ is the maximum difference of strain in one cycle and is taken from the middle point of the riser having two joint and is expressed as follows:

$$\Delta\varepsilon = \pi^2 A_o (\frac{D}{L})^2 \tag{19}$$

where Ao is the amplitude of the middle point of the riser [m]. By substituting Eqs. [17], [18] and [19] into Eq. [16] we can obtain the value of Di for t = 1 year as follows:

$$D_i = \sum_i \frac{f_i t_i A_{0,i}^4 (\frac{D}{L})^8}{6.745 \times 10^{-12}} \tag{20}$$

Assuming, $T_i = \frac{t_i}{3600\times365}$ Ti=ti3600×365 and substituting it into Eq. [20], we can obtain the fatigue lifetime of the riser in years as follows:

$$D_i = \frac{5.133 \times 10^{-18} (\frac{L}{D})^8}{f_n \sum_i (\frac{f_i}{f_n}) T_i A_{o,i}^4} \tag{21}$$

C.6. Case Study

Table C-1. Basic parameters

Parameter	Value	Unit	Parameter	Value	Unit
V_c	0.78	m/s	EI	418	MN.m^2
L_w	224	m/s	T_0	150000	N
ω_w	0.523	Rad/s	ζ_s	0.0018	
T_w	12.014	S	ρ	1025	Kg/m^3
H	10	m	ω_s	0.2917	rad/s
k	0.0280	m^{-1}	C_L	2.4	
c	1000	m	C_d	0.6	
D	0.6049	m	C_a	1	
t_r	0.0254	m	K_d	310.0113	Kg/m^2
$\bar{m}$	974.2	Kg/m	m'	294.5648	Kg/m

The calculated coefficients considering top tension are shown in Table 2.

Table C-2. Natural frequencies of riser

Mode n	Natural frequencies of riser (λ_n)	Natural frequencies of bending vibration of the riser ($\lambda_{B_n}^2$)	Natural frequencies of axial vibration of the riser ($\lambda_{C_n}^2$)
1	0.003142	0.00004180	0.4837
2	0.006283	0.0006687	0.9674
3	0.009424	0.003385	1.4512

4	0.01257	0.01070	1.9349

C.6.1. Dynamic Response Analysis of Marine Risers

As the length of the marine risers increases, their natural frequencies tend to decrease. However, resonance is likely to occur when the natural frequency of the riser is close to the vortex shedding frequency. Applying the Runge-Kutta Method, the equations can be reduced as follows:

$$Y_1 = y_1 \tag{22}$$

$$Y_2 = \frac{dY_1}{dt} = \frac{dy_1}{dt} = y_1' \tag{23}$$

$$Y_3 = y_2 \tag{24}$$

$$Y_4 = \frac{dY_3}{dt} = \frac{dy_2}{dt} = y_2' \tag{25}$$

$$Y_5 = y_3 \tag{26}$$

$$Y_6 = \frac{dY_3}{dt} = \frac{dy_3}{dt} = y_3' \tag{27}$$

$$Y_7 = y_4 \tag{28}$$

$$Y_8 = \frac{dY_7}{dt} = \frac{dy_4}{dt} = y_4' \tag{29}$$

where, Y_1, Y_2, Y_3, Y_4, Y_5, Y_6, Y_7 and Y_8 are values of iterations in meters.

Figure C-2 shows the first four modal responses of the riser under the combined interaction of wave and current. Based on this figure, the dynamic amplitude of the first-order mode is greater than the amplitude of higher-order responses.

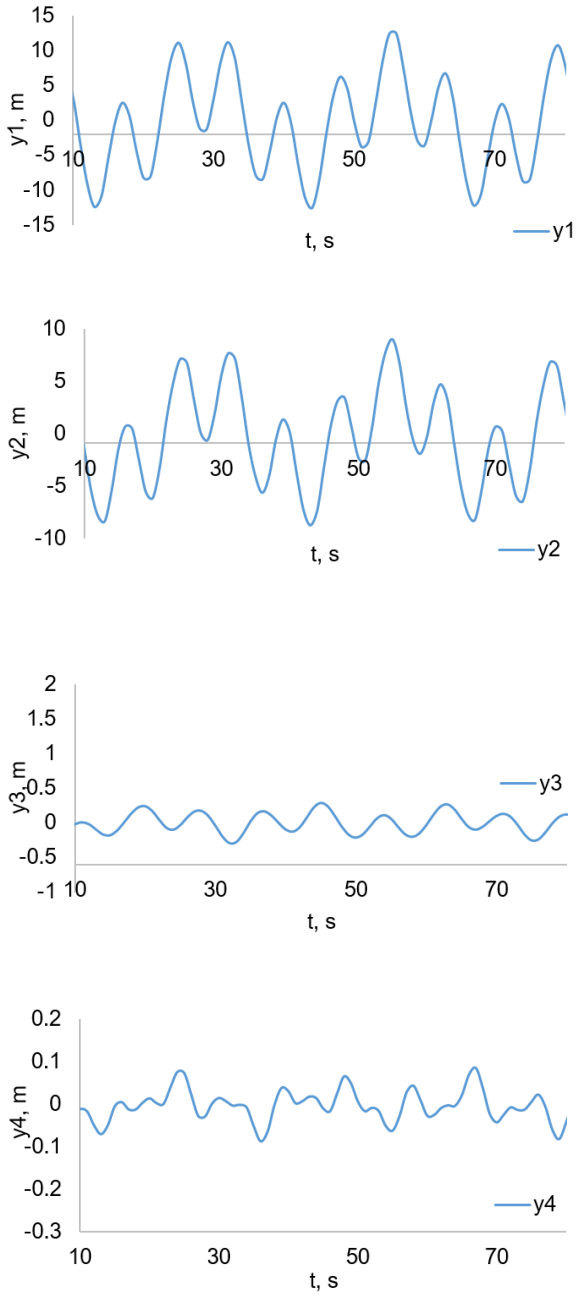

Figure C-2. Modal response considering the combined wave-current interaction

Eq. [14] can be modified as follows:

$$M(z,t) = EI\frac{\partial^2 y}{\partial z^2}$$

$$= EI\left\{y_1(t)\sin(\frac{\pi z}{l}) + 4y_2(t)\sin(\frac{2\pi}{l}) + 9y_3(t)\sin(\frac{3\pi z}{l})\right. \quad (30)$$

$$\left. + 16y_3(t)\sin(\frac{4\pi z}{l})\right\}$$

Hence, $z = l/2$, for the middle point of the riser. Therefore, the dynamic displacement becomes:

$$M\left(\frac{l}{2},t\right) = EI\frac{\partial^2 y}{\partial z^2} = EI\left\{y_1(t)\sin(\frac{\pi z}{l}) + 9y_3(t)\sin(\frac{3\pi z}{l})\right\} \quad (31)$$

Eq. [31] shows that $y_3(t)$ has a significant influence on the bending moment when, $z = l/2$. Figure C-3 and Figure C-4 show the responses of dynamic moment and dynamic shear force when the primary resonance is generated. Figure 5 shows the responses of dynamic moment at the middle point and the dynamic shear force at the bottom of the riser.

Since the natural frequency of marine risers increases with top tension, vortex-induced vibration can be avoided by increasing the top tension.

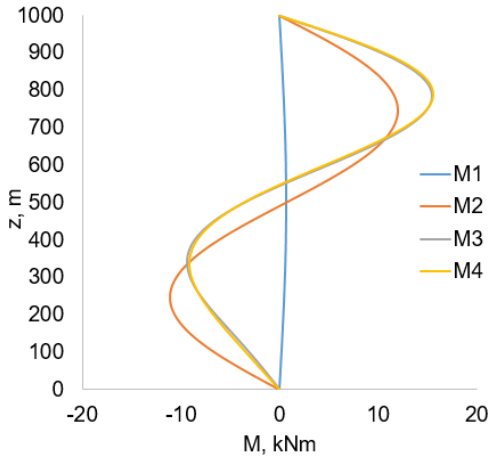

Figure C-3. Dynamic moment responses considering combined wave-current loads

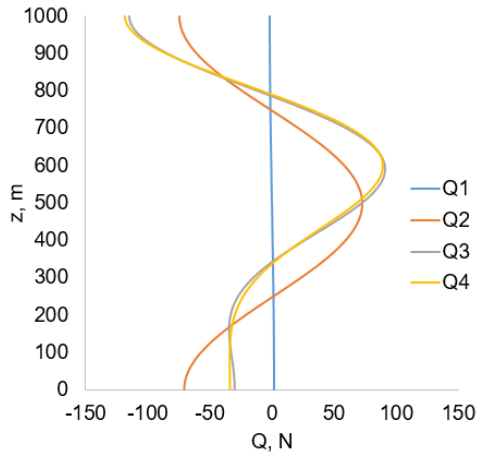

Figure C-4. Shear force responses considering combined wave-current loads

C.7. Calculation of Fatigue Life

In Newfoundland and Labrador, the offshore fields are located on the Grand Banks in the Jeanne d'Arc Basin and the current is assumed to be constant all year round. In order to perform the fatigue analysis on a riser for a 20 year period Eq. [21] is used. One of the key technical challenges of deepwater drilling is riser fatigue due to VIV. Therefore, the effect of vortex induced vibration should be considered during the design of the marine riser. Figure C-5a and b show the dynamic moment response and shear force at the middle point and bottom point of the riser respectively.

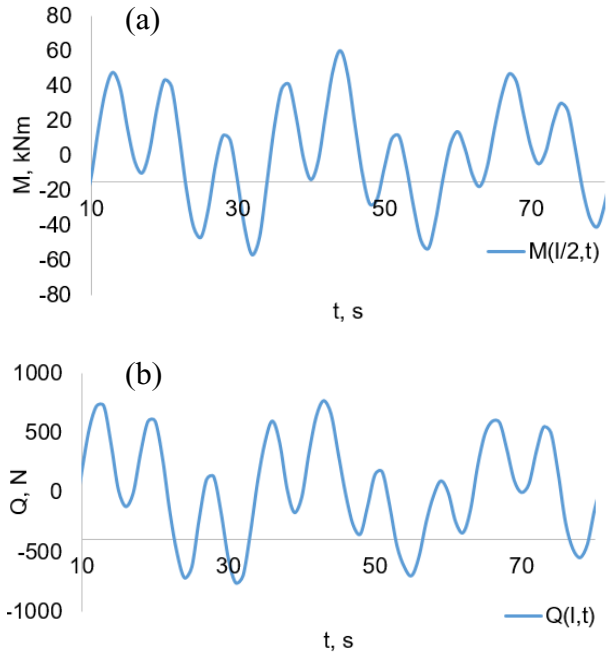

Figure C-5. (a) Dynamic moment response at the middle point, (b) shear force at the bottom of the riser

C.8. Conclusion

Offshore drilling is very challenging and with the increase of operations in Newfoundland and Labrador's offshore oil and gas industry, the need for thorough assessment of drilling riser strength and stability is of paramount importance as it becomes more critical in harsh environments. From the analytical results, it can be concluded that the first-order mode dynamic response is greater than higher-order mode responses at primary resonance. In addition, the natural frequency of a riser decreases with increasing length but increases with increasing top tension. The need for VIV suppressors should be investigated with respect to VIV effects as part of a riser fatigue damage assessment. Should excessive motions be expected, effective suppressors can be selected and applied to the required riser

length. Numerical modeling of the problem is required in order to evaluate the envisaged solutions.

C.9. Acknowledgments

The authors gratefully acknowledge the financial support of this research by the Research and Development Corporation (RDC) (now Innovate NL) through the ignite funding program and Memorial University of Newfoundland through VP start-up funding support.

References

DNV. (2010). Dynamic Risers Fatigue Limit State (Vol. DNV-OS-F201).

DNV. (2012). Fatigue Design of Offshore Steel Structures (Vol. DNV-RP-C203, pp. 178).

Gardner, T.N and Kotch, M.A. (1976). "Dynamic Analysis of Risers and Caissons by the Element Method," in proceeding of the Offshore Technology Conference, Houston, TX, USA.

Jin, Y., Caihong L., Hanbin, L., Renjun, X., Shijing C. (2007). "Strength and Stability Analysis of Deep Sea Drilling Risers," Beijing Key Laboratory of Urban Oil and Gas Distribution Technology, China University of Petroleum, Beijing, China.

Kaasen, K. & Lie, H. (2003). Analysis of Vortex Induced Vibrations of Marine Risers. Modeling, Identification and Control. 24. 10.4173/mic.2003.2.1.

Larsen, C. M. (1990). Response Modelling of Marine Risers and Pipelines. Trondheim: NTNU, Division of marine structures.

Ma C., Dong Y Q. and Yang L. T. (2000) Comparative Study of Vortex-Induced Nonlinear Oscillation of TLP Tethers Under Two Different Boundary Conditions. Ship Mechanics, 4(1), pp 56-64.

Rohleder, S. A., Sanders, W. W. and Williamson, R. N. (2003). "Challenges of drilling an ultra-deep well in deepwater-spa prospect." SPE/IADC 79810.

Sparks, C.P. (2002). "Transverse Modal Vibrations of Vertical Tensioned Risers – A Simplified Analytical Approach,"

Su, Kanhua & Butt, Stephen & Yang, James & Qiu, Hongyuan. (2018). Coupled Dynamic Analysis for the Riser-Conductor of Deepwater Surface BOP Drilling System. Shock and Vibration. 2018. 1-15. 10.1155/2018/6568537.

Tofa, M & Maimun, Adi & Ahmed, Yasser. (2012). “Fundamentals of vortex induced vibration analysis of marine riser.

References

Abbassian F., Dunayevsky V.A. (1998), Application of stability approach to torsional and lateral bit dynamics, SPE Drilling Completion. 13(2) 99-107.

Amado, L., 2013. Reservoir Exploration and Appraisal, Gulf Professional Publishing.

Anchor manual 2010. Vryhof anchors BV Netherland. The Guide to Anchoring 2010.

API Recommended Practice 7G, 1998. Recommended Practice for Drill Stem Design and Operating Limits, 16th ed. Washington DC, USA: American Petroleum Institute.

API, (2011). "API Recommended Practice 2GEO/ISO 19901-4", Geotechnical and Foundation Design Considerations. 1st ed. American Petroleum Institute, Washington, DC.

Apostal MC, Haduch GA, Williams JB (1990). A Study to determine the effect of damping on finite-element-based, forced-frequency response models for bottomhole assembly vibration analysis, SPE 20458, Proceedings of the 65th SPE Annual Technical Conference and Exhibition, New Orleans, LA, September 23–25.

Ashley, D. K., McNary, X. M., and Tomlinson, J.C., 2001, Extending BRA Life With Multi-Axis Vibration Measurements, SPE/IADC# 67696, IADC/SPE Drilling Conference, Amsterdam, Netherlands.

Aubeny, C.P., Han S.W., Murff J.D., 2003a. Refined model for inclined load capacity of suction caissons. Proceedings of OMAE 22nd International Conference on Offshore Mechanics and Arctic Engineering; June 8-13; Cancun, Mexico.

Aubeny, C.P., Han S.W., Murff J.D., 2003b. Inclined load capacity of suction caissons. Int. J Numer. Anal. Methods Geomech. 27(14):1235-54. doi:10.1002/nag.319

Aubeny, C.P., Han, S.W., Murff, J.D., 2003c. Suction caisson capacity in anisotropic, purely cohesive soil. Int. J. Geomech.

Axisa F, Antunes J. (1992). Flexural vibration of rotors immersed in dense fluids: part I – theory. J. Fluids Struct. 6(1)3–21.

Baird JA, Caskey BC, Wormley DN, Stone CM. (1985). GEODYN2: a bottom hole assembly geological formation dynamic interaction computer program. In: Proceedings of the SPE#14328, SPE Annual Technical Conference and Exhibition. Las Vegas, Nevada.

Bakhtiari-Nejad F., Hosseinzadeh A. (2017), Nonlinear dynamic stability analysis of the coupled axial-torsional motion of the rotary drilling considering the effect of axial rigid–body dynamics, Int. J. Non-Linear Mech. 88; 85–96.

Banerjee A.K., Dickens J. (1990), Dynamics of an arbitrary flexible body in large rotation and translation. J Guid Control Dyn; 13(2):221–7.

Berlioz A, Hogopian JD, Dufour R, Draoui E (1996). Dynamic behavior of a drillstring: experimental investigation of lateral instabilities. Trans ASME, J Vib Acoust 118:292–8.

Besaisow AA, Payne ML (1986). A study of excitation mechanisms and resonances inducing bottomhole-assembly vibrations, SPE No. 15560, Proceedings of the 61st Annual Technical Conference and Exhibition of the Society of Petroleum Engineers, New Orleans, LA, October 5–8.

Bissett MJ, 1993. Soil resistance to chain anchor movement [dissertation]. Univ. of Western Australia.

Blasco, S., G. Fortin, P. Hill, M. O'Connor, and J. Brigham-Grette (1990). "The late Neogene and Quaternary stratigraphy of the Canadian Beaufort continental shelf in The Arctic Ocean Region."

Bradbury R.E., Wilhoit J.C. (1963), Effect of Tool Joints on Passages of Plane Longitudinal and Torsional Waves Along a Drill Pipe, ASME. J. Eng. Ind. 85;156–162.

Brett, J. F., 1992. The Genesis of Bit-Induced Torsional Drillstring Vibrations. Society of Petroleum Engineers. https://doi.org/10.2118/21943-PA

Brown, M., Power, D., King, T., McAffee, R., Dodge, K. 2016. Deepwater Newfoundland and Labrador; Technology Application and Opportunities for Exploration and Production, Proceedings of Arctic Technology Conference OTC 27468, St. John's, Newfoundland and Labrador.

Burgess TM, McDaniel GL, Das PK (1987). Improving BHA tool reliability with drillstring vibration models: field experience and limitations, SPE 16109, Proceedings of the SPE/ADC Drilling Conference, New Orleans, LA, March 15–18.

Challamel N., Sellami H., Chenevez E., Gossuin L., (2000), A Stick-slip Analysis Based on Rock/Bit Interaction: Theoretical and Experimental Contribution, Society of Petroleum Engineers.

Chen S.L., Blackwood K., Lamine E. (2002), Field investigation of the effects of stick-slip, lateral and whirl vibrations on roller-cone bit performance, SPE Drilling and Completion. 17 (1) 15–20.

Chevallier A.M. (2001), Nonlinear stochastic drilling vibrations, Diss., Rice University. https://hdl.handle.net/1911/17946.

Chevallier A.M. Politis N.P. Payne M.L. Spanos, P.D. (2003). Oil and gas well drilling: A vibrations perspective. Shock and Vibration Digest, 35(2).

Choi YJ, 2007. Reliability assessment of foundations for offshore mooring systems under extreme environments [dissertation]. The University of Texas at Austin.

Chopra, A.K., McKenna, F., 2016. Modeling viscous damping in nonlinear response history analysis of buildings for earthquake excitation. Earthq. Eng. Struct. Dyn. 45, 193–211. https://doi.org/10.1002/eqe.2622

Christoforou A.P., Yigit A.S. (1997), Dynamic modeling of rotating drillstrings with borehole interactions, J. Sound Vib. 206(2) 243–260.

Christoforou, A.P., Yigit, A.S., 2003. Fully coupled vibrations of actively controlled drillstrings. J. Sound Vib. 267 (5), 1029-1045, ISSN 0022-460X, https://doi.org/10.1016/S0022-460X(03)00359-6.

Clukey E, Banon H, Kulhawy F, 2000. Reliability assessment of deepwater suction caissons. Proceedings of Offshore Technology Conference OTC 12192; May 1-4; Houston, Texas. https://doi.org/10.4043/12192-MS

Dareing D.W., Livesay B.J. (1968), Longitudinal and angular drillstring vibrations with damping. ASME J. Manuf. Sci. Eng. 90;1–9.

Davenport AG, 1964. Note on the distribution of the largest value of a random function with applications to gust loading. Proceedings of the Institution of Civil Engineers, London, England 28(2):187–96. doi: https://doi.org/10.1680/iicep.1964.10112

Dawson R., Lin Y.Q., Spanos P.D., (1987). Drill-string stick-slip oscillations, In: Proceedings of the SEM Spring Conference on Experimental Mechanics. Houston, Texas.

de Pina, E.P.F., Carvalho, M.S., 2006. Three-Dimensional Flow of a Newtonian Liquid Through an Annular Space with Axially Varying Eccentricity. ASME. J. Fluids Eng. 128 (2), 223–231. https://doi.org/10.1115/1.2170126

De SM Costa F, Rebeiro PR (1997). Finite Element modeling of the mechanical behavior of unbalanced drill collars, SPE 39025, Proceedings of the Fifth Latin American

and Caribbean Petroleum Engineering Conference and Exhibition, Rio de Janeiro, Brazil, August 30–September 3.

Det Norske Veritas. 2010a. Position Mooring. Offshore Standard DNV-OS-E-301.

Det Norske Veritas. 2010b. Dynamic Risers. Offshore Standard DNV-OS-F201.

Det Norske Veritas. 2012. Design and Installation of Fluke Anchors. Offshore Standard DNV-RP-E301.

Det Norske Veritas. 2013. Submarine Pipeline Systems. Offshore Standard DNV-OS-F101.

Detournay E., Defourny P. (1992), A Phenomenological Model for the Drilling Action of Drag Bits, Int. J. Rock Mech. Min. Sci. Geomech. Abstr. 29;13–23.

Detournay E., Richard T., Shepherd M. (2008), Drilling Response of Drag Bits: Theory and Experiment, Int J. Rock Mech. Min. Sci. 45(8) 1347–1360.

DNV. (2010). Dynamic Risers Fatigue Limit State (Vol. DNV-OS-F201).

DNV. (2012). Fatigue Design of Offshore Steel Structures (Vol. DNV-RP-C203, pp. 178).

DNVGL-CG-0130, 2018 Edition, January 2018 - Wave loads

Dong Y. Q. (1994) Vortex-induced nonlinear oscillation of TLP (tension-leg platforms) under combined wave-current. Acta Oceanologica Sinica, 16(3), 121-129

D'Souza, R. B., Dove, P. G. S., and Kelly, P. J. (1993). Taut Leg Spread Moorings: A Cost-Effective Stationkeeping Alternative for Deepwater Platforms. Offshore Technology Conference, Houston, Texas, USA.

Dufeyte, M.-P., & Henneuse, H. (1991, January 1). Detection and Monitoring of the Slip-Stick Motion: Field Experiments. Society of Petroleum Engineers. doi:10.2118/21945-MS.

Dunayevsky, V.A., Abbassian, F., Judzis, A., 1993. Dynamic Stability of Drillstrings Under Fluctuating Weight on Bit. Society of Petroleum Engineers. doi:10.2118/14329-PA

El-Sherbiny R, 2005. Performance of suction caisson anchors in normally consolidated clay [dissertation]. The University of Texas at Austin.

Escudier, M.P., Gouldson, I.W., Oliveira, P.J., Pinho, F.T., 2000. Effects of inner cylinder rotation on laminar flow of a Newtonian fluid through an eccentric annulus. Int. J. Heat Fluid Flow. 21 (1), 92–103. https://doi.org/10.1016/S0142-727X(99)00059-4

Escudier, M.P., Oliveira, P.J., Pinho, F.T., 2002. Fully developed laminar flow of purely viscous non-Newtonian liquids through annuli, including the effects of eccentricity and inner-cylinder rotation. Int. J. Heat Fluid Flow. 23(1), 52–73. https://doi.org/10.1016/S0142-727X(01)00135-7

Finnie I., Bailey J.J. (1960), An experimental study of drill-string vibration, ASME J. Eng. Ind. 82 (2) 129–135.

Fu Z.F., He J. (2001), Modal Analysis, Elsevier Science & Technology.

Fulton TM, Stewart WP, 1994. Vertical Loads on Drag Embedment Anchors. Proceedings of Offshore Technology Conference OTC 7491; May 2-5; Houston, Texas. doi: https://doi.org/10.4043/7491-MS

Gardner, T.N and Kotch, M.A. (1976). "Dynamic Analysis of Risers and Caissons by the Element Method," in proceeding of the Offshore Technology Conference, Houston, TX, USA.

Germay C, Denol V, Detournay E (2009). Multiple mode analysis of the self-excited vibrations of rotary drilling systems. J Sound Vib325(1–2):362–81

Ghasemloonia A, Rideout DG, Butt SD. (2013). Vibration analysis of a drillstring in vibration-assisted rotary drilling: finite element modeling with analytical validation. ASME J. Energy Resour. Technol. 135(3), 032902-1-032902-18

Ghasemloonia, A., (2013) Elastodynamic and finite element analysis of coupled lateral-axial vibration of a drillstring with a downhole vibration generator and shock sub. Doctoral (PhD) thesis, Memorial University of Newfoundland.

Gilbert R, 2010. FORM analysis for suction caisson anchor [dissertation]. University of Texas at Austin.

Gourdon, D., Israelachvili, J.N., 2003. Transitions between smooth and complex stick-slip sliding of surfaces. Phys. Rev. E 68, 021602. 10.1103/PhysRevE.68.021602

Guan, Z., Su, K., Su, Y. (2009). "Analysis on lateral load-bearing capacity of conductor and surface casing for deepwater drilling, College of Petroleaum Engineering, China University of Petroleum, Dongying, China

Halsey G.W., Kyllingstad A., Kylling A., (1988). Torque feedback used to cure stick-slip motion, SPE Annual Tech. Conf. and Exhibition.

Hansford, J. E., Lubinski, A. 1964. Effects of Drilling Vessel Pitch or Roll on Kelly and Drill Pipe Fatigue. Society of Petroleum Engineers. doi:10.2118/696-PA

Hansford, J.E., Lubinski, A. 1970. Analysis of Some Factors Related to Permissible Horizontal Motions of a Floating Drilling Vessel. Society of Petroleum Engineers. doi:10.2118/2727-PA

Hansford, J.E., Lubinski, A., 1966. Cumulative Fatigue Damage of Drill Pipe in Dog-Legs. Society of Petroleum Engineers. doi:10.2118/1258-PA.

Hill, T.H., Seshadri, P.V., Durham, K.S., 1992. A Unified Approach to Drillstem-Failure Prevention. Society of Petroleum Engineers. doi:10.2118/22002-PA

Hovda, S., 2018. Automatic detection of abnormal torque while reaming. J. Pet. Sci. Eng. 166, 13–24. https://doi.org/10.1016/j.petrol.2018.02.050

Huang, L., Xue, Q., Liu, B., Yang, C., Wang, R., Han, L., 2019. Dynamic Reliability Analysis of Rotary Steering Drilling System, Mechanical Sciences 10 (1), 79–90. 10.5194/ms-10-79-2019

Jafari AA, Kazemi R, Mahyari MF (2012). The effects of drilling mud and weight bit on stability and vibration of a drill string. J Vib Acoust Trans ASME;134(1)

Jansen J.D. (1991), Nonlinear rotor dynamics as applied to oil well drillstring vibrations, J. Sound Vib. 147(1) 115–135.

Jansen J.D., van den Steen L. (1995), Active damping of self-excited torsional vibrations in oil well drillstrings, J. Sound Vib. 179 (4) 647–668.

Jin, Y., Caihong L., Hanbin, L., Renjun, X., Shijing C. (2007). “Strength and Stability Analysis of Deep Sea Drilling Risers,” Beijing Key Laboratory of Urban Oil and Gas Distribution Technology, China University of Petroleum, Beijing, China.

Kaasen, K. & Lie, H. (2003). Analysis of Vortex Induced Vibrations of Marine Risers. Modeling, Identification and Control. 24. 10.4173/mic.2003.2.1.

Kanhua S., Guan Z and Yinao S. (2008). “Mechanical Stability Analysis of Subsea Wellhead for Deepwater Drilling.” Oil Drilling & Production Technology, Vol 30(6): pp 1-4.

Kapitaniak M, Vaziri Hamaneh V, Chávez JP, Nandakumar K, Wiercigroch M (2015). Unveiling complexity of drill-string vibrations: experiments and modelling. Int. J. Mech. Sci., 101–102, pp. 324-337, 10.1016/j.ijmecsci.2015.07.008

Karnopp D. (1985), Computer simulation of stick–slip friction in mechanical dynamic systems, ASME J Dyn Syst Meas Control. 107(1) 100–103.

Khulief YA, Al-Naser H. (2005). Finite element dynamic analysis of drillstrings. J. Finite Elem. Anal. Des. 41,1270–1288.

Khulief YA, Al-Sulaiman FA, Bashmal S (2007). Vibration analysis of drillstrings with self-excited stick–slip oscillations. J. Sound Vibr. 299, 540–558

Khulief YA, Al-Sulaiman FA, Bashmal S. (2008). Vibration analysis of drillstrings with string-borehole interaction. Int. J. Mech. Eng. Sci., IMechE Part C 222, 2099–2110

Kyllingstad A, Halsey GW. (1988, December 1). A Study of Slip/Stick Motion of the Bit. Society of Petroleum Engineers. doi:10.2118/16659-PA.

Kyllingstad, A., Nessjøen, P.J., 2009. A New Stick-Slip Prevention System. Society of Petroleum Engineers. https://doi.org/10.2118/119660-MS

Lai Y, Zhu B, Huang Y, Chen C, 2020. Behaviors of drag embedment anchor in layered clay profiles. Applied Ocean Research 101, 102287, https://doi.org/10.1016/j.apor.2020.102287.

Lanan, G.A., Cowin, T.G. & Johnston, D.K. 2011, "Alaskan Beaufort Sea Pipeline Design, Installation and Operation," Proceedings of the Arctic Technology Conference, February 7 - 9, 2011, 9p.

Larsen, C. M. (1990). Response Modelling of Marine Risers and Pipelines. Trondheim: NTNU, Division of marine structures.

Leine R.I., van Campen D.H., de Kraker A., van den Steen L. (1998), Stick–slip vibrations induced by alternate friction models, Nonlinear Dyn. 16;41–54.

Leine, R.I., van Campen, D.H., Keultjes, W.J.G. (2002) Stick-slip whirl interaction in drillstring dynamics. J. Vib. Acoust. 124(2), 209–220.

Lesso B., Ignova M., Zeineddine F., Burks J., and Welch B. (2011). Testing the combination of high frequency surface and downhole drilling mechanics and dynamics data under a variety of drilling conditions. In SPE/IADC Drilling Conference and Exhibition, SPE/IADC 140347, Amsterdam, Netherlands.

Liao C.M., Vlajic N., Karki H., Balachandran B. (2012), Parametric studies on drill-string motions, Int. J. Mech. Sci. 54;260–268.

Liao, C.-M., Balachandran, B., Karkoub, M., Abdel-Magid, Y.L. (2011) Drill-string dynamics: reduced-order models and experimental studies. J. Vib. Acoust. 133(4), 041008

Liao, C.M., Vlajic, N., Karki, H., Balachandran, B., 2012. Parametric studies on drill-string motions. Int. J. Mech. Sci. 54 (1), 260–268. https://doi.org/10.1016/j.ijmecsci.2011.11.005

Ligrone, A., Botto, G., Calderoni, A. 1995. Reliability Methods Applied to Drilling Operations. Society of Petroleum Engineers. doi:10.2118/29355-MS

Lin Y.Q., Wang Y.H. (1991), Stick-slip vibration of drillstrings, ASME J. Eng. Ind. 113 (1) 38–43.

Liu M., Gorman D.G. (1995), Formulation of Rayleigh damping and its extensions, Computers and Structures. 57(2) 277–285

Liu X, Long X, Zheng X, Meng G, Balachandran B (2020). Spatial-temporal dynamics of a drill string with complex time-delay effects: Bit bounce and stick-slip oscillations. International Journal of Mechanical Sciences 170;105338.

Liu X, Vlajic N, Long X, Meng G, Balachandran B (2013). Nonlinear motions of a flexible rotor with a drill bit: stick-slip and delay effects, Nonlinear Dyn. 72 (1-2) 61-77.

Liu X., Vlajic N., Long X., Meng G., Balachandran B., (2014), Coupled axial-torsional dynamics in rotary drilling with state-dependent delay: stability and control, Nonlinear Dyn.

Liu, X., Vlajic, N., Long, X., Meng, G., Balachandran, B., 2014. State-Dependent Delay Influenced Drill-String Oscillations and Stability Analysis. ASME. J. Vib. Acoust. 136 (5): 051008. https://doi.org/10.1115/1.4027958

Liu, Y., Páez Chávez, J., De Sa, R. et al., (2017), Numerical and experimental studies of stick–slip oscillations in drill-strings. Nonlinear Dyn 90, 2959–2978. https://doi.org/10.1007/s11071-017-3855-9

Luke AM, Rauch AF, Olson RE, Mecham EC, 2003. Components of suction caisson capacity measured in axial pullout tests. Proceedings of international symposium on deepwater Mooring Systems.

Ma C., Dong Y Q. and Yang L. T. (2000) Comparative Study of Vortex-Induced Nonlinear Oscillation of TLP Tethers Under Two Different Boundary Conditions. Ship Mechanics, 4(1), pp 56-64.

Ma KT, Duggal A, Smedley P, L'Hostis D, Shu H., 2013 A historical review on integrity issues of permanent mooring systems. Proceedings of Offshore Technology Conference OTC 24025; May 6-9; Houston, Texas. https://doi.org/10.4043/24025-MS

Ma, K.T., Luo, Y., Thomas Kwan, C.T., Wu, Y., (2019). Mooring System Engineering for Offshore Structures, Elsevier.

MacDonald K.A., Bjune J.V. (2007), Failure analysis of drillstrings, Eng. Fail. Anal. 14;1641–1666.

Macdonald, K.A., Bjune, J.V., 2007. Failure analysis of drillstrings. Engineering Failure Analysis, 14 (8), 1641-1666,

Macdonald, K.A., Bjune, J.V., 2007. Failure analysis of drillstrings. Engineering Failure Analysis, 14 (8), 1641-1666,

Matlock, H (1970). "Correlations for Design of Laterally Loaded Piles in Soft Clay." Proceedings of the 2nd annual Offshore Technology Conference, Paper No. OTC 1204.

Melchers RE, Ahammed M, Middleton C, 2003. FORM for discontinuous and truncated probability density functions. Struct. Saf. 25(3):305-13. doi: https://doi.org/10.1016/S0167-4730(03)00002-X

Mihajlovic N, van Veggel AA, van de Wouw N, Nijmeijer H, (2004) Analysis of friction-induced limit cycling in an experimental drill-string system, ASME J. Dynam. Systems Measurement Control 126;709-720.

Millheim K, Jordan S, Ritter C (1978). Bottom-hole assembly analysis using the finite element method, SPE paper no. 6057;p.265–74.

Mitchell RF, Allen MB (1987). Case studies of BHA vibration failure, SPE 16675, Proceedings of the 62nd SPE Annual Technical Conference & Exhibition, Dallas, TX, September 27–30.

Mitchell, R.F., Miska, S., 2011. Fundamentals of Drilling Engineering. Society of Petroleum Engineers, Technology & Engineering

Moharrami, M.J., Shiri, H., 2018. Reliability assessment of drag embedment anchors in clay for catenary mooring systems. Marine Structures, 58, 342-360, ISSN 0951-8339,https://doi.org/10.1016/j.marstruc.2017.12.005.

Murff, J. D. and Hamilton, J. M. (1993). P-Ultimate for Undrained Analysis of Laterally Loaded Piles, J. Geot. Eng. Div., ASCE, 119(1), Jan, pp. 91-107.

Najjar SS, 2005. The Importance of lower-bound capacities in geotechnical reliability assessments [dissertation]. The University of Texas at Austin.

Nandakumar K., Wiercigroch M. (2013), Stability analysis of a state dependent delayed, coupled two DOF model of drill–string vibration, J. Sound Vib. 332 (10) 2575–92.

Navarro-López EM (2009). An alternative characterization of bit-sticking phenomena in a multi-degree-of-freedom controlled drillstring. Nonlinear Anal Real World Appl 10(5):3162–74.

Navarro-López EM, Cortes D. (2007) Avoiding harmful oscillations in a drillstring through dynamical analysis. J. Sound Vib. 307,152–171.

Navarro-López EM, Licéaga-Castro E (2009). Non-desired transitions and sliding-mode control of a multi-DOF mechanical system with stick–slip oscillations. Chaos Solitons Fractals 41(4):2035–44.

Nessjoen P.J., Kyllingstad A., Dambrosio P., Fonseca I.S., Garcia A., Levy B., (2011), Field Experience with an Active Stick-Slip Prevention System, Society of Petroleum Engineers.

Netto, T.A., Lourenco M.I., Botto, A., 2008. Fatigue performance of pre-strained pipes with girth weld defects: full-scale experiments and analysis. Int. J. Fatigue 30:767–778

Netto, T.A., Lourenco M.I., Botto, A., 2008. Fatigue performance of pre-strained pipes with girth weld defects: full-scale experiments and analysis. Int. J. Fatigue 30:767–778

Neubecker SR, Randolph MF, 1995(a). Performance of embedded anchor chains and consequences for anchor design. Proceedings of Offshore Technology Conference OTC 7712; 1995 May 1-4; Houston, Texas; pp. 191–200. https://doi.org/10.4043/7712-MS

Neubecker SR, Randolph MF, 1995(b). Profile and frictional capacity of embedded anchor chains. J. Geotech. Eng. 121(11):797-803. doi: https://doi.org/10.1061/(ASCE)0733-9410(1995)121:11(797)

Neubecker SR, Randolph MF, 1996. The performance of drag anchor and chain systems in cohesive soil. Mar. Georesources Geotechnol 14(2):77-96. doi: http://dx.doi.org/10.1080/10641199609388305

Neubecker, S.R. and Randolph, M.F. 1995a. Performance of embedded anchor chains and consequences for anchor design. Proceedings of Offshore Technology Conference OTC 7712, Houston, Texas.

Neubecker, S.R. and Randolph, M.F. 1995b. Profile and frictional capacity of embedded anchor chains. J. Geotech. Eng., Volume 121, Issue 11, p.p. 787-803

O'Neill, M. P., Randolph, M. F., and House, A. R. (1999, March 1). The Behaviour of Drag Anchors In Layered Soils. International Society of Offshore and Polar Engineers.

O'Neill, M.P., Bransby, M.F., Randolph, M.F., 2003. Drag anchor fluke-soil interaction in clays. Can. Geotech. J. 40(1):78–94. doi: 10.1139/T02-096

Oden, J.T., Martins, J.A.C., 1985. Models and computational methods for dynamic friction phenomena. Computer Methods in Applied Mechanics and Engineering, 52 (1–3), 527–634. https://doi.org/10.1016/0045-7825(85)90009-X

Oden, J.T., Martins, J.A.C., 1985. Models and computational methods for dynamic friction phenomena. Computer Methods in Applied Mechanics and Engineering, 52 (1–3), 527–634. https://doi.org/10.1016/0045-7825(85)90009-X

Oden, J.T., Martins, J.A.C., 1985. Models and computational methods for dynamic friction phenomena. Computer Methods in Applied Mechanics and Engineering, 52 (1–3), 527–634. https://doi.org/10.1016/0045-7825(85)90009-X

Ozmutlu S, 2012. The use of drag embedment anchors in offshore mooring systems. Vryhof anchors BV Netherlands. OTEO International Conference on Offshore Renewable Energy.

Ozmutlu, S. (2009, January 1). The Value of Model Testing in Understanding the Behavior of Offshore Anchors: Towards New Generation Anchors. Offshore Technology Conference. doi:10.4043/20035-MS

Paidoussis MP, Luu TP, Prabhakar S. (2008). Dynamics of a long tubular cantilever conveying fluid downwards, which then flows upwards around the cantilever as a confined annular flow. Journal of Fluids and Structures, vol. 24, pp. 111–128.

Païdoussis, M.P., Luu, T.P., Prabhakar, S., 2008. Dynamics of a long tubular cantilever conveying fluid downwards, which then flows upwards around the cantilever as a confined annular flow, J. Fluids Struct. 24 (1), 111–128, https://doi.org/10.1016/j.jfluidstructs.2007.07.004

Païdoussis, M.P., Semler, C., 1998. Non-linear dynamics of a fluid-conveying cantilevered pipe with a small mass attached at the free end. Int. J. Non Linear Mech. 33 (1) 15–32, https://doi.org/10.1016/S0020-7462(97)00002-4

Pavlovskaia E., Hendry D. C., and Wiercigroch M. (2015). Modelling of high frequency vibro-impact drilling. International Journal of Mechanical Sciences, 91(0):110 – 119.

Pavone D.R., Desplans J.P., (1994), Application of high sampling rate downhole measurements for analysis and cure of stick–slip in drilling, Society of Petroleum Engineers.

Private communications with Field operator.

Randolph, Mark, and Susan Gourvenec. Offshore Geotechnical Engineering, Taylor & Francis Group, 2011. ProQuest Ebook Central

Rao S.S. (2011), Mechanical vibrations, fifth ed., Pearson.

Rayleigh, L., 1945. Theory of Sound, 1. Dover: New York, NY.

Real FF, Batou A, Ritto TG, Desceliers C, Aguiar RR (2018). Hysteretic bit/rock interaction model to analyze the torsional dynamics of a drill string. Mechanical Systems and Signal Processing 111; 222–233

Reese, L., Cox, W. and Koop F. (1974). "Analysis of Laterally Loaded Piles in Sand." Proceedings of the 6th annual Offshore Technology Conference, Paper No. OTC 2080.

Richard T, Germay C, Detournay E (2007). A simplified model to explore the root cause of stick-slip vibrations in drilling systems with drag bits. J Sound Vib 305(3):432–56.

Richard T., Detournay E., (2000), Stick-Slip Vibrations of PDC Bits, American Rock Mechanics Association.

Richard, T., Germay, C., Detournay, E. (2004) Self-excited stickslip oscillations of drill bits. C. R., Méc. 332(8), 619–626

Ritto TG, Sampaio R (2012). Stochastic drill-string dynamics with uncertainty on the imposed speed and on the bit-rock parameters. Int J Uncertain Quantif;2(2)

Ritto TG, Sampaio R, Soize C (2009a). Drill-string nonlinear dynamics accounting for the drilling fluid. 30º CILAMCE-Iberian-Latin-American Congress on Computational Methods in Engineering, Armação dos Búzios, Rio de Janeiro, Brazil

Ritto TG, Soize C, Sampaio R, (2009b). Non-linear dynamics of a drill–string with uncertain model of the bit–rock interaction. Int J Non-Linear Mech;44:865–76

Rohleder, S. A., Sanders, W. W. and Williamson, R. N. (2003). "Challenges of drilling an ultra-deep well in deepwater-spa prospect." SPE/IADC 79810.

Rohleder,S. A., Sanders, W. W. and Williamson, R. N. (2003). "Challenges of drilling an ultra-deep well in deepwater-spa prospect." SPE/IADC 79810

Ruinen, R. (2012, January 1). The Use of Drag Embedment Anchors in Arctic Conditions. The Society of Naval Architects and Marine Engineers.

Sampaio R, Piovan MT, Lozano GV. (2007). Coupled axial/torsional vibrations of drill-strings by means of non-linear model. J. Mech. Res. Commun. 34,497–502.

Sarkar A, Eatock Taylor R, 2000. Effects of mooring line drag damping on response statistics of vessels excited by first- and second-order wave forces. Ocean Eng. 27(6):667-86. doi: https://doi.org/10.1016/S0029-8018(99)00014-1

Sarpkaya, T., Issacson, M., 1981. Mechanics of Wave Forces on Offshore Structures. Van Nostrand Reinhold, NY.

Schijve, J., 2003. Fatigue of structures and materials in the 20th century and the state of the art. Int. J. Fatigue, 25(8), 679-702

Sepehri N., Sassani F., Lawrence P.D., Ghasempoor A. (1996), Simulation and experimental studies of gear backlash and stick-slip friction in hydraulic excavator swing motion, ASME J Dyn Syst Meas Control. 118;463–467.

Serrarens A.F.A., van de Molengraft M.J.G., Kok J.J., van den Steen L. H∞ control for suppressing stick – slip in oil well drillstrings IEEE Control Systems Magazine, 18 (1998), pp. 19-30

Silva-Gonzalez F, Heredia-Zavoni E, Valle-Molina C, Sanchez-Moreno J, Gilbert RB, 2013. Reliability study of suction caissons for catenary and taut-leg mooring systems. J. Struct. Saf. 45:59–70. doi: http://dx.doi.org/10.1016/j.strusafe.2013.08.011

Silva-Gonzalez, F., Heredia-Zavoni, E., Valle-Molina, C., Sanchez-Moreno, J., Gilbert, R.B. 2013. Reliability study of suction caissons for catenary and taut-leg mooring systems. J. Struct. Saf.

Silveira M. (2011), A comprehensive model of drill-string dynamics using Cosserat rod theory, (2011) Diss., University of Aberdeen.

Spanos PD, Payne ML, Secora CK. (1997). Bottom-hole assembly modeling and dynamic response determination. ASME J. Energy Resour. Technol. 119(3), 153–158

Sparks, C.P. (2002). “Transverse Modal Vibrations of Vertical Tensioned Risers – A Simplified Analytical Approach,”

Sparrevik, P. (1998), Suction Anchors – A Versatile Foundation Concept Finding its Place in the Offshore Market, OMAE 98-3096, 17th International Conference on Offshore Mechanics and Arctic Engineering, Lisbon, Portugal.

Stephens, R,I., Fatemi, A., Stephens, R.R., Fuchs, H.O., 2001. Metal Fatigue in Engineering, 2nd ed. New York: Wiley.

Su, Kanhua & Butt, Stephen & Yang, James & Qiu, Hongyuan. (2018). Coupled Dynamic Analysis for the Riser-Conductor of Deepwater Surface BOP Drilling System. Shock and Vibration. 2018. 1-15. 10.1155/2018/6568537.

Taylor R, Valent P, 1984. Design guide for drag embedment anchors.

Tian Y, Randolph MF, Cassidy MJ, 2015. Analytical solution for ultimate embedment depth and potential holding capacity of plate anchors. Géotechnique 65(6):517–30. doi: https://doi.org/10.1680/geot.14.P.228.

Tofa, M & Maimun, Adi & Ahmed, Yasser. (2012). "Fundamentals of vortex induced vibration analysis of marine riser.

Trindade M., Sampaio R. (2002), Dynamics of beams undergoing large rotations accounting for arbitrary axial rotations. J Guid Control Dyn; 25(4):634–43.

Trindade MA, Wolter C, Sampaio R. (2005). Karhunen–Loeve decomposition of coupled axial/bending vibrations of beams subject to impacts. J. Sound Vib. 279, 1015–1036

Tucker R.W., Wang C., (1999). On the effective control of torsional vibrations in drilling systems, Journal of Sound and Vibration 224;101–122.

Tucker, R.W. Wang, C., (2003). Torsional vibration control and cosserat dynamics of a drill-rig assembly. Meccanica, vol. 38, n. 1, pp. 143–159.

Valle-Molina C, Heredia-Zavoni E, Silva-González FL, 2008. Reliability analysis of suction caissons for FPSO systems. Proceedings of the ASME 27th International Conference on Offshore Mechanics and Arctic Engineering OMAE 57140; June 15-20; Estoril, Portugal; pp. 1–6.

Valle-Molina, C., Heredia-Zavoni, E., Silva-González, F.L. 2008. Reliability analysis of suction caissons for FPSO systems. Proceedings of the ASME 27th International Conference on Offshore Mechanics and Arctic Engineering OMAE 57140, Estoril, Portugal, pp. 1–6.

Vlajic, N., Fitzgerald, T., Nguyen, V., Balachandran, B., 2014a. Geometrically exact planar beams with initial pre-stress and large curvature: Static configurations, natural frequencies, and mode shapes. Int. J. Solids Struct. 51 (19–20), 3361–3371. https://doi.org/10.1016/j.ijsolstr.2014.05.026

Vlajic, N., Liu, X., Karki, H., Balachandran, B., 2014b. Torsional oscillations of a rotor with continuous stator contact. Int. J. Mech. Sci. 83, 65–75. https://doi.org/10.1016/j.ijmecsci.2014.03.025

Vlasov V.Z. (1961), Thin Walled Elastic Beams, second ed., National Science Foundation, Washington, DC, Israel Program for Scientific Translation, Jerusalem, Israel [First edition – Stroizdat (in Russian) Moscow, 1940].

Vromen, T., van de Wouw, N., Doris, A., Astrid, P., Nijmeijer, H., 2017. Nonlinear output-feedback control of torsional vibrations in drilling systems. Int. J. Robust Nonlinear Control. 27, 3659– 3684. https://doi.org/10.1002/rnc.3759

Vryhof (2000), Anchor Manual, Vryhof Anchors B.V., Krimpen a/d Yssel, The Netherlands.

Vryhof Anchors. 1990. Anchor manual. Krimpen ad Yssel, The Netherlands.

Vryhof Anchors. 2010. Anchor manual. Krimpen ad Yssel, The Netherlands.

Vryhof Manual (2015), The Guide to Anchoring, Vryhof Anchors B.V., 2015

Wang LZ, Guo Z, Yuan F, 2010. Quasi-static three-dimensional analysis of suction anchor mooring system. Ocean Eng 37(13):1127–38. doi:10.1016/j.oceaneng.2010.05.002

Y. Kim and S. Jeong (2011). "Analysis of Soil Resistance on Laterally Loaded Piles Based on 3D Soil–Pile Interaction." Computers and Geotechnics 38.

Yigit A.S., Christoforou A.P (1998), Coupled torsional and bending vibrations of drillstrings subject to impact with friction. J. Sound Vib. 215;167–181.

Yigit A.S., Christoforou A.P. (2000), Coupled torsional and bending vibrations of actively controlled drillstrings Journal of Sound and Vibration, 234, pp. 67-83

Yigit A.S., Christoforou A.P. (2006), Stick-Slip and Bit-Bounce Interaction in Oil-Well Drillstrings, ASME J. Energy Resour. Technol. 128(4) 268–274.

Zamanian M., Khadem S.E., Ghazavi M.R., (2007), Stick-slip oscillations of drag bits by considering damping of drilling mud and active damping system. Journal of Petroleum Science and Engineering, 59;289–299.